

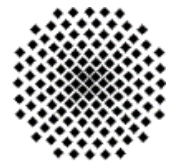


Max-Planck-Institute für Intelligente Systeme
Stuttgart

**Tailored Magnetic Properties of
Exchange-Spring and Ultra Hard Nanomagnets**

Kwanghyo Son

Dissertation
An der
Universität Stuttgart



2017

Tailored Magnetic Properties of Exchange-Spring and Ultra Hard Nanomagnets

**Von der Fakultät Mathematik und Physik der Universität Stuttgart
zur Erlangung der Würde eines
Doktors der Naturwissenschaften (Dr. rer. nat.)
genehmigte Abhandlung**

Vorgelegt von
Kwanghyo Son
aus Seoul, SüdKorea

**Hauptberichter: Prof. Dr. Gisela Schütz
Mitberichter: Prof. Dr. Sebastian Loth**

Tag der mündlichen Prüfung: 04. Oktober 2017

**Max-Planck-Institut für Intelligente Systeme, Stuttgart
2017**

Contents

Contents.....	1
Chapter 1.....	1
General Introduction	1
Structure of the thesis	3
Chapter 2.....	5
Basic of Magnetism	5
2.1 The Origin of Magnetism	5
2.1.1 Magnetic moment	5
2.1.2 Magnetization and Field.....	6
2.2 The Classes of Magnetic Materials	7
2.2.1 Ferromagnetism	7
2.2.2 Antiferromagnetism and Ferrimagnetism	9
2.2.3 Paramagnetism.....	10
2.2.4 Diamagnetism	11
2.3 Basics of Ferromagnetic Hysteresis loop	12
2.3.1 The Stoner-Wohlfarth (S-W) model	14
2.3.2 Preisach model and First Order Reversal Curves	15
2.4 Micromagnetism.....	17
2.4.1 Magnetic free energy	17
2.4.2 Domain and Domain Walls.....	19
2.4.3 Single- and Multi-Domain particles	20
2.4.4 Coercivity and Microstructural parameters	22
2.5 X-ray and Magnetism	24
2.5.1 X-ray Absorption Spectroscopy (XAS)	24
2.5.2 X-ray Magnetic Circular Dichroism (XMCD)	26
2.5.3 Sum rules	28

Chapter 3.....	33
Basic of Nanosized Exchange Spring Magnets	33
3.1 Nanomagnets	33
3.2 Exchange-Spring magnet	36
3.2.1 Soft and Hard Ferromagnetic materials.....	37
3.2.2 Exchange-coupling effect	39
3.2.2.1 Critical size for exchange-coupling effect.....	40
3.3 L1 ₀ -FePt / Co composition ES magnet.....	41
3.3.1 Phase diagram and Crystal Structures of FePt and Cobalt	42
3.3.1.1 FePt.....	42
3.3.1.2 Cobalt.....	44
 Chapter 4.....	 45
Experimental methods: Fabrication & Characterization.....	45
4.1 Sample preparation	45
4.1.1 Sputter deposition of thin films (Magnetron Sputtering)	45
4.1.2 Manufacture of regular nanopatterns	46
4.1.3 Structure and microstructure characterization method.....	49
4.1.3.1 X-ray diffraction (XRD)	49
4.1.3.2 Atomic / Magnetic force microscopy (AFM, MFM).....	50
4.1.3.3 Scanning electron microscopy (SEM).....	51
4.1.3.4 Wavelength-dispersive X-ray analysis (WDX_EPMA).....	51
4.1.3.5 Transmission electron microscopy (TEM).....	51
4.2 Characterization of magnetic properties via SQUID.....	53
4.2.1 SQUID magnetometry	53
4.2.1.1 Correction of Diamagnetism	54
4.2.2 Magnetic parameters	54
4.2.2.1 Saturation polarization J_s	54
4.2.2.2 Anisotropy constant K_1	55
4.2.2.3 Exchange stiffness constant A	56
4.2.2.4 Microstructural parameter, α , and N_{eff}	57
4.2.3 First order reverse curves (FORC) measurement	58
4.2.3.1 FORC density analysis.....	58
4.3 Characterization of magnetic systems via XMCD	60
4.3.1 Synchrotron Radiation - WERA beamline at ANKA.....	60
4.3.1.1 Total Electron Yield (TEY) mode.....	63
4.3.1.2 Correction of Saturation effect _self-absorption	64

Chapter 5.....	67
Results: Artificially structured exchange-spring nanomagnets	67
5.1 L1 ₀ -FePt / Co nanopatterned samples	68
5.1.1 Characterization of the thin film structure.....	69
5.1.1.1 Crystal structure	69
5.1.1.2 SEM images of the continuous films	70
5.1.2 Characterization of the nanopattern structure.....	71
5.1.2.1 AFM and MFM results.....	71
5.1.2.2 TEM images of the nanomagnets	72
5.2 Magnetic properties	73
5.2.1 Temperature dependence of hysteresis loops	75
5.2.2 Microstructural parameters	79
5.2.3 FORCs results	80
5.2.4 Magnetic reversal process in partially coupled ES magnet	82
5.3 Conclusion: Influence of the soft magnet fraction in artificial nanosized exchange-spring magnets.....	83
 Chapter 6.....	 85
Results: Exchange-spring granular nanomagnets	85
6.1 L1 ₀ -FePt/ Pt/ Co composition island structure	85
6.1.1 Crystal structure	86
6.1.2 Morphology	87
6.2 Characterizations of magnetic properties	88
6.2.1 Temperature dependence of hysteresis loops	90
6.2.2 Micromagneticstructure parameters	94
6.2.3 Extended FORCs results	95
6.2.4 XMCD results	97
6.2.5 Hysteresis with XMCD.....	99
6.3 Conclusion: Influence of the thickness of a Pt interlayer between a L1 ₀ -FePt hard and a Co soft magnetic layer on the magnetic behavior of exchange-spring nanomagnets	101
 Chapter 7.....	 103
Results: Realized high coercive field and maximum energy product (BH) _{max} with ultra-hard nanomagnets	103
7.1 L1 ₀ -FePt island structure	104

7.1.1	Crystal structure	105
7.1.2	Morphology	106
7.2	Characterizations of magnetic properties	107
7.2.1	Magnetic hysteresis curves	107
7.2.2	Energy product.....	108
7.2.3	X-ray Magnetic Circular Dichroism Results	110
7.3	Conclusion: Realize huge coercive field and maximum energy product $(BH)_{\max}$ with ultra-hard nanomagnet.....	113
Chapter 8	115
Summary	115
Chapter 9	119
Zusammenfassung	119
Appendix A	123
Appendix B	135
Appendix C	141
Literature	143
Acknowledgement	151
Curriculum Vitae	152

List of Abbreviations

AF	Antiferromagnetic
AFM	Atom Force Microscopy
AI	Angle Incidence
ECC	Exchange-Coupled Composition
EDX	Energy-dispersive X-ray spectroscopy
EPMA	Electron Probe Micro-Analyzer
ESM	Exchange-Spring Magnet
FM	Ferromagnetic
FiM	Ferrimagnetic
FORC	First Order Reversal Curve
ICP-RIE	Inductively coupled plasma-Reactive-ion etching
RT	Room Temperature
MAE	Magnetic Anisotropy Energy
MFM	Magnetic Force Microscopy
NI	Normal Incidence
NIL	Nanoimprint lithography
SOC	Spin-Orbit Coupling
SQUID	Superconducting Quantum Interference Device
SEM	Scanning Electron Microscopy
TEM	Transmission Electron Microscopy
TEY	Total Electron Yield
WDX	Wavelength Dispersive X-ray Analysis
XAS	X-ray Absorption Spectroscopy
XMCD	X-ray Magnetic Circular Dichroism
XRD	X-Ray Diffraction

Chapter 1

General Introduction

Magnetism is an attractive and exciting area in condensed matter physics, fascinating for fundamental research and various technological applications. Magnetism has been studied on natural permanent magnetic materials for almost three thousand years. Today, scientific and technological interests in magnetism extend over a wide field of different subjects, from massive magnets to low-dimensional systems. Technologically, magnetic materials issue a variety of different applications in electrical power generation, power generators, transmission lines, and conversion and transportation systems including suitable permanent magnets. In recent times, magnetic systems with reduced dimensions have been studied and applied: as high-density magnetic storage devices, sensors, in spintronic applications, in nanomedicine, and many other fields. Such systems have different physical and chemical properties because e.g. the surface to volume ratio increases, the interaction between different grains changes and the dimensions of the grains often approach the critical domain size for magnetic systems. In a number of studies, especially the magnetic properties of such nano-sized magnets have been engineered by precise size control and by varying the composition of the magnetic materials [1-5]. Examples of these systems are exchange-spring magnets that are subject of this thesis.

The exchange-spring magnet (ESM), also called exchange-coupled composition (ECC) magnet, is composed of magnetically hard and soft materials. Therefore, they exhibit as an advanced attribute the huge coercivity H_c of the hard magnets and the high magnetization M_s of the soft magnets (see Fig. 1.1). To realize these ECC magnets, rare-earth permanent magnets or $L1_0$ -phase alloys (e.g. FePt, CoPt, FePd and MnAl) with strong uniaxial anisotropy are exchange-coupled with transition metals, such as pure Fe, Co, Ni, or soft magnetic alloys such as Permalloy. As a result, the magnetic hysteresis loop reflects the combination of hard and soft magnetic components (see Fig. 1.1). Therefore, the ideal hysteresis loops of exchange spring magnets can have much higher energy products than those of the components themselves which are desirable for many applications, in particular also for traction motors, electric vehicles and magnetic data storage devices. In addition to combining magnetically hard and soft materials, tuning the size of the magnetic particles can be used to modify the magnetic properties. This has been shown by our group in previous research by tuning in this way the coercive field of pure FePt nanomagnets [3].

In this thesis, FePt/Co exchange-spring nanomagnets of various sizes were prepared starting with thin Co/FePt films on single crystalline MgO. The films consisted of layers of chemically ordered $L1_0$ -phase FePt (magnetically hard) and - on top - layers of Co (magnetically soft) of various thicknesses. The films were nano-patterned in order to obtain the desired nano-magnets. The structures were capped by a thin Pt film as a protective layer. In the second set of samples, thin Pt layers were introduced as buffer layers in between the FePt and the Co films.

$L1_0$ -FePt is well known as a typical rare earth-free hard-magnetic material with high magneto-crystalline anisotropy ($K_u = 6.6 \text{ MJ/m}^3$, $J_s = 1.43 \text{ T}$). The chemically ordered $L1_0$ phase shows a face-centered tetragonal (fct) crystal structure. The magnetization of these thin films on MgO (100) substrates orients the tetragonal c-axis perpendicular to the film plane. To realize high coercive fields in the nano-magnets, the samples can be post-annealed.

As transition metal, Co is appropriate as soft magnet component ($K_1 = 0.45 \text{ MJ/m}^3$, $J_S = 1.76 \text{ T}$). As demonstrated in this thesis, the general magnetic behavior of such a FePt/Co couple can be modified by changing the nominal thickness of the Co layer or by introducing a thin Pt buffer layer in between.

The structural properties of the samples were investigated by X-ray diffraction (XRD), atomic/magnetic force microscopy (AFM, MFM), scanning electron microscopy (SEM) and transmission electron microscopy, the magnetic properties by SQUID magnetometry and the XMCD (X-ray circular dichroism) technique.

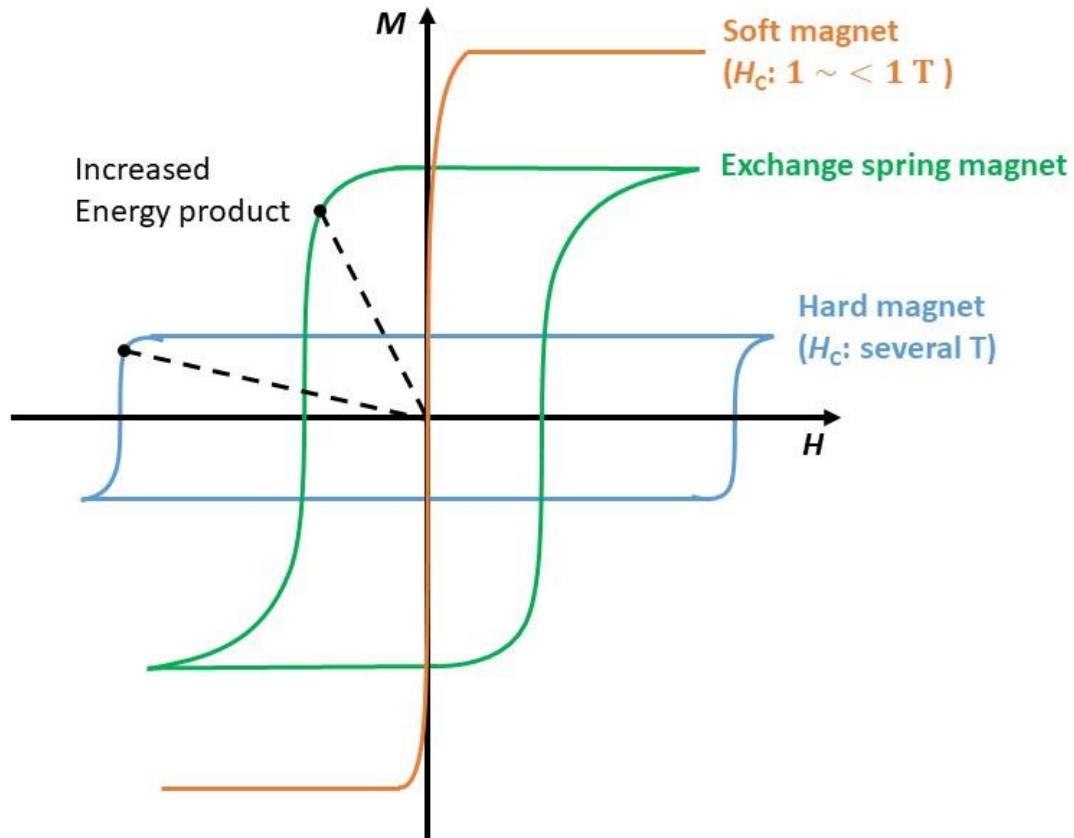


Fig.1. 1 The magnetic hysteresis loops of hard (blue), soft (orange) and exchange-spring magnets (green). H is the applied external magnetic field and M is the magnetization of the materials.

Structure of the thesis

Chapter 2 introduces the basics of magnetism, outlines the fundamentals of micromagnetism, and gives an introduction to the theory and application of the method of “First order reverse curves (FORCs)” [6, 7] and into X-ray circular dichroism (XMCD) measurements[8], techniques that allow to study magnetic properties in detail.

Chapter 3 deals with exchange-spring magnet materials. Hard magnets and soft magnets are introduced. Especially, the L1₀-FePt hard magnet and the Co soft magnet are explained in detail.

Chapter 4 presents the fabrication routes and the various techniques applied to characterize the structure and the magnetic properties of the samples. The sample structure was studied by X-ray diffraction (XRD), atomic/magnetic force microscopy (AFM, MFM), scanning electron microscopy (SEM) and transmission electron microscopy, the magnetic properties by SQUID magnetometry and XMCD (X-ray circular dichroism). To vary the coercivity, the size and composition of the magnetic particles were changed.

Chapter 5 describes how the magnetic properties of the nanosized exchange-spring magnets, which are artificially fabricated, change with different thicknesses of the Co layer. This gives an idea how to optimize the ES nanomagnets.

Chapter 6 describes how the strength of the exchange coupling between the Co and the FePt layer can be controlled by a Pt interlayer and how this influences the magnetic properties of naturally formed nano-islands of exchange spring magnetics. The presence of different 3d elements involved- here Fe and Co – allows in particular to investigate the magnetic reversal process by element-specific XMCD.

Chapter 7 describes the realization of the large coercive field and maximum energy product $(BH)_{\max}$ with L1₀-FePt hard magnetic phases.

Chapter 2

Basic of Magnetism

This chapter provides a brief summary of the basics of magnetism as found in standard text books.[8-10] General magnetism, types of magnetism and related phenomena, micromagnetism and the theory of the experimental techniques will be explained.

2.1 The Origin of Magnetism

Magnetism originates from the spin and orbital magnetic moment of electrons in atoms. The orbital motion of an electron with a negative charge around the nucleus is similar to the current in a loop of wire. The spin is the intrinsic angular momentum of an electron. The magnetic moments of nuclei of atoms are about 2000 times smaller than the moments of the electrons. To describe the properties of the atoms properly, quantum mechanics must be applied. Here, quantum numbers describe the state of electron levels and are called angular momentum l , spin projection quantum number s and the total angular momentum j .

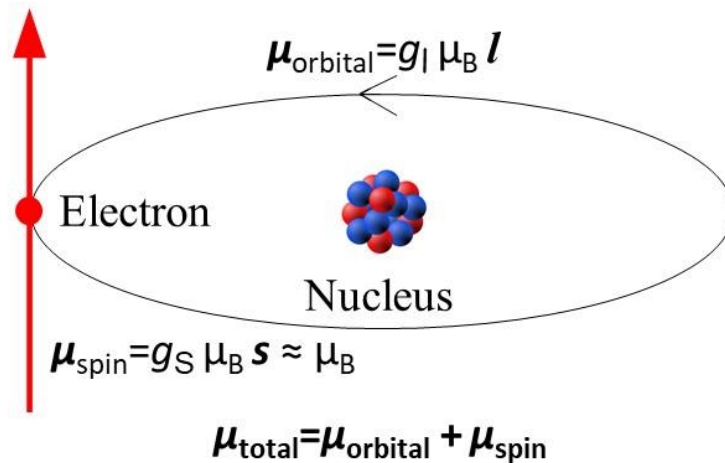


Fig.2. 1 Origin of Magnetism. Magnetism in materials originates from the electrons of the atom. Electrons have a spin moment and an orbital moment. The latter is due to the orbital motion of the electrons around the nucleus. The spin moments of the nuclei are negligible.

2.1.1 Magnetic moment

The magnetic moment \vec{m} of a current loop is given by

$$\vec{m} = IS\hat{n} \quad (2.1)$$

Here, \hat{n} is the unit vector with direction perpendicular to the current loop in the right-hand-rule direction. The amount of the magnetic moment \vec{m} is equal to the product of the area S of the current loop and the current I through this loop. Therefore, the unit for magnetic moment is ampere square meter ($A m^2$) or joule per tesla (J/T) in the International System of Units (SI). The quantity J/T says that the magnetic moment is the ratio of the magnetic energy and the external field.

In an atom, the spin and orbital angular momentum are present, if the atomic level as the 3d and 5d shell in transition elements and the 4f shell in Rare Earths are unfilled. Hereby, in the L-S coupling, scheme following Hunds Rule the individual electrons couple to the total spin momentum S and an angular orbital momentum L . The total angular momentum J is given by $J = L - S$ for less than half-filled shells and $J = L + S$ for more than half-filled levels. For the most important magnetic transition elements Fe, Co and Ni and the 5d element Pt the corresponding values are listed in Table. 2.1. It also includes the measured magnetic moments for the pure metal, which differ significantly. This phenomenon will be outlined in more detail in the next chapter

	S	L	J	$m_j[\mu_B] (g[J(J+1)]^{1/2})$	Pure metal	
					$m_s[\mu_B]$	$m_l[\mu_B]$
Fe	2	2	4	6.7	1.98	0.083
Co	1.5	3	4.5	6.63	1.55	0.153
Ni	1	3	4	5.59	0.6	0.06

Table 2. 1 Spin, orbital, and total magnetic moment of Fe, Co, Ni, and Pt. [11, 12]

2.1.2 Magnetization and Field

The magnetization or magnetic polarization expresses the vector field density of the magnetic moment in a magnetic materials. The magnetization also describes the magnetic induction by an external magnetic field and is defined as the vector sum of all magnetic moments in the magnetic material. Generally, magnetic moments per unit volume are assumed, in some cases also moments per unit mass are considered.

$$\vec{M} = \frac{1}{V} \sum \vec{\mu} = \frac{\vec{m}}{V} \quad (2.2)$$

In other words, the induced magnetic moment in a certain volume of a homogeneously magnetized medium is given by multiplication of magnetization by the volume.

In the applied magnetic field, the magnetic moments in materials tend to align to the field direction. In most case, the magnetization is just proportional to the external magnetic field. These kinds of magnetization are described by:

$$\vec{M} = \chi \vec{H}, \chi = \frac{\partial M}{\partial H} \quad (2.3)$$

where χ is the magnetic susceptibility which is a dimensionless quantity. The \vec{H} is the magnetic field. The magnetic flux density \vec{B} in a material is represent by,

$$\vec{B} = \mu_0(\vec{H} + \vec{M}) = \mu_0(1 + \chi)\vec{H} = \mu_r \mu_0 \vec{H} = \mu \vec{H} \quad (2.4)$$

Here, μ_0 is vacuum permeability with $4\pi \cdot 10^{-7} \text{ Vs/Am}$. Materials with small χ are called diamagnetic or paramagnetic, according to the minus or plus sign of χ . In strong magnets, such as ferromagnets, the magnetic moments are correlated and ordered even at field zero.

2.2 The Classes of Magnetic Materials

Magnetic materials can behave quite differently in the presence of an external magnetic field. Most materials can be classified as diamagnetic, paramagnetic or ferromagnetic and ferrimagnetic.

2.2.1 Ferromagnetism

Ferromagnetism results from a spontaneous magnetization even without external magnetic field. Ferromagnetic are only a few metals such as iron, cobalt, nickel and rare earth metals at low temperatures. Most of the ferromagnets are alloys. Among them, rare-earth magnets are very strong permanent magnets e.g. alloys of samarium and neodymium with cobalt or iron. Hereby, due to so called positive exchange interaction, spontaneous magnetic moments occur. This long-range ordering phenomenon forms a domain; i.e. regions with the magnetic moments line up parallel. An applied external magnetic field orients the domains in the field direction. Ferromagnets remember their magnetic history (in dependence of the magnetic field). The magnetic history is called hysteresis. It includes the saturation magnetization, remanence, and coercive field.

For a detailed understanding of ferromagnetism, a number of different models exist. Among them, the Stoner criterion and the Heisenberg model will be discussed here.

Stoner model for metallic ferromagnets

Spontaneous magnetizations in ferromagnetic metals occur, if the Stoner criterion is fulfilled. Non-magnetic metals have equal, ferromagnetic metals an imbalanced density of states (DOS) of spin-up and down electrons at Fermi level. If metals are in a magnetic field, their spin population is properly aligned in the field. Due to spontaneous splitting electrons gain kinetic energy within a narrow energy strip (δE) at the Fermi edge (E_F). The total increase in kinetic energy is given by

$$\Delta E_{K.E.} = \frac{1}{2} g(E_F) (\delta E)^2 \quad (2.5)$$

with the density of electron states at the Fermi level $g(E_F)$.

On the other side, the interactions of spins with the molecular field decrease potential energy. The molecular field ($\lambda \mathbf{M}$) is due to exchange by Coulomb interaction and proportional to the magnetization \mathbf{M} . The number density of up and down electrons is $n_{\uparrow/\downarrow} = \frac{1}{2}(n \pm g(E_F)\delta E)$, with the total number density of electrons, n . The magnetization can be expressed by the difference of the number density of spin up and down electrons, $M = \mu_B(n_{\uparrow} - n_{\downarrow})$. The molecular field energy is

$$\Delta E_{P.E.} = - \int_0^M \mu_0 (\lambda M') dM' = -\frac{1}{2} \mu_0 \lambda M^2 = -\frac{1}{2} \mu_0 \mu_B^2 \lambda (n_{\uparrow} - n_{\downarrow})^2 = -\frac{1}{2} U (g(E_F) (\delta E))^2 \quad (2.6)$$

with Coulomb energy $U = \mu_0 \mu_B^2 \lambda$.

The total change in energy is given by

$$\Delta E = \Delta E_{K.E.} + \Delta E_{P.E.} = \frac{1}{2} g(E_F) (\delta E)^2 (1 - U g(E_F)) \quad (2.7)$$

Thus spontaneous ferromagnetism is possible, if the total change in energy is less than zero. $\Delta E < 0$.

It means

$$Ug(E_F) \geq 1 \quad (2.8)$$

This is the Stoner criterion. Large density of state at Fermi energy and the strong Coulomb effects are favorable for ferromagnetism. In the absence of an applied magnetic field, the exchange splitting δE , which is the energy splitting between the spin-up and -down bands, is due to spontaneous ferromagnetism.

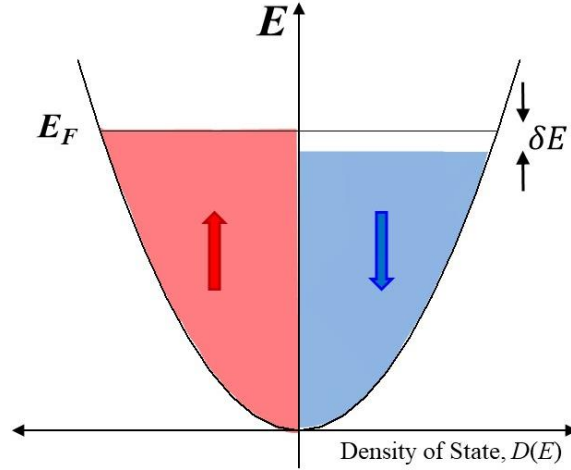


Fig.2. 2 Density of state (DOS) of spontaneous splitting in energy bands without an applied magnetic field. Ferromagnetic materials can become spin-split spontaneously.

Heisenberg Model

In this model, the magnetic interaction is estimated in the frame of a mean field approximation. A single magnetic moment produces a magnetic field interacting with the neighbors and aligning them. The exchange energy can be described by the Heisenberg Hamiltonian:

$$\hat{H} = - \sum_{i,j} J_{ij} \vec{S}_i \cdot \vec{S}_j \quad (2.9)$$

J_{ij} is the exchange constant between neighboured spins. \vec{S}_i and \vec{S}_j represent their spin moments. Positive J_{ij} value is meant ferromagnetic interaction, negative J_{ij} value in an antiferro- or ferri-magnetic. To explain magnetic ordering in an external magnetic field, the Heisenberg model is used as a mathematical model in statistical mechanics.

$$\hat{H} = - \sum_{i,j} J_{ij} \vec{S}_i \cdot \vec{S}_j - \mu \sum_i \vec{S}_i \cdot H \quad (2.10)$$

The second term in the Hamiltonian of Eqn. 2.10 describes the interaction with the external magnetic field H .

All ferromagnets have a critical temperature, known as the Curie temperature T_c . Pure Iron, Cobalt, and Nickel have critical temperatures T_c of ~ 1043 K, 1388 K, and 627 K, respectively.[11] Above T_c , ferromagnetic phase changes into paramagnetic. Here the individual magnetic moments react independently on temperature. The spins are uncorrelated and oriented randomly. Below T_c , there exists an ordered magnetization even at field zero with spontaneous ferro- or ferromagnetic magnetization.

The temperature dependence of spontaneous magnetization is described by Bloch's law.

$$\vec{M}(T) = \vec{M}(0)(1 - (T/T_C)^{3/2}) \quad (2.11)$$

where $\vec{M}(0)$ is the spontaneous magnetization at 0K. It is depicted in Fig. 2.3. With increasing temperature the spontaneous magnetization decrease and is zero at T_C . The Curie temperature T_C can be determined by the Curie-Weiss law ($\chi = C/(T - T_C)$).

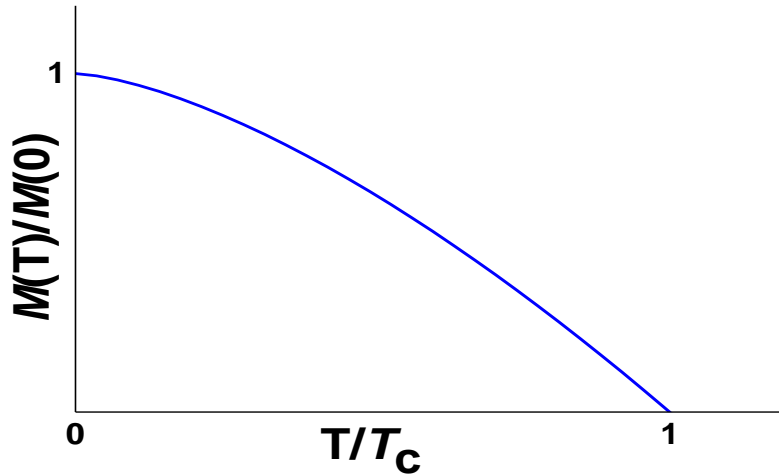


Fig.2 3 Temperature dependence of the saturation magnetization. Bloch's $T^{3/2}$ law. Spins in of graph line show correlated thermal fluctuations and outside random thermal fluctuations.

2.2.2 Antiferromagnetism and Ferrimagnetism

Also, antiferromagnetic and ferrimagnetic materials are materials with ordered magnetic spins. In these materials, neighboring magnetic moments are aligned in the opposite direction. If the magnitudes of spins are the same, the materials are called antiferromagnetic; if they are different, they called ferrimagnetic. (see figure 2.4) Also, the antiferromagnetism is temperature dependent with a magnetic phase transition at the Néel temperature. If no external magnetic field is applied, the total magnetization of antiferromagnetic materials vanishes. With an external magnetic field applied, antiferromagnetic materials align their spin component of the antiferromagnetic coupling sublattice. In practice, antiferromagnets adopt multidomain configuration. Alloys of iron manganese (FeMn) and nickel oxide (NiO) are typical antiferromagnetic materials.

Ferrimagnets exhibits, like ferromagnets, show a spontaneous magnetization below the Curie temperature. Ferrimagnetism has the magnetization compensation point with a net magnetic moment of zero. This is different from ferromagnetism. Ferrimagnetism is found in ferrites, magnetite (Fe_3O_4) and magnetic garnets.

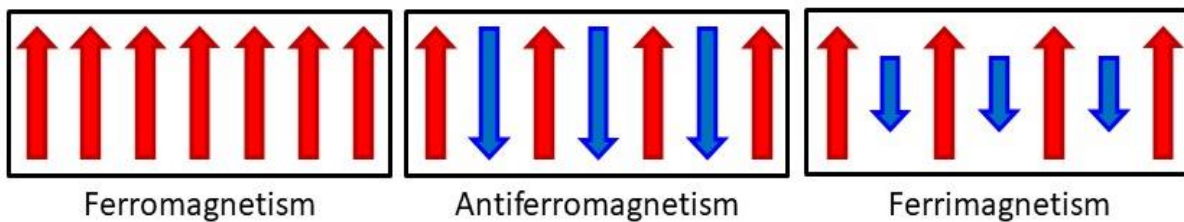


Fig.2. 4 Magnetic structure. Spin ordering in ferro-, antiferro- and ferri- magnets. Ferromagnets order with one direction. And antiferromagnets order opposite direction with the same strength. Ferrimagnet also orders opposite direction, though strengths are different.

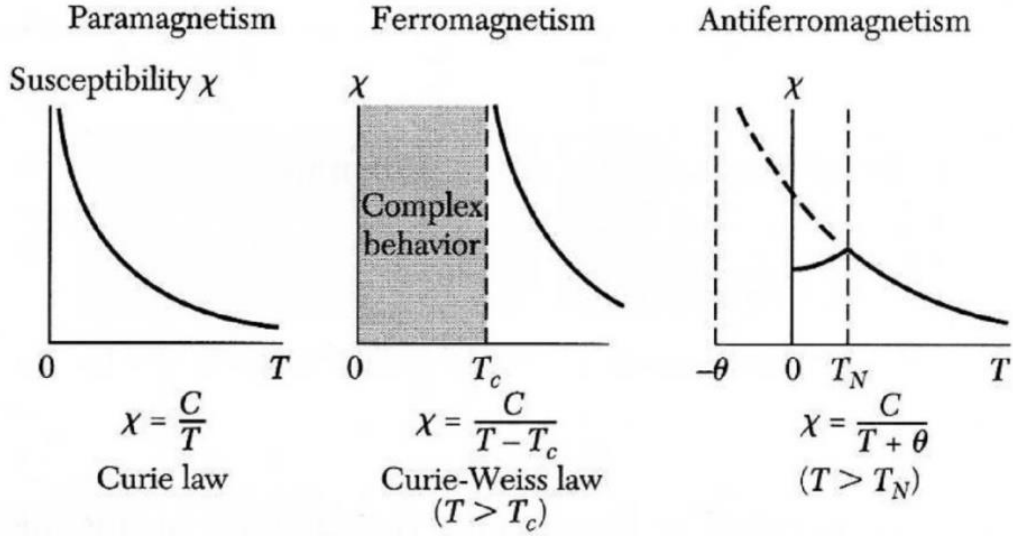


Fig.2. 5 Temperature dependence of the magnetic susceptibility in para-, ferro- and antiferro-magnets. The magnetic structure of the material can be assumed by temperature with Curie temperature T_C for ferromagnetism, Néel temperature T_N for antiferromagnetism. [2]

2.2.3 Paramagnetism

Paramagnetic media have a positive susceptibility χ . When an external magnetic field is applied, the magnetic moment aligned parallel to the field direction. In field zero, the magnetic moment vanishes. Most chemical elements with an open atomic shell are paramagnetic. The magnetization \vec{M} as a function of the applied magnetic field \vec{H} and the temperature T is given by

$$\vec{M} = Ng\vec{j}\mu_B B_J(x), \quad \vec{M}_S = Ng\vec{j}\mu_B \quad (2.12)$$

$$B_J = \frac{2J+1}{J} \coth\left(\frac{2J+1}{2J}x\right) - \frac{1}{2J} \left(\coth\frac{1}{2J}x\right), \quad (x \equiv gJ\mu_B H/k_B T) \quad (2.13)$$

Here M_s is the saturation magnetization, g is Landé-factor, \vec{j} is the total angular momentum. $B_J(x)$ is the Brillouin function. At low magnetic field and not to low temperatures the susceptibility can be approximated by:

$$\frac{\vec{M}}{\vec{H}} = \frac{N\vec{j}(\vec{j}+1)g^2\mu_B^2}{3k_B T} = \frac{C}{T}, \quad C = \frac{N}{3k_B} \mu_{eff}^2, \quad (\mu_{eff} = g\sqrt{\vec{j}(\vec{j}+1)}\mu_B) \quad (2.14)$$

This formula is called Curie law. The Curie constant C is a material specific constant. The magnetization \vec{M} is related to temperature T .

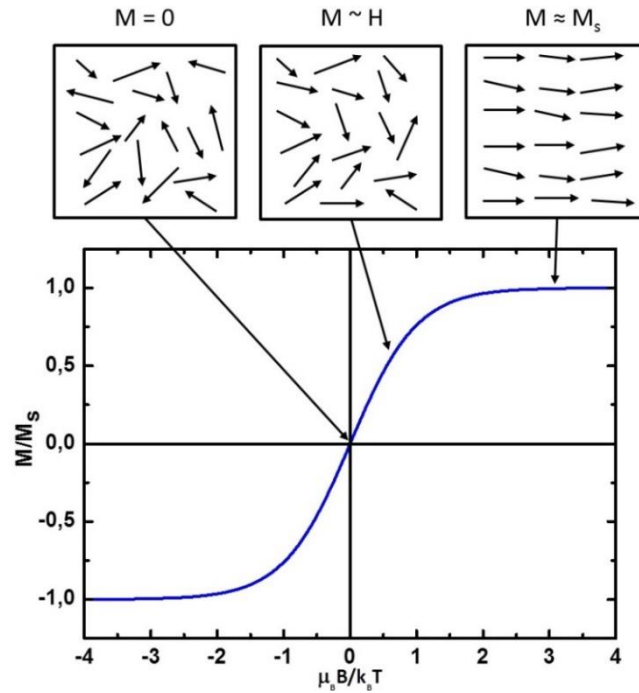


Fig.2. 6 Brillouin function. The Brillouin function is a special function for calculation of an ideal paramagnetic material in statistical mechanics. The magnetization is related to the applied magnetic field and the total angular momentum quantum number J in Eqn. (2.13).

2.2.4 Diamagnetism

The diamagnetism is described by Larmor susceptibility. In atom, electrons generate a current around the nuclei. A magnetic field B applied to an electron (charge e and mass m) produces a current that causes a magnetic moment opposite to the field. The current of Z electrons is given by:

$$I = -\frac{Ze^2B}{4\pi m} \quad (2.55)$$

The magnetic moment \vec{m} of a current loop is given by the product of current and area of the loop. The average loop area is assumed to be $\pi \langle \rho^2 \rangle$ with ρ being the mean radius. Therefore, the magnetic moment is:

$$\vec{m} = I \times \text{area} = -\frac{Ze^2B}{4m} \langle \rho^2 \rangle = c\vec{H} \quad (2.16)$$

where c is small negative constants.

All atoms exhibit diamagnetism.

2.3 Basics of Ferromagnetic Hysteresis loop

The magnetic material behavior as a function of an external magnetic field is characterized by the hysteresis loop, i.e. the relation between external magnetic field H and the sample magnetization M . Characteristic properties are the saturation magnetization M_s , the remanence M_r , and the coercivity H_C , (see, Fig 2.7).

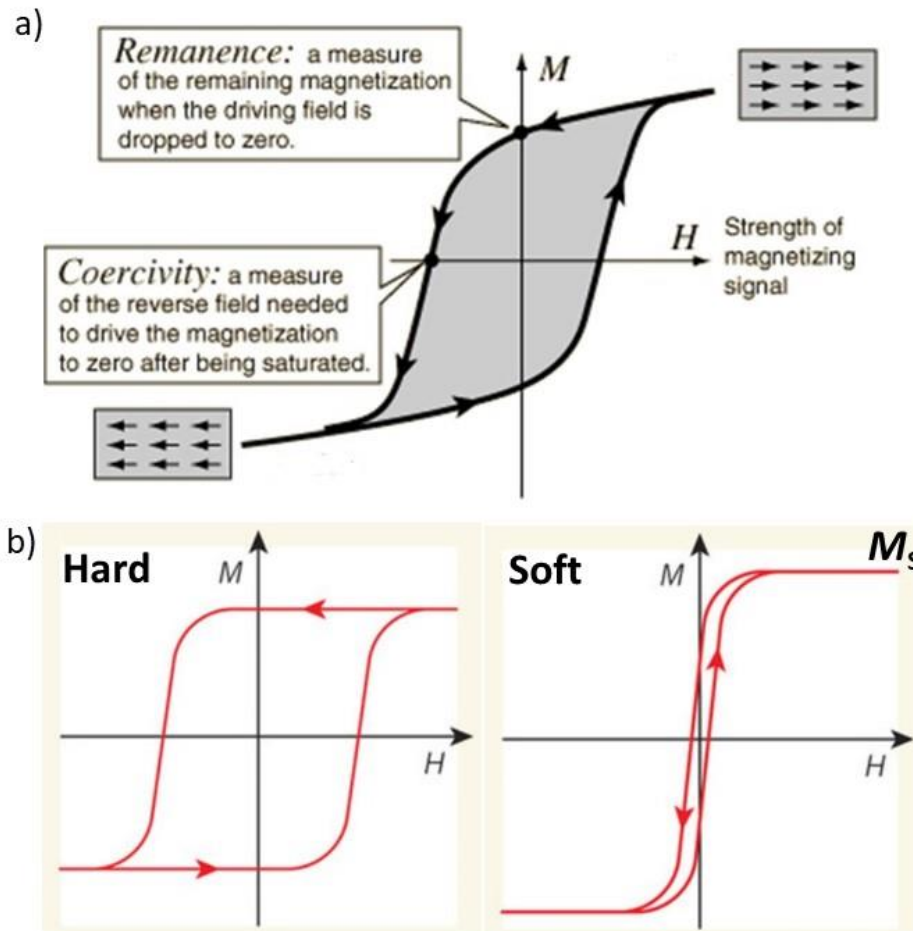


Fig.2. 7 Schematic hysteresis loop. a) Characteristic properties in hysteresis loop.[5] Change of magnetization M in ferromagnet by an applied magnetic field H is indicated by the hysteresis loop. By increasing applied field, magnetization is approached magnetic saturation. If the applied field reaches to zero, the retained magnetization is called remanence M_r . The applied field to decrease magnetization to zero after saturation is coercivity or coercive field H_C . b) Typical hysteresis loops in hard and soft magnets.[6]

The saturation magnetization M_s is the maximal value. By reducing the magnetic field to zero, the remaining magnetization is defined as remanence M_r . Increasing of the magnetic field to opposite direction removes the magnetization at the coercive field H_C . Continuously, increasing the applied field along the negative direction provides opposite saturation magnetization. By forward turning the magnetic field the $M(H)$ curve forms a closed loop.

Fig. 2.7 b) shows a typical hysteresis loop for hard and soft magnets. Hard magnetic materials are used as stable, permanent magnets. Very soft magnetic materials are easily magnetized and demagnetized with a smaller coercivity.

The coercivity can vary between the lowest values of 10^{-5} mT to about 12 T, as for Mu-metal (76 % Ni, 5 % Cu, 2 % Cr) and L1₀-phase FePt, respectively (as also shown in this thesis). The highest saturation magnetization is approached in Ho metal with a value of 3 T (at 4K, $H > 3T$, $T_C \sim 20$ K)

The magnetic anisotropy energy (MAE) is a prerequisite for hysteresis. It depends on the preferred direction of the magnetization by the crystal structure and the shape of the sample or internal gains. The crystal structure dependent anisotropy is called magnetocrystalline anisotropy (MCA) and results from the spin-orbit interaction, since the orbital motion of the electrons couples with the crystal electric field. The other contribution to the MAE is the shape anisotropy and related to the demagnetizing field which depends on the geometry of the system. The demagnetizing field will be explained in more details later on.

One technologically significant value for permanent magnets is the energy product $(BH)_{max}$. Nowadays, the highest value of 59 MGOe was found for NdFeB.[13] The maximum energy product can be deduced from the hysteresis as shown in Fig. 2.8.

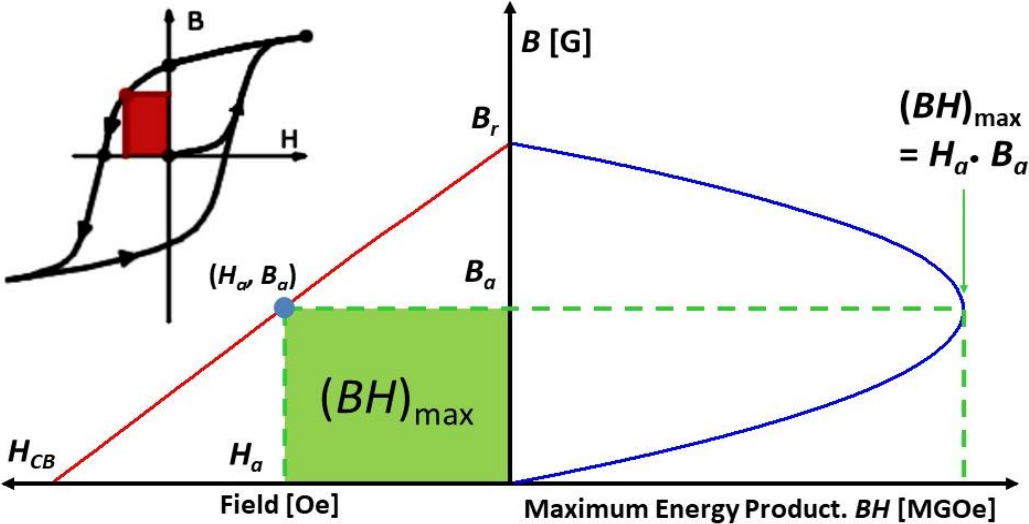


Fig.2. 8 The maximum energy product $(BH)_{max}$ calculation from BH curve

2.3.1 The Stoner-Wohlfarth (S-W) model

The Stoner-Wohlfarth model is one of the most commonly used models for the numerical calculation of single-domain magnetic hysteresis curves; it provides a relation between the external magnetic field H , the easy axis direction of the magnetization vector, and the projection of the magnetization along the applied magnetic field. The variation of the external field leads to a coherent rotation of the magnetization. The direction of the magnetization and the anisotropy constant of a ferromagnet of the sample are given by the angle ψ and θ , respectively.[14]

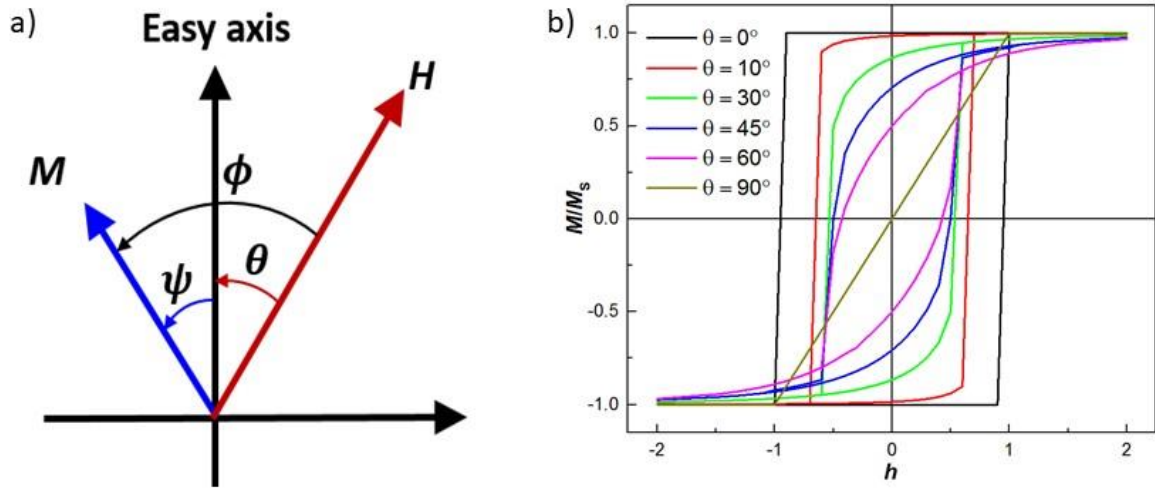


Fig.2. 9 Stoner-Wohlfarth model. a) Arrangement of angle in the S-W model. The orientation of sample magnetization and the external field H with respect to the easy axis given by the angle ψ and θ , respectively. b) Hysteresis loops calculated by S-W model for different angles θ between external field and anisotropy axis.

The energy of the system is written regarding the anisotropy energy E_A and the Zeeman energy E_Z [14].

$$E_T = E_A + E_Z = K_u V \sin^2 \psi - \mu_0 M_S V H \cos \phi, \quad \psi = \phi - \theta \quad (2.67)$$

To minimize energy for the longitudinal hysteresis curve, the corresponding $\cos \phi$ is varied.

The Stoner-Wohlfarth model is used to calculate the hysteresis loop with intrinsic magnetic properties of materials, such as magnetocrystalline anisotropy energy and saturation magnetization. However, in bulk hard magnet materials there are multi-domain states, which result in a non-trivial calculation of the complete hysteresis loop. An empirical approach is given by the Kronmüller equation (2.18), which is inspired by the Stoner-Wohlfarth model.[15]

$$H_C = \alpha 2K_1 / \mu_0 M_S - N_{eff} M_S \quad (2.78)$$

where α and N_{eff} are experimental parameters. The Kronmüller equation will be referred later in section 2.4.4.

2.3.2 Preisach model and First Order Reversal Curves

The Preisach, also one model for hysteresis loops based on the concept of parallel connection of relay hysterons.[6] In ferromagnetic materials, small domains are distributed and network with each other, and generate the total magnetic moments. The relay hysteron is the basic block of the Preisach model and has two values of 1 and 0 with switch between the on-off condition. It forms a loop, as shown in fig.2.10.

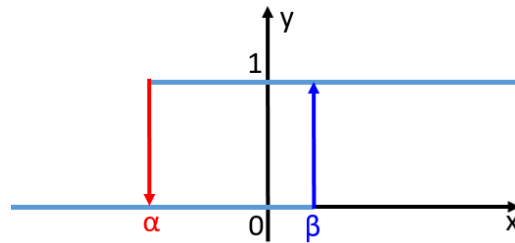


Fig.2. 10 The operation of the relay hysteron. α and β define the switch-off and on the threshold, respectively.

It is mathematically described as:

$$y(x) = \begin{cases} 1 & \text{if } x \geq \beta \\ 0 & \text{if } x \leq \alpha \\ k & \text{if } \alpha < x < \beta \end{cases} \quad (2.19)$$

where $k = 0$ if the previous region is in $x \leq \alpha$. And $k = 1$ if the previous region is in $x \geq \beta$.

The entire hysteresis loop is formed by parallel connection and summation of these hysterons, which have different α and β thresholds and are scaled by μ . Fig. 2.11 a) is block diagram to explain hysteron builds up the hysteresis loop. By increasing the relay hysterons number N , the hysteresis curve can be represented with high accuracy. In Fig.2.11 b), the $\alpha\beta$ plane describes a number of relay hysterons. It is considered the half-plane $\alpha < \beta$ and a right-angle triangle, the plane is divided by $\alpha = \beta$. There is the Preisach density function $\mu(\alpha,\beta)$, which describes a number of relay hysterons of each different value of (α_i,β_i) . Outside of the right-angle triangle has a value of $\mu(\alpha,\beta) = 0$. By the $\alpha\beta$ plane, hysteresis curve can be approximated.[7]

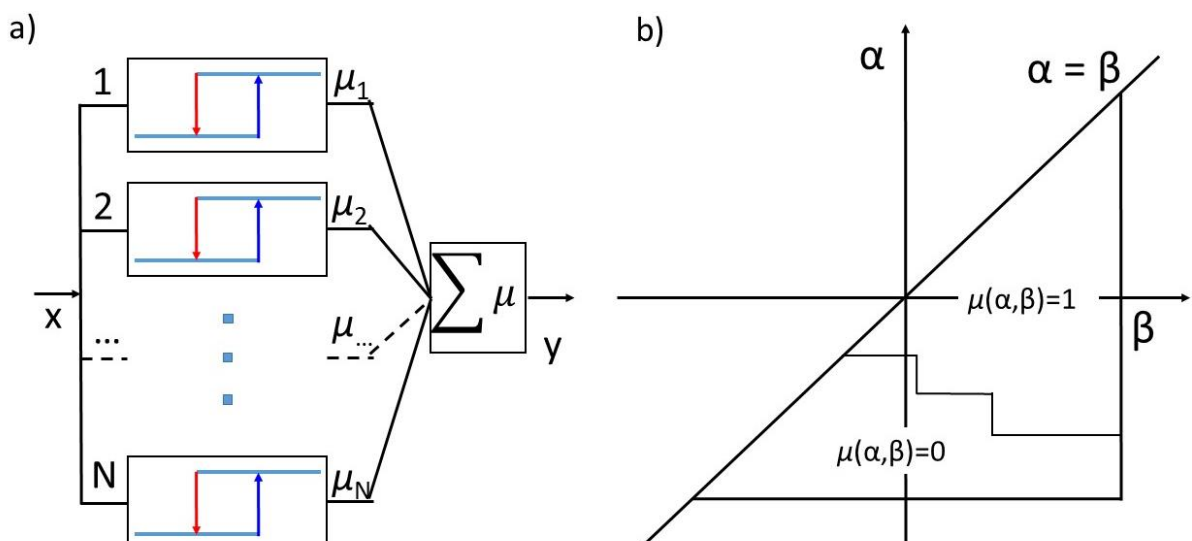


Fig.2. 11 The mathematical Preisach model. a) The block diagram of Preisach model, consists of many relay hysterons connect in parallel. b) Geometrical representation of Preisach (α - β) plane

The Preisach model could be experimentally determined by first-order reversal curves (FORCs), as developed by Mayergoyz.[16-18] FORCs measurements are a useful practical method to obtain the intrinsic distribution of magnetic interaction and coercive fields of hysterons or domains with magnetostatic interactions in various types of complex magnet samples systems, such as bulk, thin films layer systems, magnetic arrays or magnetic nanoparticles.[19-24] The intrinsic field distribution can be obtained from measurements of main and minor reverse hysteresis curves with a specific reversal field H_r . An FORC distribution is defined by a mixed second-order derivative of the magnetization M by both a reversal field H_r and an increasing external field H for saturation, which is given by

$$\rho(H_r, H) = -\frac{1}{2} \frac{\partial^2 M(H_r, H)}{\partial H_r \partial H} \quad (2.20)$$

This eliminates the purely reversible components of the magnetization. Any nonzero ρ corresponds to an irreversible switching process.[25] The FORC density resembles the Preisach model.[6] However, not all of the experimentally obtained FORC distributions are a good representation of the magnetization behavior of the sample. This is only the case, if all of the minor loops are perfectly closed with small steps of reversal field. Also, minor loops must be independent and congruent. This is called the congruency and wiping out property.[16] The experimental details will be explained later in chapter 4.

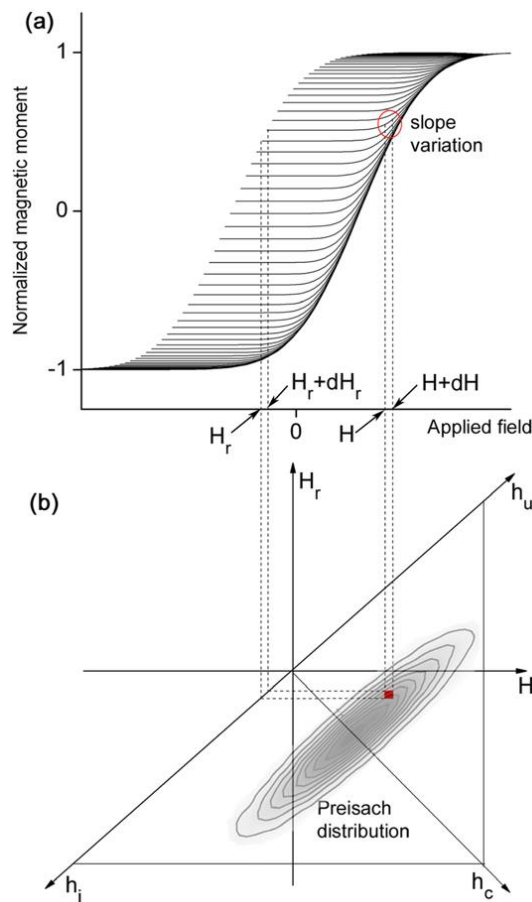


Fig.2. 12 FORCs and the Preisach model in both coordinate systems.[25]

2.4 Micromagnetism

In theoretical physics, ferromagnetic materials can be described from several viewpoints according to length scales. These models are shown in table 2.1.[26]

Model	Description	Length Scale
Atomic level theory	Quantum mechanical ab initio calculations	< 1 nm
Micromagnetic theory	Continuous description of the magnetization	1 – 1000 nm
Domain theory	Description of domain structure	1 – 1000 μ m
Phase theory	Description of ensembles of domains	> 0.1 mm

Table 2. 2 Established models for the description of ferromagnetism on different length scales

Micromagnetism, which describes the individual spin arrangement by a continuum theory, is a reliable model to calculate the magnetization behavior on the submicron scale. In contrast to atomic level theory, it can be solved numerically for a large number of atoms system. On the other hand, the micromagnetic theory is able to resolve relatively small structure in the compare to domain theory. Magnetic dipoles of cells favor locally parallel spin alignment due to exchange interaction. The spatial distribution of the polarization \vec{J} or the magnetic moment \vec{m} is determined by minimizing the magnetic free energy as a stable state. The stable configuration, the domain structure and magnetic hysteresis loops as a function of an external field could be calculated using normalized components of the polarization vector, $\vec{J}(\vec{r}) = J(\vec{r})/J_s$ with unit vector $\vec{r} = \sqrt{r_1^2 + r_2^2 + r_3^2} = 1$, the saturation polarization $J_s = \text{constant}$, and the value of the directional cosines. Micromagnetism combines classical field theory, like the continuous magnetization field which is a common parameter in classical electrodynamics[27], and quantum mechanics, such as the exchange interaction, thus is often referred to as semi-classical continuum theory.[26]

2.4.1 Magnetic free energy

The total energy of ferromagnets in the continuum theory of micromagnetism is described as the sum of a quantum mechanical origin and a classical description. The stable magnetization configurations can be found by local minima of the energy function. Exchange energy and the anisotropy energy are quantum mechanical effects. Stray field energy (demagnetization energy) and Zeeman energy are classical descriptions. The total magnetic free energy density according to

$$E_t = E_{ex} + E_K + E_S + E_H \quad (2.21)$$

is composed of exchange, anisotropy, stray field and Zeeman energies.[28]

1. Exchange Energy E_{ex} :

The exchange energy can be derived from exchange interaction of the Heisenberg model introduced by equation (2.13). It provides a preferred parallel alignment of nearest neighboring atoms in localized electrons of a ferromagnet. By continuum variable $\gamma_n(\vec{r})$, homogeneous and inhomogeneous magnetic configurations can be described.

$$E_{ex} = A \int \sum_{i=1}^3 (\nabla \gamma_i)^2 dV \quad (2.22)$$

Here, A is the exchange stiffness constant and γ_i is the local direction cosines. The exchange stiffness constant A can be obtained by Bloch $T^{3/2}$ law that is relation between the temperature dependence of the saturation polarization J_s and Curie temperature T_C .

2. Magnetocrystalline anisotropy energy E_K :

The magnetocrystalline anisotropy energy depends on the crystal structure of the material. Magnetic polarization has a preference alignment parallel to certain axis, so-called easy axis. This anisotropy energy is based on the interaction of the orbital moment with the crystal and the spin-orbit interaction.[29] Based on the symmetry of the crystal more than one easy axes can be present. This anisotropy energy is given by

$$E_K = \int K_1 \sin^2 \theta + K_2 \sin^4 \theta + \dots dV \quad (2.23)$$

where θ is the angle between the polarization J and a well-defined axis in the crystal. K_n are the different crystalline anisotropy constants sorted by the order of θ . The cubic lattice structure has naturally three pairwise orthogonal easy axes, thus the anisotropy energy is written by

$$E_K = \int [K_1(\gamma_1\gamma_2 + \gamma_2\gamma_3 + \gamma_1\gamma_3)^2 + K_2(\gamma_1\gamma_2\gamma_3)^2 + \dots] dV \quad (2.24)$$

3. Stray field energy E_S :

The stray field energy, also called demagnetization energy, is the magnetostatic energy of the magnetization in its own stray magnetic field. [30] According to classical electrodynamics, the energy is given by

$$E_S = \frac{\mu_0}{2} \int \vec{j} \cdot \vec{H}_S dV \quad (2.25)$$

where the factor 1/2 is correction factor for twice contribution in integration due to dipole-dipole interaction.

4. Zeeman energy E_H :

The Zeeman energy is also one of the magnetostatic energies, while it is based on the external field. It describes the interaction of the polarization \vec{j} with an applied field.

$$E_H = - \int \vec{j} \cdot \vec{H}_{ex} dV \quad (2.26)$$

To determine the equilibrium magnetization configuration, this is the minimization of the magnetic free energy the total magnetic free energy of a magnetization is calculated by differentiation.

$$\delta E_{total} = \delta(E_{ex} + E_K + E_S + E_H) = 0 \quad (2.27)$$

2.4.2 Domain and Domain Walls

A magnetic domain is a region of a uniform magnetization. A large number of atomic magnetic moments are parallel aligned in small regions. The stray-field created by a magnetic domain results is effectively interacting with the neighboring domains. These structures are formed to minimize the total energy.[31] To reduce the magnetostatic energy E_S outside the material, magnetic domains can split into two or more.

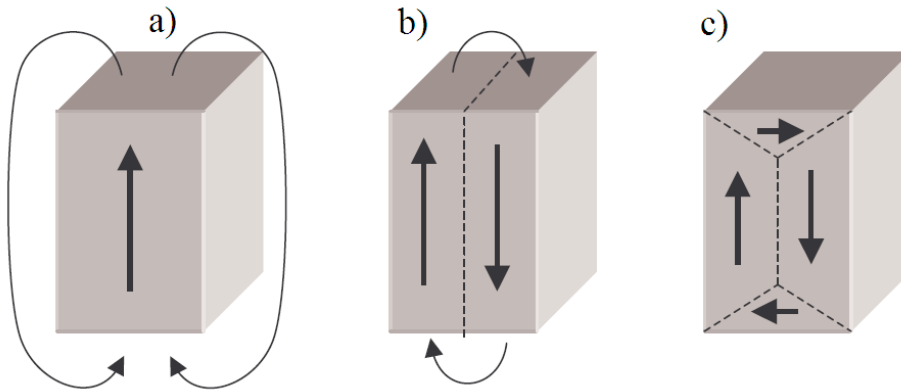


Fig.2. 13 Domains on the basis of energy minimization.[32]

In Fig. 2.13 shows how a ferromagnetic material is split into magnetic domains for reducing the magnetostatic energy; it is depicted stray field on the outside of the magnet. a) Single domain: higher energy around the magnet, b) two domains: reduced the magnetostatic energy, c) multiple domains with closure domains: minimum energy state.

Magnetic domains are separated by domain walls, where the magnetization aligns by gradual rotation to next domain. Domain walls require wall energy composed of exchange and anisotropy energy, both necessary for changes of the magnetization direction. Two types exist for 180° walls. In bulk material, Bloch walls are formed, since the system is large enough to include these walls. Magnetization vectors turn through the plane parallel to the wall plane, where only small stray magnetic fields are present at the rim of the sample. In thinner films, Néel walls appear, if the exchange length is larger than the thickness. The magnetization rotates within the plane of the domain wall. See Fig. 2.14.

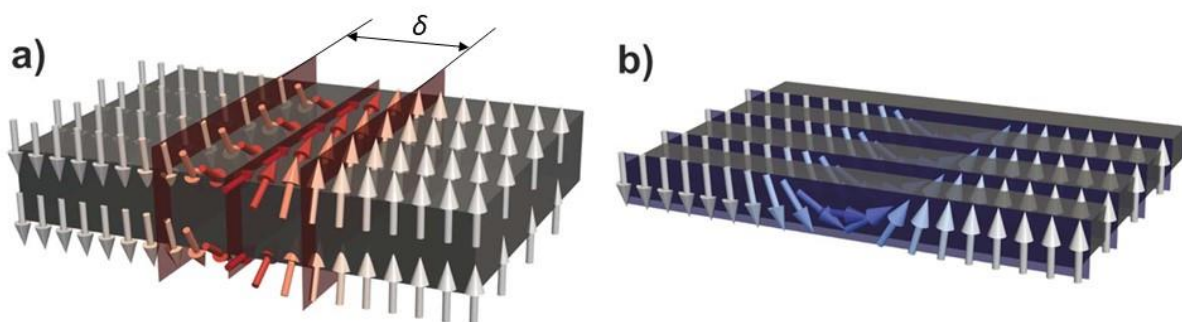


Fig.2. 14 The structure of the Bloch wall (left) and Néel wall (right) in a thin film[2][33]

For uniaxial systems, these values are determined by the exchange stiffness constant A and the anisotropy constant K_1 .

The wall energy γ , the exchange length l_K and the domain wall thickness δ for the stray field free wall given by

$$\gamma = 4\sqrt{AK_1}, \quad l_K = \sqrt{A/K_1} \quad \text{and} \quad \delta = \pi l_K = \pi\sqrt{A/K_1} \quad (2.28)$$

The magnetization can change by domain walls moving and domain rotation. In the field dependent magnetization, the main increasing process is wall motion with a sharp increase in the $M(H)$ curves. At the larger field, there is a region close to saturation dominated by rotation, which can happen against the anisotropy forces. The magnetization process separated in rotation and motion of the domain walls is indicated in Fig.2.15.

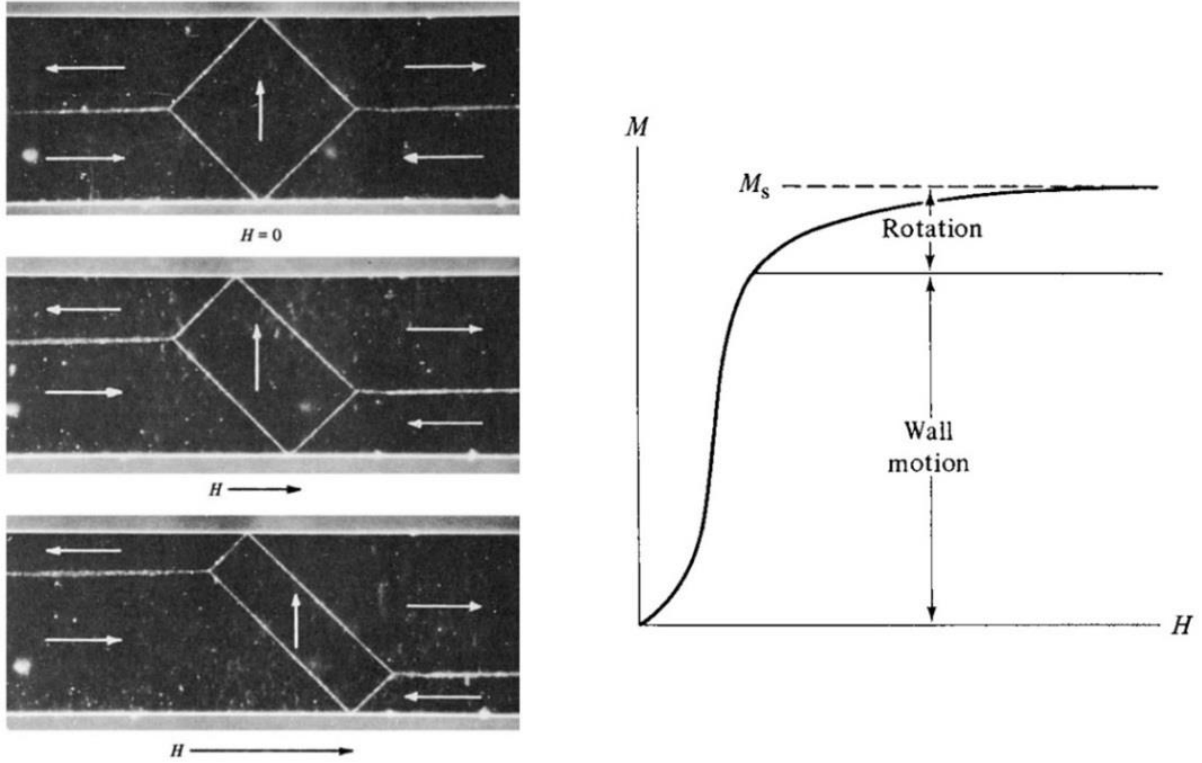


Fig.2. 15 The wall motion occurs in an applied field and magnetization processes.[32]

2.4.3 Single- and Multi-Domain particles

When size of magnetic particles gets small, they favor forming single domains. For comparing the energy difference between single- and multi-domain particles, the particle shape is assumed to be simple ellipsoid with axes a and b , saturation magnetization J_{Sat} and demagnetization factor N . The single domain energy E_{sd} is just related to the total stray field described by

$$E_{sd} = \frac{1}{2\mu_0} N J_{Sat}^2 \cdot \frac{4}{3} \pi a^2 b \quad (2.29)$$

For the two-domain particle, the domain wall energy has to be added to give the two domains energy E_{md} as

$$E_{md} = \gamma\pi ab + \alpha \frac{1}{2\mu_0} NJ_{Sat}^2 \cdot \frac{4}{3}\pi a^2 b \quad (2.30)$$

with γ the domain wall energy per surface area and α the stray field reduction factor between the single- and multi domain state.[34] The magnetostatic energy of a two-domain particle is less compared to a single-domain particle with a lower stray field.

The critical domain diameter D_C can be found where the energy of single- and two-domain particle is equal.

$$D_C = 2a = \frac{3\gamma\mu_0}{2(1-\alpha)NJ_{Sat}^2}, \frac{18\gamma\mu_0}{J_{Sat}^2} \text{ for a sphere, } \frac{6\gamma\mu_0}{J_{Sat}^2} \text{ for a ellipsoid} \quad (2.31)$$

The diameter of D_C becomes a main criterion to consist of single- or multi- domains in ellipsoidal particles. With an external magnetic field, these spins rotate to align parallel to the field to minimise the Zeeman energy. Below critical diameter D_C the particle forms a single domain state, and for larger sizes materials form the multi domain state to reduce stray fields, where the reduction on stray field is higher in energy that the domain wall energy which have to be paid.

In Fig. 2.16, anisotropy contribution and size dependence of the coercive field are shown with magnetization modes in single domains. A D_{th} is a critical diameter for the transition from a thermally stable to an unstable state. The nucleation field for homogeneous rotation is replaced by the curling or buckling mode at a critical diameter, D_{crit}^{nuc} grain size. With increasing size of the particle, a two-domain state with a domain wall forms from D_{crit}^{do} .

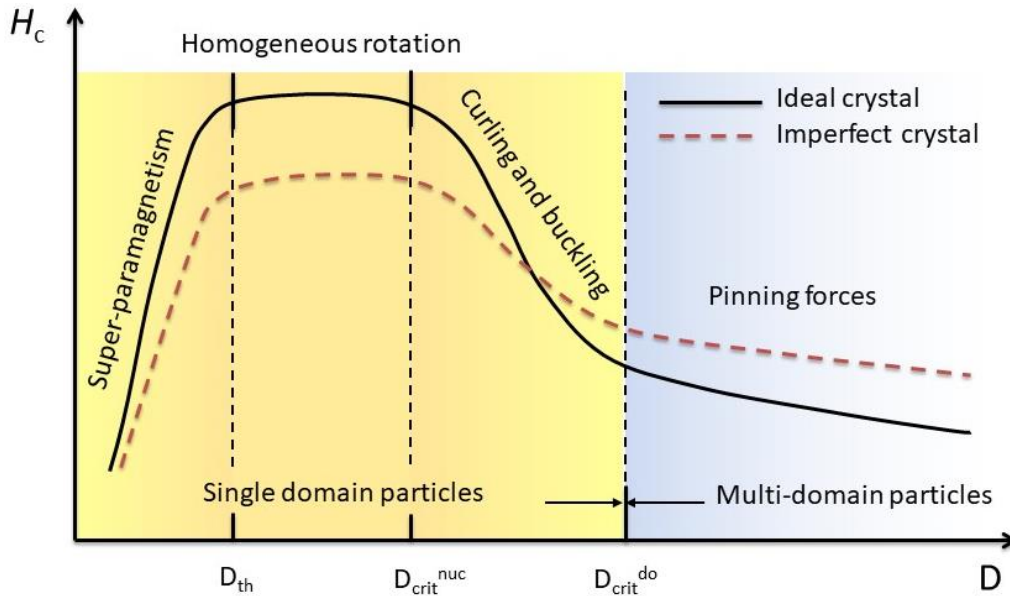


Fig.2. 16 Four regions of the coercive field dependent on grain size.[4] There exist critical diameters of a thermal state transition, D_{th} , the nucleation mode conversion D_{crit}^{nuc} and domain state change, D_{crit}^{do} .

2.4.4 Coercivity and Microstructural parameters

For single domain particle the coercive field H_C could be theoretically calculated by the linearized micromagnetic equation in the Stoner-Wohlfarth model.[15] The coercive field is then given by

$$\mu_0 H_C = \mu_0 \frac{2K_1}{J_S} - (N_{\parallel} - N_{\perp}) \frac{J_S}{\mu_0} \quad (2.32)$$

The coercive field of single-domain particle is determined from the magnetocrystalline ($2\mu_0 K_1/M_S$) with homogeneous rotation. Multi-domain particles by formation of domains originating reduced the coercive field from the shape anisotropy ($(N_{\perp} - N_{\parallel}) \cdot J_S/\mu_0$). Thermal energy overcomes the barrier and the coercive field decreases. [35, 36]

The equation 2.32 is the ideal nucleation field. The real nucleation field takes into account the effect of magnetic inhomogeneity based on microstructural effects. It could be obtained by the linearized micromagnetic equation. The difference between the ideal and the real nucleation field is known as Brown's paradox.[35] The coercive field can be well described by the universal relation of micromagnetism.[15, 37]

$$\mu_0 H_C = \mu_0 \alpha \frac{2K_1}{J_S} - N_{eff} \frac{J_S}{\mu_0} \quad (2.33)$$

α and N_{eff} are the microstructural parameters. The N_{eff} relates with the effect of an effective anisotropic demagnetizing field. α is an effective reduction parameter, which is described by a product function of the reduction of the crystal field α_K , misaligned grains α_{ψ} and exchange coupled grains α_{ex} .

$$\alpha = \alpha_K \cdot \alpha_{\psi} \cdot \alpha_{ex} \quad (2.34)$$

Those three parameters are now shortly described.

1. Nucleation for inhomogeneous regions (parameter α_K):

The crystal anisotropy is lowered by disorder, defects, and stresses of the crystal lattice. The reducing of anisotropy leads to a decline coercive field in single domain particles. For a planar grain boundary, the microstructural parameter α_K is calculated analytically by Kronmüller from micromagnetic equation.[15, 38]

$$\alpha_K = 1 - \frac{\delta_B'^2}{4\pi^2 r_0^2} \left[1 - \sqrt{1 + 4\pi^2 \frac{r_0^2 K_1 - \Delta K_1}{\delta_B^2 K_1}} \right]^2 \quad (2.35)$$

Here, $\delta_B = \pi\sqrt{A/K_1}$ is the domain wall width of the perfect crystal, $2r_0$ indicates the extension of the magnetic defect and ΔK_1 is the reduction of crystalline anisotropy in the area.

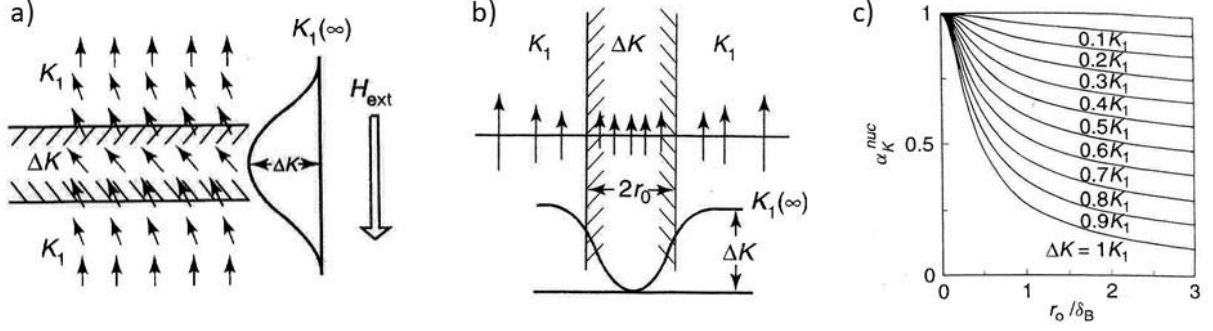


Fig.2. 17 Nucleation for inhomogeneous region α_K . A reversed domain with reduced anisotropy of width $2r_0$: Stripe a) perpendicular and b) parallel to the direction of the external field and c) the microstructural parameter α_K as a function of r_0/δ_B for various ΔK . [10]

2. Nucleation for misaligned grains (parameter α_ψ):

The applied magnetic field which misaligns under an angle ψ_0 on the easy axis of a uniaxial particle influences to reduction of coercive field by a factor α_ψ . The microstructural parameter α_ψ has been calculated by Stoner-Wohlfarth and by Kronmüller [14, 39] and is given by

$$\alpha_\psi = \frac{H_N(\psi_0)}{H_N(0)} \quad (2.36)$$

$$= \frac{1}{\{(\cos\psi_0)^{2/3} + (\sin\psi_0)^{2/3}\}^{3/2}} \left[1 + \frac{2K_2}{K_1 + (N_{\parallel} - N_{\perp})J_S^2/(2\mu_0)} \frac{(\tan\psi_0)^{2/3}}{1 + (\tan\psi_0)^{2/3}} \right]$$

The microstructural parameter α_ψ is a function of the angle ψ_0 . The minimum nucleation field has with $\alpha_\psi^{min} \approx 0.5$ at $\psi_0 = \pi/4$. The α_ψ can be substituted by $\alpha_\psi^{min} = (K_1 + K_2)/(2K_1) \approx 0.5$. In the absence of nucleation, fixed domain wall, α_ψ is described by $\alpha_\psi = 1/\cos\psi$, where the α_ψ is always greater than 1.

3. Nucleation for exchange-coupled grains (parameter α_{ex}):

The exchange-coupled grains increase the demagnetization effect to neighbor grains. It reduces the coercive field due to the exchange coupling and induces a rotation of the spontaneous polarization J_s . If the grain size D is smaller than the domain wall width $\delta_B = \pi(A/K_1)^{1/2}$, the exchange-coupled grains effect becomes important. The random anisotropy effect results in a reduction of the effective anisotropy constant. The reversal process in exchange-coupled grains is a collective process of grains demagnetized by misalignments. The average coercive field of misaligned grains is of the order of $0.25(2K_1/J_s)$. the microstructural parameter α_{ex} can be evaluated to 0.5. [40]

2.5 X-ray and Magnetism

Electromagnetic waves interact with matter via absorption and scattering. In the visible range, magnetic effects in the absorption channel occur known as Magneto-optical effects by Faraday and Kerr rotation.[41, 42], which enable the investigation of magnetic materials by light. At higher energies in the soft x-ray range in the vicinity of distinct absorption edges as the $L_{2,3}$ -edges of 3d transition elements and $M_{4,5}$ -edges of Rare Earths, the interaction between polarized x-rays and magnetic materials show extremely large magnetic absorption effects due to the occurrence x-ray magnetic circular dichroism (XMCD). The first experimental result by x-ray magnetic circular dichroism (XMCD) was reported at the K absorption edge of Fe in the hard x-ray regime [43] and subsequently at L- and M-edges.[44-47] The power of XMCD is correlated to its element-specificity as conventional x-ray absorption spectroscopy (XAS) and the extremely high magnetic contrast. Moreover, by applying sum rules [48, 49] it provides a unique possibility to determine in a quantitative manner spin- and orbital moments separately.

2.5.1 X-ray Absorption Spectroscopy (XAS)

X-ray absorption spectroscopy (XAS) gives information of the local geometric or electronic structure of samples. When the incident photon energy matches with the binding energy of core electrons, resonant excitations appear, which are visible by a strong increase of the absorption spectrum. (see fig. 2.18)

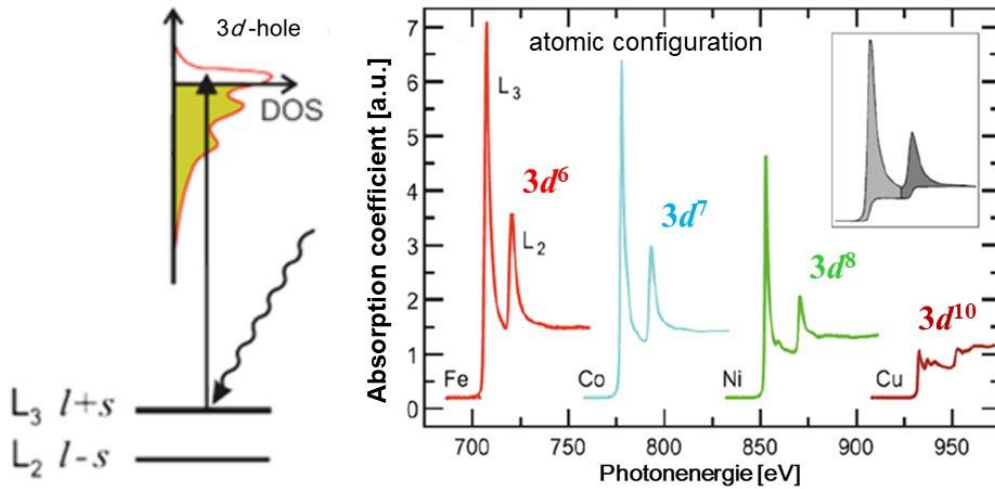


Fig.2. 18 X-ray absorption spectroscopy. Photon excites electron to 3d-hole (left), When the number of holes in the final d-states decreases XAS of transition metal Fe, Co, Ni and Cu atomic configuration at L-edge (right) [8]

The transmitted photon intensity $I(E, t)$ through a sample of thickness t is related the incident intensity I_0 by the Lambert-Beer rule,

$$I(E, t) = I_0(E)e^{-\mu(E) \cdot t} = I_0(E)e^{-\rho_a \sigma^{abs} \cdot t} \quad (2.37)$$

where $\mu(E)$ is the X-ray absorption coefficient, which is dependent on energy E and the atomic number Z with the rough relation of $\mu(E) \sim Z^4/E^3$. [50] The $\mu(E) = 1/\lambda_x$ [length⁻¹] is correlated to the atomic number, density $\rho_a = N_A \rho_m A$ [atoms/length³] and x-ray absorption cross-section σ^{abs} [length²/atom]. A characteristic length λ_x leads to an intensity attenuation by a factor $1/e$. [8]

In quantum mechanics, the absorption coefficient can be derived according to Fermi's Golden Rule. Bound inner-shell electrons transit after absorption of the photon from the initial state $|i\rangle$ to the final state $|f\rangle$ corresponding to the unoccupied density of states $\rho(E)$ above the Fermi energy. The electronic transition probability $T_{i \rightarrow f}$ is described by

$$T_{i \rightarrow f} = \frac{2\pi}{\hbar} |\langle f | \hat{H}_{int} | i \rangle|^2 \rho(E) \quad (2.38)$$

\hat{H}_{int} is the Hamiltonian for the interaction between photons and electrons. The Hamiltonian is described by

$$\hat{H}_{int} = \frac{e}{mc} \mathbf{A} \cdot \mathbf{p} \quad (2.39)$$

with the momentum operator \mathbf{p} and the vector potential \mathbf{A} . The absorption probability is shown by a combination of Eqn.(2.38) and (2.39)

$$W_{i \rightarrow f} = \frac{\pi e^2}{2\hbar m^2 c^2} A_0^2 |\langle f | \mathbf{p} \cdot \mathbf{A} | i \rangle|^2 \rho(E) \delta(E_f - E_i - \hbar\omega) \quad (2.40)$$

Here, $\hbar\omega$ is the energy of the incident photon. For the absorption of x-ray the dipole approximation is valid and eqn.2.40 can be written as

$$W_{i \rightarrow f} = \frac{\pi e^2}{2\hbar m^2 c^2} A_0^2 |\langle f | e^{i\mathbf{k}\cdot\mathbf{r}} \mathbf{e} \cdot \mathbf{p} | i \rangle|^2 \rho(E) \delta(E_f - E_i - \hbar\omega) \quad (2.41)$$

In the dipole approximation the electron transitions are follow the dipole selection rules.

$$\begin{aligned} \Delta\ell &= \pm 1 \text{ (not zero)} \\ \Delta m_\ell &= 0, \pm 1 \\ \Delta m_s &= 0 \\ \Delta j &= 0, \pm 1 \end{aligned} \quad (2.42)$$

By photon emission and absorption, the orbital angular momentum quantum number is always changed by 1. The magnetic quantum number and the total angular momentum can change by zero or one. For right and left circular polarization of the absorbed photon $\Delta m_l = +1$, $\Delta m_l = -1$, respectively.

In particular for magnetic x-ray studies, $L_{2,3}$ -edges of 3d transition metal (TM) appear between 400-1200 eV. These edges are further characterized by the spin-orbit configuration ($2p_{1/2}$ and $p_{3/2}$ for the $L_{2,3}$ -edges). This energetic splitting of the spin-orbit states by about 10 eV for L-edges of 3d TM are in general much larger than the experimental resolution in the range of typically 100meV. The corresponding atomic transition and the measured XAS absorption profile for the late 3d transition metals (Fe, Co, Ni and Cu) metal are shown in Fig. 2.19. The picture indicates, that the XAS profile reflects the density of the final states involved. This matches with theoretical expectation, that the transition matrix elements to be nearly energy independent in the energy range covered by an absorption line.

2.5.2 X-ray Magnetic Circular Dichroism (XMCD)

X-ray magnetic circular dichroism (XMCD) is one of the key methods for x-ray based magnetic property investigations. It has been verified, that the absorption of circularly polarized x-ray light at the vicinity of an absorption edge is dependent on the orientation and strength of the magnetization.

The origin of XMCD is a result of dipole selection rules. Fig.2.19 shows excitation of $2p$ core level electrons to $3d$ valence band by absorption of a right circularly polarized electron for only the spin quantum numbers of the electronic transition involved. Here the difference in transition probability is only given by the quantum mechanical vector coupling coefficients (Clebsch-Gordan coefficients). The spin polarization of the excited electron at both initial spin-orbit partner amounts to $-1/2$ at the L_2 - and $+1/4$ at the L_3 -edge with a ratio of -2 . The same consideration for the orbital polarization shows that the corresponding orbital polarization is identical for both edges and amount to $+3/2$. Therefore the excited core electrons can be considered as a spin and orbital source probing the spin and orbital polarization of the final $3d$ states. These values also indicate that the sensitivity to an orbital moment is considerably larger compared to the spin sensitivity.

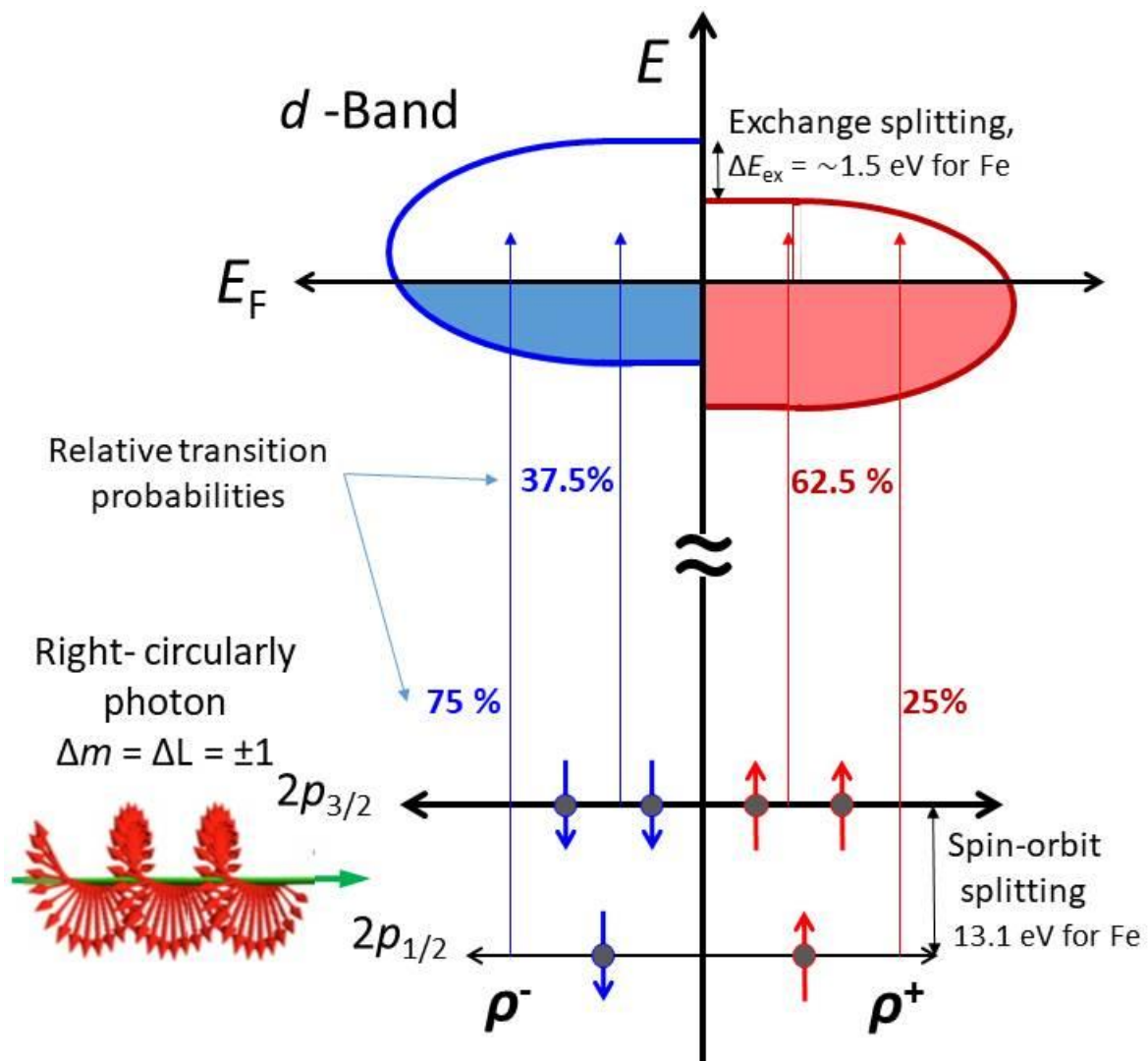


Fig.2. 19 Schematic diagram of XMCD phenomenon. In core level, straight and round arrows describe spin and orbital momentum of electrons, respectively.

The spin and orbital polarization direction of the emitted electrons are given by propagation direction i. e. the polarization vector \vec{P} of the absorbed light. Thus the XMCD effect scales with the projection of the magnetization \vec{M} onto the x-ray k -vector \vec{P} .

According to the helicity directions, the circularly polarized x-ray polarizations are parallel (+) or antiparallel (-) with respect to the magnetization directions, the absorption coefficient differs. This is the circular dichroism phenomenon. When the dichroism part $\Delta\mu$ of absorption coefficient scales with the scalar product $\vec{P} \cdot \vec{M}$. The relation is given by

$$\Delta\mu = \mu_+ - \mu_- \approx \vec{P} \cdot \vec{M} = |\vec{P}| \cdot |\vec{M}| \cos(\vec{P}, \vec{M}) \quad (2.43)$$

where \vec{P} is the incident polarization vector and \vec{M} is the magnetization of the sample.

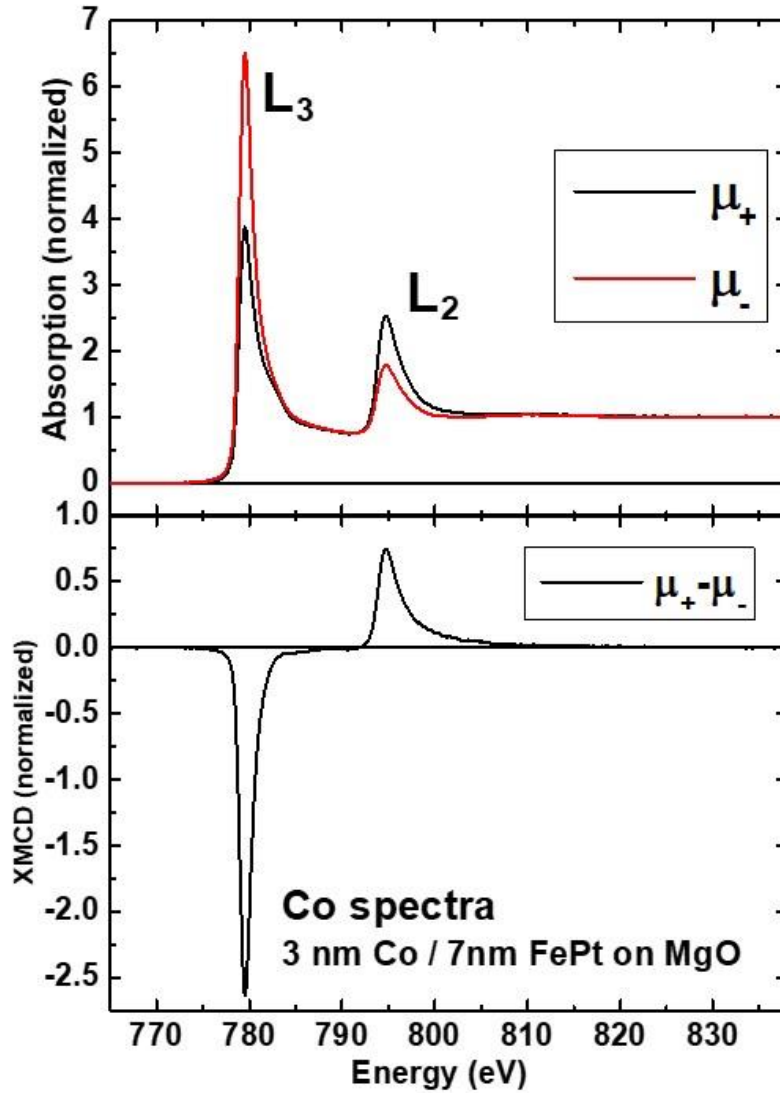


Fig.2. 20 Experimental example of XMCD effect. X-ray absorption spectra with parallel and antiparallel alignment of helicity and magnetization (top) and XMCD spectrum of Co L-edges on 7 nm FePt / 3 nm Co / 2 nm Pt exchange-spring magnetic multilayers (our result) fully oriented onto the saturation field.

2.5.3 Sum rules

Orbital and Spin magnetic moments

B. T Thole and Paolo. Carra derived the sum rules for determination of spin- and orbital-moments by x-ray circular magnetic dichroism. [48, 49] They have shown a relation of orbital moment expectation values with the integrated XMCD for direct measure of $\langle L_Z \rangle$ in Ni, first.[48] Ground-state expectation values of L_Z , S_Z , and T_Z are obtained in Fe, Co, and Ni metal.[49] C. T. Chen has demonstrated how to determine magnetic moment from the integrals of the XAS and XMCD spectra utilizing these sum rules in a quantitative manner.[12] The number of holes n_h can be estimated by theoretical considerations or XAS measurements.

$$\langle I \rangle = \langle I_{L_3} + I_{L_2} \rangle = C \cdot n_h = \mathcal{A} \mathcal{R}^2 \frac{L}{3(2L + 1)} n_h \quad (2.44)$$

I is the averaged XAS intensity, \mathcal{A} is proportional constant and \mathcal{R} is the radial dipole matrix element of the core-valence transition. [8]

First, the ground-state orbital moment expectation value $\langle L_Z \rangle$ is related with an experimentally measurable quantity ρ .[48]

$$\rho = \frac{\int_{edge} d\omega (\mu_+ - \mu_-)}{\int_{edge} d\omega (\mu_+ + \mu_- + \mu_0)} = \frac{1}{2} \frac{c(c+1) - l(l+1) - 2\langle L_Z \rangle}{l(l+1)(4l+2-n)} \frac{1}{\hbar} \quad (2.45)$$

where $\int_{edge} d\omega$ indicates integration range of the l^n (the l subshell with number of electrons, n) to cl^{n+1} (final state configuration, where c denotes the angular momentum of core hole) edges. The c indicates the angular momentum of the core hole. μ_+ and μ_- are the absorption coefficient of the circularly polarized light ($q = \pm 1$) and μ_0 is the absorption coefficient for linear polarized light ($q = 0$) and equal to $\mu_0 = \frac{\mu_+ + \mu_-}{2}$.

Next, the spin sum rule can be obtained by relation between a measurable quantity δ , which is defined from the spin-orbit splitting of the core level, and the ground-state spin moment $\langle S_Z \rangle$ and magnetic dipole $\langle T_Z \rangle$ expectation values.[49]

$$\begin{aligned} \delta &= \frac{\int_{j_+} d\omega (\mu_+ - \mu_-) - \left[\frac{c+1}{c}\right] \int_{j_-} d\omega (\mu_+ - \mu_-)}{\int_{j_+ + j_-} d\omega (\mu_+ + \mu_- + \mu_0)} \\ &= \frac{l(l+1) - 2 - c(c+1) \langle S_Z \rangle}{3c(4l+2-n)} \frac{1}{\hbar} \\ &+ \frac{l(l+1)[l(l+1) + 2c(c+1) + 4] - 3(c-1)^2(c+2)^2 \langle T_Z \rangle}{6lc(l+1)(4l+2-n)} \frac{1}{\hbar} \end{aligned} \quad (2.46)$$

Where j_{\pm} indicates spin-orbit coupling of the core hole ($c \pm 1/2$), c and l describe the shell and subshell orbital quantum numbers of the initial and final states, respectively. n is the initial number of electrons in the final state shell.

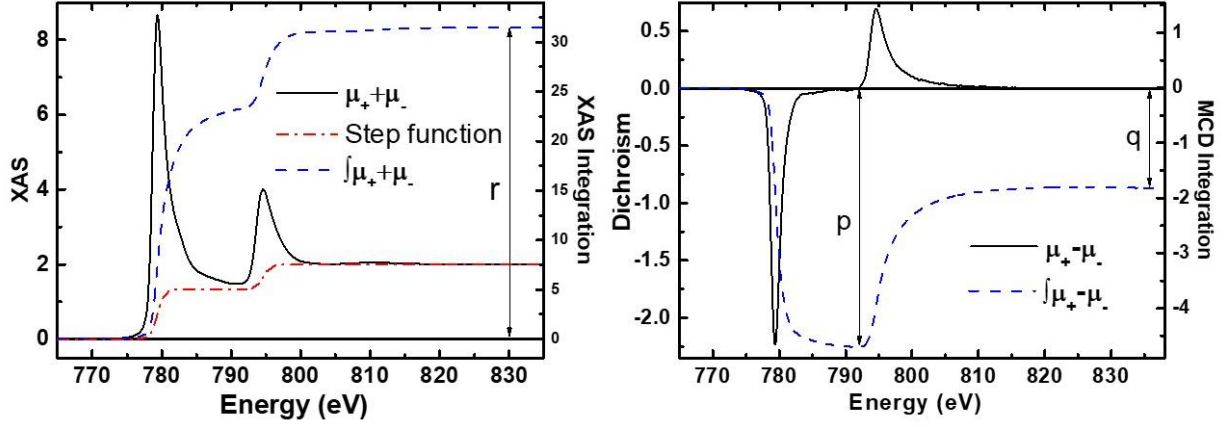


Fig.2. 21 XAS and MCD spectra of cobalt at $L_{3,2}$ -edges.

In fig.2.21, the Co spectrum was dealt with equation (2.47) for orbit moment and Eqn. (2.48) for a spin moment.

$$m_{orb} = -\frac{4\int_{L_3+L_2}(\mu_+ - \mu_-)d\omega}{3\int_{L_3+L_2}(\mu_+ + \mu_-)d\omega}(10 - n_{3d}) = -\frac{4q(10 - n_{3d})}{3r} \quad (2.47)$$

$$m_{spin} = -\frac{6\int_{L_3}(\mu_+ - \mu_-)d\omega - 4\int_{L_3+L_2}(\mu_+ - \mu_-)d\omega}{\int_{L_3+L_2}(\mu_+ + \mu_-)d\omega}(10 - n_{3d})\left(1 + \frac{7\langle T_Z \rangle}{2\langle S_Z \rangle}\right)^{-1} \quad (2.48)$$

$$= -\frac{(6p - 4q)}{r}(10 - n_{3d})$$

The magnetic dipole term T_Z and Magnetocrystalline anisotropy energy, MAE

The magnetic dipole operator is defined by

$$\mathbf{T} = \sum_i \mathbf{S}_i - 3\hat{\mathbf{r}}_i(\hat{\mathbf{r}}_i \cdot \mathbf{S}_i) \quad (2.49)$$

where \mathbf{S}_i is the spin moment of the i -th electron and $\hat{\mathbf{r}}_i$ is the unit position vector of the electron associated with the spin moment \mathbf{S}_i . The magnetic dipole term relates to the quadrupole moment of the spin density distribution. It can be obtained by comparison between normal incident and angle dependent measurement.[51]

In this work only the 2p to 3d transition from corresponding $L_{3,2}$ -edges of the transition metals are addressed. A visualized sum rules calculation is shown in Fig. 2.22.

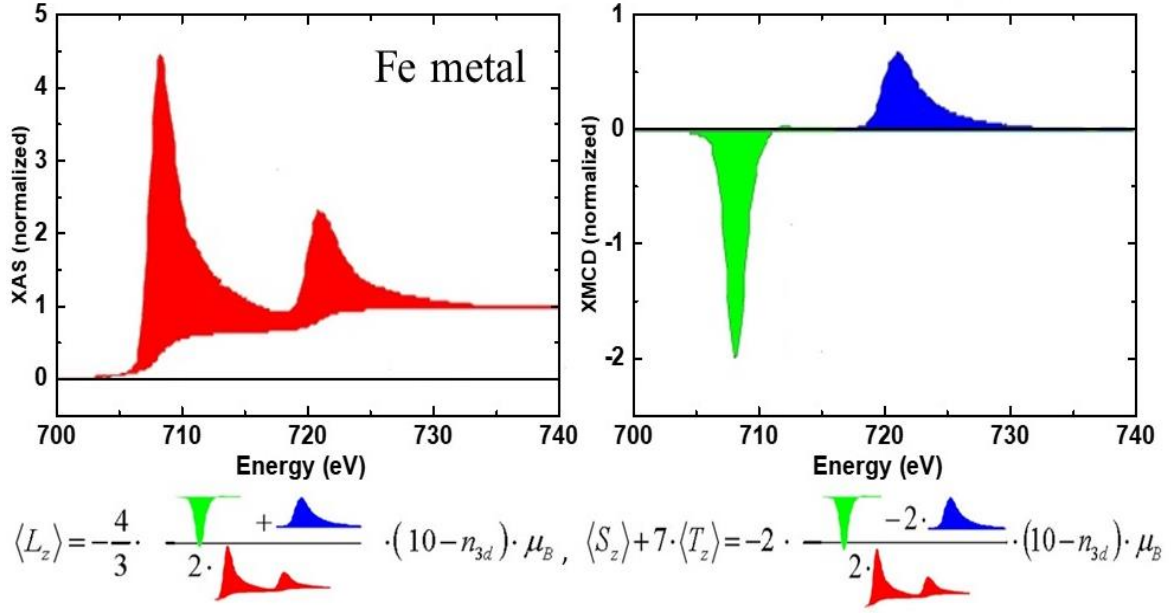


Fig.2. 22 Quantitative determination of magnetic moments by Sum Rules. The normalized XAS is the spin averaged or non-magnetic spectrum (top-left) and difference XMCD spectrum measured by flipping the magnetization or the light or helicity (top-right). Relation between spectral areas and L_z , S_z and T_z expectation values

In bulk cubic or polycrystalline samples with arbitrary grain orientation, T_z term could be ignored for the 3d TM. However, in ultrathin films and surfaces with perpendicular magnetic anisotropy (PMA), the T_z term can have a sizable effect on XMCD based effective spin magnetic moments.

The magnetic dipole term T_z presents in the case of symmetry breaking by uniaxially squeezed (see fig.2.23 a)) or a quadrupolar spin distribution of electrons. The increased charge along the z-direction reduces along the x-y directions. Mathematically, it is correlated to the spin magnetic dipole operator as shown by in Eqn. 2.50. When the spin-orbit coupling is small, it can be re-written as[52, 53]

$$\mathbf{T} \approx -\frac{2}{7} \mathbf{Q} \cdot \hat{\mathbf{S}}, \quad \mathbf{Q} = \mathbf{L}^2 - \frac{1}{3} L^2, \quad T_z = \frac{S_z(1 - 3\cos^2\theta)}{2} \quad (2.50)$$

\mathbf{Q} is the quadrupole moment of the charge distribution. T_z is for $\hat{\mathbf{S}}$ aligned along the z direction. In 3d transition metal, the magnetic dipole term can be determined by the symmetry relation. $\langle T_x \rangle + \langle T_y \rangle + \langle T_z \rangle = 0$. [54] It can be written in the absence of in-plane anisotropy. $m_T^\perp + 2m_T^\parallel = 0$. To determine T_z and MAE, the moments of $m_{spin} - 7m_T^\theta$ and m_{orb}^θ are deduced by the sum rules. From these values and relation, m_T or m_{orb}^θ can be obtained.

$$m_{T,orb}^\theta = m_{T,orb}^\perp \cos^2\theta + m_{T,orb}^\parallel \sin^2\theta \quad (2.51)$$

Moments from angle dependent have this relation, too.

$$m_{T,orb}^\theta = m_{T,orb}^0 - \Delta m_{T,orb} \sin^2\theta, \quad \Delta m_{T,orb} = m_{T,orb}^\perp - m_{T,orb}^\parallel \quad (2.52)$$

By these relations, $m_{T,orb}^\parallel$ can be determined. Δm_{orb} is related spin-orbital interaction.

On the basis of spin-orbit coupling, orbital moment is enhanced along the easy axis of anisotropic magnetic material. The spin-orbit energy tries to align the spin moment along the direction with enhanced orbital projections. (see fig. 2.23 b)) The magnetocrystalline anisotropy energy, MAE relates to orbital moment and the magnetic dipole term. Bruno model relates the energy anisotropy in a perturbation theory to the spin-orbit interaction, ($\mathbf{H}_{sox} = \xi \mathbf{L} \cdot \mathbf{S}$).[55, 56]

$$\Delta E_{SO} = -c \frac{\xi}{4\mu_B} (m_{orb}^\perp - m_{orb}^\parallel) \quad (2.53)$$

where $\Delta E_{SO} = E_{SO}^\perp - E_{SO}^\parallel = -K_1$ with $E_{SO} = K_0 + K_1 \sin^2 \theta$. And c is the factor dependent on the band structure. ξ is the spin-orbit coupling constant. ($\xi \leq 0.1$ eV). The magnetocrystalline anisotropy energy (MAE) is given only orbital magnetic moments, while the spin-orbit interaction is treated in second order. In here, the anisotropy of the field of the spin, is expressed by the magnetic dipole moment.[52] The MAE is given as

$$\delta E = -\frac{1}{4} \xi \hat{\mathbf{S}} \cdot [\langle \mathbf{L}^\downarrow \rangle - \langle \mathbf{L}^\uparrow \rangle] + \frac{\xi^2}{\Delta E_{ex}} \frac{21}{2} \cdot \hat{\mathbf{S}} \cdot \langle \mathbf{T} \rangle \quad (2.54)$$

with $[\langle \mathbf{L}^\downarrow \rangle - \langle \mathbf{L}^\uparrow \rangle] = [\langle \mathbf{S} \rangle - 2\langle \mathbf{L}^\uparrow \rangle]$. And ΔE_{ex} , is the exchange splitting of the two spin bands and can be obtained from band structure calculations. The spin-orbit constant ξ depends strongly on atomic number Z , and also on the radius of the atomic shell. For the $3d$ transition metals, the spin-orbit interaction energy in the $3d$ band is small value of the order of several meV,[57] which is considerably weaker than the exchange interaction (~ 1 eV).

By angle-dependent measurement, the contribution of crystallographic related T_z term and its contributions to the magnetocrystalline anisotropy energy can be determined.[51]

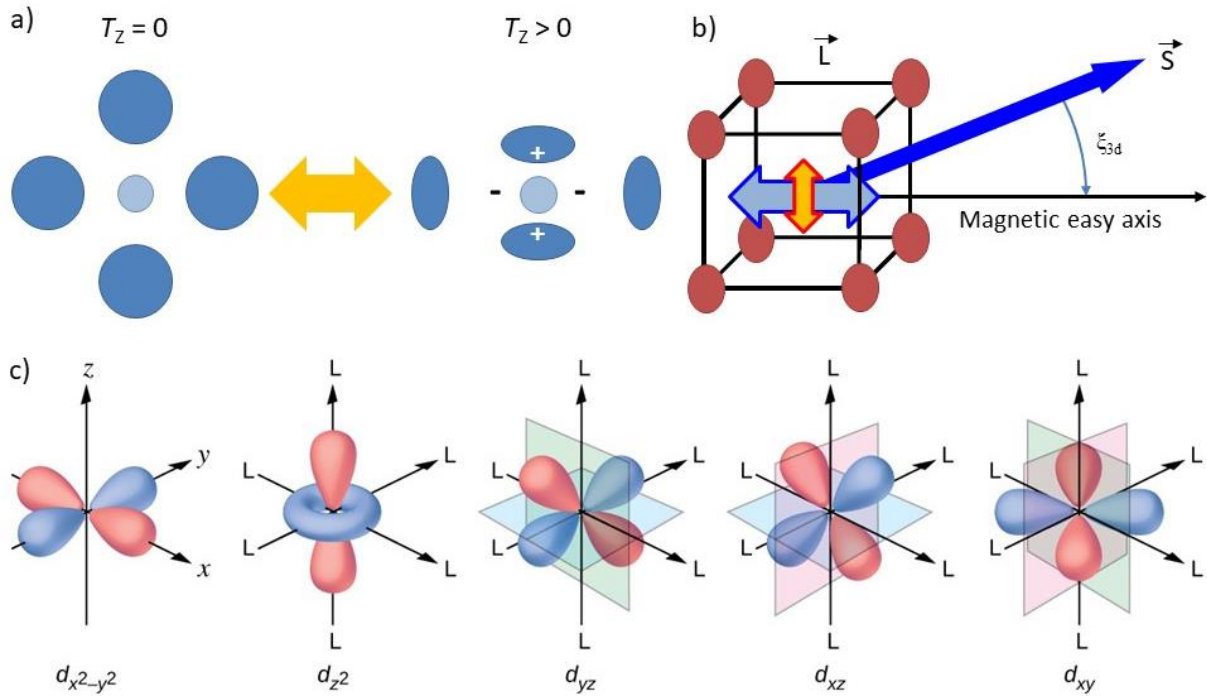


Fig.2. 23 The T_z term and the spin and orbital relation. a) Schematic of the charge and spin distribution for T_z term. b) Bruno model of the magnetocrystalline anisotropy. c) The shapes and labels of the five 3d orbitals.[58]

Chapter 3

Basic of Nanosized Exchange Spring Magnets

Nanosized magnets, like magnetic nanoparticles, single molecular magnets, nanomagnet patterns, clusters and so on, can be investigated for an understanding of fundamental physical phenomena [59, 60] and for application as ultra-high density magnetic information storage, catalysts, spintronic device or biomedical therapy.[61-63] Exchange-spring magnets, which are composed of magnetically hard and soft magnets, were developed as a concept for permanent magnets with tailored coercive fields and saturation magnetization. [64, 65] These combinations of high performances nanosized and exchange-spring magnets are achieving lots of applications and have also been studied from a fundamental point of view. [66, 67]

3.1 Nanomagnets

Between macroscopic and nanometer sample dimensions of the same material, different magnetic behaviors have been observed, which arise for example from a higher proportion of atoms on the surface, broken translation symmetry in nanometer scales and the geometrical constraints. Nanomagnetism is the area of research in physics focusing on the magnetic properties of nanosized objects. Nanomagnetism in solid state science includes application and the study of properties of the magnetism of nanoparticles, nanodots, nanowires, thin films, and multilayers. [68] Natural magnetic nanoparticles exist in many rocks and soils, where the nanoparticles are usually based on magnetite. Nanomagnets have also been found by biomineralization in bacteria, insects, birds and other creatures, where their magnetic moments are aligned or interacting with the earth's magnetic field.[69] Today, magnetic recording is a prominent successful application of nanomagnetism. In this technology, the areal bit density of magnetic hard disks has increased by a factor of tens of millions. Fig.3.1 shows growth of areal densities.[70] The application to spintronic devices has also increased, rapidly.

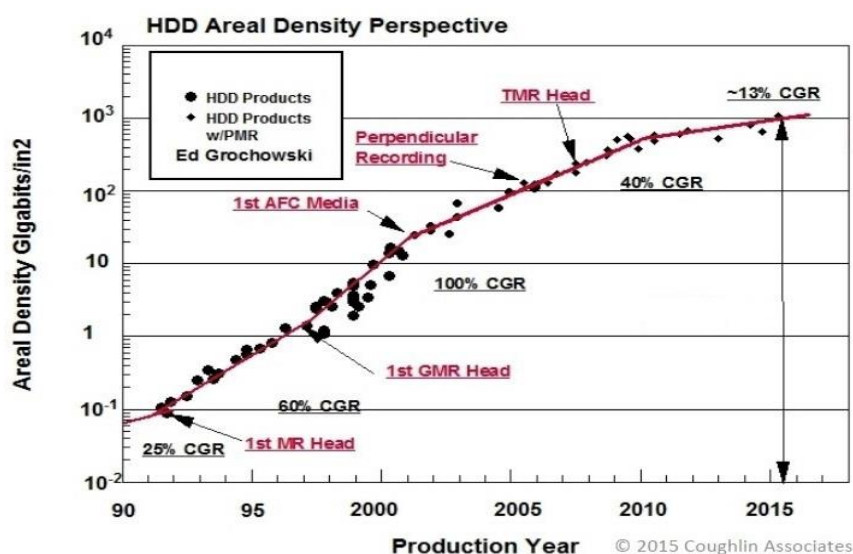


Fig.3. 1 Historical areal density trends for magnetic hard disk drives.[70] by Coughlin Associates in Storage Developer Conference (SDC 2015). CGR: compound growth rate, MR: magnetoresistance, GMR: giant MR, AFC: anti-ferromagnetically coupled and TMR: tunnel MR

The unusual phenomena of nanomagnetism have several reasons, since the sample dimensions meet the characteristic length scales. Nanomagnets can be formed with a size smaller than critical domain size D_{cr} and smaller than superparamagnetic critical diameter D_{cr}^{spm} . Therefore nanomagnets become superparamagnetic.[71] The exchange length $l_{ex} < 100$ nm which can be usually ignored in bulk systems, effects nanomagnets. The characteristic lengths scales, which should be compared to the size of nanoobjects, are shown in Table3.1.[68]

Symbol	Length	Typical magnitude (nm)
d_a	Interatomic distance (Fe)	2.5×10^{-1}
d_{ex}	Range of exchange interaction	$\sim 10^{-1} - \sim 1$
d_{RKKY}	Range of RKKY interaction	$\sim 10^{-1} - \sim 10$
d_c	Domain size	$10 - 10^4$
D_{cr}^{spm}	Superparamagnetic critical diameter	$\sim 1 - \sim 10^2$
D_{cr}	Critical single-domain size	$\sim 10 - \sim 10^3$
δ_0	Domain wall width	$\sim 1 - \sim 10^2$
l_{ex}	Exchange length	$\sim 1 - \sim 10^2$
λ_{mfp}	Electron mean free path	$\sim 1 - \sim 10^2$

Table 3. 1 Typical magnitudes of some characteristic lengths in magnetism.[57]

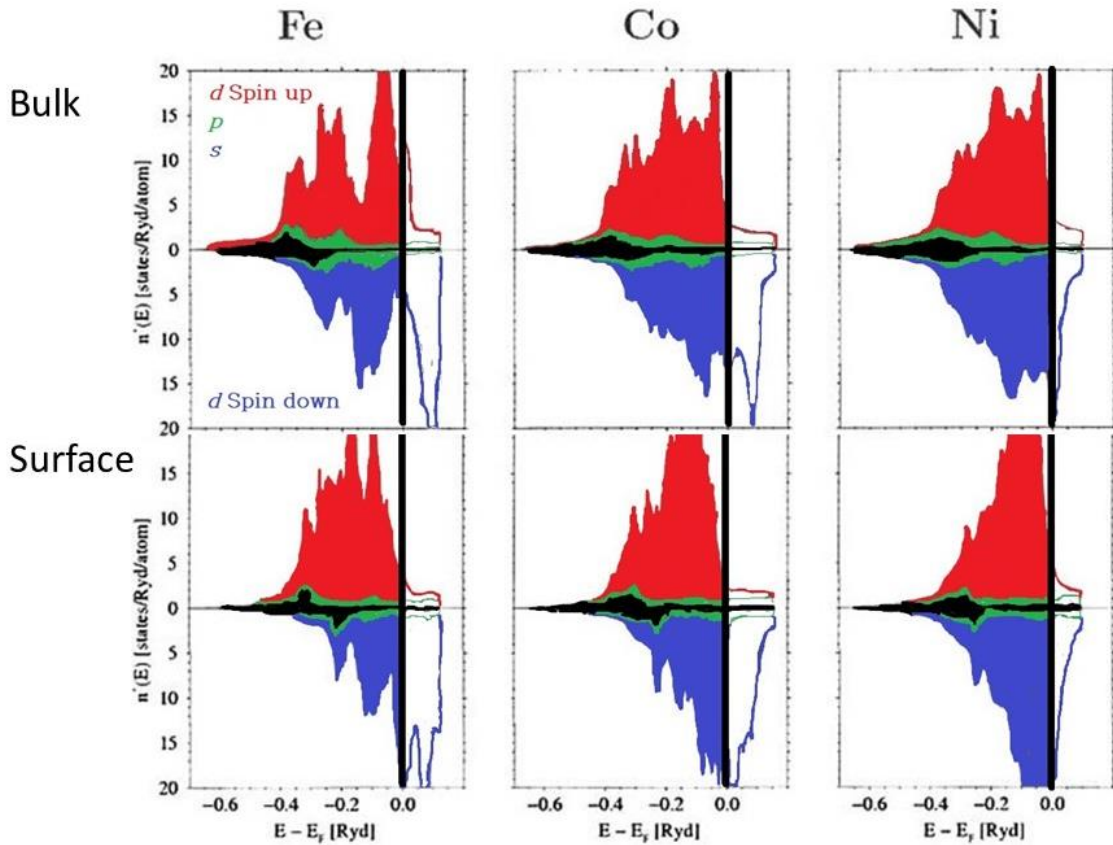


Fig.3. 2 Density of states for Fe, Co, and Ni in bulk metals (above) and a (100) surface (below)[63] d-state Spin up (red) Spin down (blue), p-state (green) and s-state (black)

In low dimensional materials, the broken translation effects atoms most prominent by the change in the nearest neighbor coordination, as it happens at surfaces or interface regions. In general, the electronic structure of the atoms on the surface is different compared to atoms in bulk. Usually, the

bandwidth is narrowed by reduction of the coordination number. The comparison of the density of states of bulk and surface Fe, Co and Ni is shown in Fig. 3.2. The density of state curves of the (100) surface atoms is narrowed compared to bulk samples of the same materials.

In addition, due to the symmetry breaking and the non-cubic crystal field, the orbital contribution to the magnetic moment increases with decreasing dimensionality.[72] Table 3.2 shows the increasing of the orbital moment and anisotropy energy by going from the bulk to the single atom.

	Bulk	Monolayer	Diatomic wire	Monoatomic wire	Two atoms	Single atom
Orbital moment ($\mu_B/atom$)	0.14	0.31	0.37	0.68	0.78	1.13
Anisotropy energy (meV/atom)	0.04	0.14	0.34	2.0	3.4	9.2

Table 3. 2 Magnetic orbital moments and anisotropy energy. Co on Pt with different dimensionalities.[64][73]

The presence of defects and impurities, such as adsorbates, change the strain and modify not only the lattice parameter. These factors also influence to the magnetic properties of atoms nearby. Furthermore the crystal structure of nanosized materials is also formed differently from the bulk. For instance, metallic cobalt particles smaller than approximately 30 nm diameters reveal fcc (face-centered cubic) structure, compared to bulk hcp (hexagonal close-packed).[68]

3.2 Exchange-Spring magnet

An exchange spring magnet (ESM) consists of more than one type of FM phases usually comprising a hard and a soft magnetic phase, also called exchange-coupled composition magnet (ECC magnet).[64] The magnetic properties of ESM are based on the exchange interaction between those two hard and soft magnetic materials. The main reason to use ESMs is the possibility to tailor the magnetic properties by a combination of the hard and soft magnet, which could not be simply done by the optimization of just a single component material. Fig. 3.3 and Fig. 3.4 show schematic and experimental examples of ESMs, which have a high coercivity from the hard phase and a higher magnetization from the soft phase.

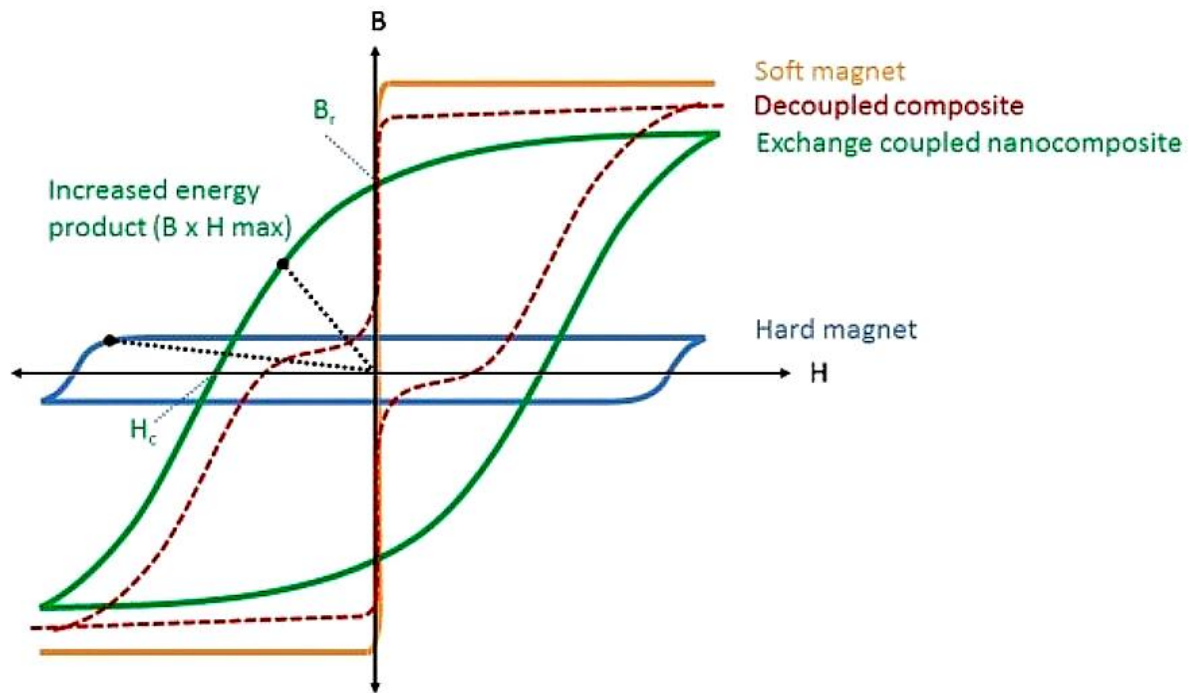


Fig.3. 3 Demonstration of the hysteresis loops of hard and soft phase, decoupled and exchange coupled ESMs

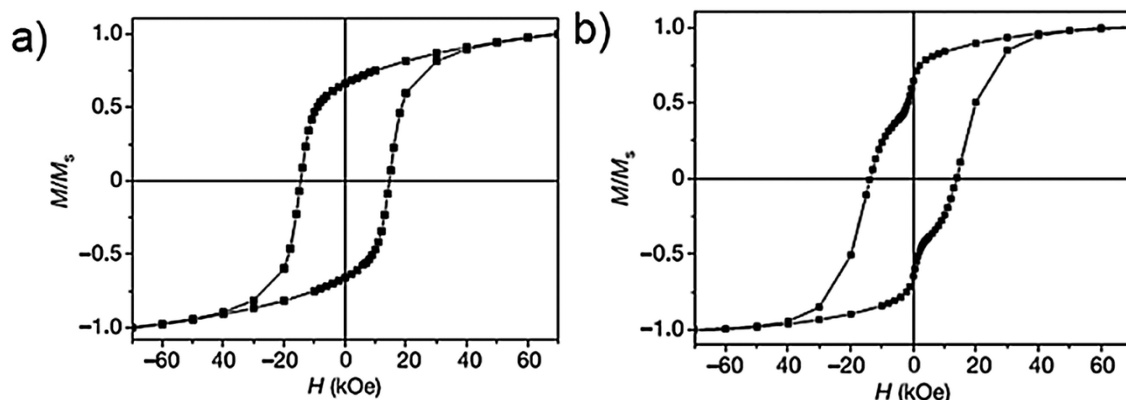


Fig.3. 4 Hysteresis loops of $\text{Fe}_3\text{O}_4:\text{FePt}$ nanocomposites. a) Single phase behavior with effective exchange coupling between two phase by $\text{Fe}_3\text{O}_4(4 \text{ nm}):\text{FePt}(4 \text{ nm})$ assembly and b) the phase separation hysteresis by $\text{Fe}_3\text{O}_4(12 \text{ nm}):\text{FePt}(4 \text{ nm})$. [65]

3.2.1 Soft and Hard Ferromagnetic materials

Ferromagnetic materials are separated into two broad classes corresponding to their hysteresis loops, which reflect the energy stability and thermal dissipation by their open area.[74] Soft magnetic materials are easily magnetized, because of small coercivity and small total anisotropy energy K . Soft materials are characterized by high permeability and low losses. Permeability is the degree of magnetic response of a material to an applied field. The pinning of domain walls at inclusions and grain boundaries can affect the behavior of soft materials.[75, 76] Examples transition metals (TM, e.g. Fe, Co, and Ni), as components in silicon steels, Fe-Ni-Co alloys, amorphous alloys, nanocrystalline alloys, and soft ferrites (MnZn, NiZn). These magnetic materials are used in motors, generators, and transformers.[76, 77] Table 3.3-4 show intrinsic magnetic properties of some famous soft magnetic materials

Metal	Bohr magneton number per atom at 0°K	Saturation magnetization 10 ⁵ Am ⁻¹ or 10 ² G, at		Curie temperature	
		0°K	17°C	°K	°C
Iron	2.216	17.45	17.08	1043	770
Cobalt	1.716	14.30	13.98	1400	1127
Nickel	0.616	5.22	4.84	631	358

Table 3. 3 Intrinsic magnetic properties of ferromagnetic metals.[78]

Composition	Saturation polarization (T)	Coercivity (Am ⁻¹)	Curie temperature (°C)	Permeability at $H=4\text{mAm}^{-1} \times 10^3$
Fe ₆₇ Co ₁₈ Si ₁ B ₁₄	1.80	5 (~0.06Oe)	~550	1.5
Fe ₃₉ Ni ₃₉ Mo ₂ Si ₁₂ B ₈	0.8	2	260	20
Fe ₇₄ Co ₂ Mn ₄ Si ₁₁ B ₉	1.0	1.0	480	2
Fe _{73.5} Cu ₁ Nb ₃ Si _{13.5} B ₉	1.25	1	600	100

Table 3. 4 Survey of soft magnetic amorphous and nanocrystalline alloys.[79]

Hard magnetic materials, which are used as permanent magnets, are hard to magnetize and difficult to demagnetize. These magnets have a higher coercive field (coercivity, H_C) and maintain their magnetism without field after they have been magnetized (remnant, M_r). The origin is the high pinning force of domain and their walls.[80] Permanent magnets have been developed to increase the energy products from naturally abundant lodestone, high carbon steels, tungsten/chromium steels, ferrite magnets, AlNiCo, up to the well-known rare-earth (RE) based magnets, as shown figure 3.5 by the increase of the maximum energy product and a decrease of effective volume of the magnet.[81]

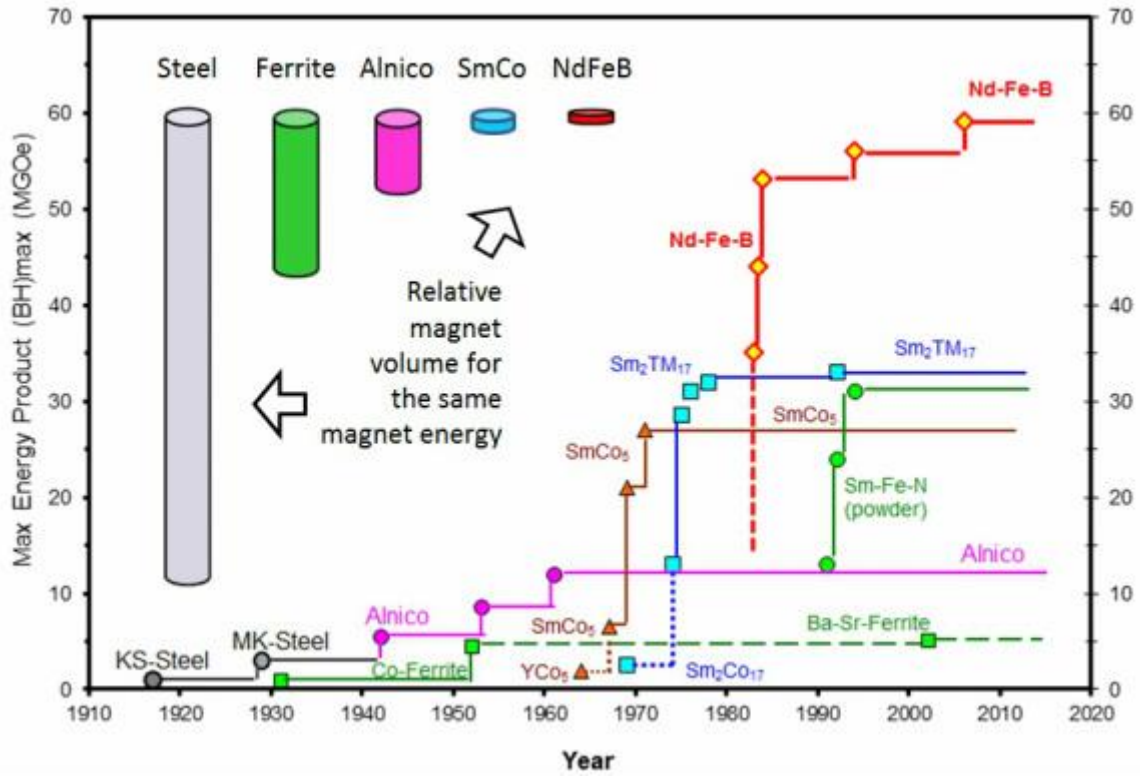


Fig.3. 5 Historical development of different types of permanent magnets, plotted their maximum energy product $(BH)_{max}$. [82]

The high energy product of the rare-earth magnets with a small volume is very attractive and has big advantages. Table 3.5 provides a comparison of the intrinsic magnetic properties of some related hard magnetic materials.

Phase	symmetry	J_s [T]	T_c [K]	$\mu_0 H_C$ [T]	K_1 [MJ/m ³]	A [pJ/m]	δ_B [nm]	D_C [nm]
α -Fe	cubic	2.15	1043	-	0.048	20.7	11.26	20
Co	cubic	1.76	1131	0.20	0.45	-	-	-
Co	hexagonal	1.81	1390	0.76	0.45	36.2	14	68
L1 ₀ -FePt	tetragonal	1.43	750	11.5	6.6	10	6.3	359
L1 ₀ -CoPt	tetragonal	1.00	720	12.3	2.8	10	7.4	479
L1 ₀ -FePd	tetragonal	1.39	760	3.5	1.8	-	11.5	330
SmCo ₅	hexagonal	1.07	1020	3.9	16.6	12	3.6	1137
Sm ₂ Co ₁₇	rhombohedral	1.22	1190	6.5	3.2	17	8.6	401
Nd ₂ Fe ₁₄ B	tetragonal	1.61	585	7.6	4.3	7.3	3.9	196

Table 3. 5 Intrinsic magnetic properties of different magnetic materials. J_s : Spontaneous polarization, T_c : Curie temperature, $\mu_0 H_C$: Coercive field, K_1 : Magnetocrystalline anisotropy energy, A : Exchange constant, δ_B : Domain wall width, D_C : Single-domain particle diameter. [83-85]

However, the expensive cost of rare-earth elements in scarcity situations causes the need for new magnets with lean and/or cheaper rare-earth elements. One way is to use exchange-coupling effect.

3.2.2 Exchange-coupling effect

Exchange coupling materials as described here consist of the soft phase aligned to the magnetization vector of a hard magnetic phase due to the exchange coupling effect. As described before, materials can have high saturation magnetization and high remanence by a proper of these phases resulting in a significant large maximum energy product $(BH)_{max}$ could be obtained by exchange coupling effect. However, the coercivity will usually decrease by exchange coupling effects with a soft magnetic second phase.[86]

The first actual exchange spring magnet was observed by Coehoorn et al. in 1989.[87] The theoretical presentation was presented by E. F. Kneller in 1991. Figure 3.5 is the schematic of 1-dimensional exchange-coupling from E. F. Kneller.[64]

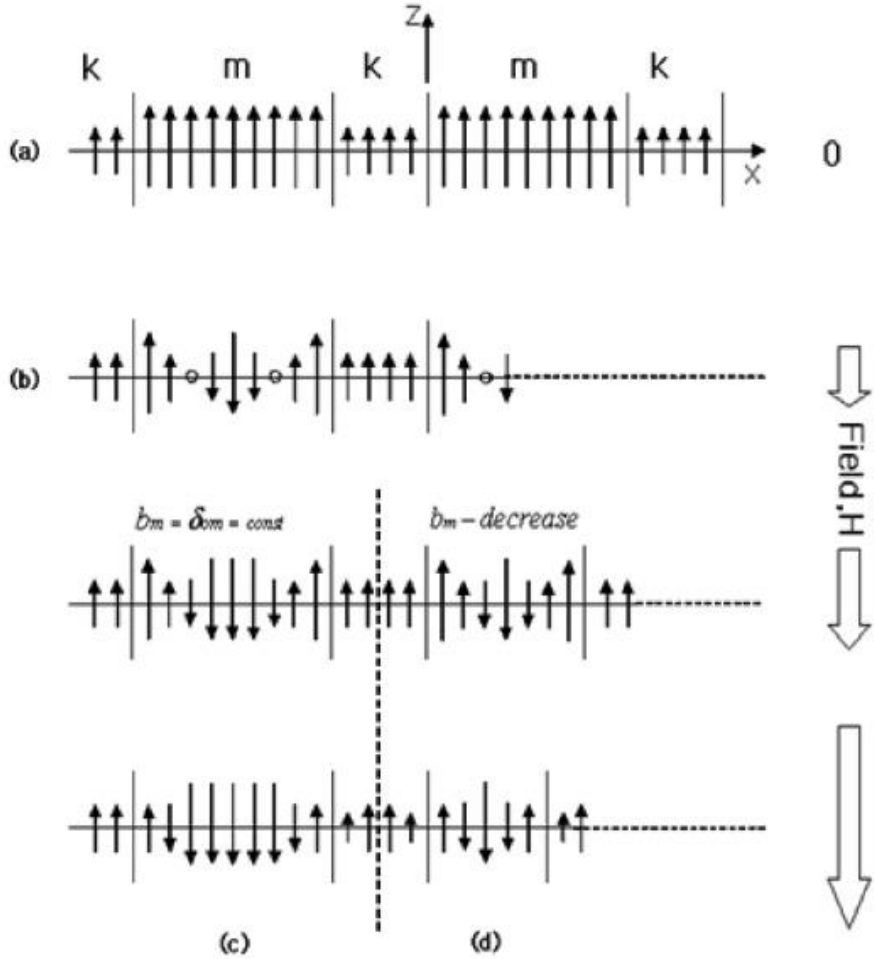


Fig.3. 6 1-D schematic of one-dimensional model of the micromagnetic structure of exchange-coupling effect. This is alternation structure of k -(hard) and m -(soft) phases. (a) Saturation remanence. (b-c) Demagnetization in an increasing reverse field H . (d) Demagnetization at decreasing width. [53]

The k phase is a hard magnetic material with high magnetocrystalline anisotropy energy, and the m phase is a soft magnetic material with high saturation magnetization. In figure 3.6 (a), if the external magnetic field is zero, the magnetizations of a hard and a soft magnet are arranged in the same direction. In fig. 3.7 (a-c). At a low field H , the hard magnet spins keep the direction. Increasing H , the soft magnetic spins show the inclination to reverse. However, the spins adjoined to interface maintain

the initial state by exchange interaction with the hard magnet spins. At a high field, all spins are reversed along the external field direction, exclusive of interface spin at the hard magnet (see Fig.3.6 between (c) and (d)). This effect, the maintenance of soft magnetic spin by a hard magnet on the interface in the applied field is called exchange coupling effect. By this effect, the composition of the hard and soft magnet has high coercivity. Likewise, the saturation magnetization depends on the amount of soft magnet phase. With exchange-coupling effect, the magnet has high saturation magnetization and large coercive field, although both are reduced. The magnetic property of composition has to be investigated and tuned to achieve for an appropriate application and dependent on the fraction of hard and soft magnetic material and shape.

3.2.2.1 Critical size for exchange-coupling effect

The critical size for effective coupling between the hard and the soft magnetic material has been theoretically and experimentally investigated.[64, 88-90] Energy products have been increased with the higher remanent field. For melt-spun 30 nm $\text{Nd}_2\text{Fe}_{14}\text{B}$ / 10 nm Fe_3B - α -Fe mixtures the maximum energy product has been increased up to 11 MGOe.[87] A. Manaf et al. has reported a higher maximum energy product of 19MGOe by the combination of NdFeB and α -Fe, too.[89] The 70 % of $\text{Sm}_2\text{Fe}_{17}\text{N}_x$ and 30% of α -Fe 20 nm grain size composition has demonstrated 25.8 MGOe with a high remnant magnetization of 80% with respect to the saturation magnetization.[91] These results clearly show that the grain size of soft magnetic materials has to be nm size. The maximum energy product is affected according to the soft magnetic layer, which has a critical thickness.[90, 92]

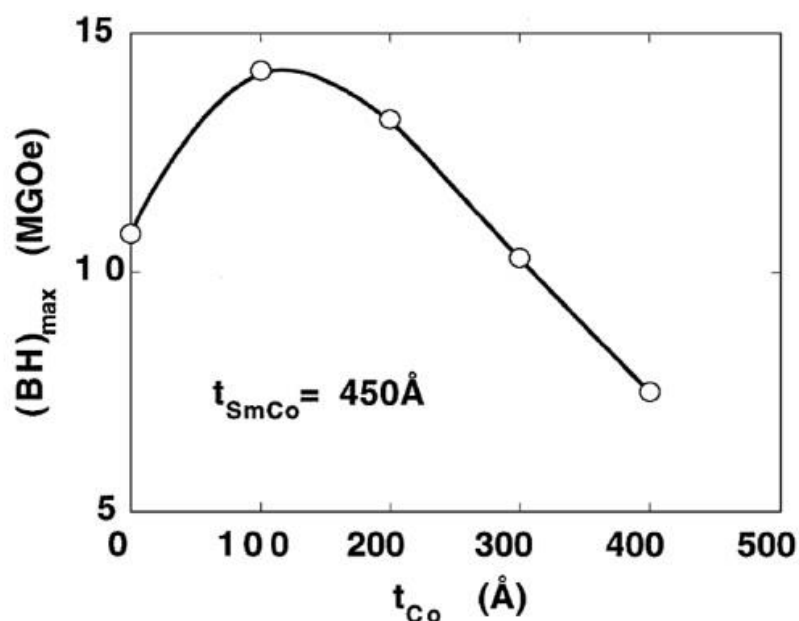


Fig.3. 7 Energy product variation for Co thickness changes in SmCo/ Co multilayer[90]

In figure 3.7, Co soft magnetic layers are deposited with a thickness range from 10 to 40 nm deposited on 45 nm thick SmCo. The Co layer of 10 nm has the highest maximum energy product of 14 MGOe.[90]

3.3 L1₀-FePt / Co composition ES magnet

For this work, we selected L1₀-FePt and cobalt for ESMs. The uniaxial magnetocrystalline anisotropy in the hard magnetic L1₀-FePt layer could be prepared to have its easy axis perpendicular to the film plane. Co has high saturation magnetization and high fractional remanence.[85]

Today, investigation on FePt and Co exchange spring magnet compositions have been started for applications and fundamental magnetic research on thin films and nanoparticles. [2, 93] In Fig. 3.8 and Fig. 3.9, magnetic properties of thin films and nanoparticles of ES nanomagnets are shown, which are composed of FePt, Co and Fe and tailored by exchange coupling effects.

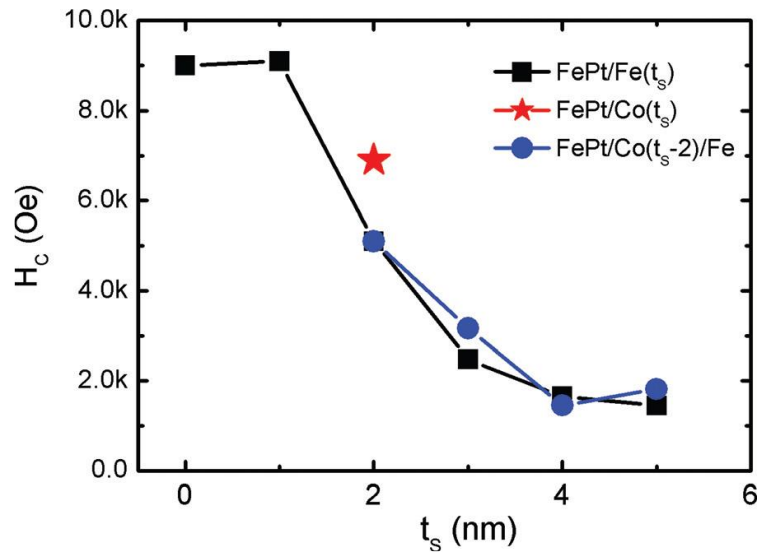


Fig.3. 8 Exchange coupling effect to the coercive field on FePt/Fe and FePt/Co/Fe film.[80]

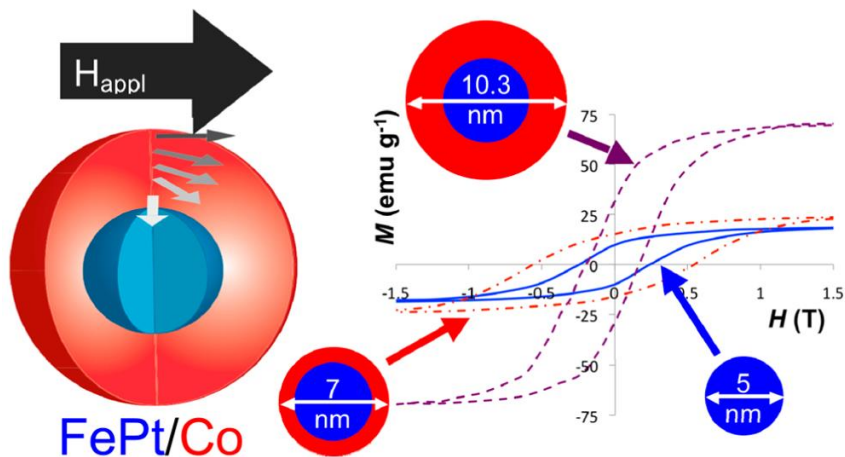


Fig.3. 9 Diagram of ESM and hysteresis loop for FePt@Co nanoparticles.[2]

Further systems are FePt core particles (5 nm diameter) surrounded with a soft magnetic Co shell (0.6 to 2.7 nm thick) by microwave synthesis. The ES magnetic nanoparticle led to a 4-fold enhancement in the energy product as compared to the energy product of bare FePt with coercivity and saturation moment.[2]

3.3.1 Phase diagram and Crystal Structures of FePt and Cobalt

3.3.1.1 FePt

The $L1_0$ chemically-ordered FePt has attracted attention due to their excellent intrinsic magnetic, chemical and mechanical properties. Therefore, $L1_0$ -FePt is a good candidate for magnetic recording with very high uniaxial magnetocrystalline anisotropy.[83] We will discuss the essential properties of the FePt material system. In particular, the composition dependent crystal structure is explained. The magnetic properties of the $L1_0$ -phase are discussed and compared with other materials in the previous section.

1. Phase diagram

Chemically disordered (A1-phase, face-centered cubic) FePt is present for temperature below 600 °C and above 1350 °C, as shown in the phase diagram in Fig. 3.7. Chemically-disordered means that Fe or Pt atoms occupy statistically the lattice sites of the fcc-elementary cell. In the composition range, FePt can be three different crystalline phases. (FePt₃: $L1_2$ (fcc) phase from 15 to 32 % Fe, FePt: $L1_0$ (fct) phase from 35 to 55 % Fe and Fe₃Pt: $L1_2$ (fcc) phase from 55 to 80 % Fe). The chemically ordered phase ($L1_0$ -phase, face-centered tetragonal) in the composition range from Fe₄₅Pt₅₅ to Fe₆₅Pt₃₅ can be formed with high crystallinity in the temperature range of 600 °C to 1300 °C with high chemical order and a layered anisotropy. Fe and Pt atoms occupy (110) planes in an alternating layered way. In fig. 3.10, unit cells are presented. The strong directional crystalline anisotropy has a large effect on the magnetic behavior, as shown in Table3.6.

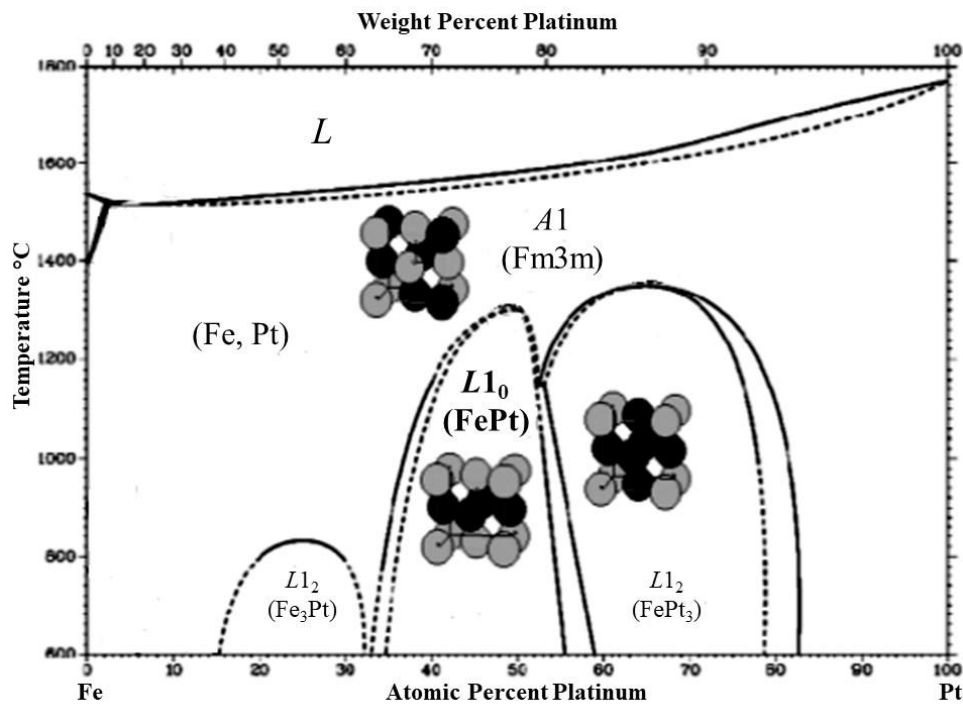


Fig.3. 10 Equilibrium phase diagram of the Fe-Pt system.[83]

	L1 ₂ -Fe ₃ Pt	L1 ₀ -FePt	L1 ₂ -FePt ₃
Disordered	Para	Ferro $\mu_0 M_S \approx 1.5 T$ low H _C	Ferro
Ordered	Ferro $\mu_0 M_S \approx 1.7 T$ low H _C < 1 T	Ferro $\mu_0 M_S \approx 1.43 T$ high H _C > 1 T	Para antiferro T < 160 K

Table 3. 6 The magnetic behavior and magnetic properties at room temperature of the main phases in the Fe-Pt system.[83]

2. Crystal structure

In Fig.3.11 shows a comparison of the unit cells between the fcc- and fct- crystal structures. The L1₀- phase has a four-fold rotational symmetry along the (001) axis. The unit cell of the fct structure is slightly compressed along the c-direction (001). The fcc unit cell has a lattice constant of 3.81 Å whereas the fct unit cell has a larger lattice constant $a = 3.852 \text{ \AA}$, and for the cubic face the lattice constant of $c = 3.716 \text{ \AA}$ is smaller.

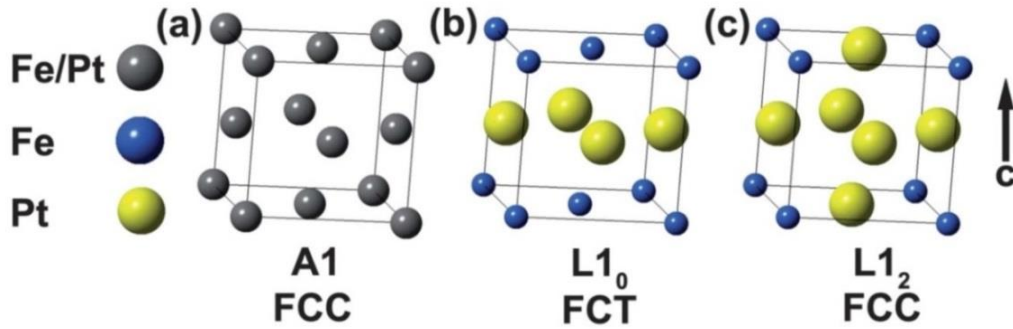


Fig.3. 11 The unit cells for the different phases of FePt: (a) A1 alloy, face-centered cubic, (b) L1₀ FePt intermetallic, face-centered tetragonal, and (c) L1₂ FePt₃ intermetallic, face-centered cubic.[82]

If FePt alloy contains Fe of 68-85%, a chemically ordered phase forms Fe₃Pt. This crystal phase is likewise cubically centered with L1₂ symmetry. At a larger Pt excess, FePt₃ can also be formed fcc-phase as shown in fig. 3.11 (c). The L1₀-Phase of FePt layers or Fe-Pt multiple layers on suitable substrates (MgO (100), LSAT (100)) can be formed at high temperature. In the range of high temperature treatment, decreasing temperature to room temperature does not affect FePt materials.[94, 95] In the case of L1₀-FePt thin films, the fct ordering is formed directly during the deposition process at suitable conditions, such as temperature and pressure. Alternatively, after RT deposition films have to be annealed for subsequent ordering. Both of grains coalescence in the ordered phase may occur during the annealing process.

Thin films of L1₀-FePt are known to have high coercive fields with huge magnetocrystalline anisotropy energy ($K_u = 6.6 \times 10^6 \text{ Jm}^{-3}$), which is reported in theoretically and experimental studies.[96, 97] The coherent rotation model indicates the possibility to achieve coercive fields of L1₀-FePt almost reaching 12 T ($2K_u/M_S \sim 120 \text{ kOe}$ at 300 K).[98] Fig.3.12 shows the magnetization curve for a 5 nm thick thin film measured at 4.5 K along the perpendicular film plane direction.

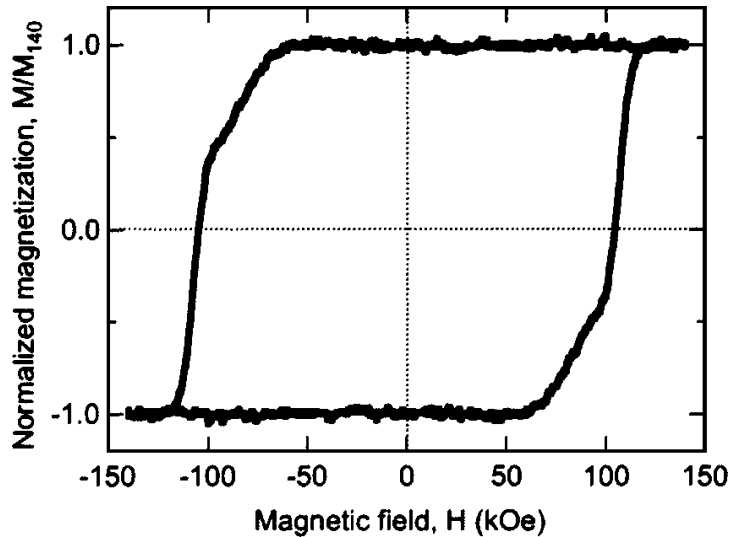


Fig.3. 12 Out-of-plane hysteresis loop of the FePt film with 5 nm thickness measured at 4.5 K.[86]

3.3.1.2 Cobalt

Cobalt is a representative transition metal and also a RT ferromagnetic material. Cobalt has two crystalline phases, one is hexagonal close-packed (hcp) and the other is face-centered cubic (fcc, also called cubic close-packed). In fig. 3.13 (left), the phase diagram of cobalt is shown. At room temperature cobalt is hcp. The phase can be changed to fcc at a temperature depending on the sample grain size.[99] The hysteresis of cobalt thin films shows typical soft ferromagnetic behaviors with high saturation magnetization and low coercive field in Fig. 3.13 (right).[100]

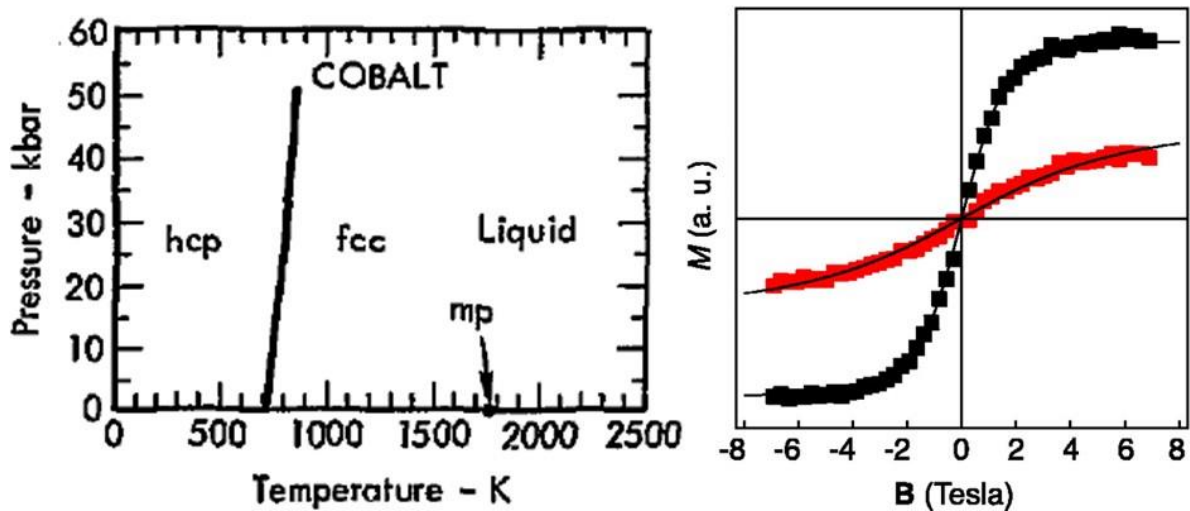


Fig.3. 13 Phase diagram of cobalt and hysteresis loops. Magnetic hysteresis loops of the Co atom at 5.5 K, $\theta = 0^\circ$ (black squares) and $\theta = 70^\circ$ (filled triangles) relative to the surface normal.[1]

Chapter 4

Experimental methods: Fabrication & Characterization

4.1 Sample preparation

4.1.1 Sputter deposition of thin films (Magnetron Sputtering)

In this work thin films have been produced by Magneto co-sputtering, basically, a physical vapor deposition method (also known as physical vapor deposition (PVD) coating). The schematic of a RF (Radio Frequency) magnetron sputtering device is shown in Fig. 4.1. In the sputtering chamber, filled with low-pressure Ar gas, a plasma is generated by positively charged Ar^+ ions that are accelerated towards targets by an applied constant voltage of a few hundred volts. An elaborate electronic control allows one to ignite the plasma even at low pressure. A magnetron gun improves both, deposit speeds and film quality by increasing the fraction of ionized atoms. A magnetic field keeps the plasma in front of the target to intensify the bombardment of ions. The sputtered target atoms are condensed onto a substrate and form there either continuous films or islands, depending on the target and substrate material and sputtering conditions. It is possible with this technique to deposit as well single atoms as molecules. It can provide extremely pure thin films with high performance and is very useful for thin film preparation.

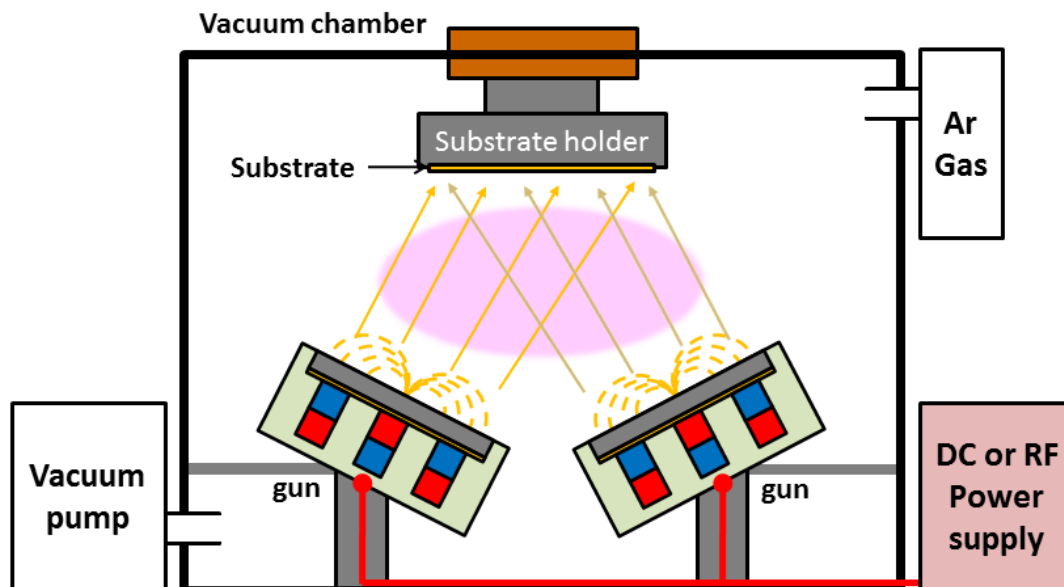


Fig.4. 1 Schematic of RF magnetron sputtering. [93] Ar^+ ions hit targets. Sputtered target atoms are deposited on the substrate.

For FePt thin film layers and FePt/ Co multilayers, a magnetron sputtering system as described above has been used. Three different targets can be mounted with separate sputtering power supplies. Thus, alloys with well-defined compositions (by controlling the individual deposition rates) can be produced

by simultaneous sputtering (co-sputtering). The system includes a substrate heating which provides temperatures up to 800° C that are necessary for forming the FePt L1₀-phase.

4.1.2 Manufacture of regular nanopatterns

Regular nanopatterns can be realized by means of bottom-up or top-down methods. By using the bottom-up methods, it is attempted to arrange free nanoparticles regularly on a substrate by self-organization. Top-down methods use lithography processes to imprint patterns into a sample (e.g. by photo-, electron-, ion beam lithography and nanoimprint lithography).

Before presenting the technique used in this thesis, I would like to introduce a few other techniques, first. Bottom-up processes are also used for producing nano-patterns by chemical synthesis of colloids.[5, 101, 102] FePt nanoparticles can be formed by thermal decomposition of Fe(CO)₅ and reduction of Pt(Acetylacetonate, acac)₂. Nanoparticles on a substrate can be produced with a hexagonal pattern by applying the spin coating. However, with this method homogeneous pattern in a few micrometers periods can be produced. A further method is a combination of block copolymer micellar nanolithography (BCML) and glancing angle deposition (GLAD).[103, 104] With this approach feature size of ~100 nm can be obtained. However, chemically synthesized FePt nanoparticles with excellent magnetic properties are not reported.

Most of the top-down methods use lacquer masks. The lacquer is typically applied by a spin coating (in order to obtain a homogeneous lacquer thickness) and subsequently processed to transfer the structure into the thin film. [105] Several top-down methods will be introduced. In photolithography, a lacquer mask covers certain parts of the sample and is then exposed to UV light. Molecular bonds in the lacquer are either ultimately dissolved or newly generated, depending on the type of lacquer (positive or negative). The exposed lacquer is removed during subsequent development or remained as structures on the substrate. In optical photolithography, the structure, sizes are limited to 250 nm due to the wavelength of light.

Electron beam lithography uses a focused electron beam for patterning, which is accelerated at a few 10kV. The areas of the lacquer to be patterned are exposed to the beam. The advantages of electron beam lithography consist in the fact that the electron beam can deflect easily and that any structures can be written. [106-108] with an accuracy slightly below 10 nm.[109] However, electron beam lithography is extremely time-consuming, especially for preparing large area. Structures cannot be written in parallel which can take several hours or even days.

Nanoimprint lithography (NIL, O₂-plasma stripper, RIE-Etcher)

For fast and small size patterning over large areas, nanoimprint lithography (NIL) is suitable technique. NIL uses a stamp, which is structured by e-beam lithography. The size of the structure can be a few nanometers. [109] NIL is possible two ways: in a positive (lift-off) and negative process. In case of the positive process (the structure is transferred with a stamp) the substrate is coated with a thin lacquer in which the structure is transferred by pressing the stamp into the lacquer. It is squeezed out from the areas where the stamp touches the substrate, leaving lacquer-covered and lacquer-free structures on the substrate. (see Fig.4.2) Subsequently, the material to be structured is deposited on the structured lacquer that now acts as a mask. When now the lacquer is removed by lift-off, the deposited material on top of the lacquer is removed together with the lacquer, while the material deposited directly on the substrate remains. The obtained pattern is the same as the pattern on the stamp (positive process). The process of this lift-off is illustrated in Fig. 4.2.[110]

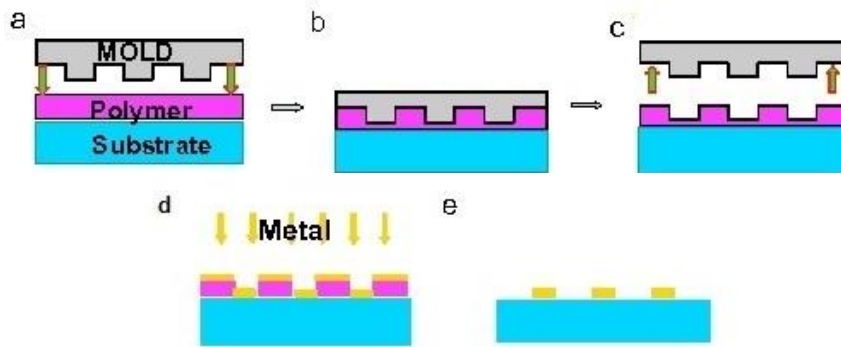


Fig.4. 2 Illustration of the process of nanoimprint lithography (NIL). a) The lacquer coated on the substrate. b) The stamp is pressed on lacquer. c) The stamp is demold from lacquer. d) Materials deposit on substrate and lacquer. e) The remained lacquer as a mask are removed. The pattern transfers to materials.

A lift-off process is, however, not suitable for L1₀-Phase FePt. In order to obtain chemically ordered structure (face-centered tetragonal, fct), Fe and Pt have to be deposited at temperature of 600 – 800 °C. The temperature is much higher than the glassy temperature of the lacquer and the lacquer will be burned or carbonized. Moreover, carbon will be dissolved in FePt film and disturbed the formation of the L1₀-phase.

In the negative process, which requires the transference of the opposite structure to the stamp, the L1₀-phase FePt thin films have to be deposited directly on the substrate. The lacquer is then spin-coated on FePt thin films. The stamp is pressed on the lacquer at appropriate temperature and pressure. The structured lacquer is then hardened to provide the mask. Subsequently, the uncovered part of the FePt thin film is etched away together with the protective lacquer. In the end, a FePt negative of the stamp structure is left, as desired.

The special difficulties of NIL technique are substrate unevenness (roughness), thermal stresses and the lifetime of the stamp. The stamp can be polluted by resist and its structure destroyed by particles. These problems often prevent to obtain good structures. Obducat, a company that produces imprint equipment, developed special polymer materials and a special processing to solve these problems. One is “Intermediate Polymer Stamp”; it is called IPS foil and a flexible polymer foil, transparent for light. The other is a “Simultaneous thermal and UV” (STU) process, which is a combination of thermal and photo imprint lithography. These are realized in the Eitre 3 equipment of Obducat. In the first process, an IPS foil is placed on the stamp, a pressure applied of a few bar, and the stamp and the foil heated above the glass transition temperature (T_g). When stamp and foil are kept at appropriate temperature and pressure for a certain time, the polymer fills up the structure. After cooling off of the stamp and foil below T_g , the IPS foil is taken off from the master stamp by carefully pulling it off in one sweep. A pattern replica inverse to the original master stamp is now on the IPS foil. The next process is the transfer of this negative on the IPS foil onto the actual lacquer. When this step is successful, the lacquer shows the same pattern as the master stamp. The lacquer has to be chosen according to the size and shape of the structures. TU2-35 by Obducat is such a lacquer. It is a TU-series photoresist which is a combined thermal and UV imprint lacquer. A thin film of the this lacquer is brought on top of the FePt thin film by spin coating. Then the IPS foil is put on top of the lacquer layer, which is brought to the glass transition temperature. When slight pressure is applied the lacquer takes over the structure of the IPS foil. By UV curing the lacquer is hardened and its structure stabilized. For curing the UV lacquer is exposed to mercury light of 250-400 nm wavelength. The positive pattern has now been transferred to the lacquer. The IPS film can be taken easily off the lacquer film. The scheme of all processes is shown in Fig. 4.3. [111]

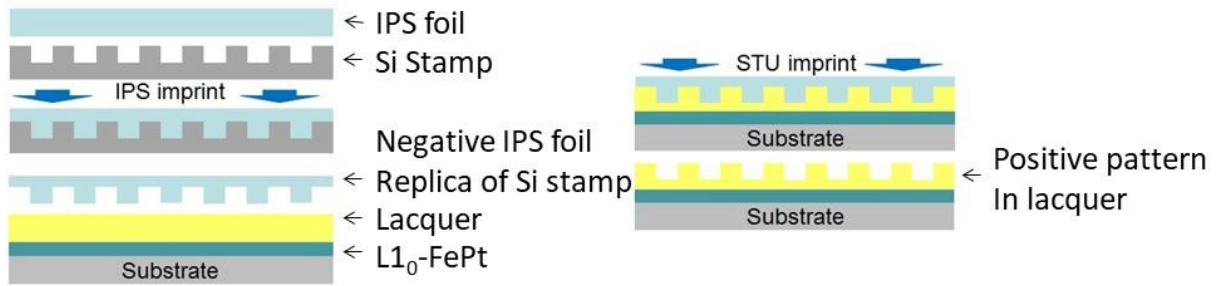


Fig.4. 3 Schematic of the IPS and STU imprint process. Two steps for the transference of the stamp structure to lacquer. IPS imprint step uses thermal imprint, and STU imprint step uses a combination of thermal and UV curing.

Typically still some lacquer (a few nm in thickness) is remaining between the positive structures after the last step, as indicated in Fig. 4.3. It is removed with an O₂-Plasma treatment. The etching rate for the TUV lacquer (TU2-35 by Obducat) is around 3.4 nm/min in the O₂-plasma. By means of reactive ion etching, the lacquer structure is then transferred to the FePt film (inductively coupled ICP-RIE Ar-plasma, FePt etching rate approximately 60 nm/min, lacquer etching rate 80 nm/min). The etching processes are depicted in Fig 4.4.

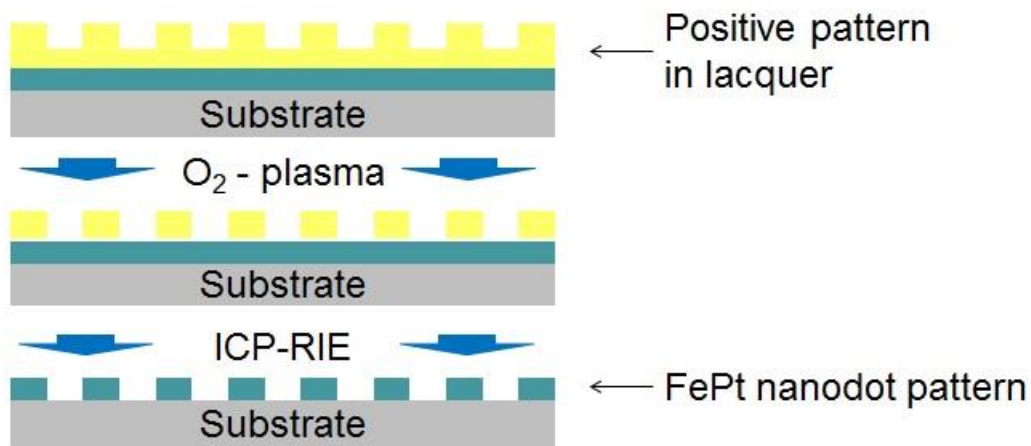


Fig.4. 4 Schematic of the etching steps. The lacquer structure transfer into the metal layer.

According to the various conventional methods presented in chapter 4.1.2, the bottom-up method, such as the block co-polymer micellar nanolithography (BCML) can produce rapid lithography and a large-area patterning. However, magnetic properties of these structures are not sufficient and not uniform over the patterned area. Electron beam and ion beam lithography can be fabricated to structures of less than 100 nm with high resolution, but these processes take too much time. The nanoimprint lithography has the double advantages since the entire surface is patterned in one process and the large area can be structured. In this work, stamp with 60 nm dot sizes 150 nm period pattern has been used for artificial nanostructures.

4.1.3 Structure and microstructure characterization method

4.1.3.1 X-ray diffraction (XRD)

X-ray diffraction is a common method to study the crystal structure of solids. A beam of monochromatic X-ray is diffracted by the atomic crystal lattice of the matter, at an diffraction angle and intensity characteristic for the crystal structure. XRD patterns can also give information about the elements present in a sample and their concentrations. In a simple picture, parallel planes scatter the radiation and, by interference, yield the well-known Bragg reflections, i.e. maxima in X-ray intensity along particular scattering angles. The relation between the diffraction angle θ , the distance between neighbored atom planes d , and the X-ray wavelength λ with a positive integer n is known as the Bragg law.[112]

$$2d\sin\theta = n\lambda \quad (4.1)$$

A system of lattice planes in a crystal is characterized by the so-called Miller indices (h, k, l) . By means of these indices also the inter planar distance d can be expressed: for a cubic crystal one obtains the following equation,

$$d = \frac{a}{\sqrt{h^2 + k^2 + l^2}} \quad (4.2)$$

where a is the lattice constant. In practice, the lattice constant a of crystal structure can be obtained by combination of Bragg's law and eqn. (4.2). The degree of ordering of atoms A and B on the lattice sites in binary alloys can be quantified by the ordering parameter S , which is given by

$$S = \frac{r_A - X_A}{1 - X_A} = \frac{r_B - X_B}{1 - X_B} \quad (4.3)$$

where X_A is the mole fraction of element A in the alloy and r_A is the probability of an A -site being occupied by A atom (the same for B). In the case of FePt, the ordering parameter can be indicated by $S = r_{Pt} + r_{Fe} - 1 = (r_{Pt} - x_{Pt})/y_{Fe} = (r_{Fe} - x_{Fe})/y_{Pt}$. [83] The diffraction line from disordered and ordered phase are called fundamental lines. The extra line appear in the pattern of an ordered phase are called superlattice lines. A superlattice line is evidence of the ordering transformation. The ordering parameter S is obtained as the intensity ratio of the superlattice line to the fundamental line.

$$S = \frac{I_{superlattice}}{I_{Fundamental}}, S_{FePt} = \frac{I_{(002)}}{I_{(001)}} \quad (4.4)$$

In the case of FePt, the (001)-reflection can be used as the fundamental reflection and the (002)-reflection as the superlattice reflection. In this thesis, X-ray diffraction has been used for confirmation of L1₀-Phase and ordering parameter S .

4.1.3.2 Atomic / Magnetic force microscopy (AFM, MFM)

Atomic force microscopy (AFM) is a method to characterize the surface morphology of sample. It is a high-resolution type of scanning probe microscopy (SPM) with sub-nanometer resolution. For AFM microscopy, a cantilever is used which is oscillated with proper frequency. The cantilever carries a very sharp tip at its end for the imaging of nanostructure (fig.4.5). During tapping of the AFM tip on the surface, the oscillation of a laser beam reflected by the cantilever is measured with an array of 2×2 photodiodes. At rest, the laser beam is precisely adjusted to the center of the four photodiodes. The amplitude of the oscillation can be output as the difference in the photoelectric voltages of the photodiodes.

By means of a piezoelectric control in z-direction (i.e. vertical to the sample surface), the tip is slowly approached to the surface of the sample. The force of the approaching atoms in the surface exerted on the tip damps the oscillation amplitude and shifts the resonance frequency of the AFM cantilever. Piezoelectric elements attached to the cantilever are used to do the x-y scanning while the vertical z-position is readjusted to maintain the oscillation amplitude constant. A topographic image is obtained from the x-, y, and z-positions.

Magnetic force microscopy (MFM) is similar to AFM. The magnetic force between material and tip is detected in addition to the z-direction. For this purpose the MFM tip is made by a magnetic material coating on AFM tip. During a measurement, atomic and magnetic forces can be clearly separated by repeating a scan along the same scanning line at different distance z from the surface. Generally, the magnetic forces are further reaching than the atomic forces. Therefore, for a MFM measurement the distance is doubled. Due to the forces of a thin magnetic layer, the phase of the vibration is shifted about 1° - 10° , which allows to distinguish the forces also qualitatively. For the measurement in this work, measurement of images has been used Nanoscope V from Bruker (formerly Veeco). AFM and MFM have been used in this thesis to verify pattern structure and domain structure of nanomagnets.

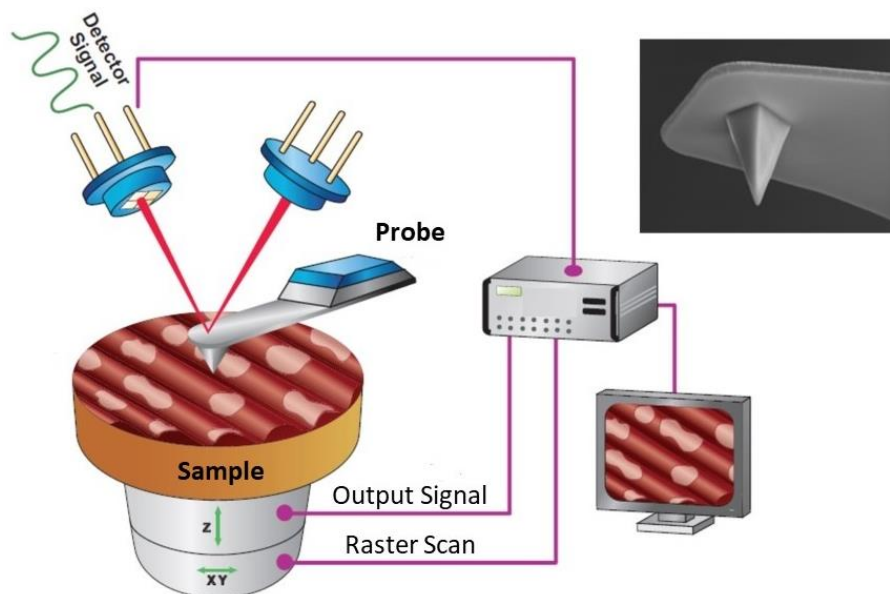


Fig.4. 5 Illustration of actuation principle of Atomic Force Microscopes and SEM image of AFM tip (inset)[109]

4.1.3.3 Scanning electron microscopy (SEM)

Scanning electron microscopy (SEM) is a method to image the morphology of a sample. Hereby, electrons are released from a thermal electron source and accelerated by a high voltage of 5 kV ~ 30 kV. The electron beam is focused by magnetic coils to a small spot in the nm range and scanned across the sample. When the electron beam is incident on the surface of the sample, secondary electrons are emitted and collected as a function of the beam position. In this way information is obtained on the surface topography. SEM can achieve a resolution down to ~1 nanometer. When the electron beam collides with the sample, also various other phenomena occur such as back scattering of electrons or emission of Auger electrons and X-rays. By registering these particles or quanta, various types of analysis measurements can be performed. Different materials influence to image contrast, too: heavy elements cause stronger scattering. For SEM measurements high vacuum is needed in order to prevent scattering of the electron beam by the atoms in the air and contamination of the sample the deposition of carbon. For the SEM measurements in this work an ULTA55 by Zeiss was used. SEM has been used in this thesis for verification of the morphology of nano insular thin film.

4.1.3.4 Wavelength-dispersive X-ray analysis (WDX_EPMA)

Wavelength-dispersive X-ray analysis (WDX), is also called electron probe microanalysis (EPMA), is performed for elemental analysis of solid specimens. In WDX, electrons in the sample are excited and atoms ionized by the electrons beam. When created inner core hole is filled by electron transitions characteristic X-rays are emitted that are collected and analyzed by an energy-resolving detector. The intensity of the element-specific spectra can be converted into percentage of the respective element in the sample. In addition, WDX gives sample information about the interaction depth of the electron beam, about atomic percentage, and weight percentage, density and thickness of the sample. This technique has been used in this thesis to optimize sputter power for high quality Fe₅₁Pt₄₉ of defined composition.

4.1.3.5 Transmission electron microscopy (TEM)

Transmission electron microscopy (TEM) provides microscopic images with sub-nm resolution. The electrons release by a pin cathode are accelerated by a high voltage of 80 kV – 400 kV and focused onto a small spot on the sample under investigation. the beam penetrates the sample and is focused in an additional step onto the image plane. An image of the sample is obtained due to absorption contrast, whereby, different parts of the samples reduce the local beam intensity differently (due to stronger or weaker interaction with the atoms in the sample). If the sample is crystalline, a TEM can also be used to image the diffraction pattern of the sample, i.e. the pattern of the electron beam diffracted by the crystalline parts of the sample. In this way local information about the sample structure is obtained. Moreover, besides the direct beam which is commonly used for imaging (bright field imaging), a diffracted part of the beam can be also used dark field imaging. This can provide information about structures that influence diffraction contrast, such as dislocations or stacking faults. In contrast to SEM, the backscattered electrons are not used for image in TEM. However, the sample can be excited by the electron beam. By analyzing the emitted X-rays or Auger electrons, information about the composition of the sample can be obtained. The basic structure of TEM corresponds to a light microscope. In this work, a JEOL 4000 Fx microscope is used with a maximum acceleration voltage of 400 kV and a lateral resolution of 1.9 Å. The sample thickness has to be several hundred

nanometer or less. For this purpose the sample have to be thinned by mechanical polishing to a layer thickness of approximately 100 μm and subsequently thinned further by either chemical etching or ion milling. TEM has been used in this thesis for pattern structure and phase distributions in nanopatterns.

4.2 Characterization of magnetic properties via SQUID

4.2.1 SQUID magnetometry

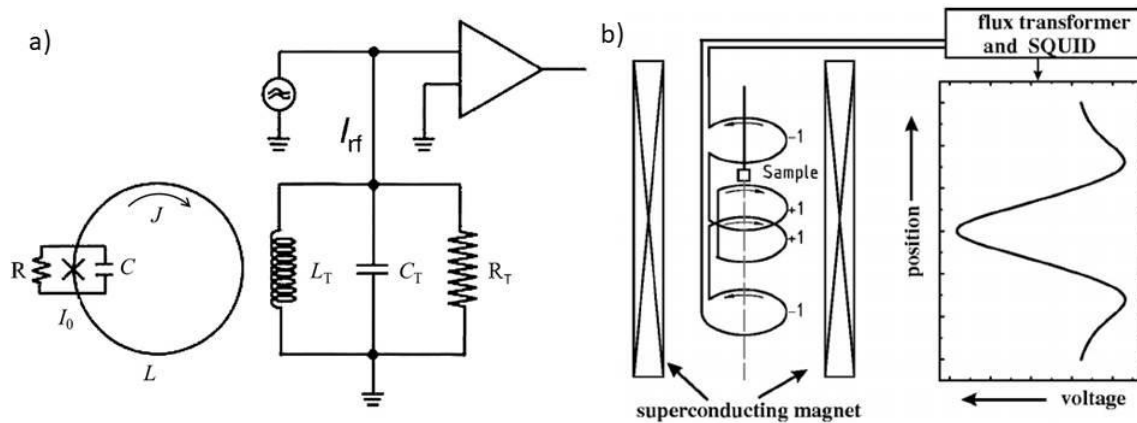


Fig.4. 6 Schematic representation of a) the rf SQUID, with tank circuit and preamplifier. The operation is set by the amplitude of the rf bias current, I_{rf} . The circle (left) is SQUID ring and the circuit (right) is tank circuit to read signal **and b) pick-up coil constitution in MPMS-XL.** To measure magnetic moment, sample moves in pick-up coils.[113]

In this work, a Superconducting QUANTUM Interference Device (SQUID) magnetometer by the company Quantum Design (MPMS-XL) is used.

The superconducting quantum interference device (SQUID) is sensitive to magnetic flux in the quantum limit. Fig. 4.6 a) shows the rf SQUID, which employs a single Josephson junction in a superconducting ring. The inductance L in the ring is coupled to the inductor L_T of a tank circuit via mutual inductance $M=k(LL_T)^{1/2}$, k is optimal coupling factor.[114] A current oscillation drives the tank circuit. The oscillating bias current $I_{rf}\sin\omega_{rf}t$ induces a current $I_T\sin\omega_{rf}t = QI_{rf}$ in the inductor; here Q is the quality factor on resonance with the SQUID. The peak rf flux in the SQUID ring is $\Phi_{rf}=MI_T$. The tank circuit with connection to a preamplifier serves to read out the applied flux Φ_a . The amplitude of the rf voltage $V_T\sin\omega_{rf}t$ is periodic in Φ_a with period Φ_0 . This is a highly sensitive instrument for measuring magnetic flux which can be detected in extreme cases down to 5×10^{-18} T.[113]

A SQUID magnetometer combines a SQUID, superconducting magnet, pick-up coil, flux transformer and superconducting shields. The sample is scanned through the center of a first- or second-order superconducting gradiometer. Fig. 4.6 b) represents a SQUID magnetometer and the calibrated output from SQUID electronics Flux transformer as a function of position. The magnitude and shape of curve is analyzed to obtain the magnetic moment of the sample. The MPMS-XL system offers the ability to measure in applied fields of up to 7 T in a temperature range from 350 K down to below 2 K in standard mode.

4.2.1.1 Correction of Diamagnetism

In this part of the work, thin films are deposited on a MgO(100) substrate that has a strong diamagnetic signal. Fig. 4.7 (left) shows the magnetic hysteresis curve of 40 nm FePt on MgO (500 μm thick) is over layered by a diamagnetic background (negative slope due to negative susceptibility).

To correct the hysteresis curve for the diamagnetic signal, first the diamagnetic susceptibility was

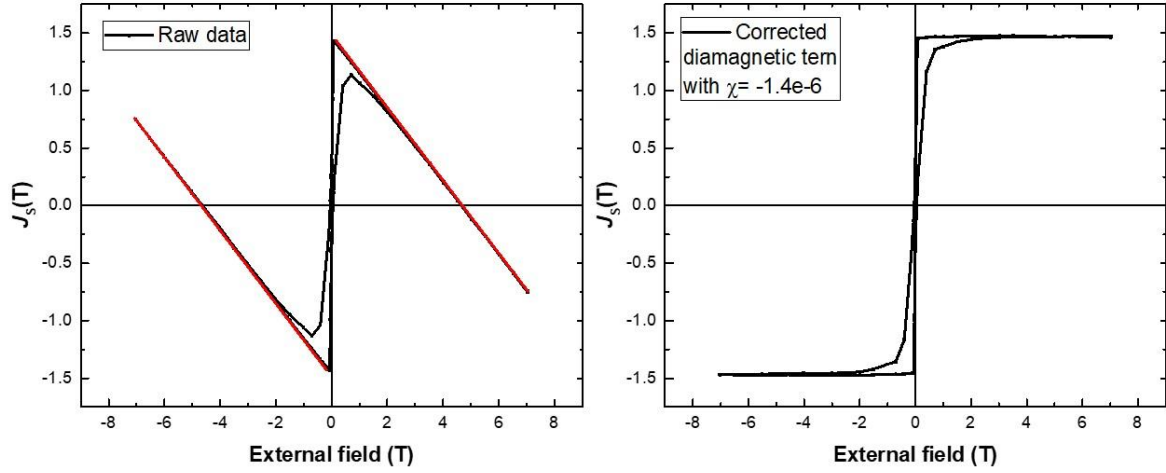


Fig.4. 7 Out of plane hysteresis curve of 40 nm thickness L1₀-FePt on MgO substrate. Without correction of diamagnetic properties (left) and corrected magnetization with value of $\chi = -1.4e^{-6}$ (right).

determined from the following equation:

$$\chi = \frac{J}{\mu_0 H_{ext}} < 0 \quad (4.5)$$

As the susceptibility of a diamagnetism is constant, J is directly proportional to the applied field, the diamagnetic contribution can be corrected for by subtraction of $J = \chi H_{ext}$. For the determination of diamagnetic term, the slope at saturation field of L1₀-FePt and Co is used, i.e. far away from field zero.

4.2.2 Magnetic parameters

4.2.2.1 Saturation polarization J_s

The saturation polarization can be evaluated from the hysteresis curve in the easy axis direction, directly. In this work, For L1₀-FePt/ Co magnets, the polarization can be saturated at maximum field of 7 T. The magnetometric system used in this work measures magnetic moment m in units of emu. The magnetic moment m can be transformed into the saturation polarization by dividing the saturation magnetic moment [emu] by cubic centimetre volume $V(\text{cc})$ giving the saturation magnetization in cgs units. Multiplying the magnetization in cgs units by the conversion factor, ($\mu_0 \times 10^3 = 4\pi \times 10^{-4}$) gives the saturation polarization in SI unit. The relation between emu and T is given by [115]

$$J[\text{T}] = \mu_0 \frac{m [\text{emu}] \times 10^3}{V [\text{cc}]}, M[\mu_B] = \frac{m [\text{emu}] \times 10^{-3} \left[\frac{\text{Am}^2}{\text{emu}} \right]}{9.274 \times 10^{-24} \left[\frac{\text{Am}^2}{\mu_B} \right]} \quad (4.6)$$

4.2.2.2 Anisotropy constant K_1

The anisotropy constant K_1 describes the energy necessary to rotate the magnetization from easy to hard direction in ferromagnetic materials. The directions are connected with the crystal axes in a crystal lattice and caused by the electric field in a crystal, the strain or stress in a magnetic phase or the shape of a magnetic sample. The anisotropy constant, K_1 (MAE) can be determined as the sum of the magnetocrystalline anisotropy (MCA, K_u) and shape anisotropy K_{shape} (see Eqn. 4.8). First, the MCA is calculated from the susceptibility χ of the in-plane hysteresis curve (hard-axis) or the initial magnetization curve of the out-of-plane hysteresis curve (easy-axis) [28, 116] The magnetocrystalline anisotropy energy, K_u is given by [116]

$$\chi = \frac{J_S^2}{2\mu_0 K_u}, K_u \approx \frac{J_S^2}{2\mu_0 \chi} \quad (4.7)$$

In this work, for the determination of the magnetocrystalline anisotropy K_u , the slope of in-plane hysteresis curves between 2 T and 4 T and the saturation polarization of out-of-plane hysteresis curve are compared (see Fig. 4.8).

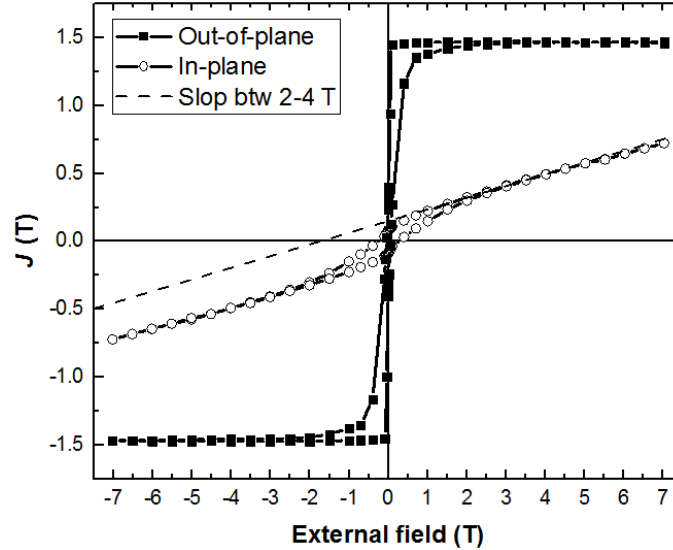


Fig.4. 8 Out-of-plane and in-plane hysteresis curve of 40 nm thickness $L1_0$ -FePt thin film on MgO substrate, to obtain magnetocrystalline anisotropy constant K_u . The susceptibility χ is from slope of in-plane hysteresis curve. The saturation polarization J_S is obtained by out-of-plane hysteresis curve.

The shape anisotropy can be obtained from the saturation polarization J_S and the demagnetization factors by used of the following relation. [117-119]

$$K_{shape} = \frac{1}{2} (N_{\perp} - N_{\parallel}) \frac{J_S^2}{\mu_0} \quad (4.8)$$

N_{\perp} and N_{\parallel} are the demagnetization factors perpendicular and parallel to the external magnetic field, respectively.

The anisotropy constant, K_1 can then be determined by means of the relation:

$$K_1 = K_u + K_{shape} \quad (4.9)$$

4.2.2.3 Exchange stiffness constant A

The exchange stiffness constant A , which is a characteristic of a ferromagnetic material, is the strength of interaction between adjacent magnetic moments due to exchange interaction. It cannot be determined directly but calculated from the temperature-dependent spin wave stiffness constant D_{sp} [28]. However, also the spin wave stiffness constant D_{sp} cannot be directly determined, either. It can be obtained from the plot of (temperature dependent) easy axis saturation polarization $J_S/J_{S,0}$ versus $(T/T_0)^{3/2}$, according to Bloch's $T^{3/2}$ -law.

$$J_S(T) = J_{S,0} \left(1 - \left(\frac{T}{T_0} \right)^{3/2} \right) \quad (4.10)$$

In this work, the saturation polarization values in the temperature range from 50 K to 350 K are used to determine $J_{S,0}$ and T_0 . $J_{S,0}$ is obtained by extrapolating the $1/H$ plot to saturation field. By the temperature dependences of $J_S(T)$, the characteristic temperature T_0 can be determined by the plot of $J_S(T)$ as function of $T^{3/2}$, which leads to a linear relation (Eqn. 4.10).

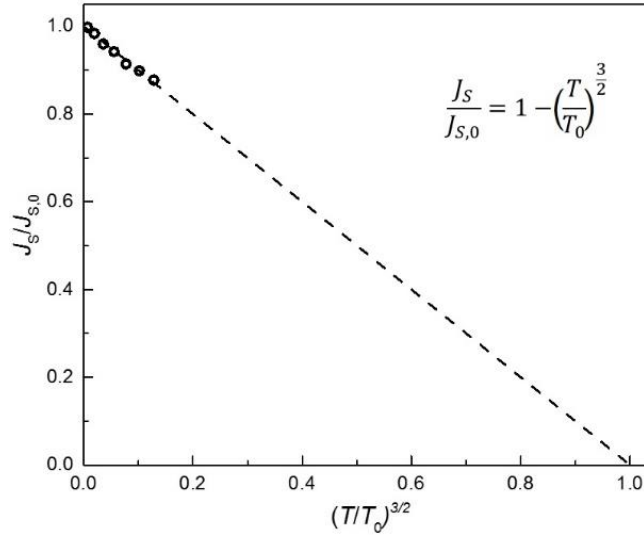


Fig.4. 9 The plot of Bloch $T^{3/2}$ -law to determine $J_{S,0}$ and T_0 . The linear fitting gives the characteristic temperature T_0 .

Then, D_{sp} is related to T_0 and $J_{S,0}$ by equation (4.11).

$$T_0 = \left(\frac{J_{S,0}}{0.117\mu_0\mu_B} \right)^{2/3} \frac{D_{sp}}{k_B} \quad (4.11)$$

The temperature dependence of the exchange stiffness constant A can be obtained with Eqn. 4.12.

$$A(T) = \frac{J_S(T)D_{sp}}{2g\mu_0\mu_B} = \frac{J_S(T)k_B T_0}{2g\mu_0\mu_B} \left(\frac{0.117\mu_0\mu_B}{J_{S,0}} \right)^{2/3} \quad (4.12)$$

where g is the Landé-factor. For $L1_0$ -FePt, it can be set to 2.

4.2.2.4 Microstructural parameter, α , and N_{eff}

The microstructural parameters give information about grains in ferromagnetic materials, such as nucleation, homogeneity, misaligned grains, exchange coupling, grain shape effect, and magnetic reversal process.[37] The microstructural parameters can be obtained by plotting $\mu_0 H_C(T)/J_S(T)$ versus $\mu_0 H_N^{min}(T)/J_S(T)$ according to Eqn. 4.13. Both coordinates are temperature dependent. Eqn. (4.14) is a transformation of eqn.2.33.

$$\frac{\mu_0 H_C}{J_S} = \alpha \frac{\mu_0 H_N}{J_S} - N_{eff} = \alpha \frac{2\mu_0 K_1}{J_S^2} - N_{eff} \quad (4.13)$$

For the determination of the microstructural parameters, hysteresis loops as function of temperatures are needed. The slope and the y-axis intersection of a linear fit to the measurements provide pertinent values for α and N_{eff} , respectively.

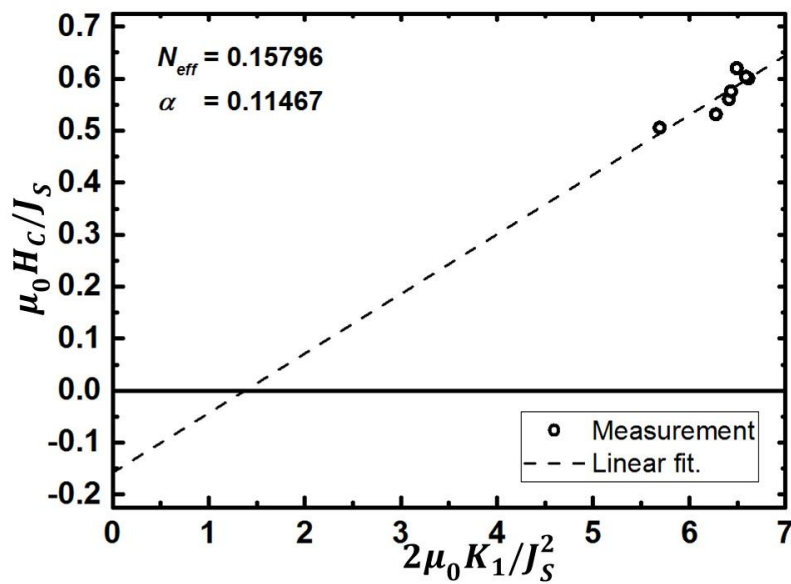


Fig.4. 10 The plot of $\mu_0 H_C(T)/J_S(T)$ versus $2\mu_0 K_1(T)/J_S^2(T)$ to determine the microstructural parameters α and N_{eff} of 20 nm thickness $L1_0$ -FePt 100 nm dot size / 200 nm period nanopattern in the temperature range of 50 K to 350 K.

4.2.3 First order reverse curves (FORC) measurement

For FORC measurement, first, a sample was magnetized to saturation in a field H_{Sat} . Then the external field was decreased to a reversal field H_r , then magnetic moment is measured during sweep back to H_{Sat} . This procedure is repeated many times by series of H_r . By this process, the major hysteresis loop and minor hysteresis loops are obtained. Loops are drawn function of H_r and H , as $M(H_r, H)$.

4.2.3.1 FORC density analysis

The FORCs density is already referred in chapter 2 with Preisach model. To calculate the FORCs density, hysteresis loops, which procedure is explained above, are used. Nowadays, the density measured and analyzed with higher accuracy and faster with a new method using MOKE by J. Gräfe.[120] However, in this work, classical mathematical method, which consists in two sub-sequential derivatives of hysteresis loops with respect to the external field H and reversal field H_r , is used to obtain the density from first-order reversal curves. Since, the magnetic moment signals are quite small ($\sim 10^{-5}$ emu range) due to the nanosized magnets, and because the samples have a large coercive field, since they are hard magnets a SQUID has to be used. Eqn. 2.20 is re-written to read:

$$\rho(H_r, H) = -\frac{1}{2} \frac{\partial^2 M(H_r, H)}{\partial H_r \partial H} = -\frac{1}{2} \frac{\partial}{\partial H_r} \frac{\partial M(H_r, H)}{\partial H} \quad (4.14)$$

The process to obtain the FORCs density will here be shown step by step by means of collected minor loops of first order reverse curves measurement to density diagram. Fig. 4.13 is minor loops of nanopatterns for 100 nm dot size and 200 nm periods.

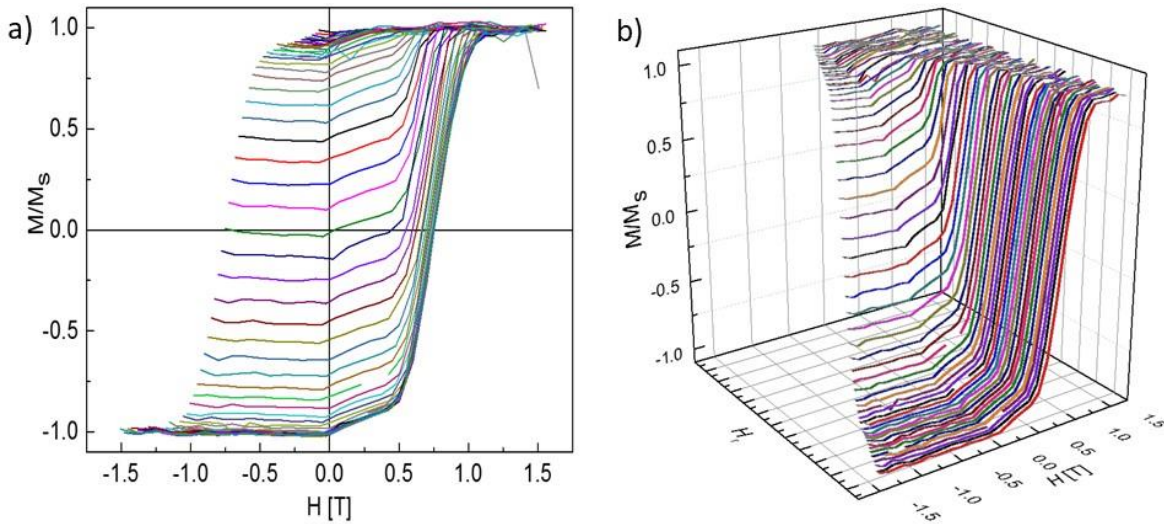


Fig.4. 11 Minor hysteresis loops of L1₀-FePt hard magnet with 100 nm / 200 nm (dot size/period) nanopatterned. a) 2 D view as function of external field and b) 3 D view by dividing each minor.

The reversal curves then, partially differentiated with respect to the external field H . Fig. 4.12 a) shows the first derivative of the graphs of the minor curves of fig.4.11, i.e. the results of $\partial M(H_r, H) / \partial H$. These first derivative results are again partial differentiated with respect to the reverse field H_r . Graphs of these second derivative are shown in fig.4.12 b), i.e. $\partial^2 M(H_r, H) / \partial H_r \partial H$.

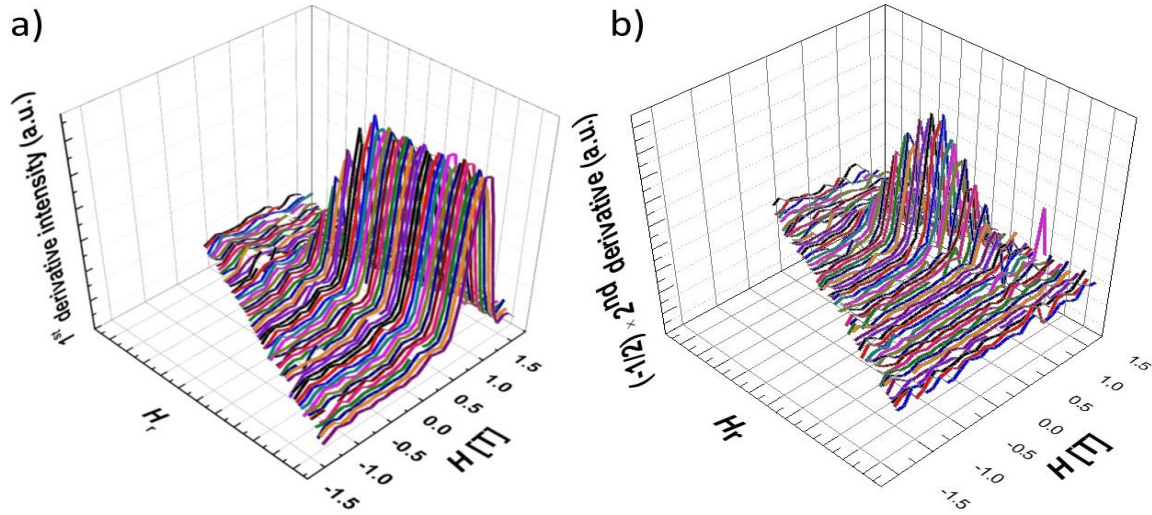


Fig.4. 12 Differential results of each minor loops. a) First differential and b) second differential multiplied with $-1/2$ of 100 nm / 200 nm (dot size/period) nanopatterned L1₀-FePt hard magnet.

Finally, these double derivatives of the hysteresis loops are multiplied by $-1/2$ and drawn in the form of a contour map. Furthermore, the axes of H and H_r are rotated 45° for changing coordinates. The rotational transform is given by the relations: $H_u = (H + H_r)/2$ and $H_c = (H - H_r)/2$. Here H_u is distribution of the interaction field and H_c is the distribution of coercive field. Fig. 4.13 shows the final result of the FORCs density contour calculation, which provides the relation proportions of the components of magnetization due to magnetic interactions, which are irreversible.

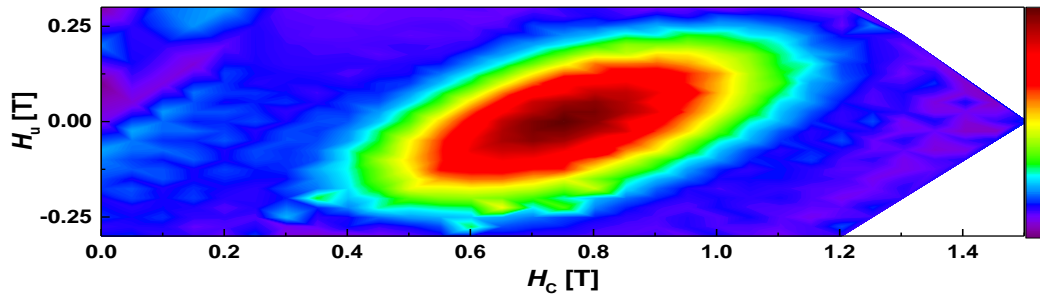


Fig.4. 13 The contour plot of the corresponding FORCs distribution of 100 nm / 200 nm (dot size/period) nanopatterned L1₀-FePt hard magnet.

4.3 Characterization of magnetic systems via XMCD

4.3.1 Synchrotron Radiation - WERA beamline at ANKA

Electromagnetic radiation is generated when charged particles are accelerated. In an electron storage ring highly relativistic electrons are forced onto a closed circular path by magnetic fields and emit X-rays tangential to their direction of motion. For an overview of accelerator physics including synchrotron science since the development of the synchrotron principle in 1945 is given in [12]. In the first step, these electrons are produced from a hot cathode and accelerated to almost light speed by a microtron. By the magnets systems, accelerated electrons are injected into the synchrotron, and then electrons are further accelerated to their terminal energy. The electrons are injected from synchrotron into the storage ring.

The often called synchrotron consists of a storage ring, essentially. A circular path of suitable magnets systems can hold the high-energy electrons. As an example for a third generation source, which is used as a source of x-rays in this thesis, is the ANKA Synchrotron at Karlsruhe. Fig. 4.14 shows schematic of a synchrotron storage ring and an undulator.

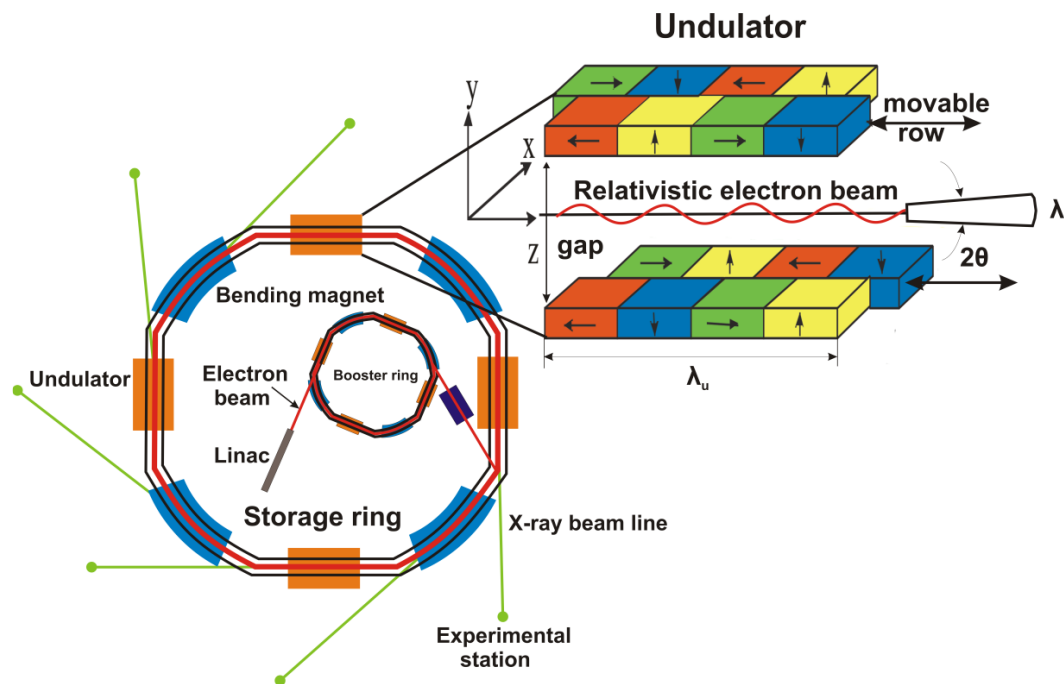


Fig.4. 14 Schematic of a synchrotron storage ring and an undulator. [99] The relativistic electrons are injected into the ring from a linear accelerator (Linac) and a booster synchrotron. As the electrons travel through the insertion devices (bending magnets, undulator and wiggler) synchrotron radiation is emitted as a narrow cone tangential to the path of the particle.[121]

The ANKA accelerator consists of a 53 MeV microtron, a 500 MeV booster synchrotron and a 2.5 GeV storage ring with a nominal current of up to 200mA.[122]

The radiation emitted from a **bending magnet**, which is used to maintain a circulating beam with bending electrons into an orbit, emits synchrotron radiation with well-defined polarization characteristics as depicted in Fig.4.15. In the plane of the electron orbital, the radiation is linearly polarized, while right- and left- circularly polarized light can be obtained in small angles above and below the electron orbits. A polarization of typically 80-85% can be obtained at a several mm above and below position to the credit of an intensity reduction of about a factor 3.

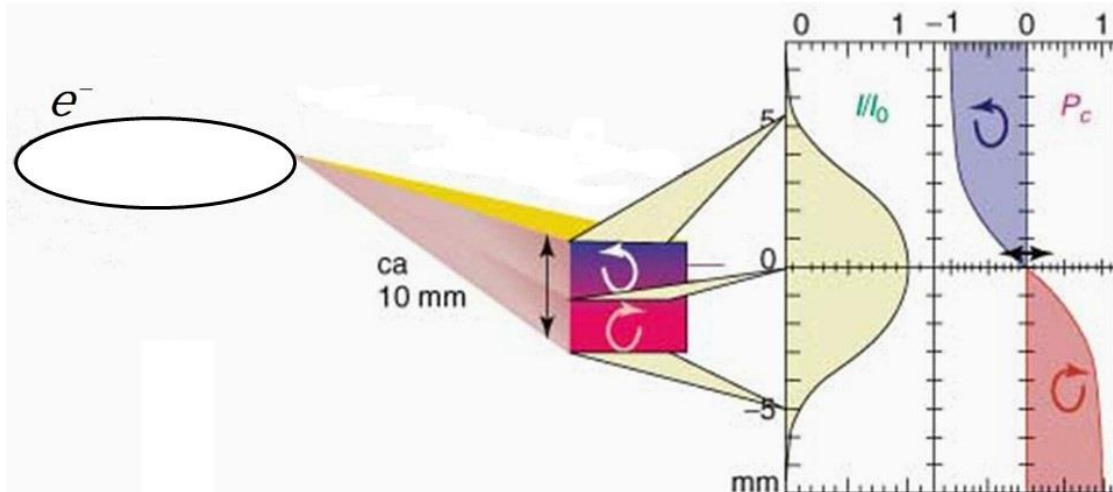


Fig.4. 15 Circularly polarized radiations are emitted to set circular direction by position above and below from the electron orbit. [30, 120]

An undulator consists of a periodic arrangement of hard magnets which produces synchrotron radiation with higher brightness and extends the energy range. Interference effects in undulator produced radiation peaks at tunable wavelengths with high spatial and spectral brightness. The narrow construction of magnets raises interference, its higher harmonics and increases the intensity.[123]. With a defined shift of the magnetic arrangement linearly or right and left circularly polarized x-ray can be created as shown in Fig. 4.16.

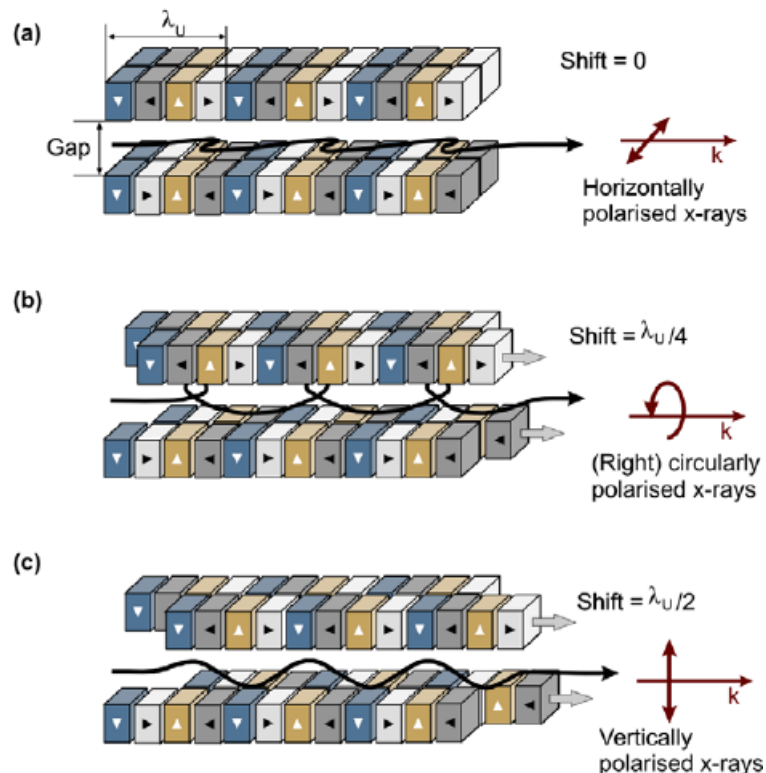


Fig.4. 16 Schematic setting of three type undulator to obtain (a) horizontally polarised, (b) right circularly polarized or (c) vertically polarized x-ray by shifting two of the four rows of magnets in parallel mode. [124-126]

The WERA beamline at ANKA

The corresponding scheme of the WERA (Weichröntgenanalytikanlage, soft x-ray analytics facility) beamline at the ANKA synchrotron is shown in fig.4.17. This beamline is sourced from a bending magnet of 1.5 T dipole ($E_C = 6.235$ keV), 10 mrad horizontal, 3 mrad vertical or insertion device, alternatively. The x-ray, beam passes an aperture and is monochromatized by a spherical grating monochromator.

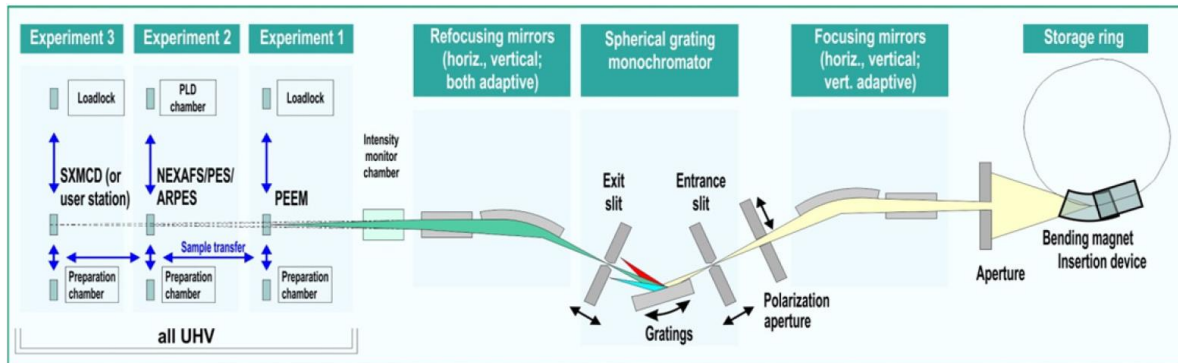


Fig.4. 17 Schematic layout of the WERA beamline at ANKA. [121]

The WERA beamline provides radiation for soft x-ray spectroscopy and microscopy in the photon energy range 100 – 1500 eV with a typical energy resolution of $\Delta E/E \sim 2 \cdot 10^{-4}$, maximum $\Delta E/E < 1 \cdot 10^{-4}$. The dipole source has typical beam size of $0.4 \text{ mm} \times 0.1 \text{ mm}$ FWHM. The circular and linear polarization can be quickly selected by aperture. In this work, the degrees of circular polarization are 81% for Fe and, 84% for Co. The spherical grating monochromator consists of 3 gratings with movable entrance and exit slits. Available methods at the beamline are Photoemission Electron Microscope (PEEM) for imaging of chemical and magnetic contrast with less than 100 nm resolution, Photoemission (PES), angle-resolved, resonant PES (ARPES, ResPES) for study of electronic, band structure with 2 meV energy resolution, Near-edge X-ray absorption (NEXAFS) by fluorescence yield, total/partial electron yield and Soft X-ray magnetic circular dichroism (SXMCD) for element-specific spin and orbital magnetic moment, as shown in fig.4.17.

By our department, the soft x-ray magnetic circular dichroism setup was designed especially for 7 Tesla fast field switching. The magnet is driven by a power supply with the maximum ramp rate of 1.5 T/s to 5 T and 0.7 T/s to a maximum field of 7 T. Two cryocoolers cool the magnet system to the superconducting state. The chamber of the setup is under the base pressure usually $3 \cdot 10^{-10}$ mbar. The temperature can be set from 10 to 350 K. The absorption can be measured by three kinds; total electron yield (TEY), total fluorescence yield (TFY) and a transmission photodiode. The sample can be rotated both azimuthal 0° to 360° and polar 0° to 90° in principle. The sketch and real pictures of the setup are shown fig.4.18.

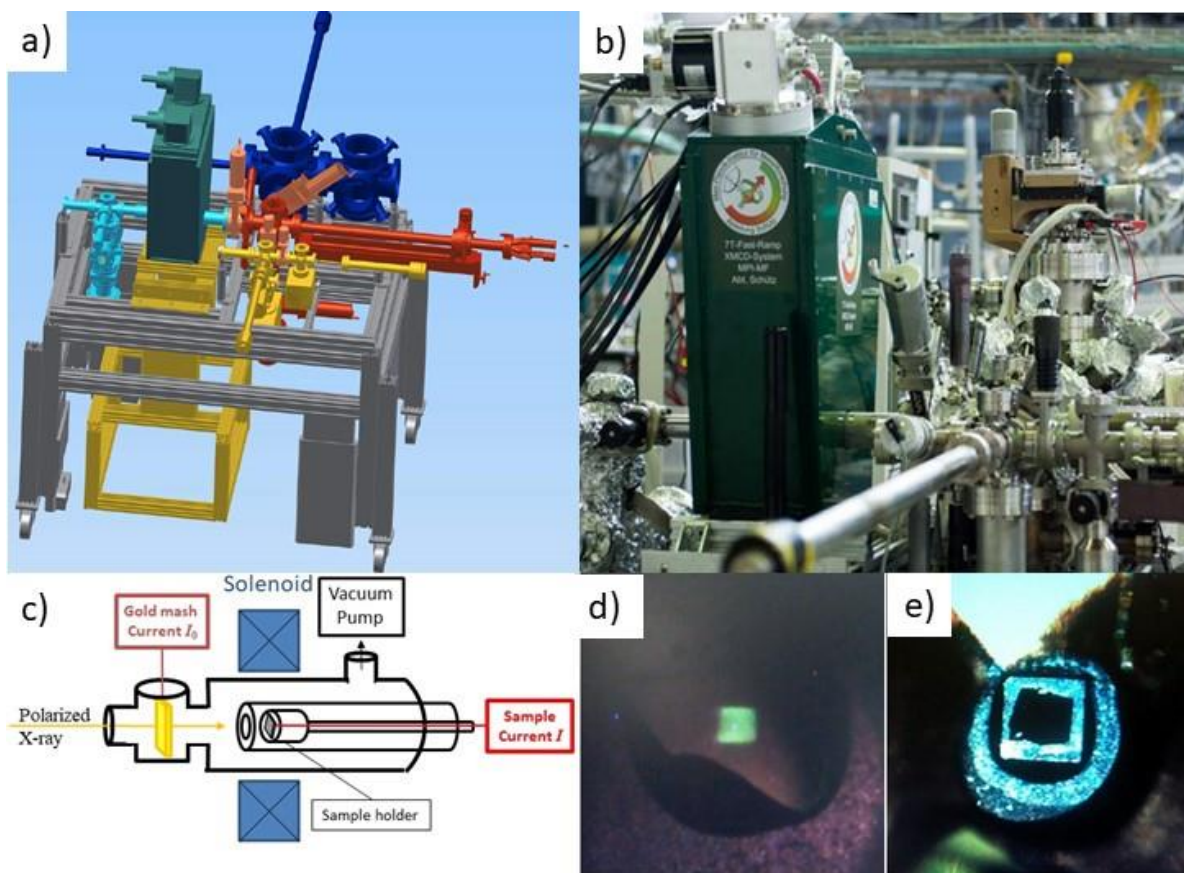


Fig.4. 18 Experimental setup for XMCD for TEY mode at WERA beamline in ANKA. a, b, c) 7 Tesla fast switching XMCD setup, designed, developed and constructed at the Schütz department, Max-Plank-Institute for Intelligent Systems.[11]. d, e) Pictures of x-ray beam spot and sample on a sample holder in setup.

4.3.1.1 Total Electron Yield (TEY) mode

Traditionally, XAS measurements were performed in transmission mode, which is measured the intensity of x-ray beam before and after transmission through a thin film. Transmission method is suitable for hard x-ray and required a transparent, thinned sample and thinned substrate. The mean absorption length (attenuation length) of soft x-ray is very short of the penetration depth and at the absorption edges is only 20-50 nm in soft x-ray region.[127, 128] To conquest these points, the absorption should be measured by means of secondary processes, like fluorescence yield, total / partial electron yield or even ion yield. The photocurrent is nearly proportional to the number of absorption. In this work, only total electron yield method is used for XAS and XMCD studies.

By absorption of x-ray photons, holes are formed an inner shell. The hole is closed again by an electron transition from an outer shell. During this process, the released energy emits and transfers to other electrons, which is torn out of their bond. It is so-called the Auger effect and is repeated for the secondary electrons. Some of these electrons can leave the sample surface, if these electrons have a higher energy than the work function. This induces a currents of typically 10^{-12} A which are measured by a Keithley amperemeter. A schematic of the experimental setup of TEY measurement is described in fig4.19.

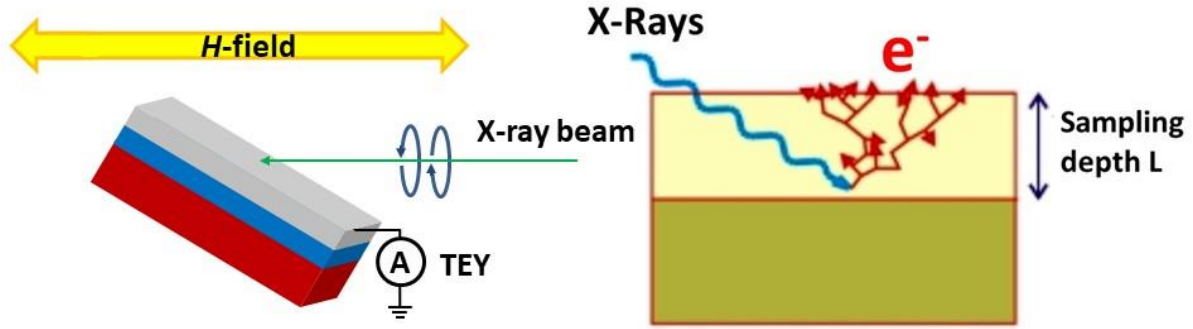


Fig.4. 19 Total electron yield method. The incident radiation is absorbed, and Auger process occurs. The current of Auger electrons, which leave the sample, is measured by electrometer and is proportional to the absorbed intensity.[58]

The current is nearly proportional to the absorption of photons. This method also has experimental obstacles to overcome. The Lorentz force by the applied magnetic field affects the leaving electrons. Some electrons move on spiral and return to the sample, which can modify the current. To prevent this, the sample is set to a negative voltage. Another feature of the TEY measurements, the strong surface sensitivity, limits the range of probing depth to a few nm. For thin film, a saturation effect, which is also called self-absorption effect occurs.[129] These effect cannot be removed these experimentally. It has been evaluated after measurement, subsequently. The correction of saturation effect will be referred next section. On the execution of angle-dependent measurements, the correction of saturation effect have to be dealt, necessary.

4.3.1.2 Correction of Saturation effect _self-absorption

The measurement in the TEY mode gives an error to measured absorption peaks for the film as thin as 5 nm. Depending on film thickness and X-ray incident angle.[129] In this work, the correction of self-absorption effect follows the procedure developed by Dr. Eberhard Goering.[130] To correct $I_{TEY}(E)$ signal, the origin signal have to be known by the relation with absorption coefficient and length. The TEY signal of a sample of the thickness of d is obtained by the total number of charge carriers $n^{esc}(d,E)$. The $n^{esc}(d,E)$ is determined by the number of charge carriers generated in the depth z along the path of photons.

$$n(z, E) = k \cdot I_0(E) \cdot \frac{\mu(E)}{\cos\theta} \cdot e^{-z \cdot \frac{\mu(E)}{\cos\theta}}, \quad n^{esc}(z, E) = n(z, E) \cdot e^{-\frac{z}{\xi}} \quad (4.15)$$

where k is an energy-dependent constant. $I_0(E)$ is the intensity of incident photons. θ is the incident angle from the normal direction of the sample. The number of $n^{esc}(d,E)$ is related with the average electron escape depth ξ which is limited by the electron mean free path. From this, $I_{TEY}(E)$ is given by

$$I_{TEY}(E) \propto \frac{n^{esc}(d, E)}{I_0(E)} = \frac{\mu(E)}{\frac{\cos\theta}{\xi} + \mu(E)} \cdot \left(1 - e^{-d \cdot \left(\frac{1}{\xi} + \frac{\mu(E)}{\cos\theta} \right)} \right) \quad (4.16)$$

where, $\mu_{\pm}(E)$ is absorption lengths.

The absorption lengths $\mu_0(E)$ can be obtained with the normalized measurement spectra and the absolute absorption length in μm^{-1} . The absolute absorption length can be obtained from Henke et al. [131, 132]

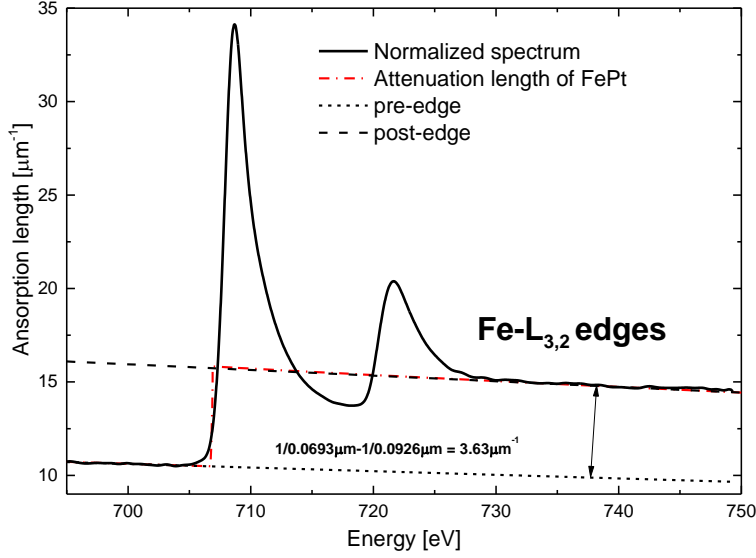


Fig.4. 20 The spectrum is converted to absorption length [μm^{-1}].

For the correction of the spectra, a correction formula is for the measured absorption $\mu_0(E)$. The true absorption $\mu(E)$ of the exponential term in Eqn. 4.16 can be replaced by $\mu_0(E)$. The equation is rewritten as

$$I_{TEY}(E) \propto \frac{\mu(E)}{\frac{\cos\theta}{\xi} + \mu(E)} \cdot \left(1 - e^{-d \cdot \left(\frac{1}{\xi} + \frac{\mu(E)}{\cos\theta} \right)} \right) \quad (4.17)$$

In the bulk samples, the absorption coefficient is $\mu(E) = \mu_0(E) / (1 - \frac{\xi \cdot \mu_0(E)}{\cos\theta})$. However, in a thin film sample of a certain thickness, the absorption signal is added to ratio of the electron charge carrier (indicating by current) according to sample thickness, $\mu(E) = \mu_0(E) / (1 - \frac{I(E,d)}{I_\infty(E)} \frac{\xi \cdot \mu_0(E)}{\cos\theta})$. The ratio can be obtained by $I(E, d) = I_\infty(E) \cdot \left(1 - e^{-d \cdot \left(\frac{1}{\xi} + \frac{\mu_0(E)}{\cos\theta} \right)} \right)$.

The absorption length can be corrected by

$$\mu(E) = \frac{\mu_0(E)}{1 - \frac{\mu_0(E) \cdot \xi}{\cos\theta} \left(1 - e^{-d \cdot \left(\frac{1}{\xi} + \frac{\mu_0(E)}{\cos\theta} \right)} \right)} \quad (4.18)$$

In this thesis, the electron escape depth ξ is determined from “universal curve for electron”. The mean free path’s depends on the kinetic energy of the electron. (about 20 Å, for the 3d metals at 700-1000 eV, 24 Å for FePt and 25 Å for Co were used).

Chapter 5

Results: Artificially structured exchange-spring nanomagnets

Exchange-spring magnets (ESMs) of ferromagnetic materials have been investigated to tune the magnetic properties of thin layers. ESMs comprise a combination of magnetically hard and the soft magnets. One of the methods for increasing the coercivity is to microstructure the magnet size to obtain a suitable size according to fig.2.17 and is used in this thesis. In this chapter, the hard magnets are artificially nanostructured by the top-down method. Moreover, ESMs have been developed to improve the relatively small magnetization of the hard magnet by a soft magnets stacked on hard magnets to control the coercivity. In the field of magnetic data storage, the patterned nanostructure is called as bit-patterned media (BPM) and ESMs are called exchange-coupled composition media (ECC media).

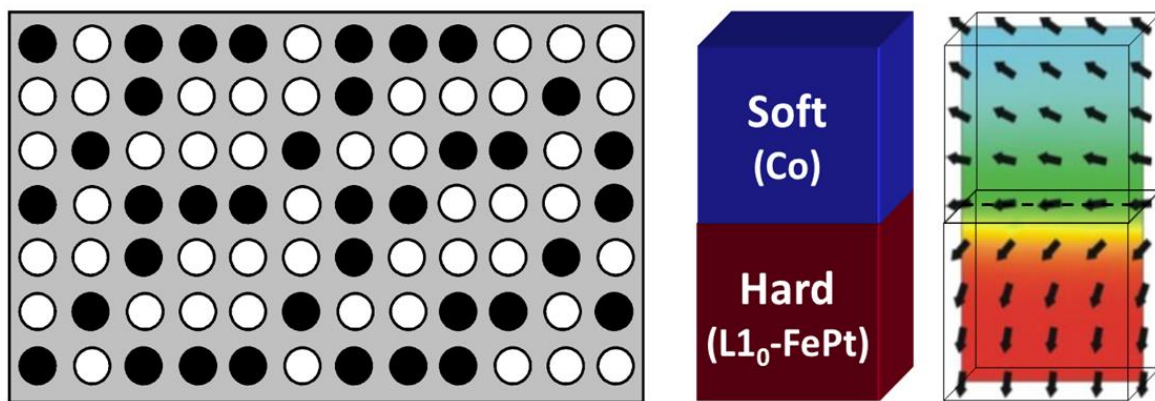


Fig.5. 1 Schematic of bit pattern media (BPM) and exchange-coupling composition media (ECC media). In this chapter, the combination of two media is investigated as exchange-spring nanomagnet pattern.

Nanopatterned magnets of excellent magnetic properties were designed and built by the combination of nanostructure and exchange-spring magnet. The magnetic properties of different ratios of the soft and hard magnets were investigated to find out how to tune the magnets and magnetic reversal process. In order to be able to compare the hard magnets and the exchange-spring magnets of different coupling strength, three kinds of magnetic thin film layers were produced by magneto co-sputtering. Sample 1 consists of a hard magnetic thin film, only. Sample 2 is an exchange-spring magnetic multilayer. For sample 3, the thickness of the soft magnetic layer was increased. In this way the fraction of soft magnetic material and the coupling strength are changed. The multilayers were checked and analyzed with respect to crystal phase and morphology by x-ray diffraction (XRD) and scanning electron microscopy (SEM). Nanopatterned films were fabricated by nanoimprint lithography (NIL) that is one of top-down techniques. In this work, the nanopatterns consisted of 60 nm diameter dot size and 150 nm period in an area of $2 \times 2 \text{ mm}^2$. The pattern structures were confirmed by atomic force microscopy (AFM). In addition, size and structure of each nanomagnet were checked by transmission electron microscopy (TEM). The distribution of the magnetic domains and the interaction between different domains in these nanomagnets were studied by magnetic force microscopy (MFM).

Superconducting quantum interference device (SQUID) magnetometry was employed to measure the magnetic properties. By temperature dependence studies of the magnetic hysteresis loops, magnetic intrinsic parameters and micromagnetic structural parameter were determined by applying in Kronmüller equation. Each nanomagnet in patterns can become the hysteron in Preisach model. Moreover, first-order reversal curves measurements were performed to obtain interaction field distribution and coercive field distribution according to the ratio of the soft and hard magnet in samples. Especially, the domain transitions on various fields were confirmed to investigate magnetic reversal process by MFM.

5.1 L1₀-FePt / Co nanopatterned samples

Overview of the systems

To investigate exchange-spring magnets with different coupling strengths, three kinds of magnetic thin film layers were prepared by magneto co-sputtering. The layer thicknesses and their compositions are shown in Fig.5.2. L1₀-chemically ordered FePt with huge magnetocrystalline anisotropy energy ($K_1 \sim 6.6 \text{ MJ/m}^3$, $J_S \sim 1.43$) has been chosen as the magnetically hard material and cobalt, a 3d-transition metal with high magnetic saturation polarization ($J_S \sim 1.76$, $K_1 \sim 0.45 \text{ MJ/m}^3$), is used as magnetically soft material. 20 nm thick L1₀-FePt films were deposited on MgO (100) substrate at 600 °C for all samples. The optimized sputter condition for the formation of L1₀-Fe₅₁Pt₄₉ and the WDX results are presented in Appendix A. 1. After the deposition of the L1₀-FePt films, the temperature of 600 °C was kept for 1 hour. For the exchange-spring magnet, Co layers of 3 and 7 nm thickness were deposited on the L1₀-FePt films, respectively (sample t_3 and t_7). temperature to prevent any inter diffusion between the layers. In addition, samples t_3 and t_7 were covered by 2 nm of Pt as protection layer to avoid sample oxidation. Fig. 5.2 shows schematic of thin films, respectively.

Sample 1 (t_0) : 20 nm FePt

Sample 2 (t_3) : 20 nm FePt/ 3 nm Co/ 2 nm Pt

Sample 3 (t_7) : 20 nm FePt/ 7 nm Co/ 2 nm Pt



Fig.5. 2 Illustration of the FePt hard magnet of 20 nm thickness and exchange-spring magnet multilayers of 20 nm FePt / 3 nm and 7 nm Co with 2 nm Pt protection layer on MgO (100) substrate.

5.1.1 Characterization of the thin film structure

5.1.1.1 Crystal structure

The thin $L1_0$ -Fe₅₁Pt₄₉ films were prepared under optimized conditions as listed in Table A3. The structures of all samples were studied by x-ray diffraction (XRD) with Cu-K α radiation as shown in fig. 5.3. FePt (001), (111) and (003) peaks are observed at $2\theta \sim 24^\circ$, $\sim 54^\circ$ and $\sim 80^\circ$, respectively. Indicating that crystal structure is $L1_0$ -phase (face-centered tetragonal, fct). Co (111) and (200) peaks are at $2\theta \sim 41^\circ$ and $\sim 54^\circ$, respectively. The peaks positions are ascribed to the face-centered cubic (fcc) crystal structure of Co. The Co (200) peak is overlapping with the FePt (111) peak, once Pt (222) peak shows up at $2\theta \sim 81^\circ$ where it overlaps with the FePt (003) peak.

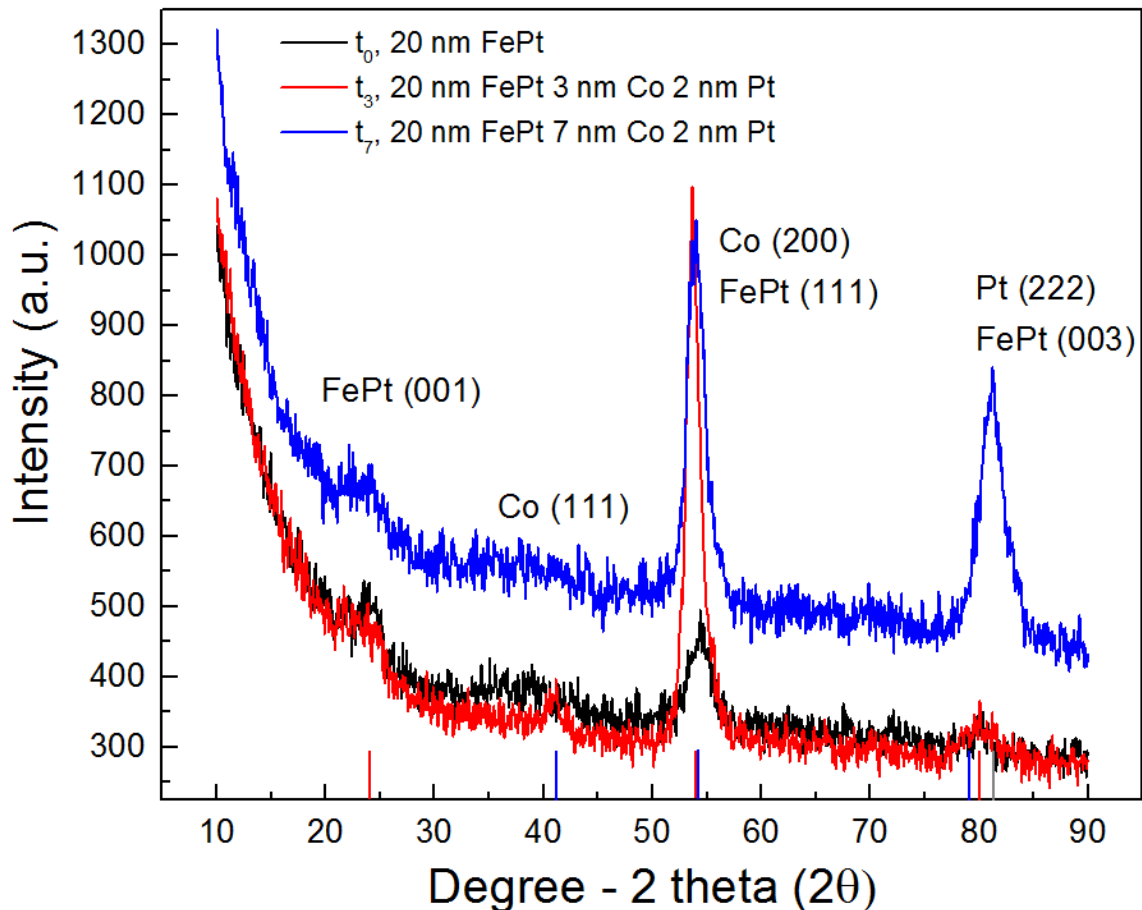


Fig.5. 3 X-ray diffraction spectra for samples, t_0 (Black), t_3 (Red) and t_7 (Blue). Peaks of FePt, Co and Pt are verified.

The tiny heights of FePt (001) peaks are similar for all these samples; there is no overlapping with other peaks. Obviously, sample t_0 contains only FePt. Samples t_3 and the t_7 show Co and Pt peaks from Co and Pt layers. There are some differences between those two exchange-spring multilayers that are not understood in all details: the Co (200) at $2\theta \sim 54^\circ$ of t_3 is stronger than t_7 , on the other had the Pt (222) at $2\theta \sim 81^\circ$ of the t_7 is stronger than that of t_3 . The latter may be due to the deep gaps seen on the surface of sample t_3 (see below). The Pt could have diffused into these gaps and, there, formed a film of different structure that does not show up here. The Co (111) peak of t_7 is broader than that of t_3 and exhibits less intensity. Nevertheless, the experiments show that an $L1_0$ -FePt film has formed that is covered by a considerable amount of Co.

5.1.1.2 SEM images of the continuous films

In order to obtain more information about the samples, they were investigated by scanning electron microscopy (SEM) as shown in Fig.5.4. According to our previous work [133], the sputtered thin FePt films first form granular islands, then become maze-like, and after a critical thickness they become thin continuous films. FePt of 20nm thickness is deposited (see top of fig. 5.4). The center and bottom parts of Fig. 5.4 show the SEM images of sample t_3 and t_7 .

As the figure shows, the thickness of 3 nm and 7 nm Co are not enough to provide perfect thin films.

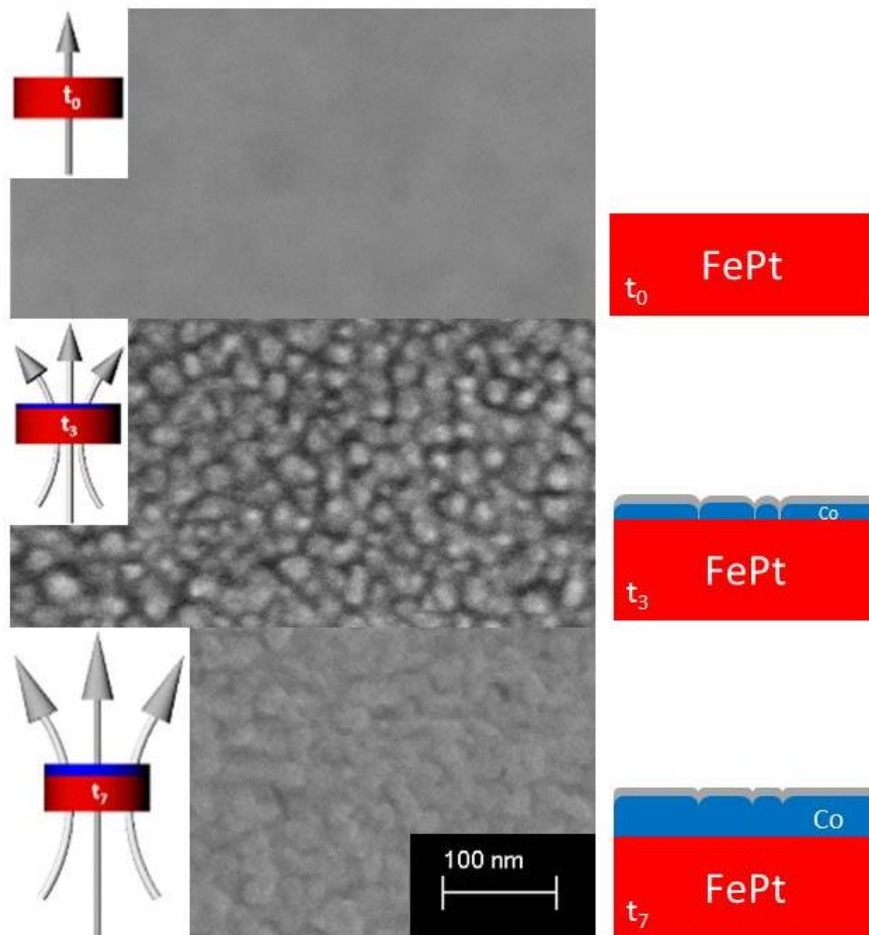


Fig.5. 4 Scanning electron microscopy images of all samples. 20 nm FePt layer on MgO (100) substrate shows the perfectly thin film (top). 3 nm Co forms granular particles on FePt thin film (middle). 7 nm Co is like a maze (bottom). Schematic of exchange-spring magnet multilayer is corrected by SEM image. (Right) The 3 nm and 7 nm on 20 nm FePt thin layer are not enough to form a thin layer. They are island-type nanostructure.

The surface of t_3 shows an island-like nanostructure. Although t_7 looks almost packed by Co, the whole area is not a continuous film. The Pt protection layer on t_3 is too thin to form a substantial crystalline Pt layer. Instead Pt is diffused into the gaps between the grains, probably forming a new phase there. A thicker Co layer forms an almost continuous Co film and allows to build up a Pt layer exhibiting the Pt crystal structure (sample t_7). The layer structures, as suggested by the SEM images, are schematically shown in Fig. 5.4 on the right hand side (compare with the intended structure as illustrated in Fig. 5.2) These SEM results will be helpful to understand the transmission electron microscopy (TEM) images of the nanomagnets shown in the next section.

5.1.2 Characterization of the nanopattern structure

5.1.2.1 AFM and MFM results

These films are then structured by NIL, explained in Appendix A. 2. For all samples only one master stamp was used. It exhibits dots of 60 nm diameters, 150 nm period and 90 nm heights. The AFM image describes the size and height of each nanomagnet and their periodicity. The MFM image shows the magnetic up and down directions of the nanomagnets. It shows that they are single domain nanomagnets without noticeable interaction. The 3-D structure and scale down images are in Appendix A. 3.

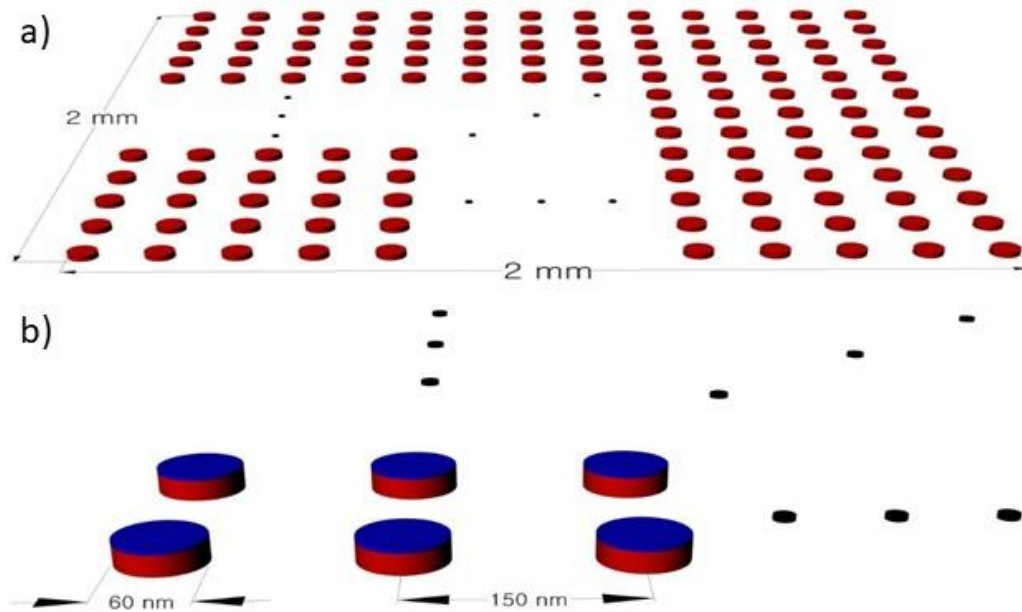


Fig.5. 5 Schematic of the exchange-spring nanomagnets produced in this part of the work a) The pattern size is a large area of 4 mm². b) The diameter of nanomagnet is 60 nm, their period 150 nm.

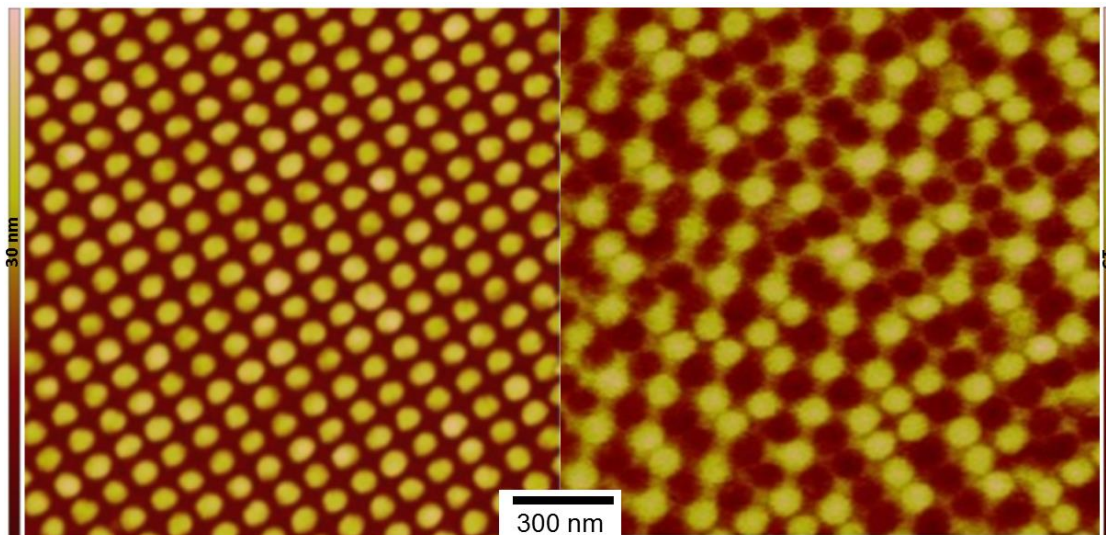


Fig.5. 6 The AFM and MFM images of samples after the etching process. All samples show the same results. The AFM images shows a uniform pattern with 60 nm size and 150 nm periods. The MFM result denotes that the individual nanomagnets are not interacting, but are single domains.

The AFM and MFM images of the nanodots are shown in Fig. 5.6. The nanomagnets are distributed homogeneously over the substrate and exhibit the same shapes, very similar to the schematic shown in Fig. 5.5.

5.1.2.2 TEM images of the nanomagnets

TEM images were taken (see Fig.5.7) direct information about the real thicknesses and shapes of the nanomagnet. The figures show that the nanomagnets deviate from a cylindrical shape. They look more like circular truncated cones, which is due to lateral etching. The height of the nanomagnets t_0 is less than 20 nm. One also can recognize something on top of these nanomagnet; this is carbon that has been deposited there during the preparation of the TEM samples. The samples t_3 and t_7 only show traces of Co on top of the FePt islands, besides rests of the lacquer from patterning. Also the TEM pictures show that the Co and Pt layers are by no means homogeneous. At the moment it is not clear why the t_7 nanomagnets exhibit an exceptionally low Co coverage.

In these TEM measurements FePt and Co layers of samples t_3 and t_7 are hard to distinguish. Therefore, in order to determine the composition of an exchange-spring nanomagnet, energy-dispersive X-ray spectroscopy (EDX) measurements were performed. Appendix A.4 presents the EDX results.

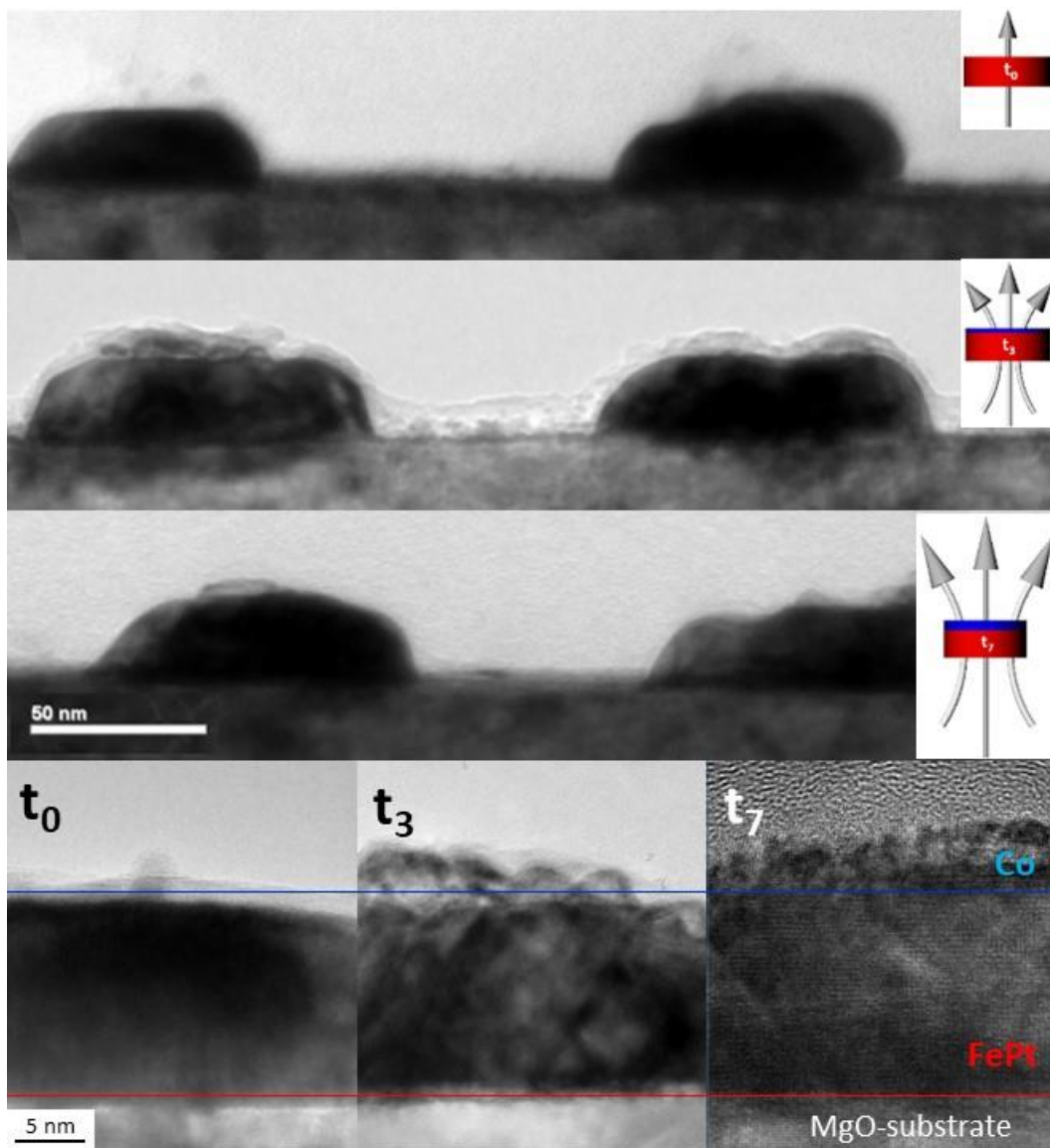


Fig.5. 7 TEM images of t_0 , t_3 , and t_7 samples. The thickness of t_0 sample is less than thin films due to etching rate. The Co layers of t_3 and t_7 are not covered whole area and thicknesses are not homogeneous.

5.2 Magnetic properties

The magnetic properties of the nanopatterned magnets were investigated with SQUID magnetometry. But before nanopatterning, also the magnetic properties of the thin films were measured. The out-of-plane and in-plane magnetic hysteresis loops at RT are shown in Fig. 5.8 showing to large out-of-plane anisotropy. With increasing thickness of the soft magnetic Co layer, anisotropy and coercivity are reduced. For comparison, the intrinsic magnetic properties of the multilayers components are presented Appendix A. 5.

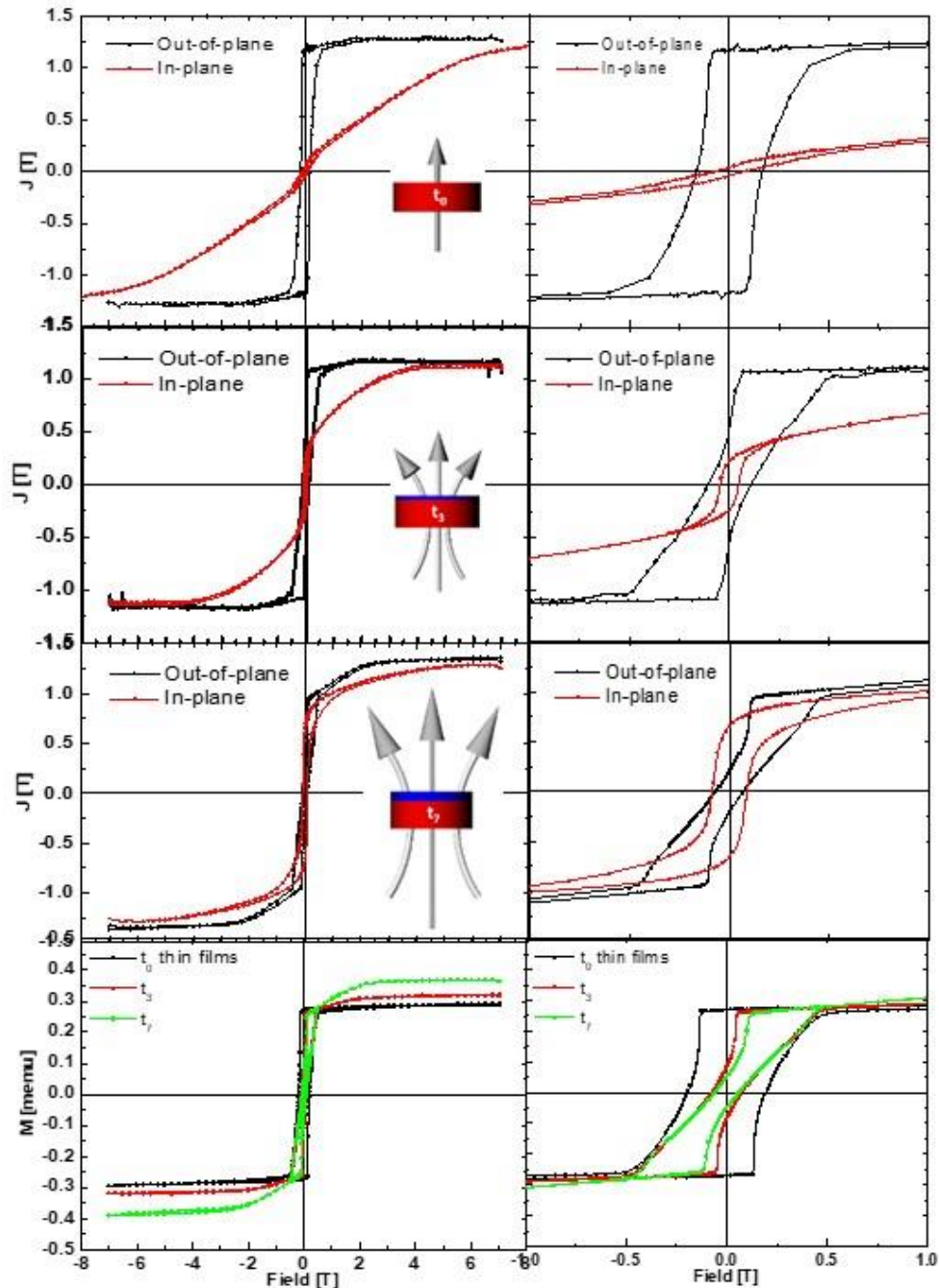


Fig.5. 8 RT out-of-plane and in-plane magnetic polarization hysteresis loops of the exchange-spring multilayers t_0 , t_3 , and t_7 before getting nanostructured. On the right-hand side a magnified version around field zero. In the bottom-line the magnetic moments of the out-of-plane hysteresis loops are compared.

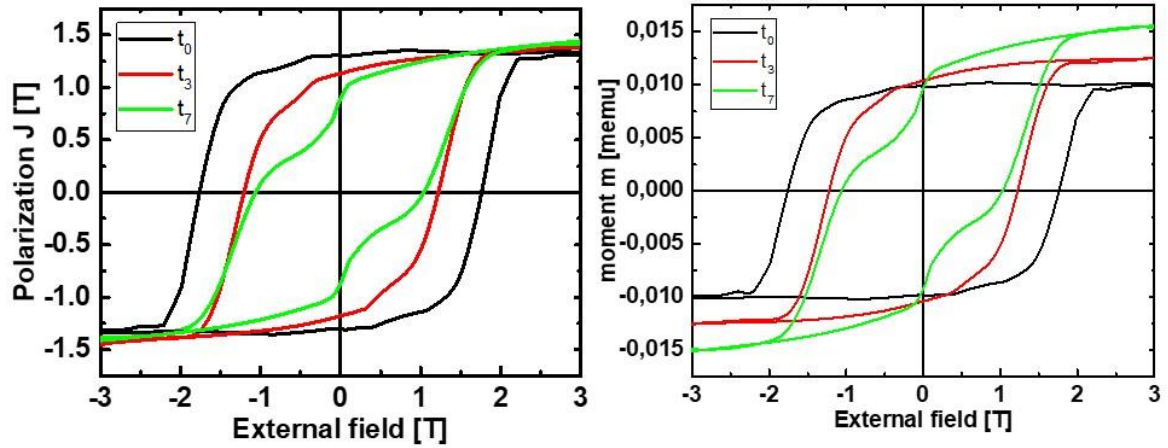


Fig.5. 9 The hysteresis loops (magnetic polarization and magnetic moments) of exchange-spring nanomagnet patterns in our-of-plane at room temperature. The saturation polarizations are similar.

The values of magnetic polarization (magnetization) are similar, because they are quantities per unit volume. The magnetic moments (fig.5.9, right) show the influence of the soft magnetic layer. The hysteresis loops of t_0 and t_3 are switching in almost one step without a significant kink. However, t_7 shows clearly two-steps switching with kink. Sample t_0 is composed of one phase, only, the $L1_0$ -FePt hard magnet. In sample t_3 there is perfect coupling between the hard and the soft Co phase. Only partial coupling, is observed for t_7 . Further details will be referred to later in this section.

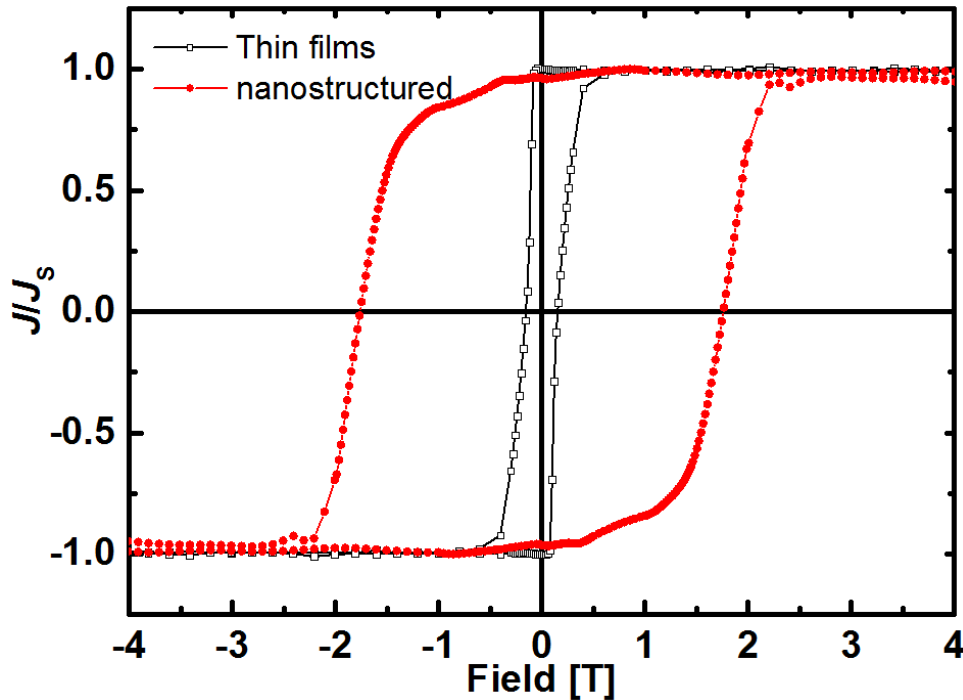


Fig.5. 10 Normalized out-of-plane hysteresis loops of 20 nm thick continuous and nanopatterned $L1_0$ -FePt on MgO (100) substrate at RT.

The out-of-plane hysteresis loops of the thin continuous film and the nanopatterned system of t_0 show big difference (see fig. 5.10). The coercivity increases from $H_C \sim 0.15$ T (thin film) to $H_C \sim 1.75$ T (nanomagnets). The magnetic parameters of the thin films are summarized in Appendix A.5

5.2.1 Temperature dependence of hysteresis loops

In order to study the magnetic reversal process by microstructural parameters, the temperature dependence of the hysteresis loops of samples have been measured in the temperature range 50 K to 350 K. The temperature dependent out-of-plane hysteresis loops of the samples are shown in Fig 5.11.

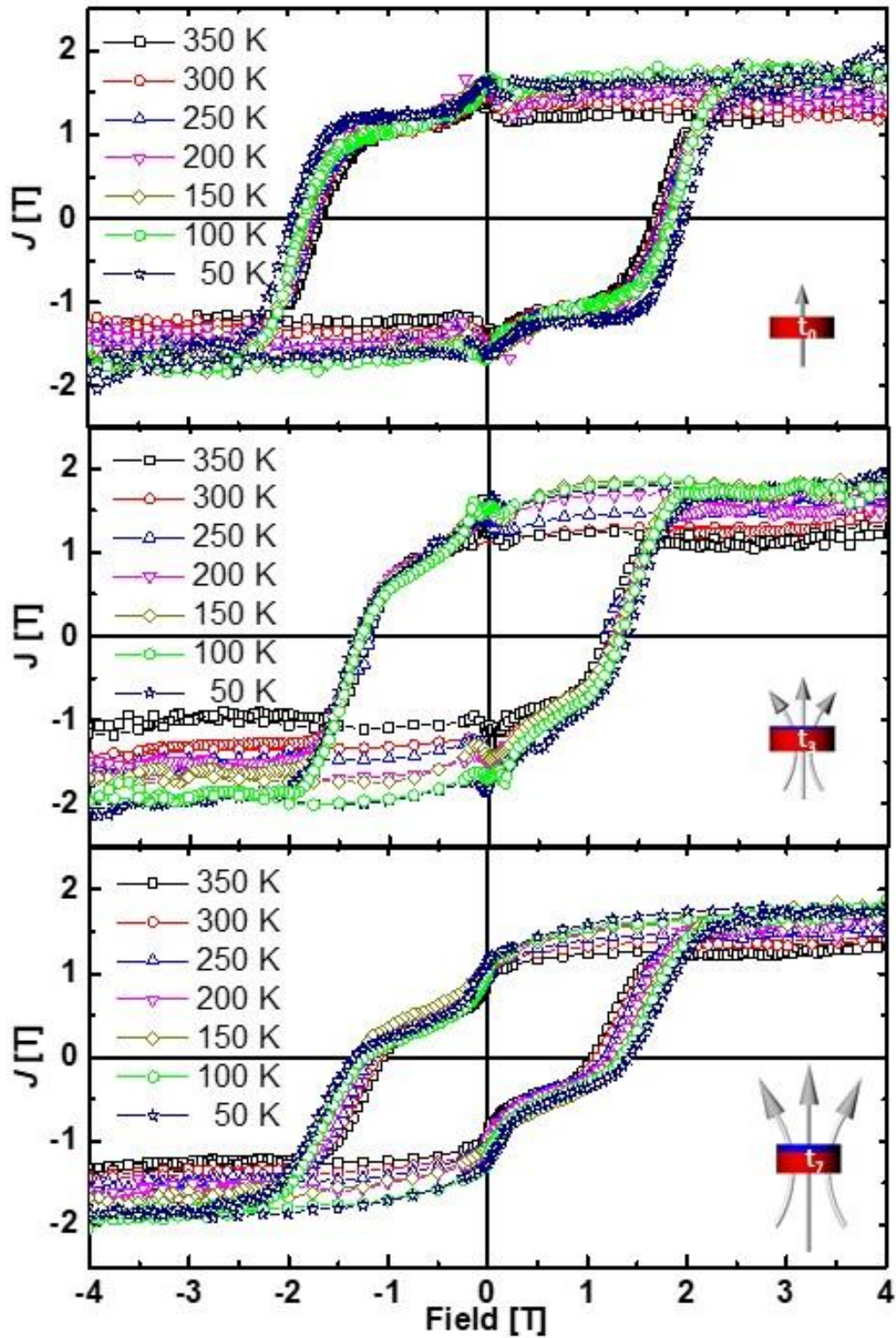


Fig.5. 11 Out-of-plane hysteresis loops of the nanomagnets t_0 , t_3 and t_7 from 50 K to 350 K.

The temperature dependence of the out-of-plane hysteresis loops of these tuned exchange-spring nanomagnets are directly consequences of the fraction of soft magnetic material on the coercive field and saturation polarization. The coercive fields H_C decrease from 1.94 T to 1.66 T for t_0 , from 1.32 T to 1.19 T for t_3 and from 1.24 T to 1.02 T for t_7 in the temperature range 50 K to 350 K. A decreasing temperature cause the coercive field to increase as expected.[133] However, the fraction of the soft magnetic material does not seem to influence the temperature dependence of the coercive field. The width distributions of H_C are 0.28 T for t_0 , 0.11 T for t_3 and 0.21 T for t_7 . The pure FePt patterns exhibit the largest change, the perfectly coupled exchange-spring magnets a smallest. Thus, the increase of the saturation polarization definitely is due to the soft magnetic layer. The saturation polarizations J_s decrease from 1.78 T to 1.15 T for t_0 , from 1.79 T to 1.20 T for t_3 and from 1.79 T to 1.26 T for t_7 in the temperature range 50 K to 350 K. With decreasing temperature the saturation polarization increases. However, the soft magnet has higher Curie temperature, and thus the decrease of the saturation polarization with temperature is less. The hard magnetic nanomagnet patterns have smallest saturation polarization. The saturation polarization distributions of the samples are 0.63 T for t_0 , 0.59 T for t_3 and 0.53 T for t_7 . The saturation polarization is related to amount of the soft magnetic material. The hysteresis loops of the hard nanomagnet pattern t_0 are almost rectangular. The increase of the soft magnet fraction bends the hysteresis shapes due to increasing coupling between the hard and soft phases. The coercive field and the saturation polarization are shown in Fig. 5.12 in dependence of temperature.

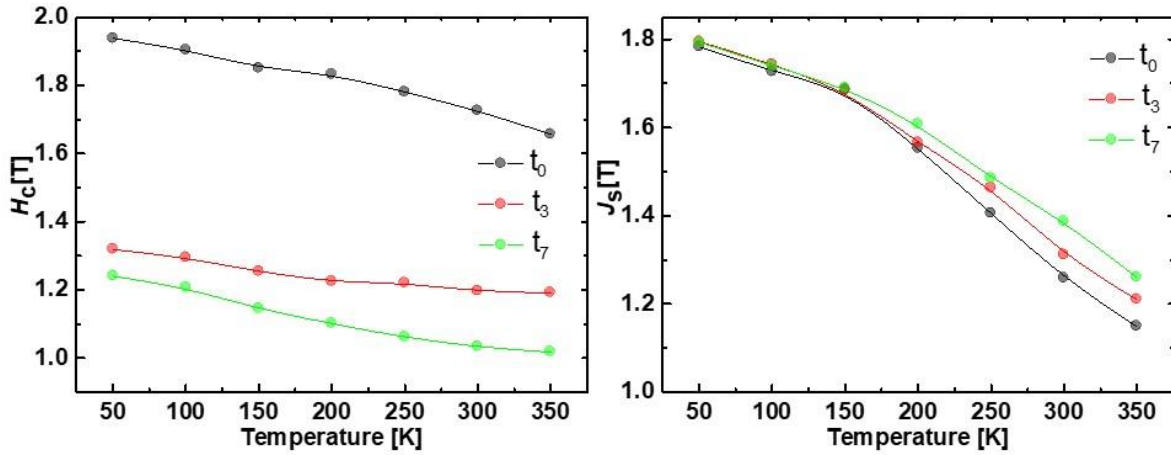


Fig.5. 12 The coercive field, H_C and the saturation polarization, J_s at various temperatures of exchange-spring nanomagnet patterns.

The anisotropy energy (MAE, K_1) were determined as the sum of the effective magnetocrystalline anisotropy energy (MCA, K_u) and the shape anisotropy (K_{shape}), [$K_1 = K_u + K_{shape}$]. The effective anisotropy can be obtained from the slope and the magnetic polarization of in-plane hysteresis loops, as described in section 4.2.2.2. The in-plane hysteresis loops of the nanopatterns are shown in Appendix A.4. The shape anisotropy was calculated from the difference of the demagnetization factors for each directions and saturation magnetization according to the formula $K_{shape} = \frac{1}{2} \mu_0 \Delta N_d M_S^2$. The values of ΔN_d are obtained 0.356 for t_0 , 0.304 for t_3 and 0.244 for t_7 by simple approximation of M. Sato.[118] The anisotropy energies are shown in fig.5.15 in dependence of temperature. The pure FePt system has a higher MAE. The slopes that can be used to calculate the effective anisotropy do not dramatically change between samples. The shape anisotropy is dependent on the saturation magnetization. An increasing of the thickness of the Co layer reduces MAE.

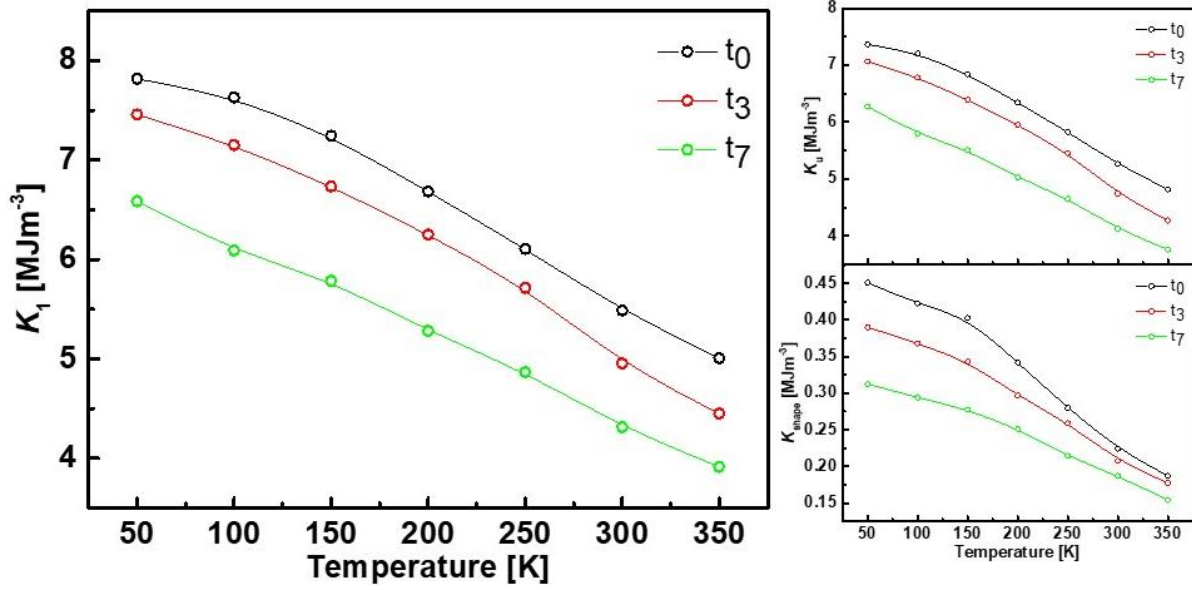


Fig.5. 13 The anisotropy constant K_1 was obtained from the magnetocrystalline anisotropy energy (MAE, K_u) and the shape anisotropy constant K_{shape} in dependence of temperature.

The temperature dependent exchange stiffness A was determined by means of Eqn. 4.11 which is relation between the saturation polarization J_s and stiffness constant D_{sp} . The stiffness constant, D_{sp} could be obtained by $J_{s,0} = J_s(T=0)$ and the characteristic temperature T_0 in Eqn. 4.19. Fig. 5.14 (left) shows the plots $((T/T_0)^{3/2}$ vs $J_s/J_{s,0}$) to obtain $J_{s,0}$ and T_0 by Eqn. 4.18. By fitting of the Bloch's $T^{3/2}$ law, the values of t_0 : $J_{s,0}$ - 1.843 T, T_0 - 663.54 K, t_3 : $J_{s,0}$ - 1.842 T, T_0 - 707.2 K and t_7 : $J_{s,0}$ - 1.835 T, T_0 - 765.22 K) are determined. The calculated exchange stiffness A by in dependence of temperature, which are shown in Fig. 5.14 (right), are smaller than for thin films. By adding of soft magnetic layers the saturation polarization at 0 K slightly decreases, the characteristic temperature increases. If the magnetic moments are aligned parallel to each other, the exchange stiffness A decreases due to a thicker domain wall.

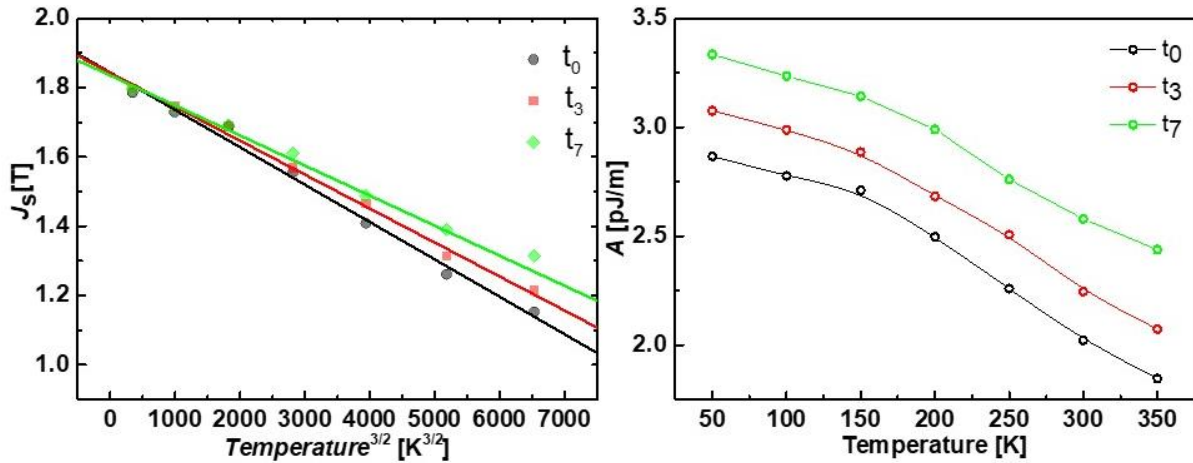


Fig.5. 14 The linear fit of experimental data to obtain $J_{s,0}$ and T_0 by Bloch's law. The exchange stiffness A of exchange-spring nanomagnet patterns.

With MAE and A , the wall energy γ , the exchange length l_k and the wall thickness δ can be calculated. The MFM results show the behavior of each nanomagnet in patterns as single domain nanoparticle. However, the hysteresis loops of t_7 are kinked: the decoupled part in exchange- spring nanomagnets seems to form multi-domains. As can be seen in fig.5.15, sample t_7 has the lowest wall energy. It

means that for sample t_7 sample it is easier to forms multi-domains. Moreover, the thicker Co soft layer is in favor of parallel alignment of the magnetic moments, which increase the domain wall thickness. The calculated exchange lengths are about double of lattice constants.

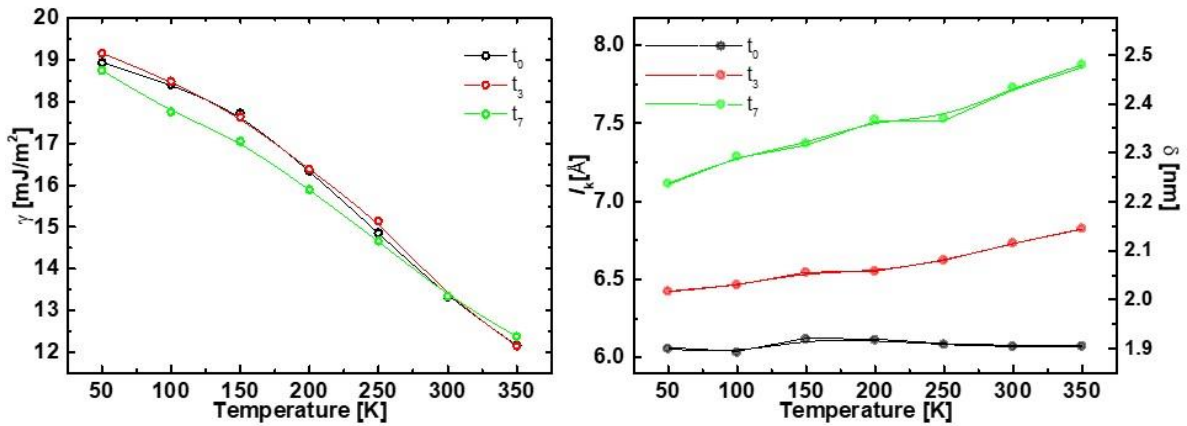


Fig.5. 15 The wall energy, the exchange length and the width of domain wall of exchange-spring nanomagnet patterns are obtained with MAE and A

The exchange stiffness A , the wall energy γ , the exchange length l_K , the domain wall thickness δ and the critical diameter D_C of samples t_0 , t_3 and t_7 at RT are listed in Table 5.1.

	A [pJ/m]	γ [mJ/m ²]	l_K [Å]	δ [nm]	D_C [nm]
t_0	2.022	13.32	6.07	1.91	42.3
t_3	2.245	13.34	6.73	2.11	39.
t_7	2.578	13.34	7.72	2.42	34.8
FePt thin film	4.2	19.15	8.7	2.75	52

Table 5. 1 The magnetic domain theory parameter of exchange-spring nanomagnet patterns at RT. 7 nm FePt thin film for comparison.[133]

5.2.2 Microstructural parameters

The microstructural parameters explain the magnetic reversal process, introduced in section 2.4.4. To obtain these parameters, the measured values of the saturation polarization J_S , the coercive field H_C and the MAE K_1 for various temperatures were inserted into the relation of $H_C(T)/J_S(T)$ vs $2K_1(T)/J_S^2(T)$.

The plot of the coercive field, the saturation polarization, and MAE relations gives the information of coercivity (switching, magnetic reversal process) mechanism by the microstructural parameters α and N_{eff} . Fig. 5.16 shows a plot of the relation by which the microstructural parameters can be determined; the slope provides α and the intersection with the y-axis are N_{eff} .

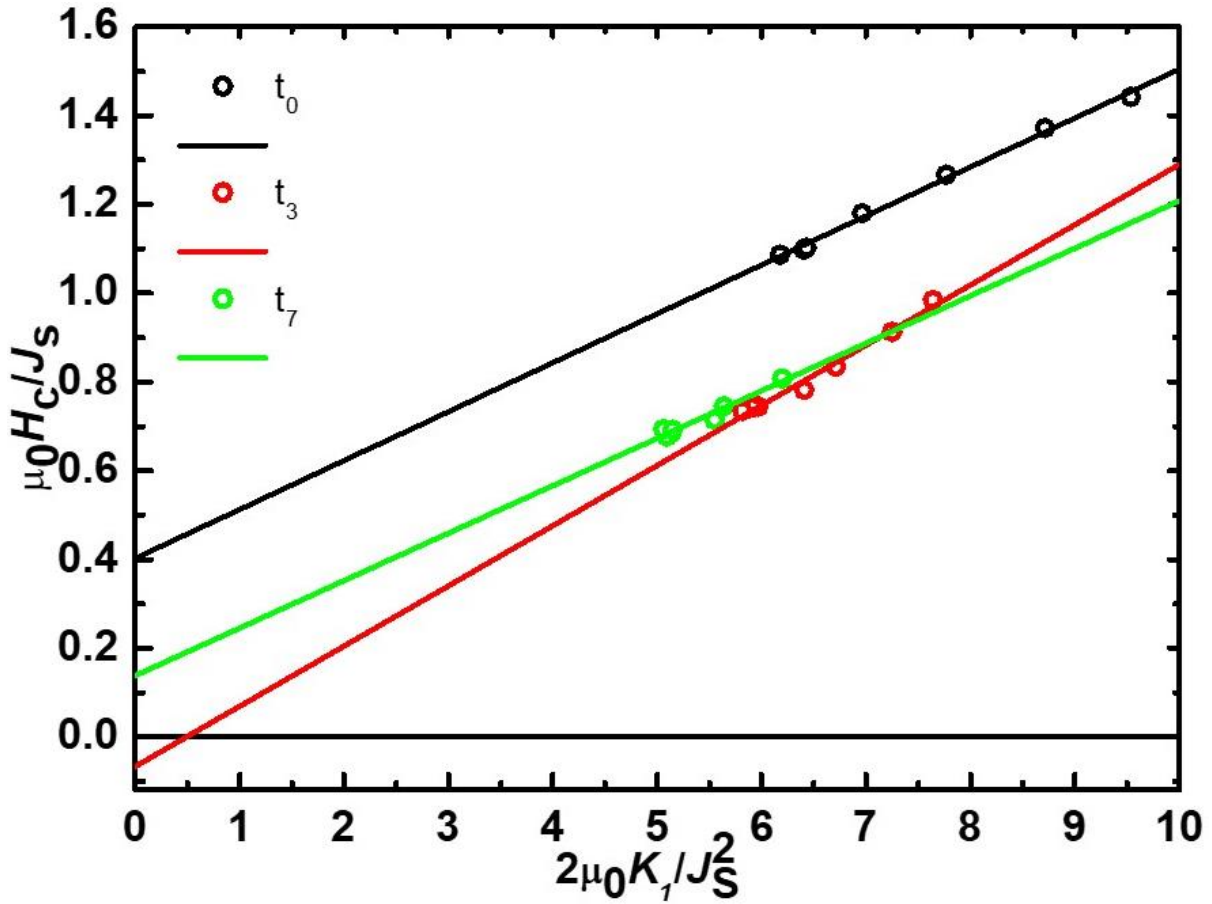


Fig.5. 16 The plot to determine the microstructure parameters α and N_{eff} of exchange-spring nanomagnet patterns with different the soft magnetic fraction.

The ideal nucleation field has $\alpha = 1$ and $N_{\text{eff}} = 0$ which is accompanied by an irreversible homogeneous rotation. However, the experimental coercivities are smaller than in the ideal case; this is known as Brown paradox. The determined parameters are summarized in Table 5.2.

	α	N_{eff}	α_K	α_{ex}
t_0	0.11	0.402	0.846	0.13
t_3	0.135	-0.066	0.768	0.175
t_7	0.106	0.138	0.742	0.142

Table 5. 2 The obtained microstructural parameters. Those parameters explain the coercive mechanism.

The obtained microstructural parameter α shows the influence of the Co soft magnetic layer. Compared to t_0 , the α is increased for t_3 , but about the same for t_7 . In order to estimate the reason of this behavior, sub-parameters (α_K , α_y and α_{ex}) of α are determined. The value of α_y is assumed by almost ~ 1 , as for the easy axis direction. α_K is due to the inhomogeneous regions which are 1.7 nm in the A1 phase for t_0 , 3 nm Co for t_3 , and 7 nm Co for t_7 . α_K is reduced due to the increasing inhomogeneous regions. The hard magnet t_0 and perfectly coupled exchange spring magnet t_3 are both magnetically homogeneous. The small value of α_K of t_7 explains that more magnetic phases than in the other cases. The smaller values of α_{ex} result from exchange-coupled grains. By all of the results, the assumed magnetic moments directions in the individual nanomagnets with real dot shape are depicted in fig. 5.17. Pure FePt has inhomogeneous region due to the etching and mismatching with the substrate. The cover by Co protects the top of FePt from being an A1 phase (α_K). No flat region at the edge of nanodots forms the angle of magnetic moments. The decoupling between the hard and the soft magnetic layers separates the magnetic moment directions of the top and bottom layers. (α_{ex}).

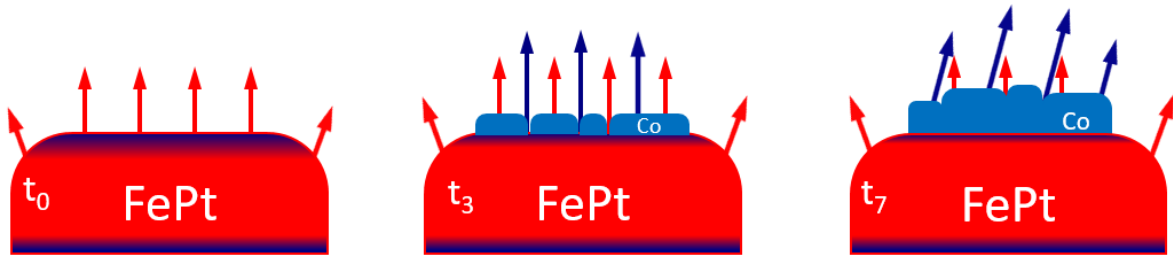


Fig.5. 17 The magnetic moment directions in the individual nanomagnets

N_{eff} is the difference $N_{||} - N_{\perp}$. The negative values of N_{eff} mean that those magnets form a demagnetization field H_d which has components in both directions, perpendicular and parallel to external field. Moreover, part of the dots extends in vertical direction. The A1 phase on t_0 and decoupled part of t_7 induce the magnetization reversal mechanism. The magnetizations in the nanomagnets of disk shape tend to be aligned parallel to the disk face. L1₀-FePt has an easy axis perpendicular to the disk face. However, the decoupled part of the Co soft magnet follows the shape anisotropy. This direction corresponds to the film direction, which is perpendicular to the external field. N_{\perp} is increased by the decoupled soft layer. Therefore N_{eff} goes down to negative values.

5.2.3 FORCs results

First-order reversal curves measurements on these nanomagnet patterns were performed to investigate the interaction field and the coercive field distribution. The measured minor hysteresis loops were analyzed by explained method in section 4.2.3.1. The FORCs densities of each sample are depicted in Fig 5.18.

The distributions of the interaction field are very narrow, supporting tiny interaction between the nanomagnet in the patterns. The coercive field distribution tells that this nanopattern is a good example for the Preisach model. Each single domain nanomagnet behaves as hysteron in the hysteresis loop. The numbers of nanomagnets is the same in all patterns, and they are uniformly distributed. The magnetization of the hard nanomagnet in t_0 is smaller than that of the others. Therefore, it has lower intensity with broader distribution. In contrast, sample t_3 shows a higher intensity and a narrower distribution. The perfect coupling of two phases has a lower potential for switching due to the soft magnetic layer. The decoupled region of the t_7 samples forms two separated mounds due to the soft magnetic layer reversal at low field and a coupled part reversing with hard magnet.

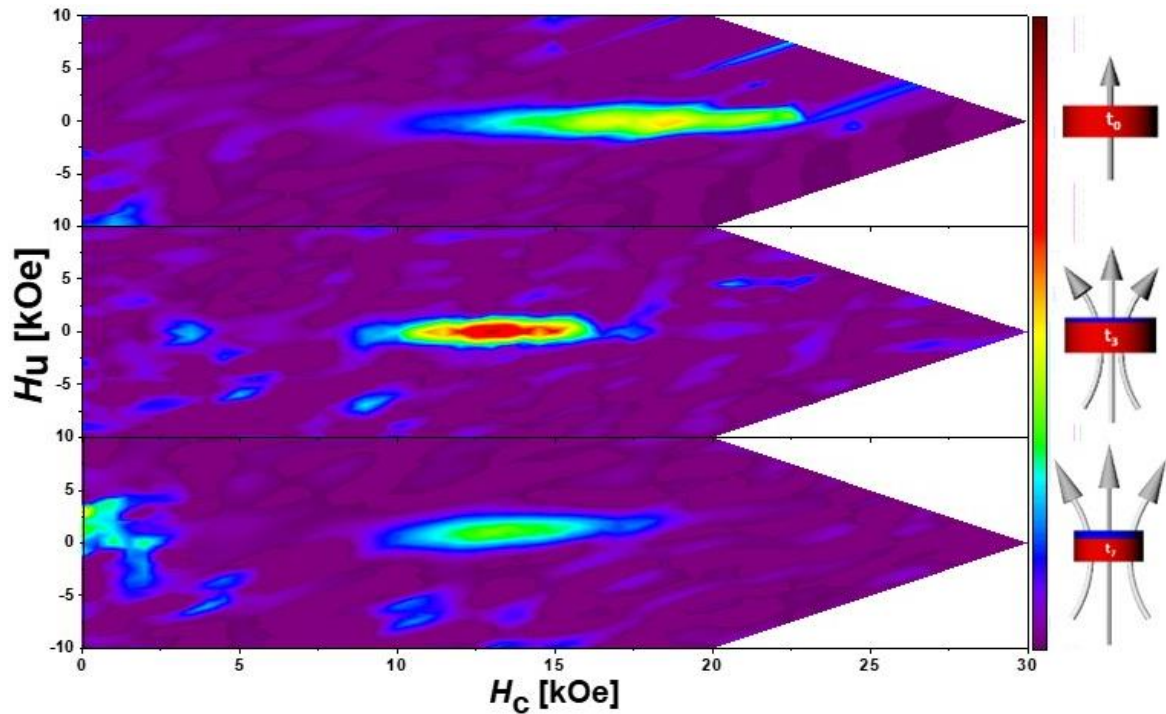


Fig.5. 18 FORC density of tuned exchange-spring nanomagnet patterns: t_0 result (top), t_3 (middle) and t_7 (bottom). The partially coupled exchange-spring magnet has two regions for distribution.

In addition, the distribution of the areas between FORCs minor loops (Fig. 5.19, Appendix A. 7) with an equal field spacing of 1000 Oe represents how many hysterons are switching by the reversal field. In Fig.5.19, the bar graph displays the difference of the area in FORCs. It also shows a modified Gaussian distribution ($G(H) = m_0 + \left(\frac{A}{\sigma\sqrt{2\pi}}\right) \exp\left(-\frac{H-H_C}{2\sigma^2}\right)$) fitted to the data (green line). The fitting results give information about m_0 , σ and H_C . m_0 indicate the amount of change by an external field of 1000 Oe. A rise of the thickness by the Co layer increase the value of m_0 from 0.00928 (ratio of area) for 0 nm Co and 0.00956 for 3 nm Co to 0.1167 7 nm Co layer. At the point of the begin of the switching, the area is smaller than m_0 . This range is assumed to result from spin tilt, not a spin flip of dots. A higher values of m_0 , the dots switch. The decoupled ES magnet has broader range of nucleation. Besides, in the partially coupled ES magnet includes broad less change range is seen almost 1 T due to decoupled part of the Co soft layer. The value of σ is reduced from 6.8 kOe for t_0 , 5.2 kOe for t_3 and 4.2 kOe for t_7 by Co layer. The coupling between dots is negligible, and patterns are almost equal. However, the narrowing of width means that the force to switch dot is reduced by soft layer.

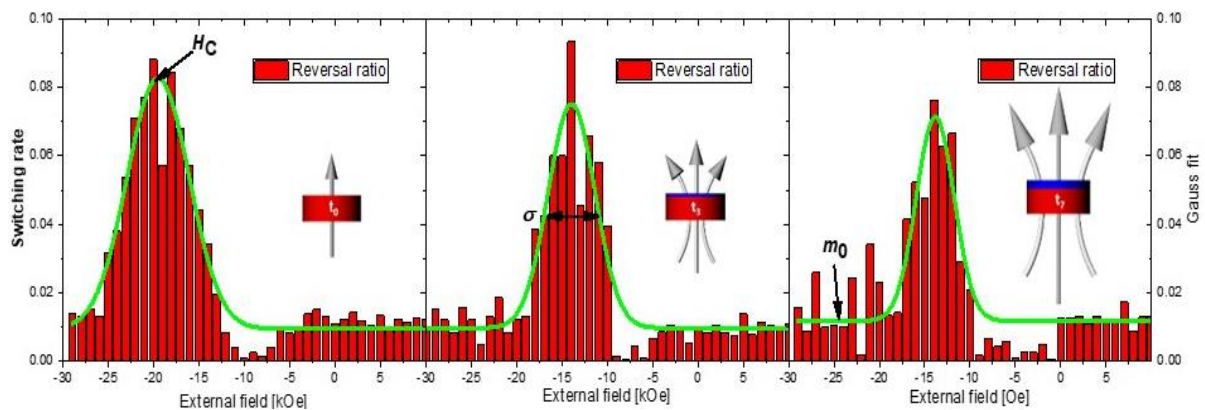


Fig.5. 19 Switching field distribution (SFD) by area of FORCs.

5.2.4 Magnetic reversal process in partially coupled ES magnet

The reversal process of a single one phase magnet (t_0) and a perfectly coupled magnet (t_3) is just one flip. However, the partially coupled magnet (t_7) has a kink in the reversal process, consisting of two steps. The decoupled part of soft magnetic layer can create a domain wall. The two domain states are confirmed by MFM. For this purpose field-dependent MFM images were taken at various fields, from 2 T to -2.5 T. Fig 5.20 are MFM images by various reversal fields measured at zero field.

The magnetic saturation at 2 T is correlated to a homogeneous pattern in the MFM image. At -0.5 T and -1 T, there seems to be two domains in one nanomagnet. A bright and a dark side of one structure is due to the Co magnetization is in-plane oriented, therefore the stray field of top of dot is a flat dipole. The MFM machine can only check -up-down directions of magnetic stray field. A hard magnetic behaviors is assumed under the soft magnet at those fields. It appears as a black-white contrast in one nanomagnet. However, at -1.25 T, the flipped nanomagnet does not show two domains. The assumed model of magnetic reversal is depicted in Appendix A.9.

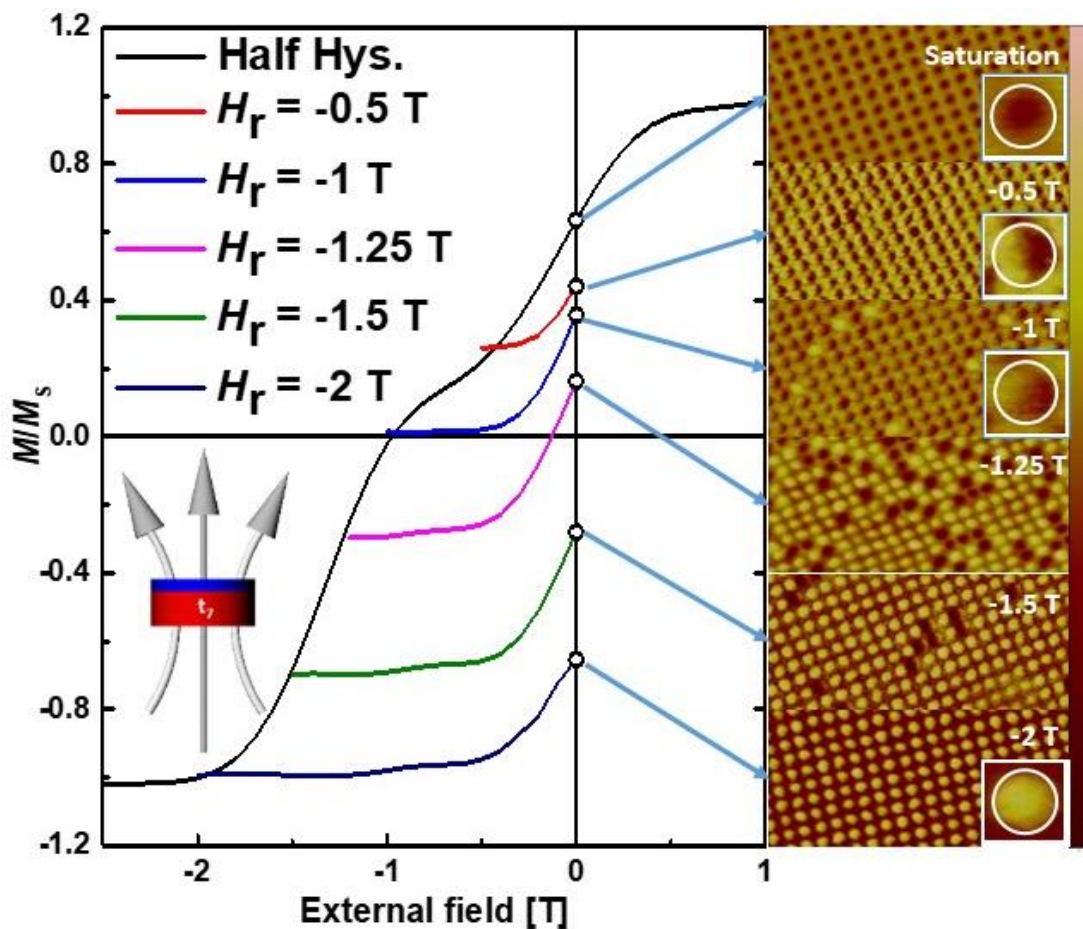


Fig.5. 20 The microscopic magnetic reversal processes by MFM images of remnant at a certain field (t_7 : Partially coupled ES magnet sample). Inset: Zoom in one particle, white circle is guide a dot.

5.3 Conclusion: Influence of the soft magnet fraction in artificial nanosized exchange-spring magnets.

It was the aim of this study to investigate the differences between the magnetic properties of one-phase nanomagnet and exchange-spring nanomagnets of different soft magnet fractions. For this purpose three kinds of thin films were prepared by sputtering with the composition: 20 nm FePt, 20 nm FePt/ 3 nm Co/ 2 nm Pt and 20 nm FePt/ 7 nm Co/ 2 nm Pt. Films qualities, crystal structure, and morphology were investigated by XRD and SEM. A nanopattern of 60 nm dot size and 150 nm period was transferred to the three thin films with nanoimprint lithography. The pattern and phase structures were investigated by AFM and TEM and how good quality.

Their magnetic properties have been investigated by SQUID magnetometry. The temperature dependent hysteresis loops gave the information about the saturation polarization and the coercive field. MAE values for various temperatures were obtained by measuring the hysteresis loops along different directions. From these measurements, the microstructural parameters, which can explain the coercivity mechanism, were determined. Different switching behavior of the nanomagnets can be explained by the obtained the microstructural parameters, where individual nanomagnets are non-interaction as a single domain. A separated nanomagnet becomes a hysteron in the sense of the Preisach model. For the verification of this, FORCs measurements were performed. The samples exhibit a narrow interaction field distribution, but a broad coercive field distribution. In a comparison of the hard and the exchange spring magnet, the pure FePt system has broader distribution of the coercivity. Moreover, the different thicknesses of the soft magnet influence the magnetic reversal behavior and exchange coupling. The latter causes either perfectly coupled or partially coupled exchange spring magnet which includes also decoupled region as be seen in FORCs density.

To check the spin tilt of the decoupled part, field dependent MFM images were performed. The decoupled cobalt parts of all nanomagnets in partially coupled magnet pattern are reversed first. At the critical field, some nanomagnets switch, and the magnetization directions of nanomagnets in the pattern are re-arranged. The assumed model of the magnetic reversal process in partially coupled magnets was depicted by field dependent MFM.

The results show that exchange spring magnet can be produced perfectly coupled or partially coupled, according to the thickness of the soft magnetic layer. The perfectly coupled exchange spring magnet exhibits a one-step hysteresis loop without kink, such as a one-phase hard magnet alone. However, the partially coupled exchange spring magnet shows two steps hysteresis loop with kink, due to the early reversal of the decoupling soft magnet. Increasing the decoupled soft layer reduces the microstructural parameter α and N_{eff} . The stacked hard and soft magnets form exchange coupled grains, misaligned grains, and inhomogeneous grains. The nucleation α in these grains causes a rotation of the spontaneous polarization with increasing demagnetization field. In consequence, these effects reduce the coercive field of the magnets as shown by the intensity of the FORCs density. The decoupled soft layer forms a metastable state with two regions. Actual magnetic reversal process of partially coupled ES magnet is shown.

It was verified that a combination of these magnets can give new magnet of excellent magnetic properties.

Chapter 6

Results: Exchange-spring granular nanomagnets

In this chapter, exchange-spring nanomagnets formed as granular, multilayered nanomagnets are investigated. The coupling strength between the hard and the soft magnetic components of these nanomagnets are tuned by a non-magnetic interlayer of varying the thickness. In this way, perfectly coupling, partially coupling and decoupling between the two magnetic layers are obtained. The aim of these studies is to get information about the influence of different type of coupling and to investigate how the magnetic properties can systematically controlled by the variation of the coupling. This is particularly important for applications.

The exchange-spring multilayers consist of 7 nm L_{10} -FePt/ x nm Pt/ 3 nm Co/ Pt layers with a varying thickness ($x = 0, 0.5, 1$ and 2) of the Pt interlayer. The samples were grown by Magneto co-sputtering. They were analyzed by X-ray diffraction (XRD) and scanning electron microscopy (SEM) to check the crystal phase and morphology. The influences of magnetic coupling on the magnetic properties were studied by superconducting quantum interference device (SQUID) magnetometry. From these measurements magnetic intrinsic parameters, microstructural parameters and first order reverse curves (FORCs) were obtained. In addition, X-ray magnetic circular dichroism (XMCD) was employed to study element specific magnetic properties. By this method, the hard magnet (by Fe $L_{2,3}$ XMCD) and the soft magnet (by Co $L_{2,3}$ XMCD) could be investigated, separately.

6.1 L_{10} -FePt/ Pt/ Co composition island structure

As hard magnet, 7 nm thick (nominal thickness) layers of L_{10} -FePt on MgO (100) substrate were used. It has been reported to show a high coercivity (H_C) of ~ 4 T with highly structural order in our previous work of our group.[133] The L_{10} -FePt layer was covered by a 3 nm thick (nominal thickness) Co layer (for the soft magnet) with Pt interlayer of various thicknesses. The whole stack was covered by a thin Pt layer as protection layer (see Fig. 6.1).

The 7 nm thick L_{10} -Fe₅₁Pt₄₉ films were grown on an MgO (100) substrate at 800 °C by following the optimized sputtering condition described in Appendix A. 1. All of other materials, the Co soft magnetic layer and Pt inter/protection layers were deposited at room temperature to prevent inter diffusion. Four multilayer stacks were prepared:

In addition, a 7 nm FePt film without any Co layer was grown as a reference. The details about this 7 nm FePt film on MgO will be referred to in chapter 7 again.

All samples are named after the thickness of the Pt interlayers, such as t_0 , $t_{0.5}$, t_1 , t_2 and t_{NoCo} . Fig.6.1 shows schematics of these exchange-spring multilayers.

t_0 : 7 nm FePt / 0 nm Pt / 3 nm Co / 2 nm Pt , $t_{0.5}$: 7 nm FePt / 0.5 nm Pt / 3 nm Co / 1 nmPt
 t_1 : 7 nm FePt / 1 nm Pt / 3 nm Co / 1 nmPt , t_2 : 7 nm FePt / 2 nm Pt / 3 nm Co / 1 nmPt
 t_{NoCo} : 7 nm FePt

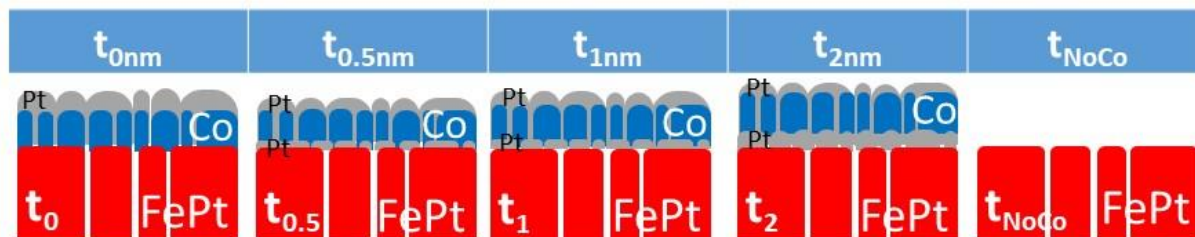


Fig. 6. 1 Schematic illustration of multilayer stacks that exhibit Pt interlayers of different thicknesses (0, 0.5, 1 and 2 nm) between a $L1_0$ -FePt hard magnet layer of 7 nm and a Co soft magnet layer of 3nm and 7 nm pure FePt without Co. They were grown on a MgO(100) substrate. All exchange-spring multilayers are covered by Pt protection layers. t_{NoCo} is only pure $L1_0$ -FePt as a reference sample. The samples are named by the thickness of interlayer: t_0 , $t_{0.5}$, t_1 , t_2 and t_{NoCo} .

6.1.1 Crystal structure

The crystal structures of the exchange-spring multilayers were identified by X-ray diffraction using $CuK\alpha$ radiation. The results of t_0 , t_1 , t_2 , and NoCo are shown in Fig. 6.2. FePt (001), (002) and (003) peaks are clearly found at $2\theta \sim 24^\circ$, $2\theta \sim 48^\circ$ and $2\theta \sim 76^\circ$ in the XRD pattern, respectively. The Co (111) and (002) peaks overlap with the MgO (002) and FePt (002) peaks. The chemical ordering parameter S of the $L1_0$ -FePt structures has been determined from the peak intensities by the numerical calculation. The S values of t_0 , t_1 , t_2 and NoCo are 0.92, 0.86, 0.99 and 0.86, respectively indicate high ordering, which is for t_1 and the NoCo samples somewhat lower.

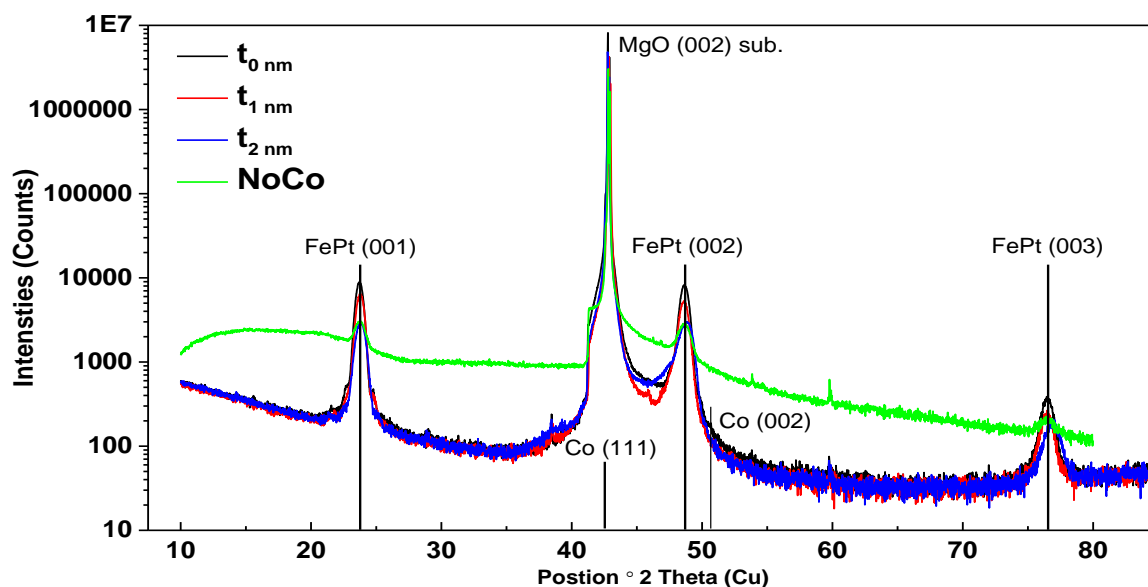


Fig. 6. 2 X-ray diffraction spectra of t_0 , t_1 , t_2 and t_{NoCo} samples. FePt (001-003) peaks indicate the crystal structure of chemically ordered $L1_0$ -phase. The highest peak is from MgO(100) substrate. Co peaks are overlapped the other peaks.

6.1.2 Morphology

Scanning electron microscopy (SEM) has been carried out to verify the morphology of the exchange-spring multilayers. The $L1_0$ -FePt thin films with nominal film thickness less than 8 nm are formed an island-type nanostructure of isolated particles with out-of-plane texture (see fig. 6.3). The c -axis of the face-centered tetragonal (fct) structure is perpendicular to MgO(100) substrate. The total thicknesses of multilayers are t_0 : 12 nm, $t_{0.5}$: 11.5 nm, t_1 : 12 nm, t_2 : 13 nm. The packing area ratios (coverage) are t_0 : 59.37%, $t_{0.5}$: 59.04%, t_1 : 60.9% and t_2 : 64.68% and used to calculate the sample volume which is needed to calculate magnetization (emu/cc, μ_B) or polarization J (T).

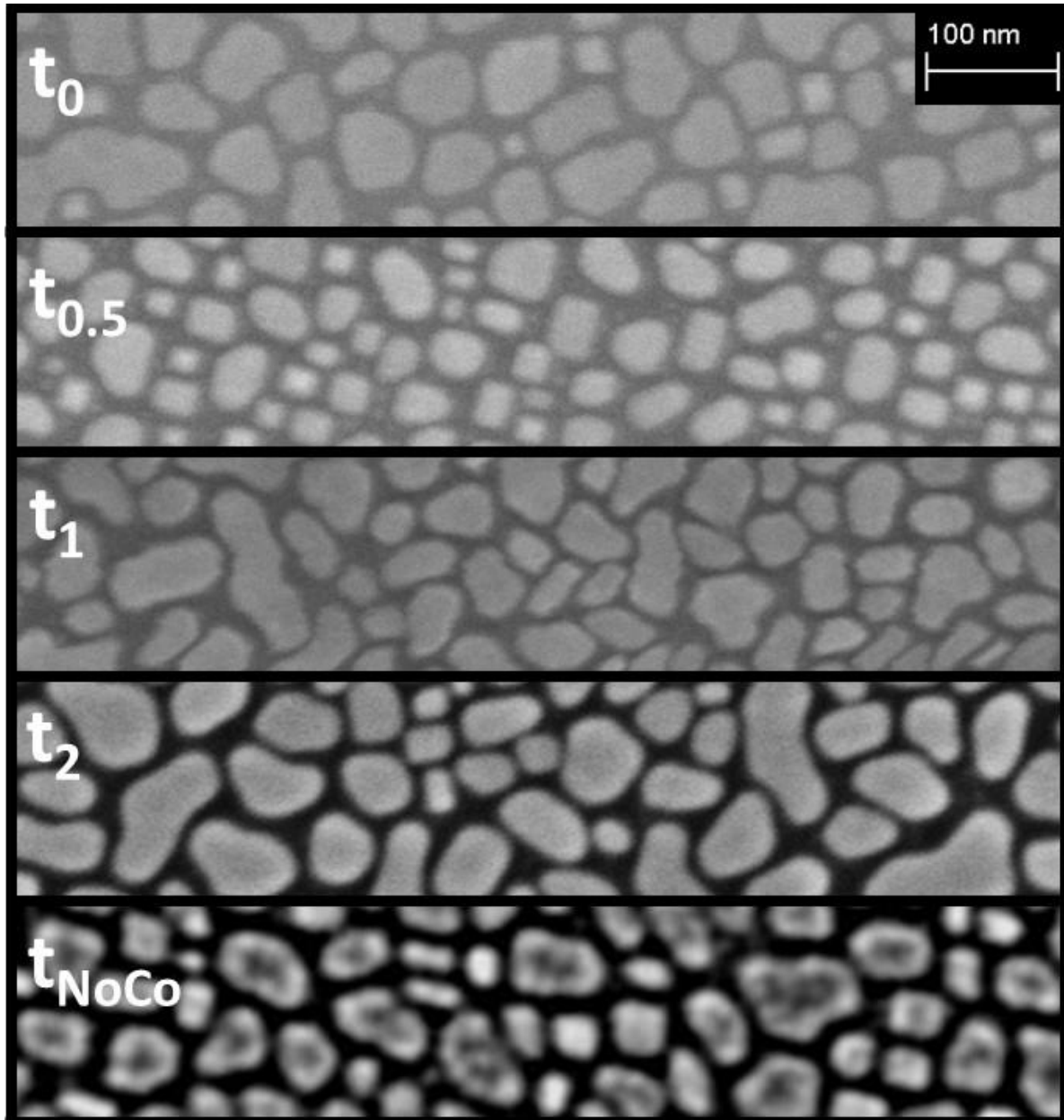


Fig. 6. 3 SEM images of $L1_0$ - FePt (7 nm)/ Pt (x nm)/ Co (3 nm)/ Pt (1 or 2 nm), (x = 0, 0.5, 1 and 2) exchange-spring magnetic multilayers and a pure 7 nm FePt grown on MgO(100) substrate. Entire thickness, grain sizes and packing ratios are different for each sample.

The diameter distribution of nanograins in ESM multilayers were obtained from SEM results in Appendix B.1.

6.2 Characterizations of magnetic properties

The SQUID magnetometry were done to study magnetic properties and magnetization reversal process of each magnetically different phase magnets in exchange-spring multilayers. The intrinsic material parameters and the micromagnetic parameters were obtained with the results of the field dependent magnetization measurements at various temperatures.

Fig 6.4 b-f) show the magnetic polarization hysteresis loops of the samples NoCo, t_0 , $t_{0.5}$, t_1 and t_2 in hard- and easy-axis at room temperature, after the correction for diamagnetism and paramagnetism of the substrate. The out-of-plane and in-plane measurements still show a strong anisotropy resulting from $L1_0$ -FePt layers, in spite of the existence of exchange-coupling with the soft magnetic layer, as expected for the chemical order in $L1_0$ -FePt phase. The maximum field of 7 T that can be applied in the SQUID magnetometer is sufficient to reach the saturation magnetization for easy-axis (out-of-plane). However, for the hard-axis (in-plane), the magnetization of the films does not reach saturation in a maximum field of 7 T.

It is obvious that the interlayer thickness plays an important role for the coupling between hard and soft magnetic phases. For t_0 , the saturation magnetization of the out-of-plane measurement is reached, because FePt is saturated due to perfect coupling to the Co soft magnet. However, the Co soft magnetic layer is saturated first and affects the $L1_0$ -FePt hard magnetic layer to saturate. This tendency can be seen by the in-plane result, since the slope (between 2 T and 4 T external field) is decreased by decoupling.

The coercive field increases with increasing decoupling, i.e. increasing Pt interlayer thickness, while the saturation polarization decreases only slightly with increasing total thickness (t_0 : 12 nm, $t_{0.5}$: 11.5 nm, t_1 : 12 nm and t_2 : 13 nm) and decoupling.

According to thickness of the interlayer, the coercive field of out-of-plane measurement increases from $H_C = 1.59$ T for t_0 (coupling to Co) to $H_C = 3.21$ T for t_2 (decoupling). For comparison: the pure 7 nm FePt in reference sample has a coercive field of 4.14 T. With increasing interlayer thickness two magnetic phases develop with a kink (two steps hysteresis) in the out-of-plane measurement. By the hysteresis behavior, the coupling can be assumed to be perfectly, partially coupled and decoupled. All out-of-plane hysteresis curves at room temperature are compared in Fig. 6.4 a). The magnetic moment and the switching field distributions (SFD, dM/dH) are compared in Appendix B.2.

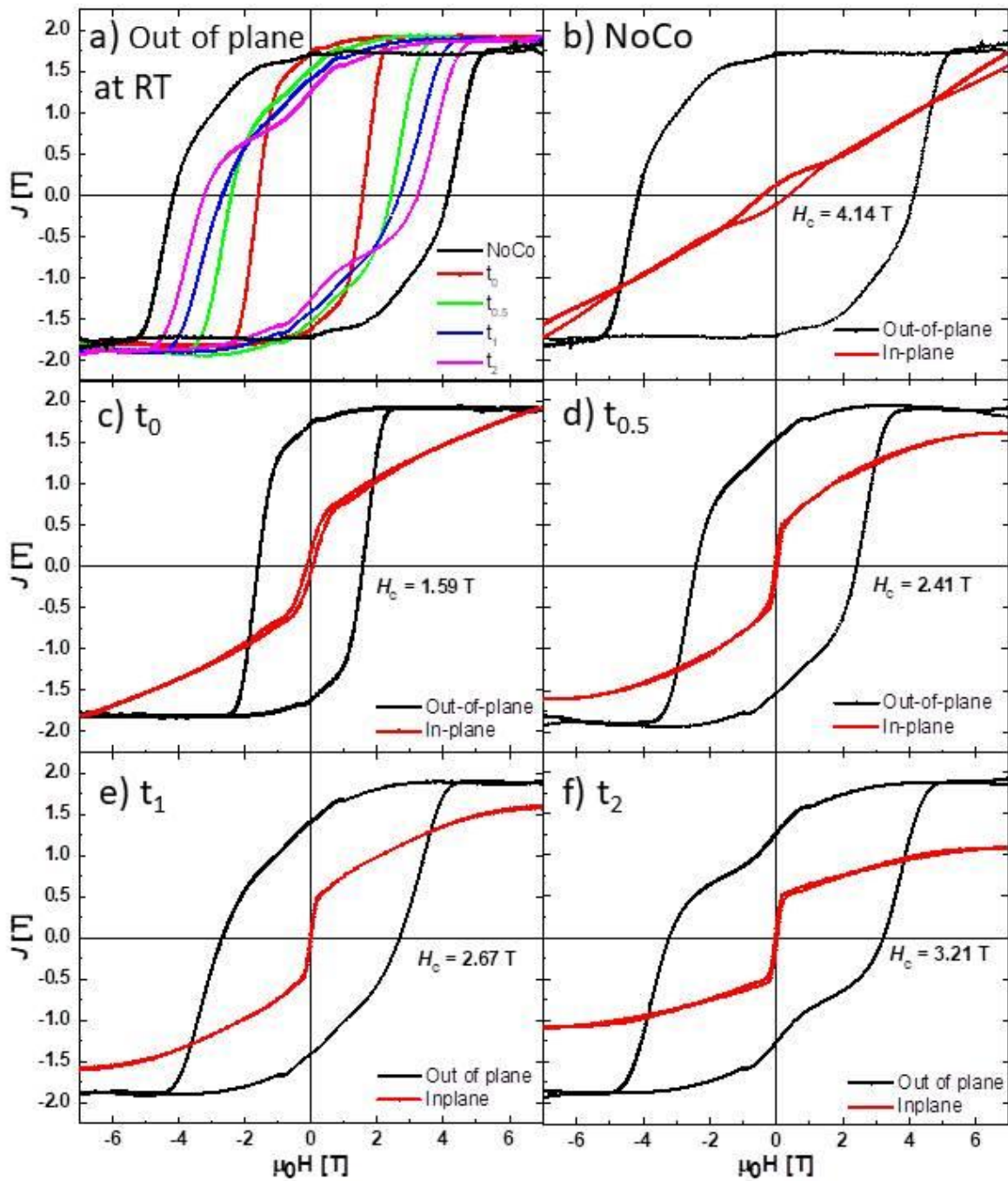


Fig. 6. 4 Hysteresis loops of magnetic polarization at RT. a) Comparison of hysteresis loops of $L1_0$ -FePt/Pt/Co/Pt exchange-spring multilayers and pure $L1_0$ -FePt on MgO(100) substrate in direction of out-of-plane at RT and b) the hysteresis loops of each samples in both direction of out-of-plane and in-plane measurements at RT.

6.2.1 Temperature dependence of hysteresis loops

The temperature dependence of the hysteresis curves are measured for all interlayer thicknesses in order to obtain the intrinsic and microstructural parameters at 50 K, 100 K, 150 K, 200 K, 250 K, 300 K and 350 K as shown in Fig 6.5. As the temperature decreases, the saturation magnetization and the coercive field increase, consistently. The coercivity of the reference sample (pure 7 nm FePt) could not be measured because the maximum external field of 7 T was not enough to obtain saturation at 50 K. it is assumed by extrapolation.

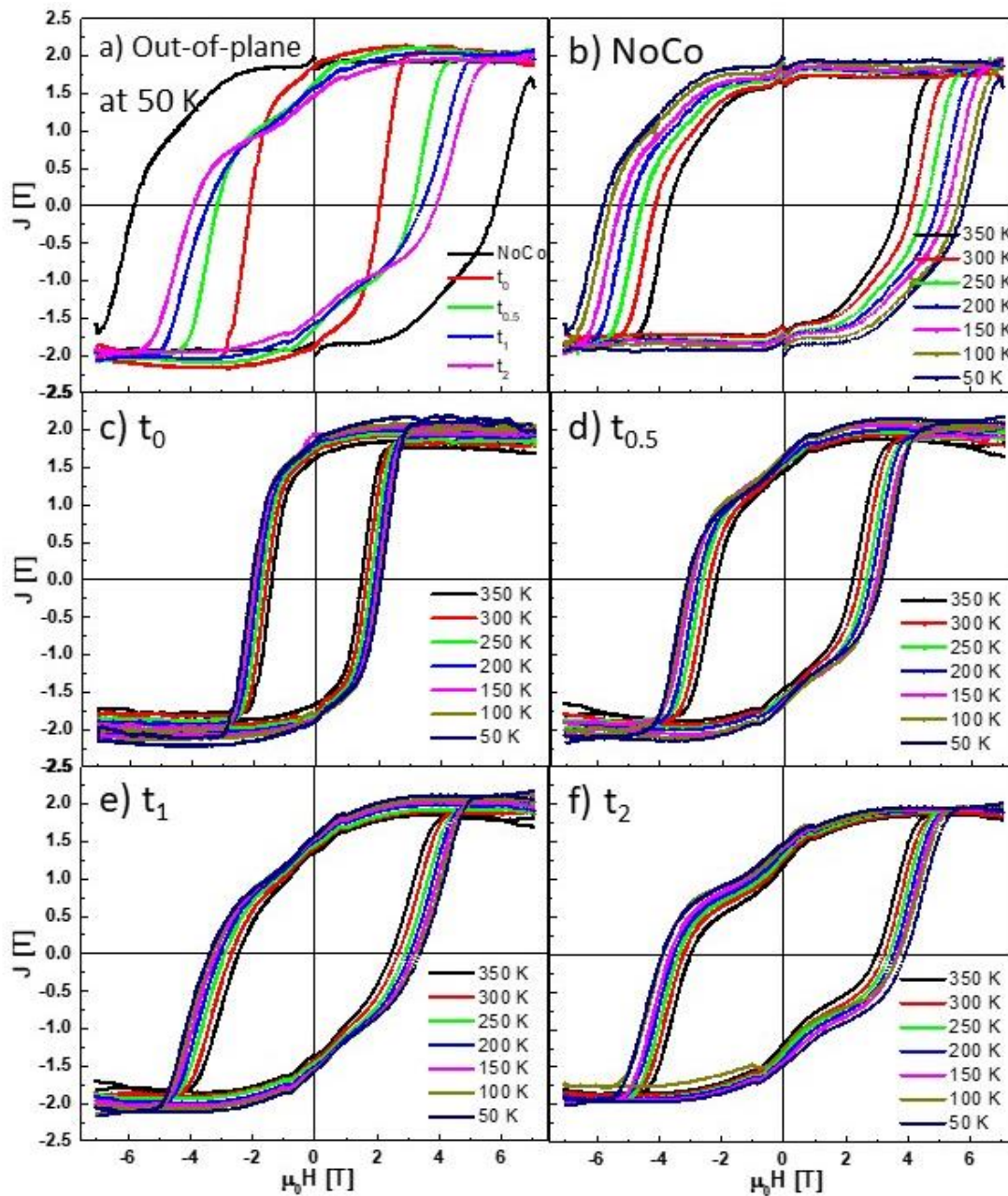


Fig. 6. 5 The temperature dependent hysteresis loops (magnetic polarization) of FePt/Pt/ Co/ Pt exchange-spring magnetic multilayers and FePt thin film on MgO(100) substrate. a) The out-of-plane hysteresis loops at 50 K and b-f) at a various temperature from 50 K to 350 K.

From these out-of-plane hysteresis, the temperature dependence of the coercive field and the saturation polarization are deduced. The coercive fields are in the range: $2.08 \text{ T} > H_C > 1.43 \text{ T}$ for t_0 , $3.1 \text{ T} > H_C > 2.19 \text{ T}$ for $t_{0.5}$, $3.37 \text{ T} > H_C > 2.45 \text{ T}$ for t_1 , and $3.9 \text{ T} > H_C > 2.99 \text{ T}$ for t_7 in the temperature range 50 K to 350 K. The decoupling apparently recovers the coercive field of the L10-FePt hard magnet. However, the temperature-dependent saturation polarization shows a smaller increase in the decoupled sample t_2 than in the coupled samples, i.e. it shows a hard-magnetic effect in the coupled samples. The Curie temperature of Co (1400 K) is much higher than that of FePt (660 K). If Co is not coupled to FePt, the Co soft magnet is almost saturated in the temperature range of the measurements, leading to the increase in saturation magnetization for better coupling. Fig. 6.6 shows the temperature dependence of the coercive field H_C and of the saturation polarization J_s for all samples studied in this part of the thesis

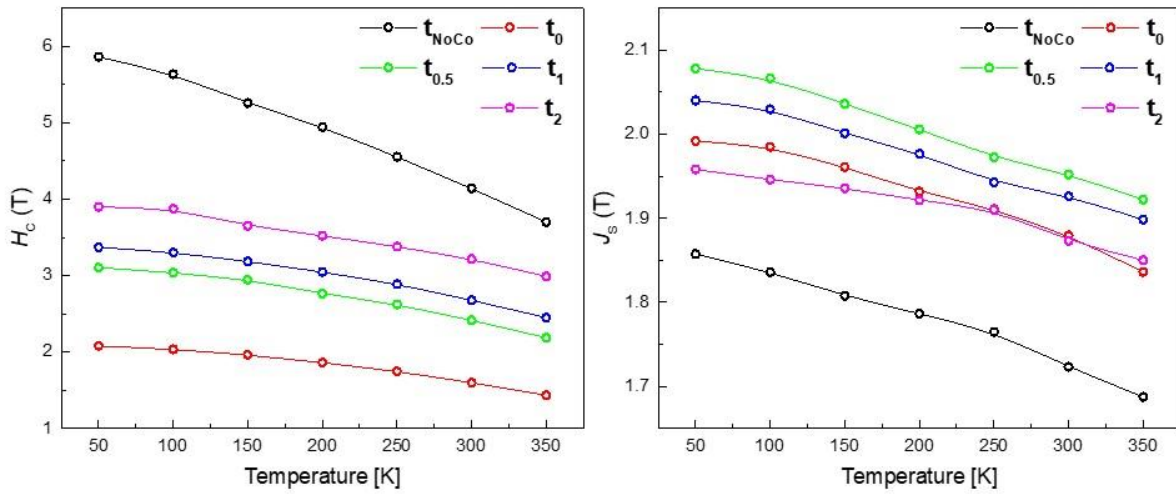


Fig. 6. 6 Temperature dependence of the coercive field H_C and the saturation polarization J_s of all samples used in this study

By comparing the out-of-plane and in-plane hysteresis curves of the multilayers, the temperature dependent magnetocrystalline anisotropy energy (MCA, K_u) could be determined. With the saturation magnetization and demagnetization factors of the hard and of the easy directions, the shape anisotropy (K_{shape}) was calculated. Temperature-dependent magnetic anisotropy constant K_1 values were obtained by the sum of these anisotropies (K_u and K_{shape}). The results for MAE as obtained from MCA and the shape anisotropy are shown in Fig 6.7. The MAE increases from perfectly coupling to decoupling due to the increasing influence of the hard magnet.

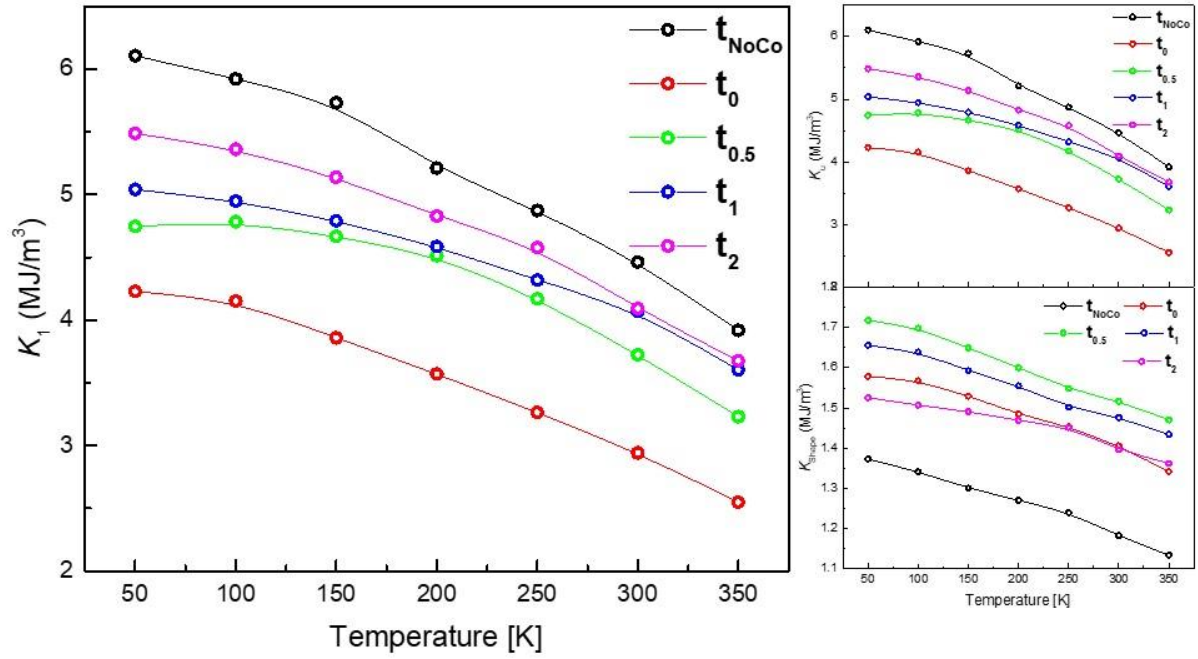


Fig. 6. 7 Temperature dependence of the magnetic anisotropy energy (MAE, K_1), the magnetocrystalline anisotropy energy (MCA, K_{eff}) and the shape anisotropy energy (K_{Shape}).

To obtain the spontaneous magnetization at temperature zero, $J_S(T)$ is plotted versus $T^{3/2}$ in fig. 6.8 for all samples. According to Bloch's law, the plots should give straight lines which is obviously fulfilled. From the slopes of the lines values for the characteristic temperatures T_0 are obtained. In the equation for the exchange stiffness $A(T)$ (equ. 4.18) $J_{S,0}$ and T_0 enter. From the relation, values for the exchange stiffness A were determined by use of the following values for $J_{S,0}$ and T_0 : t_0 : $J_{S,0} = -2.006$ T, $T_0 = -1852.68$ K, $t_{0.5}$: $J_{S,0} = -2.085$ T, $T_0 = -1864.7$ K, t_1 : $J_{S,0} = -2.047$ T, $T_0 = -1962.15$ K, t_2 : $J_{S,0} = -1.967$ T, $T_0 = -2354.02$ K and NoCo: $J_{S,0} = -1.863$ T, $T_0 = -1694.13$ K. For RT, the obtained values for the exchange stiffness are listed in Table 6.1.

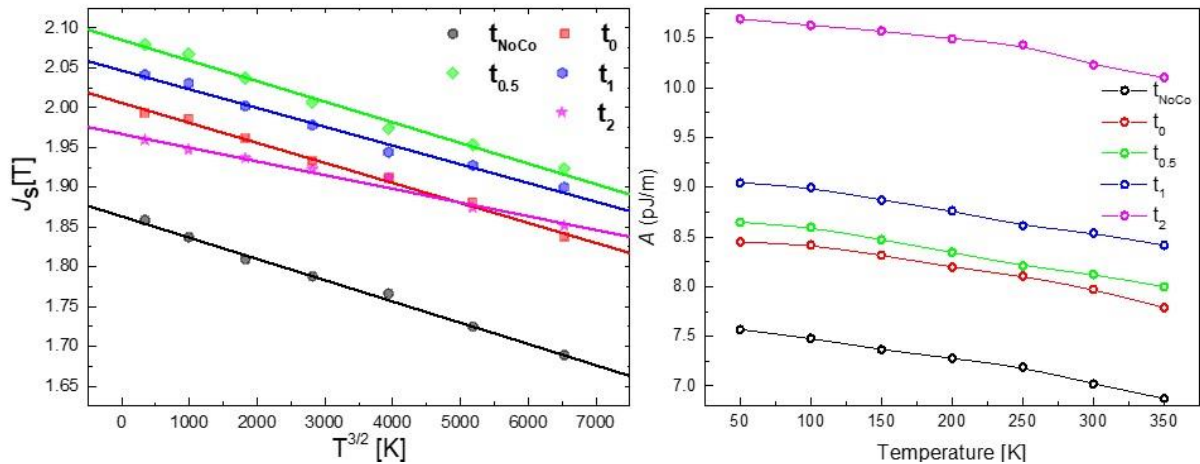


Fig. 6. 8 Left: Plots of the spontaneous magnetization versus $T^{3/2}$ according to Bloch's law, $J_S(T, 0) = J_{S,0} (1 - (T/T_0)^{3/2})$. Right: The exchange stiffness constant A can be determined by the relation of $J_{S,0}$ and T_0 (eqn.4.18).

The exchange stiffness A seems to depend on coupling (t_0 , $t_{0.5}$ and t_1) or decoupling (t_2). The domain wall energy γ , the exchange length l_K and the wall thickness δ can be obtained from values for MAE and A by use of the Eqn.(2.28). Fig. 6.9 shows the domain parameters γ , l_K and δ as a function of temperature.

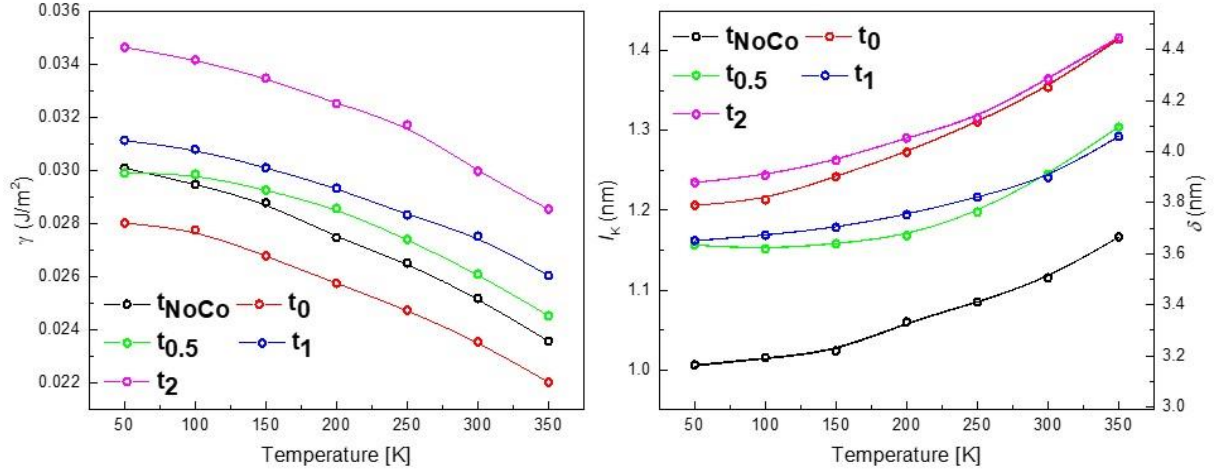


Fig. 6. 9 Temperature dependence of the domain wall energy γ , exchange length l_K and of the domain wall thickness δ . The domain parameters were obtained from MAE and A values.

For RT, the obtained exchange stiffness A , the wall energy γ , the exchange length l_K , the domain wall thickness δ and the critical domain diameter D_C (single-multiple domains) are listed in Table 6.1 for all samples.

	A [pJ/m]	γ [mJ/m ²]	l_K [nm]	δ [nm]	D_C [nm]
t_0	7.97	23.55	1.35	4.2	33.5
$t_{0.5}$	8.12	26.1	1.25	3.9	34.4
t_1	8.54	27.53	1.24	3.89	37.2
t_2	10.22	29.97	1.37	4.29	42.9
NoCo	7.02	23.6	1.12	3.5	42.6

Table 6. 1 Exchange stiffness A , the wall energy γ , the exchange length l_K , the domain wall thickness δ and the critical domain diameter D_C of all samples at RT

6.2.2 Micromagneticstructure parameters

The magnetic reversal mechanism of the samples can be described by universal relation (eqn.2.33) introduced in section 2.4.4. The plot of $H_C(T)/J_S(T)$ vs $2K_1(T)/J_S^2(T)$ at various temperatures gives information of microstructural parameter α and N_{eff} using the experimental results for the temperature dependent values of J_S and H_C .

Fig 6.10 shows plot that are used to determine the microstructural parameters α and N_{eff} .

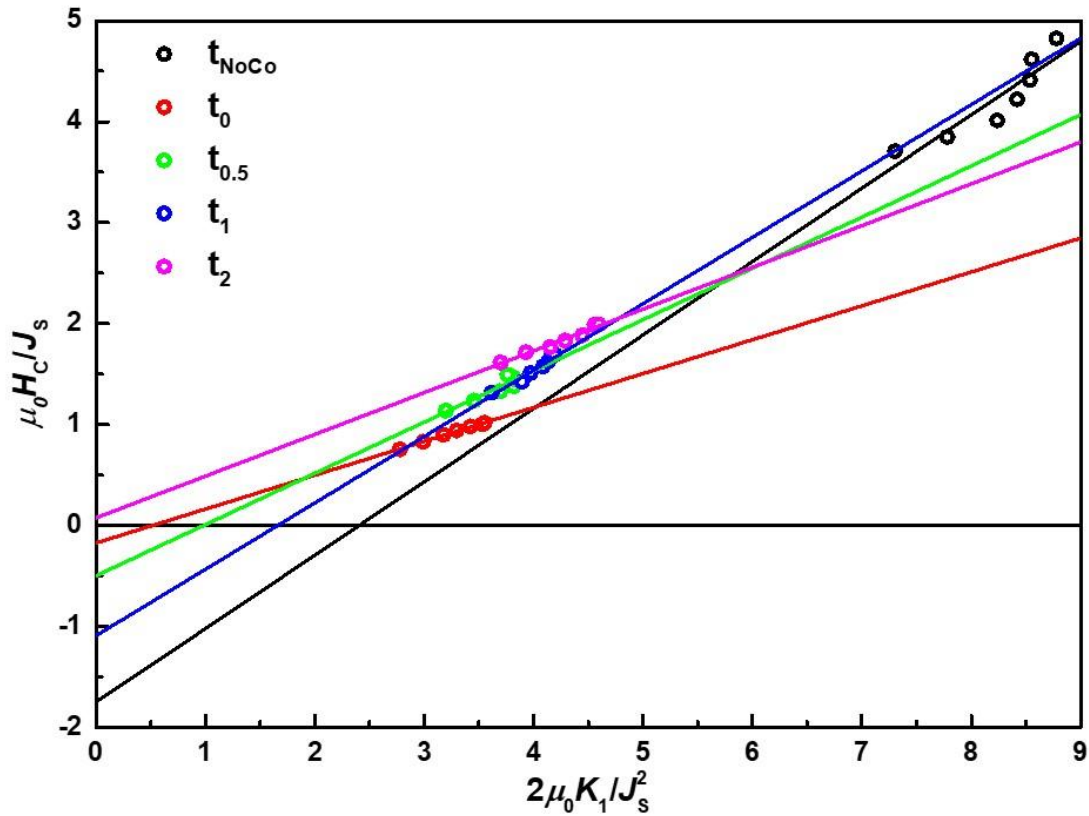


Fig. 6. 10 Plot to determine microstructural parameter α and N_{eff} , reference of 7 nm FePt (black), t_0 (red), $t_{0.5}$ (green), t_1 (blue) and t_2 (magenta), Inset: zoom in the data district.

The determined parameters α and N_{eff} are summarized in Table 6.2

	α	N_{eff}	α_K	α_{ex}
t_0	0.336	-0.173	0.815	0.412
$t_{0.5}$	0.507	-0.498	0.639	0.794
t_1	0.658	-1.091	0.526	1.251
t_2	0.414	-0.076	0.481	0.86
NoCo	0.918	1.93	0.999	0.918

Table 6. 2 The microstructural parameters α and N_{eff} of exchange-spring multilayers.

The microstructural parameter α is decreased with the reduction of coupling. However, the parameters of the decoupling samples t_2 are just the sum of the magnetic properties of both phases. In particular, the N_{eff} values show how the reduction of coupling releases the Co soft magnetic layer. It images the shape anisotropy and demagnetization of the soft layer.

6.2.3 Extended FORCs results

First-order reversal curves of the coupling-tuned exchange-spring nanomagnets were measured to study the effect of coupling on the interaction field and coercive field distribution at room temperature. The minor loops of FORCs are in Appendix B.3. The samples t_0 , t_1 , and t_2 were chosen as examples for perfectly coupling, partially coupling and decoupling, representatively. Moreover, irreversibility can be seen in extended FORCs at $H_C = 0$. The extended FORCs densities of the samples are shown in Fig. 6.11.

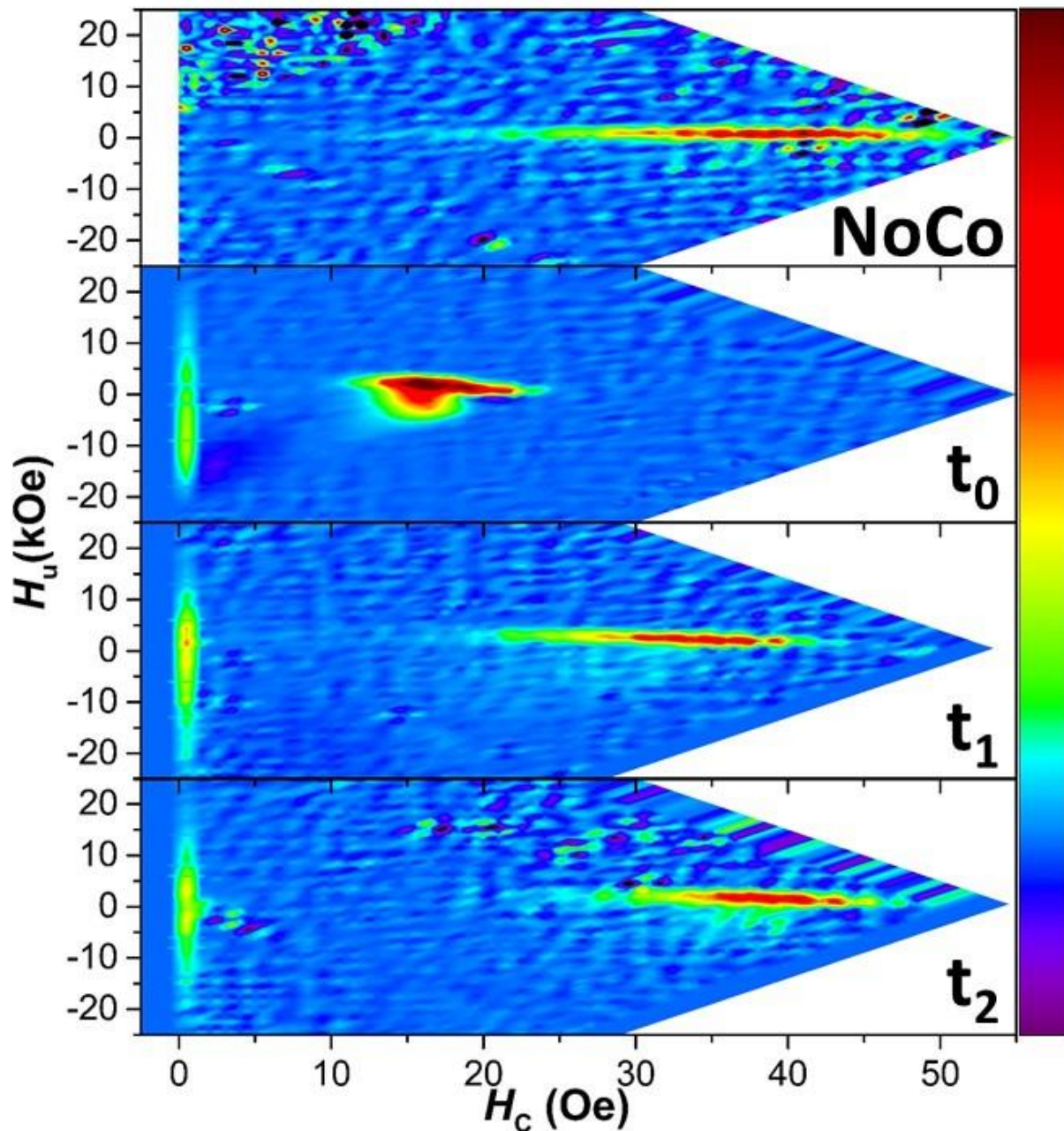


Fig. 6. 11 The extended first-order reversal curves density for the samples t_0 , t_1 and t_2 . The perfect coupling of sample t_0 can confirm with a combination of distributions (top), In FORCs density of sample t_1 , a strong irreversibility and broad distributions are seen (middle). A separation in the density distribution is found in sample t_2 (bottom).

The FORCs density also explains for exchange coupling between magnetically hard and soft phases. First of all, the ridge of interaction field at $H_C = 0$ moves from t_0 : -0.52 T, t_1 : -0.12 T to t_2 : 0.01 T. The movement has followed a shift of the reversal field range of the Co soft layer by coupling strength. Each magnetic property of the $L1_0$ -FePt hard and the Co soft layer is recovered by separation from each other. Especially, the coercive field distribution of the perfectly coupled sample, t_0 is along with a broader interaction field (~ 3800 Oe) than others (t_1 : ~ 2400 Oe, t_2 : ~ 2900 Oe). The coercive field distributions also move and broaden due to decoupling. The coercive field of the hard magnet has been reduced by the soft magnetic layer. However, the coercivity behavior of the soft magnet follows the hard magnet in sample t_0 . The coercive field of decoupling sample t_2 shows a separation of both phases. Especially, the partially coupled exchange-spring magnet t_1 has a broader coercive field distribution between the two phases with higher reversibility. The coercive field distribution at $H_u = 2500$ Oe (maximum intensity) and the interaction field distribution at $H_c = 500$ Oe are shown in Fig. 6.15 and FWHM values of the distributions are summarized in Table 6.3. Additionally, the reversibility was calculated in Appendix B.4

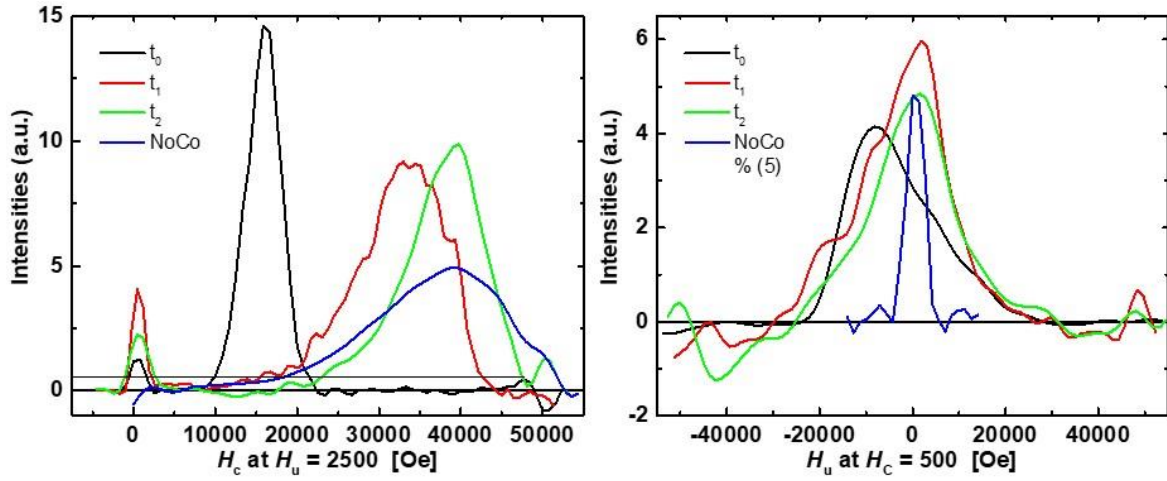


Fig. 6. 12 The coercive field distribution at $H_u=2500$ Oe and the interaction field distribution at $H_c=500$ Oe. Those fields are determined from the position of the maximum intensity.

FWHM [Oe]	H_c	H_c	H_u	H_u	H_c Center	H_u Center
	at $H_u=2500$, ρ_{max}	at $H_u = 0$	at $H_c = 500$, ρ_{max}	at $H_c = 0$	at $H_c = 2500$, ρ_{max}	at $H_c = 500$, ρ_{max}
t_0	~ 5100	~ 2000	~ 3800	~ 21200	15800	-5200
t_1	~ 13200	~ 1900	~ 2400	~ 18400	33700	-1200
t_2	~ 10300	~ 2700	~ 2900	~ 17900	39750	100
t_{NoCo}	~ 18600	-	~ 4800	-	38000	1400

Table 6. 3 The FWHM values of the coercive field and the interaction field and moving the distribution center by coupling degree.

6.2.4 XMCD results

The three samples (t_0 , t_1 and t_2) were chosen for X-ray magnetic circular dichroism (XMCD) measurements in the TEY mode. In the reference sample, the pure FePt grains are perfectly isolated each other. Therefore XMCD cannot be measured. A XMCD study of this reference sample, covered by a conducting material, will be shown in chapter 7. The three samples studied (t_0 , t_1 and t_2) have a good enough conductivity for TEY mode measurement.

All XMCD experiments were performed at the WERA beamline of the ANKA synchrotron in Karlsruhe. The XMCD spectra were measured at Fe $L_{3,2}$ -edges (690 eV to 750 eV) for the hard magnetic and at Co $L_{3,2}$ -edges (760 eV to 840 eV) for the soft magnetic component in a saturation field of ± 4 T for t_0 and ± 6 T for t_1 , t_2 at RT. To study of the anisotropy, in normal incidence (NI) geometry and at 60° measurements were undertaken. All spectra were corrected for self-absorption (saturation effect for thin film in the TEY mode) and Pt peaks (there are Pt absorption peaks in raw spectra and not visible in fig.6.16). All spectra are clear from oxidation peak, since the Pt layer works well for protection and conductivity. To confirm the shapes of the Fe spectra, we also measured 40 nm FePt forming a closed layer (see Appendix B5).

XAS and XMCD spectra (normal incidence) at the Fe $L_{3,2}$ -edge and the Co $L_{3,2}$ -edge are shown in fig.6.13 for three interlayer thicknesses.

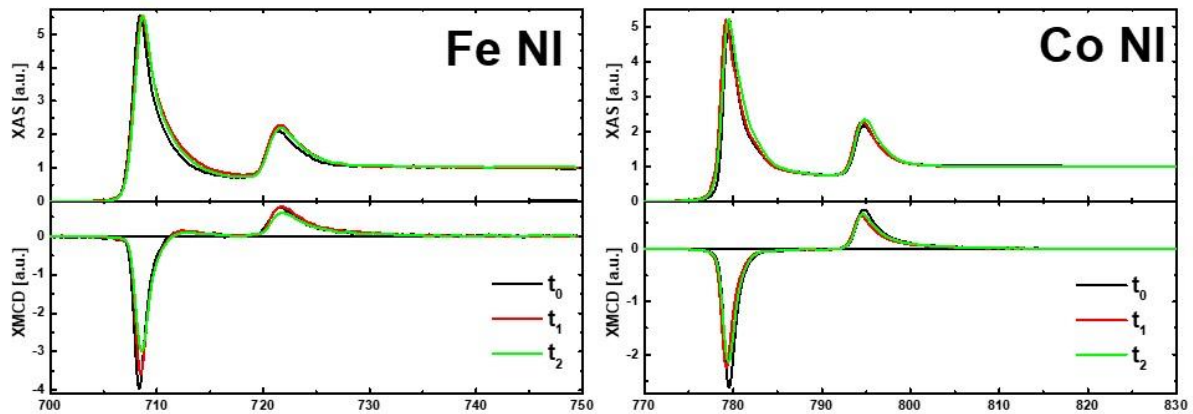


Fig. 6. 13 Normalized XAS and XMCD spectra of exchange-spring multilayers (t_0 , t_1 and t_2) at the Fe $L_{3,2}$ -edges and the Co $L_{3,2}$ -edges at RT in saturation field and at normal incidence. The spectra were corrected for self-absorption and Pt peaks.

Despite of the correction of the self-absorption, the Fe spectra of the t_2 sample shows the smaller XMCD. The t_0 sample has the highest dichroism intensity. It is assumed that it contains a softer magnetic region in an $L1_0$ -FePt layer with higher magnetization. The intensities of Co spectra are depending on the thickness of protection layer, despite of the Pt peaks correction. To obtain spin and orbital magnetic moments from the data by applying the Sum Rules, a step function and polarization degree of X-rays of 81% for Fe and 84 % for Co were applied. The number of holes n_h is taken 3.705 for Fe and 2.49 for Co.[12, 134]

The sum rules results of spin, orbital, total magnetic moments and m_l/m_s ratio are summarized in Table 6.4, and Fig. 6.14.

NI		m_s [μ_B]	m_l [μ_B]	m_{total} [μ_B]	m_l/m_s ratio
	Ref. 40 nm	2.21	0.25	2.47	0.11
Fe	t_0	2.63	0.19	2.81	0.07
	t_1	2.51	0.22	2.73	0.09
	t_2	2.28	0.26	2.54	0.11
Co	t_0	1.84	0.22	2.06	0.12
	t_1	1.44	0.18	1.61	0.12
	t_2	1.42	0.16	1.58	0.11

Table 6. 4 The Sum Rules results of XMCD measurement at normal incidence: Spin, orbital and total magnetic moment and the ratio of orbital to spin moments.

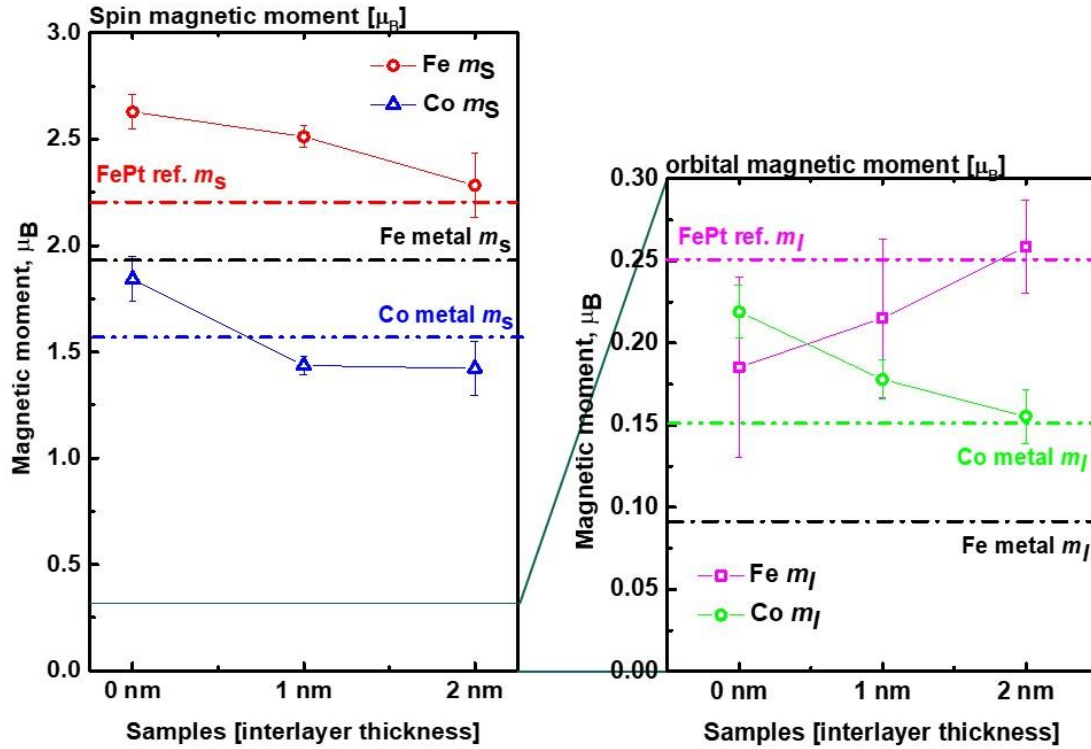


Fig. 6. 14 Sum Rules results of tuned exchange-spring multilayers. The perfectly coupled ES magnet has enhanced spin magnetic moment. The orbital moment of Fe is reduced, while the orbital moment of Co is increased by coupling.

The Fe results a tendency can be seen due to coupling. The 40 nm thick FePt sample was measured and analyzed with the result: m_s : 2.21, m_l : 0.25, m_{total} : 2.47 and m_l/m_s ratio: 0.11. The Fe result in exchange-spring magnets has higher spin moment than bulk (40 nm thick) of pure FePt. The coupling apparently generates a larger stray field, like a bulk sample. The Co results of the perfectly coupled sample t_0 and decoupled sample t_2 can be understood by coupling effects. It can be assumed, that the Co soft magnetic region in partially coupled sample has two regions. One of the parts is coupling to the near edge of the hard magnet, while the other part far away from the hard magnet at the top of the Co layer is decoupled. In this situation, the two parts can compete for the out-of-plane magnetization direction.

A result of the same propensity is shown in angle-dependent measurement on sample t_1 sample, too. The angle dependent measurements have been performed to investigate the anisotropy and the T_z term of dipole moment. The results indicate a rather small T_z value. The results of the angle dependent measurement were put in Appendix B.6.

6.2.5 Hysteresis with XMCD

The advantage of XMCD is that one can do element specific measurement. This is in particular helpful to understand the coupling behavior. By this method, the magnetic reversal process for the Fe and Co moment can be observed directly. Appendix B. 7 shows normalized hysteresis curves of Fe, Co and SQUID measurements and how they can be used together with that the total number of atoms and the total magnetic moments to reproduce the hysteresis loops.

By these hysteresis results, the magnetic reversal process can be modeled directly. The magnetic reversal process of the hard and soft phase in perfectly coupled exchange-spring multilayer t_0 shows that the magnetization of both metals, Co and Fe, proceeds almost in parallel. The reversal process of the partially coupled sample t_1 displays connection between both phases. The Co soft magnetic layer starts somewhat earlier to reverse; the FePt hard magnetic layer follows. Moreover, before 180° flips of the soft magnet, the hard magnet reaches to coercive field. In contrast, the reversals of two phases in the decoupling sample t_2 proceed almost independently. Fig. 6.15-17 is shown an illustration of assumed magnetization reversal process as derived from the XMCD hysteresis loop results.

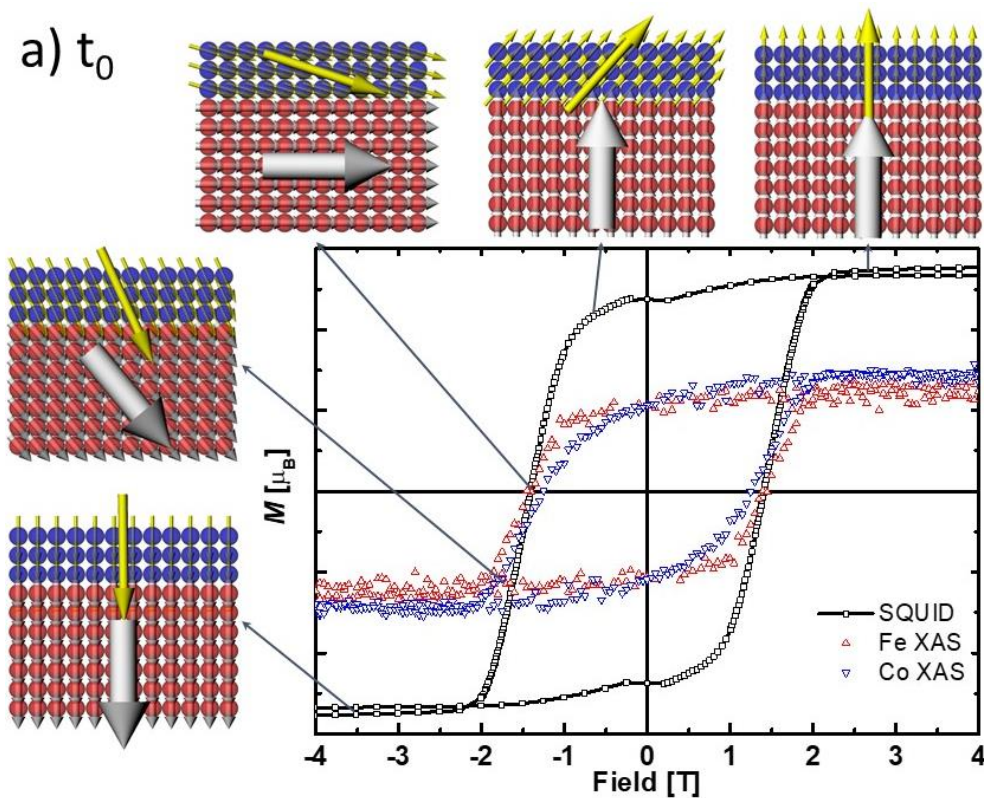


Fig. 6. 15 Illustration of magnetic reversal process in $L1_0$ -FePt/ Co /Pt exchange-spring multilayer, t_0 . The reversal of both magnetic phases proceeds almost parallel.

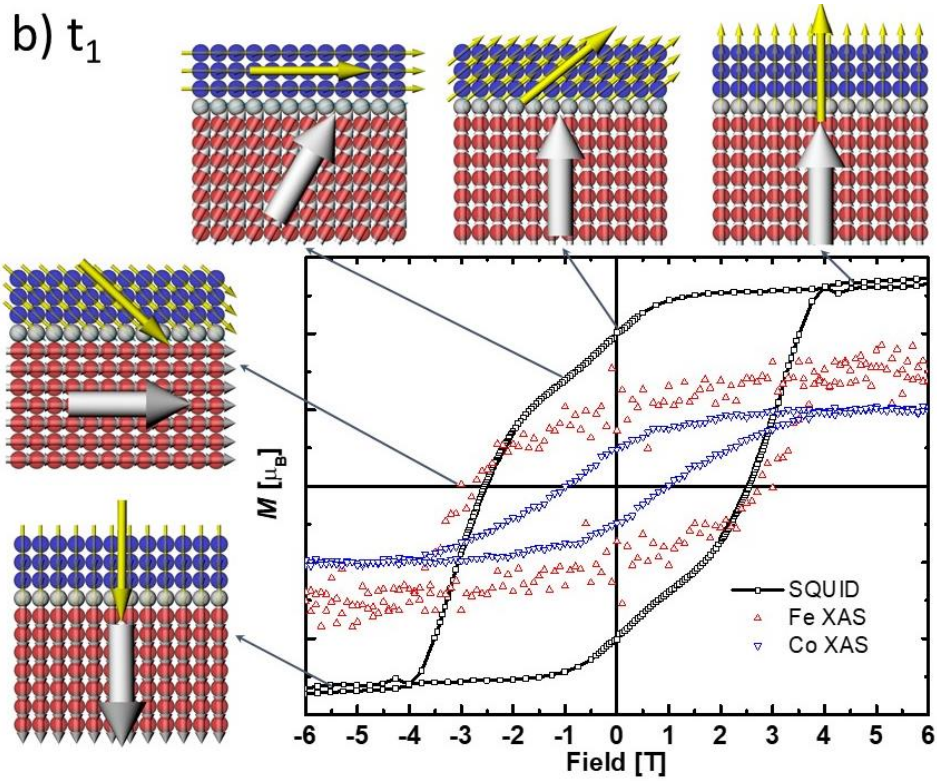


Fig. 6. 16 Illustration of magnetic reversal process in L_{10} -FePt/ Pt/ Co/ Pt exchange-spring multilayer, t_1 . The reversal of the Co soft layer starts earlier than that of the L_{10} -FePt hard layer. However, hard magnet follows to reverse, soon.

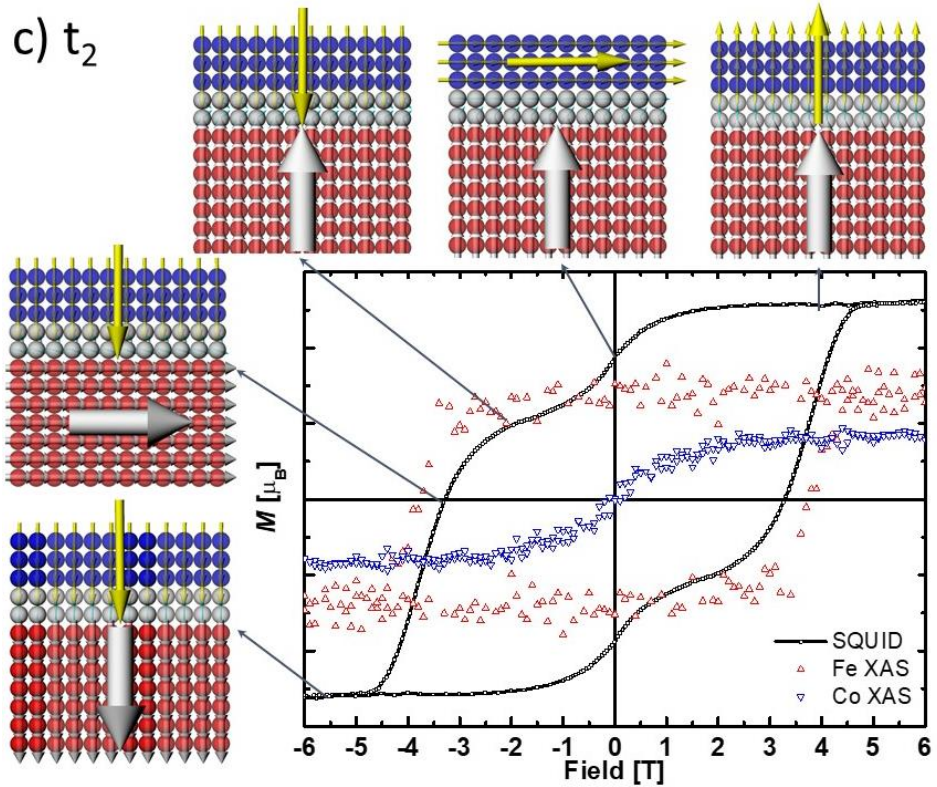


Fig. 6. 17 Illustration of magnetic reversal process in L_{10} -FePt/ Pt/ Co/ Pt exchange-spring multilayer, t_2 . The reversal of the Co soft and the L_{10} -FePt hard layers proceed almost individually.

6.3 Conclusion: Influence of the thickness of a Pt interlayer between a L1₀-FePt hard and a Co soft magnetic layer on the magnetic behavior of exchange-spring nanomagnets

Granular nanostructured 7 nm L1₀-FePt/ x nm Pt/ 3 nm Co/ Pt ($x = 0, 0.5, 1$ and 2) exchange-spring multilayer magnets with various thicknesses of Pt interlayer were obtained by magneto sputtering on a MgO (100) substrate at 800°C. The Pt and Co layers were deposited at RT. The nanomagnets were investigated by detailed SQUID measurement, by which the micromagnetic parameters are deduced. Element specific XMCD measurements have been studied, the spin- and orbital moments have been deduced and the element hysteresis determined. According to the tuned exchange-coupling strength (tuned by the thickness of the interlayer), the magnetization reversal and the magnetic anisotropy show prominent changes.

The thickness of the interlayer can regulate the exchange-coupling strength between the magnetically hard and soft magnetic layers. It can be adjusted to provide perfect coupling, partial coupling and decoupling. Perfectly coupled exchange-spring multilayer exhibit a one-step hysteresis loop without a kink, fully decoupled multilayer has a two-steps hysteresis loop with kink. The following statements could be made:

1. The size of the nanograins (real grain diameter: d) is similar to the critical domain size (critical domain diameter: D_C). The real grain size is obtained by SEM image. d are from 34 nm to 56 nm and D_C are from 34 nm to 43 nm.
2. The microstructural parameter α and N_{eff} obtained from the magnetic hysteresis loops at various temperature reveal the coercive mechanism. The reason for the reduction of the coercive field when compared to the theoretical expected value can be understood from the change of the parameter α . Moreover, demagnetization also reduces the coercive field. The effective demagnetization factor, N_{eff} depends on the exchange coupling between two phases.
3. The extended FORCs density shows the extent of the exchange-coupling and irreversibility. The variation of the coercive field distribution and the interaction field distribution with different coupling indicates magnetic reversal and that there exists a distribution of various hysterons.
4. The spin, orbit and total magnetic moments are analyzed by Sum Rules calculation of XAS and XMCD spectra. The obtained total moments are adjusted to normalized elements specific hysteresis loop with the total number of Fe and Co atoms. We observe the expected increase of the Fe spin and orbital moment as well as the m_l/m_s ratio. The SQUID hysteresis can be well explained by XMCD hysteresis for Fe and Co taken at the L₃-edge. It is helpful to understand the magnetic reversal process in exchange-spring multilayers.

Chapter 7

Results: Realized high coercive field and maximum energy product $(BH)_{\max}$ with ultra-hard nanomagnets

Since a view decades $L1_0$ chemically-ordered FePt has been investigated and discussed as rare-earth free hard magnet, as component in exchange-spring magnets and in terms of application as excellent candidate for ultra-high density information storage media. In this study, the control and especially the increase of coercive field and energy product in FePt thin film of the nanogranular structure is addressed. This was already subject of many of groups, since from theoretical calculations $L1_0$ -FePt about 12 T coercive fields and with a huge magnetocrystalline anisotropy of 6.6 MJ/m^3 have been predicted in the thin film system.[135] However, the reported experimental coercivity, H_C in similar systems one of third from the expected value.[97] The main reason for the small coercive field is assumed from oxidation and amorphous FePt component on surface and distortion of crystal structure by lattice mismatch with the substrate.

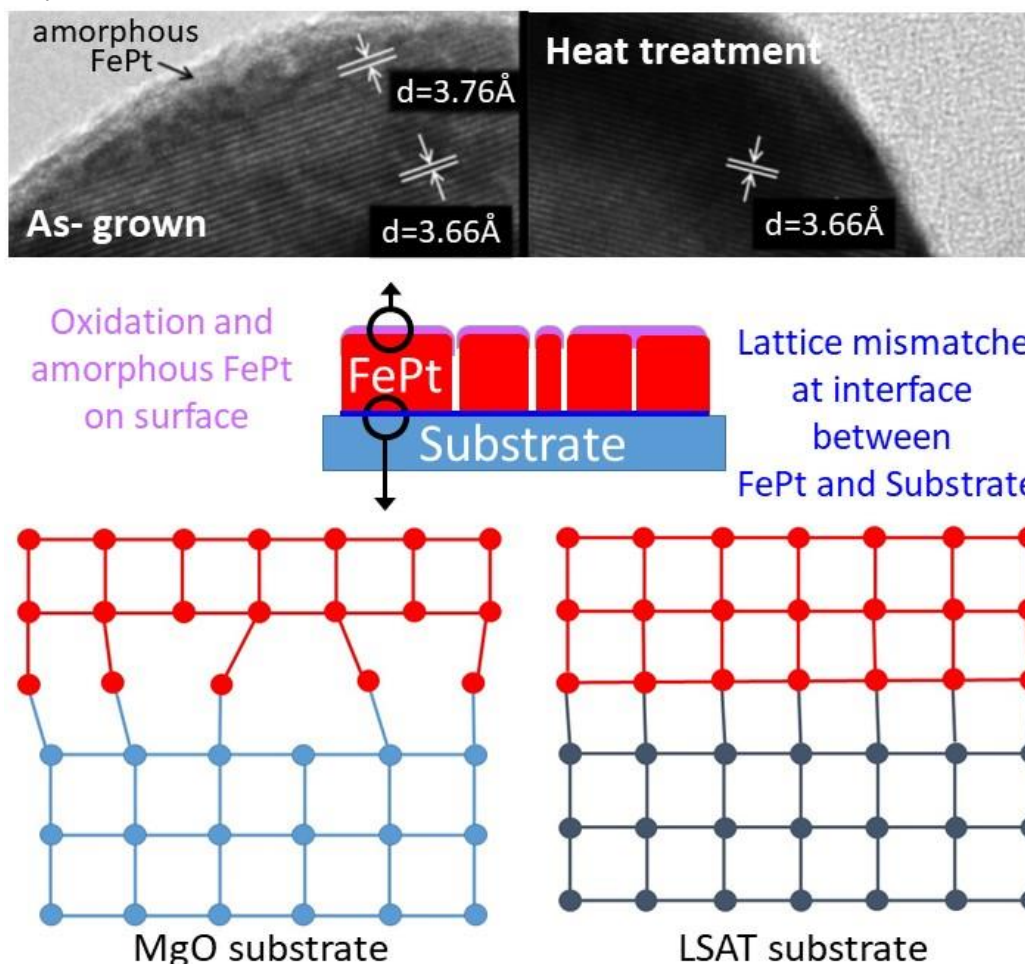


Fig.7. 1 The idea of reduction of coercive field. Oxidized material on the surface, and the lattice mismatch at the interface between FePt and substrate can contribute. To solve those problems, after grown the FePt on MgO(001) substrate, films were post-annealed at 800°C for 1 hour. To reduction lattice mismatch, also LSAT can be chosen as substrate. The lattice constant of MgO is 4.212 \AA and of LSAT is 3.87 \AA . The lattice constant a of $L1_0$ -FePt is 3.85 \AA .

To further increase the coercivity, we applied and compared two types of methods. One is heat treatment (post-heating) with quenching (rapid cooling) and the other is a selection of a better substrate in terms of lattice match. Fig.7.1 illustrates the influence of heat treatment and lattice mismatches.

This three kinds of samples were prepared by Magneto co-sputtering. We chose a layer thickness of 7 nm because which shows the highest coercivity as determined in previous work in our group.[133] Crystal structure and morphologies were confirmed by x-ray diffraction (XRD) patterns and scanning electron microscopy (SEM). Magnetic properties were studied with superconducting quantum interference device (SQUID) magnetometry. For X-ray magnetic circular dichroism (XMCD) investigation at the Fe- L- edges, new samples were prepared and covered with 3 nm of Au capping layers to provide conductivity of the sample and as oxidation protection.

7.1 L1₀-FePt island structure

Uncovered sample

L1₀-FePt (fct: face-centered tetragonal) has lattice constants a : 3.85 Å and c : 3.71 Å. The lattice constant of MgO (100) substrate is a : 4.212 Å resulting in a considerable lattice mismatch. In contrast, the lattice constant of LSAT (LaAlO₃)_{0.3}-(Sr₂AlTaO₆)_{0.7} (100) substrate provides with 3.87 Å much better match. FePt films were prepared by Magneto co-sputtering Fe and Pt targets directly onto single crystalline MgO (100) substrates and LSAT (100) substrate commercially fabricated by CrysTec in Ar atmosphere, (base pressure: 3×10^{-8} mbar, Ar pressure during sputtering: 5×10^{-3} mbar). The substrates were heated to 800 ° C during sputtering for the hard magnetic L1₀-FePt film with out-of-plane texture. After deposition, the chamber temperature of 800 ° C was kept for one hour in vacuum. The composition of FePt thin films has been adjusted with tuning the sputtering power of Fe and Pt. It is determined to be Fe₅₁Pt₄₉ with electron probe X-ray microanalysis (EPMA).

The first sample is as grown on MgO substrate. FePt can be perfectly formed in the L1₀-phase at 800 ° C deposition temperature. During decreasing of temperature; the phase can be distorted at the interface between FePt and MgO substrate while atoms set equilibrium points according to temperature. The distorted phase influences to magnetic properties.

The second sample was prepared the same way with the first one. Additionally, FePt thin film on MgO substrate was post-heat treatment with a heating parameter of 800 ° C in Ar atmosphere for 1 hour. The heat treatment the sample was quenched (rapid cooling). The quenching process does not give enough time to thermos-equilibrium of FePt to the substrate and can hold the L1₀-phase of FePt. Moreover, some oxidized FePt layer on the surface also vanished.

The third sample was deposited on LSAT (100) substrate also at 800° substrate temperature without further heat treatment. The distortion of FePt at the interface is expected to be significantly reduced due to the better match of the lattice constants.

These three samples are called MgO, Heat, and LSAT, respectively.

Au covered sample

Au covered samples were prepared for XMCD measurement. The 7 nm thick $L1_0$ -FePt on MgO (100) substrate and LSAT (100) substrate were deposited with the same condition. In addition a 3 nm Au layer were magnetron sputtered at room temperature. The 3 nm Au capping layers give conductivity and protect from oxidation. However, the heat treated sample is assumed to formed few nanometer dilutions at the interface between FePt and Au.

These three samples are called Au MgO, Au Heat and Au LSAT, respectively.

7.1.1 Crystal structure

To verify ordering of samples, X-ray diffraction (XRD) were measured. In fig. 7.2, XRD patterns of samples show 001 (at $\sim 24^\circ$), 002 (at $\sim 49^\circ$) and 003 (at $\sim 76^\circ$) peaks of FePt and substrate peaks $\sim 42^\circ$ for MgO (002) and $\sim 46^\circ$ for LSAT (002). The peak of LSAT substrate is closer to FePt (002) peak than MgO substrate peak. Long-range chemical ordering parameter S of $L1_0$ -FePt films has been calculated with XRD spectra. All of the samples are well ordered. Heat treatment gives the highest ordering with S value of 0.91 and LSAT sample also has quite high S parameter with $S = 0.9$. The ordering parameter of MgO sample is also good with $S = 0.86$.

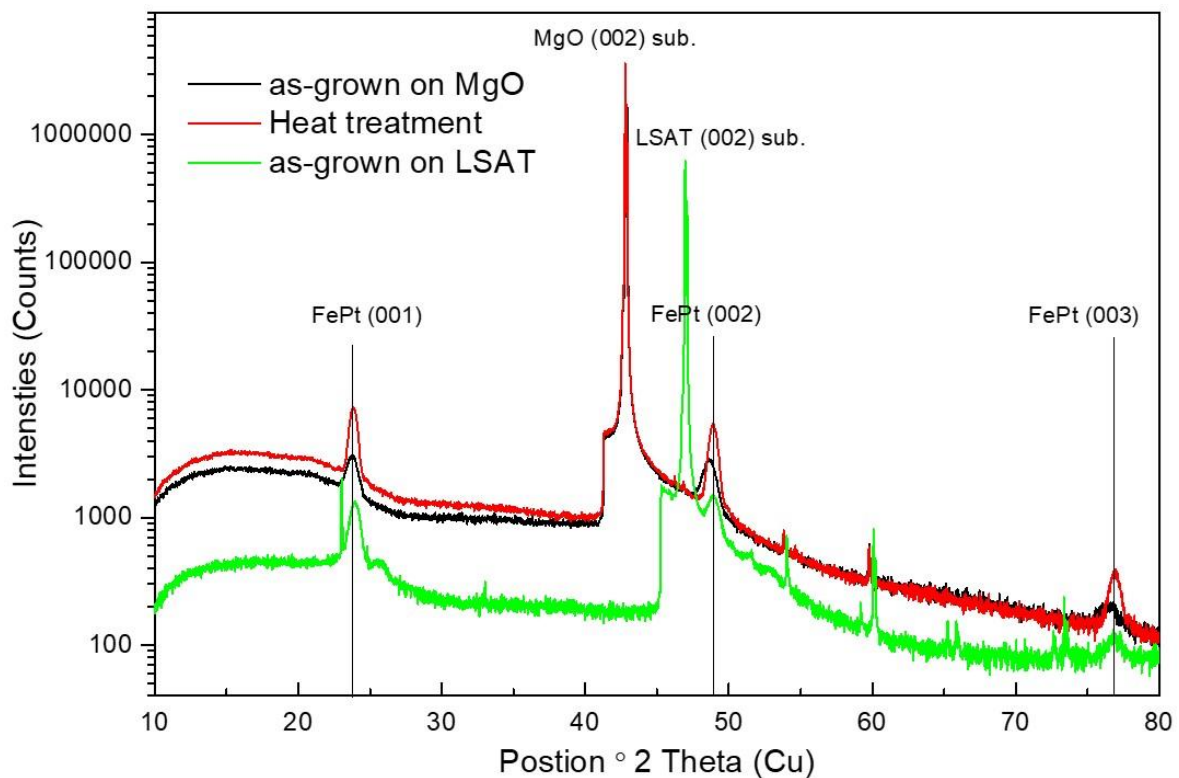


Fig.7. 2 X-ray diffraction patterns of as-grown on MgO (black), heat treatment (red) and as-grown on LSAT (green). All of the samples are shown FePt 001, 002 and 003 peaks. It formed $L1_0$ -phase (fct). Chemical ordering parameter $S = 0.86, 0.91$ and 0.90 respectively.

7.1.2 Morphology

In Fig. 7.3 scanning electron microscopy (SEM) images are presented, from which the distribution and the particle diameter can be deduced which are also shown in Appendix. C.1. The packing ratios are quite different despite the same thickness obviously by lattice mismatch. The packing ratios are 58.6% for MgO, 53.8 % for Heat and 56.4% for LSAT. Au covered samples are 3 nm thicker and more packed than uncovered samples. The packing ratios are obtained 65.0% for Au MgO, 60.6% for Au Heat and 62.2% for Au LSAT. The grains of samples are well separated expect the Au Heat system which some interconnection seems to be present. MgO has bigger diameter with $d_{avg} = 55 \pm 17$ nm and similar distribution with Heat. The Heat and LSAT show well separated grains with a broader diameter distribution with a similar with average value $d_{avg} = 48 \pm 17$ nm for Heat and $d_{avg} = 43 \pm 22$ nm for LSAT.

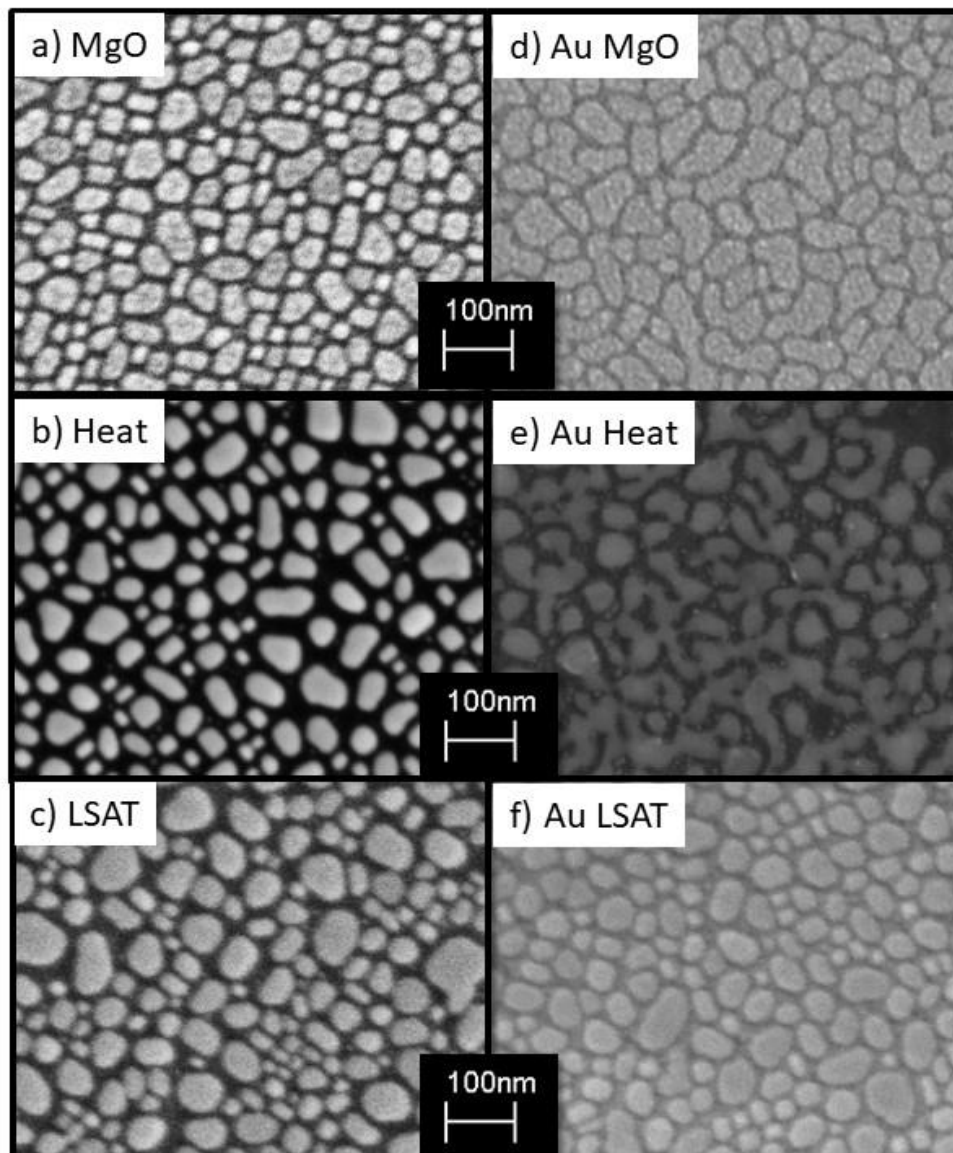


Fig.7. 3 SEM images and particle size distributions of (a) as-grown on MgO, (b) heat treatment on MgO and (c) as-grown on LSAT. Both of as-grown samples on MgO and LSAT have bigger size grains. Samples of heat and LSAT with fewer rate mismatches have small size grains

7.2 Characterizations of magnetic properties

7.2.1 Magnetic hysteresis curves

The magnetization hysteresis loops with out-of-plane and in-plane direction were measured at room temperature proving that all of the samples have huge anisotropy with the magnetization preferential to out-of-plane (Fig. 7.4 (a-c)). In-plane curves of as-grown MgO and LSAT samples indicate small in-plane easy axis component. Especially, the in-plane curve of heat sample shows perfectly proportional slope behavior. In the possible maximum field of 7 T only the MgO sample has reached saturation. Therefore an additional hysteresis measurement was performed to LSAT sample using a using 14 T physical property measurement system (PPMS) (see the blue line in fig.7.4 c)). It can be saturated above 7.5 T field. Hysteresis loops of Au covered samples are shown with initial curve in fig. 7.4 (d-f). Hysteresis loops without Au capping layer indicate tiny two phases with two steps shape. The results with capping layer cannot be seen any step. It is surmised that capping layer protects the surface of FePt. The results show that the coercivities are smaller than without capping layer, but obviously the saturation magnetization is increased considerably (increased 7 % for MgO, 15 % for Heat and 18 % for LSAT, it summarizes in table7.1).

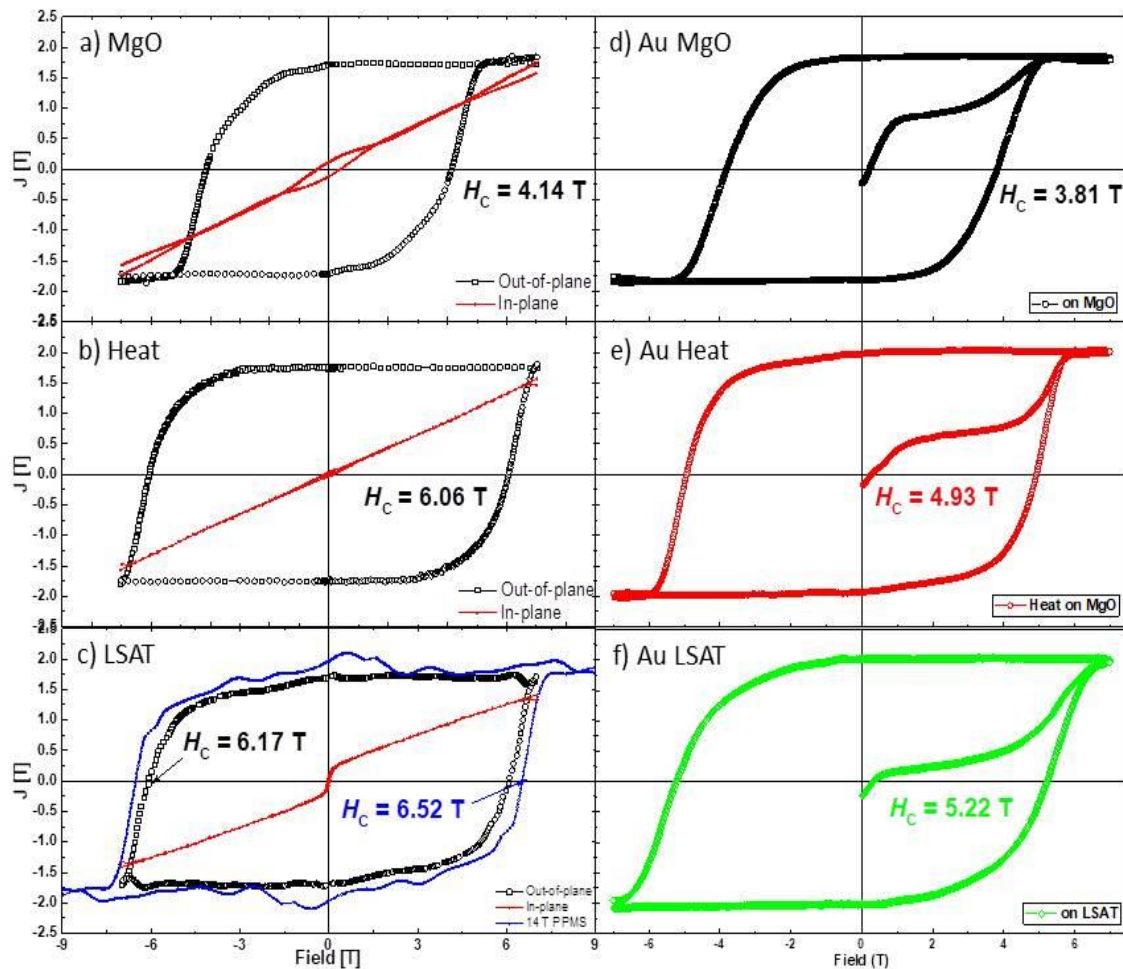


Fig.7. 4 Out-of-plane (easy-axis) and In-plane (hard-axis) hysteresis loops of a) MgO b) Heat and c) LSAT samples. Out-of-plane hysteresis loops hysteresis loops of d) Au MgO, e) Au Heat and f) Au LSAT at RT.

To determine magnetocrystalline anisotropy, the difference of magnetization curve between out-of-plane and In-plane directions was used, the shape anisotropy was determined by demagnetizing factor and magnetization. As expected by results of in-plane magnetization curves, the heat sample without Au has highest magnetic anisotropy energy. The magnetic properties are set in table 7.1.

Sample	H_c [T]	J_s [T]	K_1 [MJ/m ³]	$(BH)_{max}$ [MGOe]
MgO	4.14	1.72	5.644	65.7
Heat	6.06	1.76	6.618	75.6
LSAT	6.17	1.72	6.087	73.6
Au MgO	3.81	1.85	-	80.2
Au Heat	4.93	2.03	-	92.2
Au LSAT	5.22	2.03	-	97.1

Table 7. 1 The coercivity, saturation polarization, magnetocrystalline anisotropy energy and maximum energy product of 7 nm FePt and 7 nm FePt/ 3nm Au samples.

We tried to measure hysteresis loops from 50 K to 350 K temperature for the microstructural parameter. However, the heat and LSAT samples have a coercivity of 6 T at room temperature. The maximum magnetic field of 7 T is not enough to saturate at low temperature. Only for the MgO sample the hysteresis loops could be measured in the temperature range of 50 K to 350 K. The microstructural results were shown in Chapter 6 for a reference sample of exchange spring magnet. The initial magnetization curves study is shown in Appendix. C.2.

7.2.2 Energy product

The corresponding magnetic energy product of nanostructured samples were calculated and compared. Fig. 7.5 illustrates B - H curves and maximum energy product $(BH)_{max}$ of uncovered and Au covered samples. To calculate energy product, packing area were utilized for volume. The measured $(BH)_{max}$ for the MgO sample is 65.2 MGOe. The Heat sample $(BH)_{max}$ reaches 75.6 MGOe. LSAT stretches to 75.2 MGOe. Heat and LSAT exceed the value for MgO about 15 %. This $(BH)_{max}$ enhancement indicates effective heat treatment and fewer mismatches.

Au covered samples have a higher energy product $(BH)_{max}$ than uncovered samples. The shapes of hysteresis loops are almost rectangular with a high ratio of remnant magnetization. The coercive field is still high. It gives high maximum energy product $(BH)_{max}$ of 80.2 MGOe. The Au Heat $(BH)_{max}$ reaches 92.2 MGOe. Especially, LSAT stretches over Au Heat sample with a value of 97.1 MGOe. With Au capping layer, the maximum energy product $(BH)_{max}$ is increased above 1.2 times in all samples determined up to now as shown in Table 7.2.

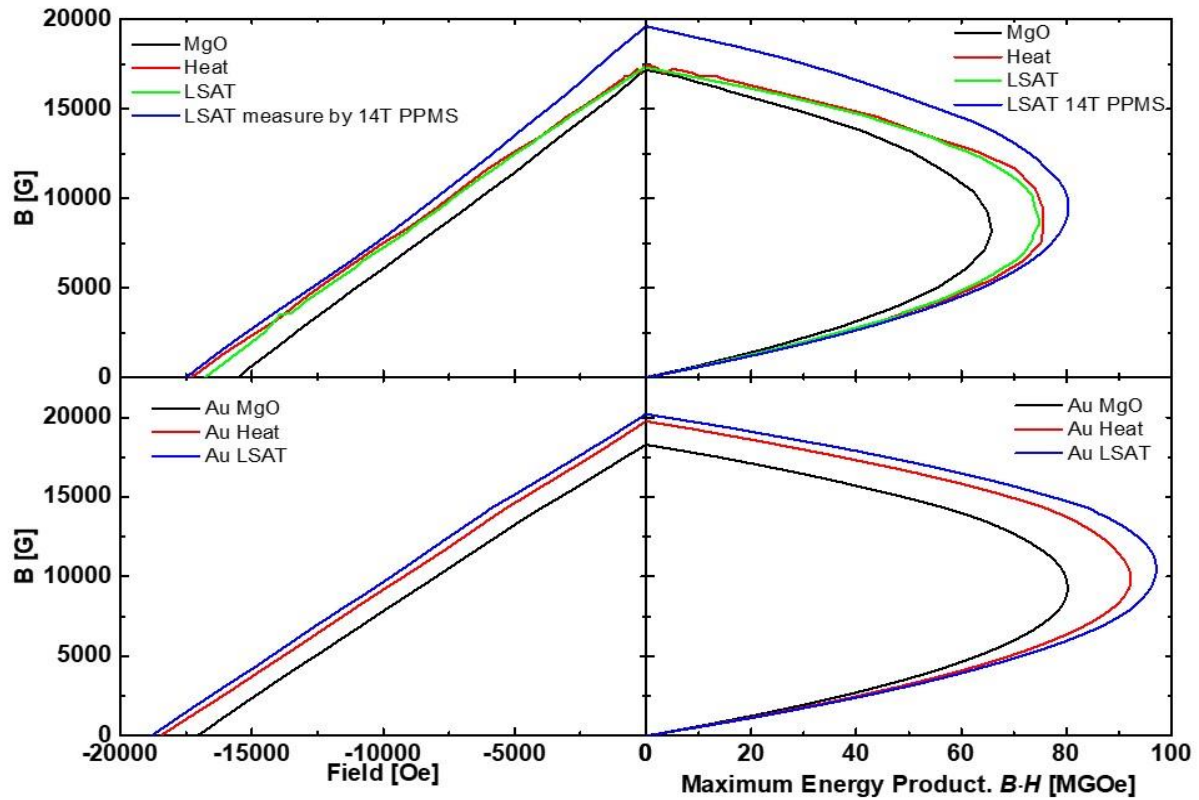


Fig.7. 5 $(BH)_{\max}$ illustration and Vertex of a parabola for energy product of out-of-plane at RT of as-grown on MgO (black), heat treatment (red) and as grown on LSAT (blue).

		Theoretical limit [MGOe]	Experimental highest value [MGOe]
	FePt		54 [136]
	NdFeB	64 [137]	59 [13]
	FePt/ Fe ₃ Pt		53 [138]
	NdFeB/ FeCo		61 [139]
	FePt / Fe	90 [140]	
	FePt/ FeCo	97 [141]	
	SmFeN/ FeCo	120 [88]	
Our results	FePt		75.6
	FePt/Au		97.1

Table 7. 2 List of reported high maximum energy product $(BH)_{\max}$ and our result.

7.2.3 X-ray Magnetic Circular Dichroism Results

Au covered samples

For XMCD measurements the system at WERA beamline in ANKA set up, where the spectra are recorded with total electron yield (TEY) method. This mode needs conductive targets. Since, thin films are formed nanoisland which is perfectly isolated from each other it is not possible to study XMCD. Au covered samples were prepared with 3 nm Au capping layers, which provide the required conductivity and furthermore protect the surface from oxidation.

XMCD measurement

XAS and XMCD measurement were carried out at the Fe $L_{3,2}$ -edges from 690 eV to 750 eV with applied maximum field of 7 T magnetic field and alignment of normal incident (NI) direction at RT. XMCD was determined by absorption measurement with energy scans in ± 7 T applied field and positive and negative helicity. The shapes of spectra were compared with the spectrum of 40 nm thickness FePt. Fig. 7.6 shows the normalized XAS and XMCD spectra at the Fe $L_{3,2}$ -edges in the Au MgO and Au Heat and Au LSAT samples. A standard two-step-like function is subtracted to separate the electron excitations to unoccupied d states.

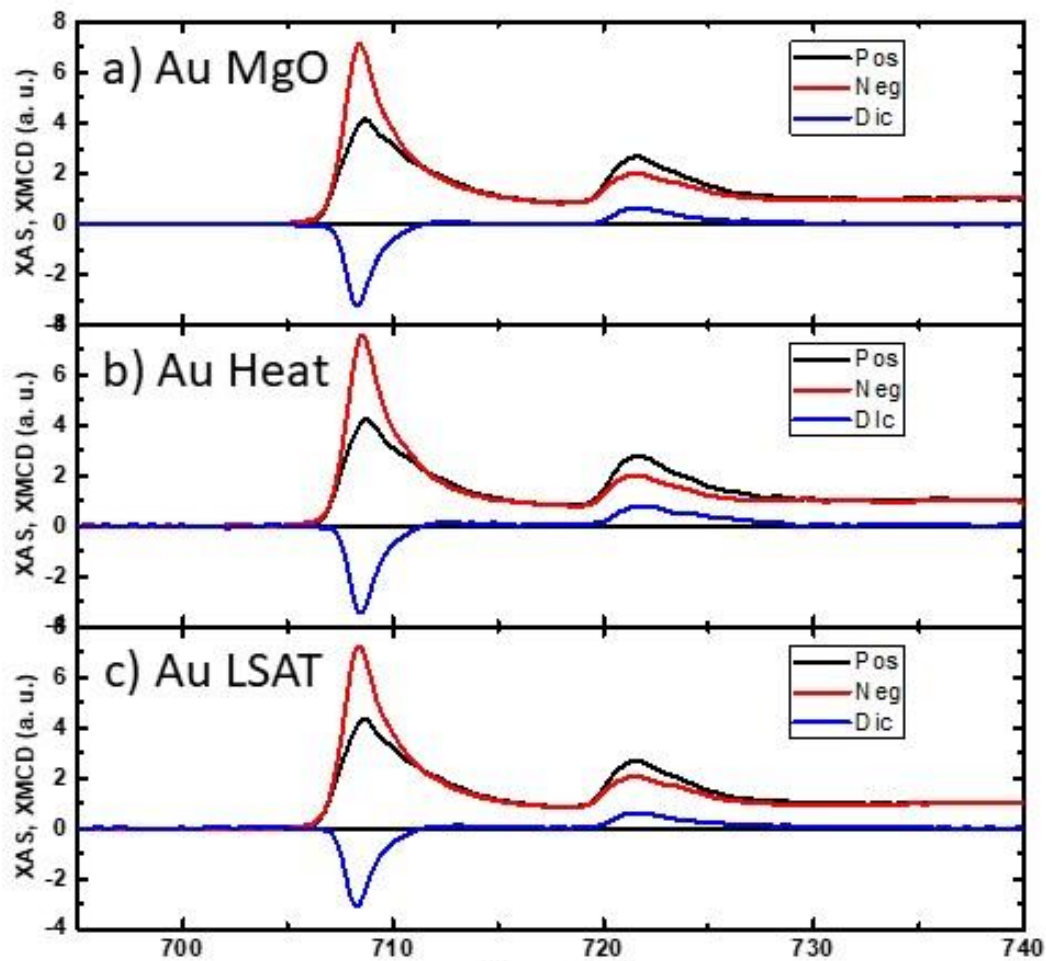


Fig.7. 6 XAS and XMCD spectra at RT for FePt a) on MgO, b) Heat treatment and c) on LSAT at the Fe $L_{3,2}$ -edges.

By applying the XMCD sum rules, spin magnetic moment, μ_s and orbital magnetic moment, μ_l are determined. The theoretical numbers of d holes $n_h=3.705$ were used for calculation. The sum rules results of spin, orbital, total magnetic moments and m_l/m_s ratio are summarized in Table 7.2. And Fig. 7.7 shows comparison of spin and orbital magnetic moment each sample. The Au Heat sample has highest spin moment while lowest orbital moment. Both as-grown samples on MgO and LSAT have smaller spin moment than reported values of $\sim 2.4 \mu_B$. All of samples have higher magnetic moment than reported values of $\sim 0.2 \mu_B$.

	$m_s [\mu_B]$	$m_l [\mu_B]$	$m_t [\mu_B]$	m_l/m_s
MgO	2.18(4)	0.26(1)	2.45	0.12
Heat	2.62(3)	0.22(3)	2.85	0.086
LSAT	2.22(1)	0.25(2)	2.47	0.114

Table 7. 3 The obtained spin and orbital magnetic moment by Sum Rules.

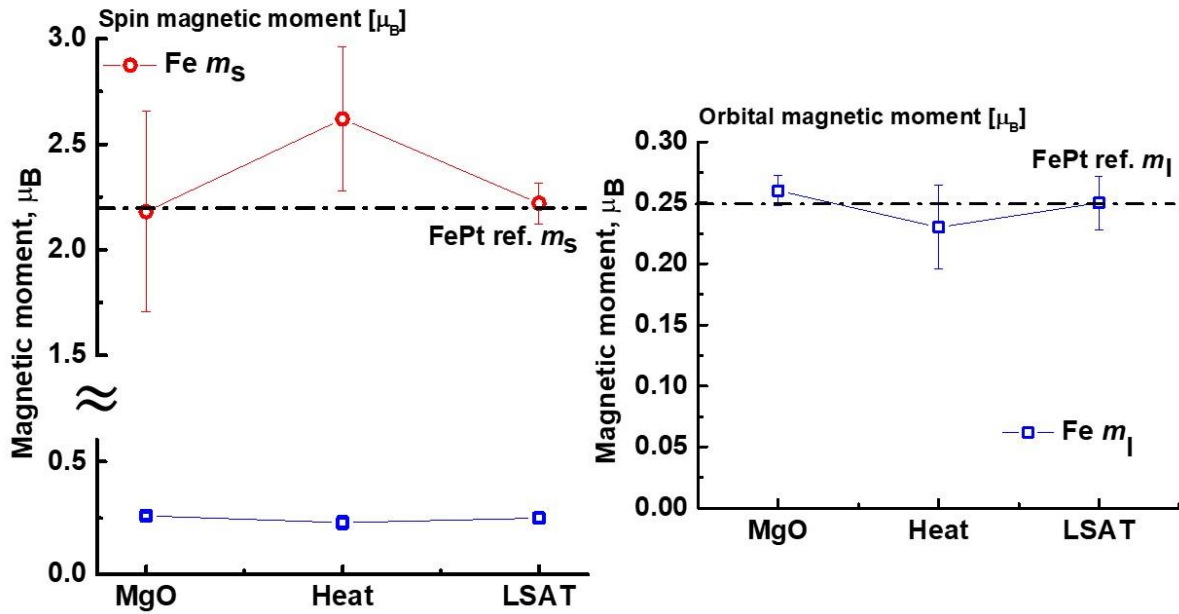


Fig.7. 7 Spin and orbital moment of MgO, Heat and LSAT samples consisting of 7 nm thickness FePt and 3 nm thickness Au by Sum Rules.

It is obvious, that the MgO and LSAT systems show a lower moment than expected for the FePt L1₀ in general ($\sim 3 \mu_B$). This seems to be in contradiction to the enhanced polarization. This needs further intensive studies to clarify the occurrence of the highest energy product found so far.

Hysteresis loops with XAS

Fig. 7.8 shows a comparison between SQUID hysteresis loops and XAS hysteresis at Fe L_3 -edge. The curves are normalized to the saturation magnetization. The saturation field is 7 T. As expected; hysteresis loops indicate hard magnetic behavior with the huge coercive field. The coercivity of hysteresis from L_3 -edge XAS are larger than SQUID results. We assumed that, L_2 -edge XAS hysteresis loops will be compensated with L_3 -edge result.

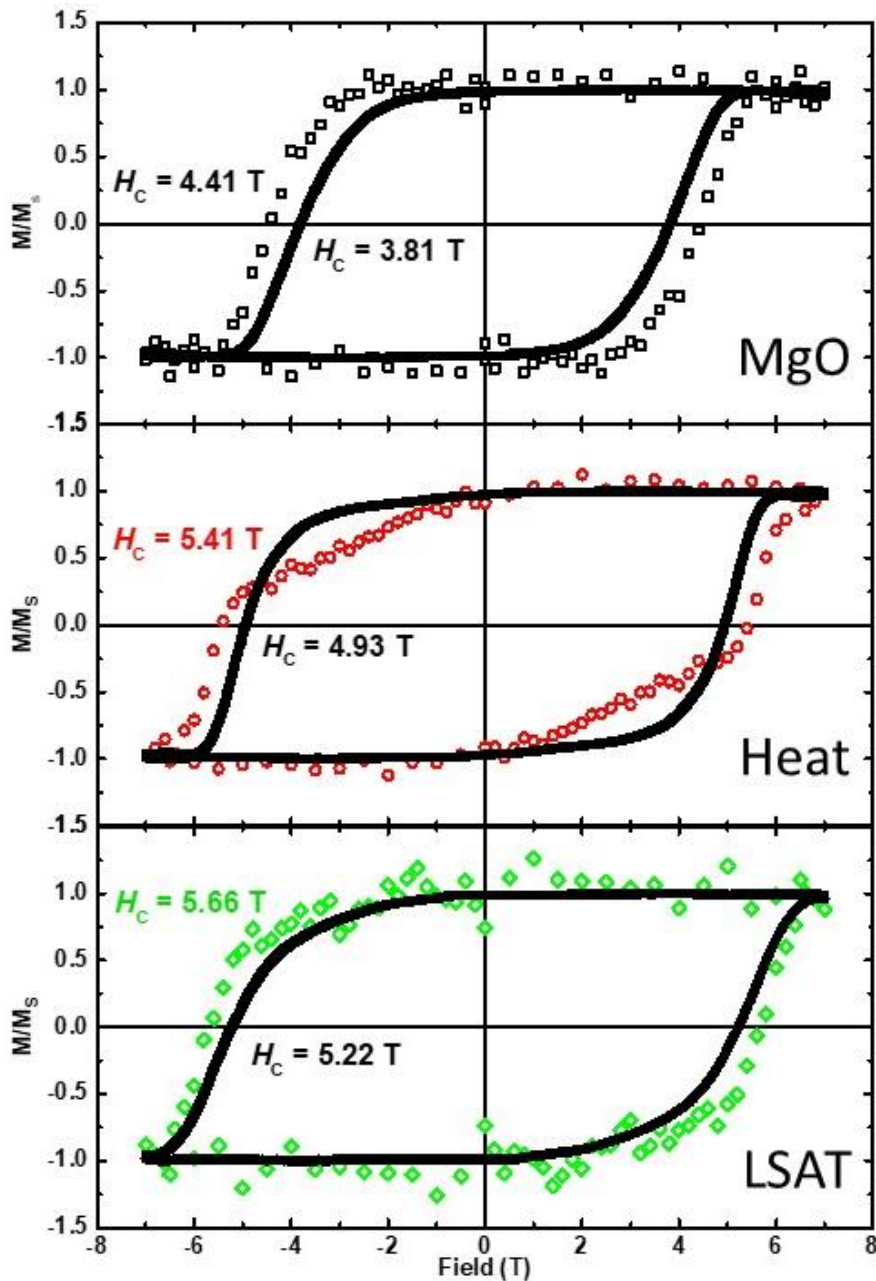


Fig.7. 8 Comparison of SQUID and XAS hysteresis loops. Lines are SQUID hysteresis loops, and scattered data are L_3 -edge XAS hysteresis loops. Coercive fields of Fe by XAS are bigger than total magnetic hysteresis loops by MPMS. The capping layer reduces coercivity. The surface of heat treatment sample is diluted by Au capping layer during post heat treatment

7.3 Conclusion: Realize huge coercive field and maximum energy product $(BH)_{\max}$ with ultra-hard nanomagnet

The L1₀-chemically ordered FePt granular nanostructured hard magnets were modified by two lattice mismatch reduction method, heat treatment (post-annealing) and changes the substrate. The 7 nm thickness of FePt that has the highest coercivity of ~4 T depends on thickness was chosen to realize huge coercive field. The coercivity of FePt is expected to reach 12 T with theoretical calculation.

The reasons of less coercivity are assumed A1 phase with amorphous or oxidation of material on surface and lattice mismatch between FePt and substrate. The heat treatment can effect to phase and oxidized Fe atoms on the surface. The 7 nm thickness FePt on MgO (100) substrate heated up to 800 °C and kept for 1 hour at Ar gas atmosphere. The phase of FePt in the thin film becomes L1₀-phase (fct: face-centered tetragonal). After that, quenching process (rapid cooling) can keep the phase at the interface with avoidance of thermos-equilibrium.

The lattice constants of L1₀-FePt are $a=3.85 \text{ \AA}$ and $c=3.71 \text{ \AA}$. The MgO (100) substrate has a lattice constant of $a=4.212 \text{ \AA}$. The lattice mismatch is about 10 %. The lattice constant of (LaAlO₃)_{0.3}-(Sr₂AlTaO₆)_{0.7} (100) substrate is $a= 3.87 \text{ \AA}$ with a lattice mismatch of ~0.005 %.

The magnetic properties of three samples were studied by superconducting quantum interference device (SQUID) magnetometry and X-ray magnetic circular dichroism (XMCD) spectroscopy. Hysteresis loops are obtained for saturation magnetization and coercivity. The maximum energy product $(BH)_{\max}$ is also calculated. The coercivity is reached to ~6T by both methods at RT. The maximum energy product values are increased to 97 MGOe by the Au layer.

For the XMCD measurement, new samples were prepared with covering of 3 nm Au. The 7 nm FePt thin film has no conductivity due to nanoinsular structure. The Au layer makes it to be able to measure with TEY mode. The magnetic moments of Fe atom were determined using XMCD spectra and Sum Rules. The number of Fe atom are not big different each sample. However, the saturation magnetizations are Heat > LSAT > MgO. The magnitude order of magnetization is the same as the value order of magnetic moment of Fe atom in thin films for MgO and LSAT.

Magnetization curves are the difference between results by L₃-edge XAS and SQUID. A single Fe has bigger coercivity than total magnetization curve. Especially, the heated sample has two phases by dilution on the surface with Au capping layer.

With this study, the huge coercivity and maximum energy product $(BH)_{\max}$ are realized till 6 T and 97 MGOe by reduction of lattice mismatch.

Chapter 8

Summary

The aim of the thesis was to study the magnetic properties of the highly coercive FePt L1₀ phase in combination soft magnetic Co layers by

- tuning exchange-spring nanomagnets L1₀ FePt/Co by nanostructuring,
- modifying the coupling of L1₀ FePt/Pt/Co tuned by the thickness of the Pt interlayer between two phases
- enhancing the coercive field and energy product of L1₀-FePt single of 7 nm layer by heat treatment and reduction of the lattice mismatch with the substrate

The main material is L1₀-chemically ordered FePt (fct: face-centered tetragonal) which has large coercive field with huge anisotropy constant ($K_1 \approx 6.6 \text{ MJ/m}^3$). A continuous hard magnetic L1₀-FePt thin film with out-of-plane texture was deposited by Magneto co-sputtering on heated at 800 °C MgO(100) and LSAT substrates and partly subsequent heat treating. The Co and Pt protection layers were deposited also by magnetron sputtering at room temperature. The quality of multilayers was verified with X-ray diffraction (XRD) for crystal structure and scanning electron microscopy (SEM) and partially TEM to determine the film morphology. The nanostructures were realized by nanoimprint routes. The magnetic properties were investigated using SQUID, MFM and XMCD techniques.

Artificial regular nanopattern of L1₀-FePt / Co exchange spring magnets

Three different composition nanopatterns were produced with 20 nm thickness of L1₀-FePt at room temperature. A layer of Co with a thickness of 3 nm and 7 nm were additionally deposited.

These multilayers were structured into a regular nanopattern with a diameter of 60 nm and 150 nm periodicity over a total area of 2 mm × 2 mm by nanoimprint lithography. The combination of IPS[®] and STU[®] imprinting processes were used with the ICP-RIE plasma etching process, subsequently. The imprint parameters like pressure, time, temperature and etching time were optimized. The quality of the nanopattern structures were studied by AFM and MFM. We could get large-area exchange-spring nanopatterned magnets, successfully. TEM investigations have proven the real thickness and composition of Co layers. The nanodot structure is hemispheres due to a dome structure on the top of dots in the stamp. Co layers are not flat on FePt.

Magnetic hysteresis loops of structured exchange-spring nanomagnets show an out-of-plane texture. The coercivity has been significantly tuned from 1.72 T (without Co) to 1.03 T (for 7 nm Co). The out-of-plane hysteresis loop of the pure L1₀-FePt hard magnet is only one step. The 3 nm and 7 nm Co coupled partially with a hard magnet showing two steps hysteresis with kink.

By the hysteresis loops the intrinsic material parameters, saturation polarization J_s , anisotropy constant K_1 , exchange constant A and the critical temperature T_0 were determined and microstructural parameter α and N_{eff} deduced. Increasing the thickness of Co influences those parameters. It gives a reduction of anisotropy and coercive field and rises the saturation polarization, the exchange constant

and critical temperature. Moreover, the α -values explain a significant effect of the soft layer by coupling. The larger α -value indicates a nucleation hardened magnetic reversal mechanism. On the other hand, smaller α value of the partially coupled magnet is dominated by Co soft layer.

To investigate the origin of magnetic behavior further, FORCs measurements were performed on these nanopatterned exchange-spring magnets. The FORCs density shows the distribution of interaction field and coercive field. The FORCs density diagrams indicate the broad distribution of coercive field of all samples, and partially coupling samples have two peak regions for non-coupling and coupling.

Only FePt and the 3 nm Co decorated exchange spring nanomagnet patterns switch as single-domain such as bit (just up and down) with one step hysteresis loop. Especially, hysteresis loop of 20 nm FePt/ 7 nm Co (partially coupled exchange-spring magnet) is two steps with kink due to the non-coupling area. In this system a single nanomagnet is composed of multi-domains as confirmed with MFM image at selected fields showing a top view of magnetic structures with out-of-plane direction. At second reversal field range, each magnet behaves as single-domain magnets.

The tuned coupling by interlayer on L1₀-FePt/ Pt/ Co exchange spring nanograin magnets

In these systems the coupling strengths have been modified by the thickness of a Pt interlayer between hard and soft magnetic layer in exchange-spring magnets. The 7 nm thickness of L1₀-FePt with the coercivity of about 4 T has been chosen for the hard magnetic layer, and the 3 nm thickness of Co with the saturation polarization of 1.76 T has been deposited as a soft magnetic layer. Pt layers with thickness of Pt layer of 0.5 nm, 1 nm and 2 nm were sandwiched between two materials. The L1₀-FePt hard magnet was deposited by Magneto co-sputtering at 800 °C, the Pt interlayer and Co soft layer were deposited at room temperature to prevent dilution of materials. The crystal structure and morphology of nano insular exchange-spring magnet were verified with XRD and SEM images. The crystal structure of all samples has high ordering with chemical ordering parameter $S \geq 0.86$. SEM images indicate insular nanostructures with average island size of 34 nm to 56 nm. These values are similar to the critical diameter of 7 nm thickness FePt ($D_C \sim 55$ nm).

The magnetic properties were determined by SQUID magnetometry. Throughout for all tuned exchange-spring nanomagnets, the magnetic hysteresis loops indicate a preferred out-of-plane texture at room temperature. By the thickness of Pt interlayer of 0.5 nm and 1 nm thickness partially coupling was observed, and 2 nm thicknesses shows decoupling between L1₀-FePt hard and Co soft magnetic layers. The perfectly coupled ES magnet is of a clear one step type. The partially coupled ES magnet starts to show tiny kink at soft magnetic reversal region. Moreover, decoupled ES magnet has two steps hysteresis loop with kink. Coercive field is also controlled by modification of coupling with a thickness of interlayer, while the saturation polarization values are similar. Coupling reduces H_C . By decoupling, the coercivity of FePt tended to be recovered. For micromagnetic studies, from temperature dependent magnetic hysteresis loops the saturation magnetization J_s , coercivity H_C , magnetic anisotropy K_1 and exchange stiffness A were determined. Those parameters provide information of the domain characteristics like wall energy γ , exchange length l_K and thickness of domain wall δ .

The magnetic reversal mechanism has been analyzed by mean of the microstructural parameters α and N_{eff} . Only FePt hard magnet thin film has highest $\alpha = 0.918$ and $N_{\text{eff}} = 1.93$ to be close to $\alpha = 1$ and $N_{\text{eff}} = 0$ in the ideal nucleation case. The perfect coupling reduces the nucleation field a factor of 1/5. Decoupling is correlated to a reduction in parameter values of $\alpha = 0.414$ and $N_{\text{eff}} = -0.076$ of 2 nm thickness of interlayer. The negative N_{eff} indicate incomplete domain walls. However, the coercive

field and parameter of the FePt hard magnet are not reached to due to influence of the soft magnetic layer. Especially, the α_{ex} values are increased by decoupling, which explains directly coupling strength.

The extended FORCs can be interpreted in term of the irreversibility of domains. The FORCs density diagrams of all samples show a broad distribution of the coercive field. But the effect of the soft magnetic layer, even of the decoupled sample, cannot be seen. However, the extended FORCs indicate a moving of the interaction field distribution at $H_C=0$ caused by soft magnetic reversal.

The x-ray magnetic circular dichroism measurements were performed to investigate the element specific magnetic property in a quantitative manner. The absorption spectra were obtained in the surface-sensitive total electron yield mode (TEY) at Fe $L_{3,2}$ -edges for FePt hard and Co $L_{3,2}$ -edges for the soft magnet. As expected the total magnetic moments of Fe are increased by coupling from 2.54 μ_B / atom of decoupling to 2.81 μ_B / atom and for Co from 1.58 μ_B / atom to 2.06 μ_B / atom. Moreover, XAS hysteresis loop at L_3 -edge was also measured demonstrating that the Fe and Co components behave similar in the perfectly coupling exchange spring magnet. However, in decoupled magnet the Co hysteresis of the soft magnet is switched earlier than Fe hysteresis of the hard magnet. The results of SQUID measurements and by XAS were compared and confirmed matching each other.

Realize high energy product with the large coercive field of $L1_0$ -FePt nanoisland thin films.

The $L1_0$ chemically-ordered FePt phase is one of the hard magnetic systems with highest coercivity. Since in thin layers a maximum value was expected for the 7 nm thickness of FePt the corresponding were prepared on MgO (100) substrate and $(LaAlO_3)_{0.3}-(SrTaAlO_6)_{0.7}$ (100) substrate at the same conditions. The lattice constants of $L1_0$ -FePt are $a = 3.85 \text{ \AA}$ and $c = 3.17 \text{ \AA}$. The lattice constant of MgO and LSAT is $a = 4.212 \text{ \AA}$ and $a = 3.87 \text{ \AA}$, respectively. The main idea is a reduction of lattice mismatch by heat treatment and new substrate between material and substrate. MgO sample heated up to 800 C for 1 hour and rapidly cooled to hold the $L1_0$ -phase at surface and interface between FePt and MgO substrate

The MgO sample has a coercivity of 4.14 T, by heat treatment the coercivity is enhanced to 6.06 T. For the LSAT sample also a very high coercivity of 6.17 T was reached. The saturation polarization of 1.72 T for MgO is also grown up to 1.76 T by heat treatment and 1.68 T by using a LSAT substrate. The increase of coercivity and saturation magnetization rises the maximum energy product $(BH)_{max}$ from 65.7 MGOe to 75.6 MGOe by heat and 73.6 MGOe by LSAT.

New samples, which are covered with 3 nm thickness of Au conduction layer, were prepared for XMCD measurement by TEY mode. Due to Au layer on top of nanomagnets, the surface of samples is protected from oxidation. Surprisingly this coverage enhances the saturation polarization to 1.85 T for MgO and 2.03 for the heat and LSAT sample. Therefore despite of the reduced coercivity the maximum energy product $(BH)_{max}$ especially of LSAT is conspicuously increased to 97.1 MGOe by the Au coverage.

XMCD results indicate the highest magnetic moment of heat sample with 2.85 μ_B / atom of Fe, while the Fe moments for MgO and LSAT show a somewhat lower moment. The hysteresis loops by XAS at L_3 -edge show higher coercivity than SQUID results in all of the samples. The origin of this phenomenon could not be clarified and needs more highly precise XMCD studies which also are extended to the L_2 - edge. Also the significant increase of the saturation polarization of the FePt nanograins by a simple coverage Au seems to be not reflected by the corresponding XMCD analysis and needs further combined SQUID and XMCD studies.

However, in this thesis it could be demonstrated that heat treatment of 7 nm magneto-sputtered FePt $L1_0$ and the corresponding layers on a LSAT substrate provide a significant increase of the coercivity and maximum energy product. Additionally, an Au protection layer improves the saturation magnetization and magnetic energy product even further. The results achieved in this thesis demonstrate -to our knowledge- the highest energy product of all systems experimentally realized up to now. The value of 97 MGOe for 7 nm FePt $L1_0$ on LSAT exceeds the highest reported value of 61 MGOe for FeCo/NdFeB by more than 50 %.

Chapter 9

Zusammenfassung

Ziel dieser Doktorarbeit war die Untersuchung der magnetischen Eigenschaften der hochkoerzitiven FePt L₁₀ Phase in der Kombination mit weichmagnetischem Co um

- die Eigenschaften von „Exchange-Spring“ (ES) - L₁₀ FePt/Co Nanomagneten durch Nanostrukturierung einzustellen.
- die Kopplung in L₁₀ FePt/Pt/Co durch die Dicke der Pt Zwischenschicht zwischen den zwei Phasen zu modifizieren.
- das Koerzitivfeld und das Energieprodukt in 7 nm L₁₀ FePt Einzellagen durch anschließende Wärmebehandlung und durch ein anderes Substrat (LSAT) mit besserer Gitteranpassung zu erhöhen.

Das Basismaterial ist chemisch geordnetes L₁₀ FePt (fct: flächenzentriert-tetragonal), das ein hohes Koerzitivfeld mit einer großen Anisotropiekonstante ($K_1 \sim 6,6 \text{ MJ/m}^3$) aufweist. Ein durchgehender hartmagnetischer L₁₀ FePt Film mit einer senkrechten Textur wurde mit Magneto-Kosputtern auf 800 °C geheiztem MgO(100) und LSAT aufgebracht und teilweise einer anschließenden Wärmebehandlung unterzogen. Co und die Pt-Schutzschicht wurden ebenfalls mit Kosputtern bei Raumtemperatur abgeschieden. Die Qualität der Vielschichten wurde über XRD für die Kristallstruktur und SEM für die Morphologie geprüft. Die Nanostrukturen wurden mit Nanoimprint-Verfahren realisiert. Die magnetischen Eigenschaften wurden mit SQUID, MFM und XMCD Techniken bestimmt.

Künstliche gleichmäßige Nanostrukturen aus L₁₀ FePt/Co ES Magneten

Drei unterschiedlich aufgebaute Nanomuster aus 20 nm dickem L₁₀ FePt wurden bei Raumtemperatur produziert. Eine Co Lage mit jeweils 3 nm und 7 nm wurden zusätzlich aufgebracht.

Diese Vielschichten wurden in regelmäßigen Nanomustern mit einem Durchmesser von 60 nm und einer Periode von 150 nm auf einer Fläche von $2 \times 2 \text{ mm}^2$ mit Nanoimprint-Lithographie hergestellt. Die Kombination eines IPS und STU Prozesses mit ICP-RIE Plasma wurde nacheinander genutzt. Die Prägeparameter wie Druck, Zeit, Temperatur und Ätzdauer wurden optimiert. Die Qualität der Strukturen wurde mit SEM, AFM und MFM studiert. TEM Untersuchungen überprüften erfolgreich die reale Dicke und die Zusammensetzung der Co Schicht. Die Nanopunkte sind halbkugelförmig auf Grund der Kuppelform der Oberfläche der Stempelstrukturen. Die Co Lagen sind nicht eben auf dem FePt.

Die magnetischen Hystereseschleifen der strukturierten ES Nanomagnete zeigten eine senkrechte Textur. Die Koerzitivität ist deutlich von 1,71 T (ohne Co) auf 1,03 T (für 7 nm Co) gezielt eingestellt worden. Die senkrechte Hystereseschleife ist nur einstufig für den reinen L₁₀ FePt Magnet. Die 3 nm und 7 nm Co Lagen koppeln teilweise und zeigen eine 2-Stufen Hysterese mit einem Knick.

Über die Hystereseschleife wurden die intrinsischen Materialparameter, die Sättigungspolarisation J_s , die Anisotropiekonstante K_1 , die Austauschkonstante A und die kritische Temperatur T_0 bestimmt und

die Mikrostrukturparameter α und N_{eff} abgeleitet. Das Anwachsen der Dicke des Co beeinflusst diese Parameter. Es ergibt sich eine Verringerung der Sättigungspolarisation, der Anisotropie und des Koerzitivfeldes und es erhöht sich die Austauschkonstante und die kritische Temperatur. Weiterhin erklären die Größen α einen signifikanten Effekt des Weichmagneten durch die Kopplung. Größere Werte von α weisen auf einen nukleationsgehärteten magnetischen Umkehrmechanismus. Auf der anderen Seite werden kleinere Werte von α der teilweise gekoppelten Magnete von der weichmagnetischen Co Lage dominiert.

Um die Ursache des magnetischen Verhaltens weiter zu studieren, wurden an diesen ES-Nanomagneten FORC Messungen durchgeführt. Die FORC Dichte zeigt die Verteilung des Interaktions- und Koerzitivfeldes. Das FORC Dichte-Diagramm weist auf eine breite Verteilung des Interaktions- und Koerzitivfeldes in allen Proben hin, wobei die partiell gekoppelten Proben zwei erhöhte Bereiche zeigen für fehlende und teilweise Kopplung.

Nur das reine FePt und das mit 3 nm Co bedeckte ES Nanomagnetmuster schalten als eine Domäne wie ein Bit (nur oben oder unten) mit einer einstufigen Hysterese. Gerade die Hystereseschleife des 20 nm FePt/7 nm Co (partiell gekoppelter ES Magnet) hat 2 Stufen mit einem Knick aufgrund der nicht-koppelnden Bereiche. In diesem System besteht der Einzelmagnet aus vielen Domänen wie durch MFM Messungen bei ausgewählten Feldern bestätigt wurde, das die Obenansicht der Magnetstrukturen mit einer senkrechten Richtung zeigt. Ab einem zweiten Feldbereich verhält sich dann jeder Magnet wie ein Einzelmagnet.

Einstellen der Kopplung durch Zwischenlagen in L1₀ FePt/Pt/Co ES nanogekörnten Magneten

In diesen Systemen wurde die Kopplungsstärke modifiziert über die Dicke einer Pt Zwischenschicht zwischen der hart- und weichmagnetischen Lage in einem ES Magneten. Die Dicke von 7 nm der FePt-L1₀ mit einer Koerzitivität von etwa 4 T wurde als hartmagnetische Phase gewählt und eine 3 nm Co Schicht mit einer Sättigungspolarisation von 1,76 T als weichmagnetische Lage aufgebracht. Pt Lagen mit einer Dicke von 0,5 nm, 1 nm und 2 nm wurden zwischen den beiden Materialien eingebracht. Der FePt-L1₀ Hartmagnet wurde über Magnetron-Kosputtern bei 800 °C deponiert, die weiteren Pt- und Co-Lagen wurden bei RT aufgebracht um eine Vermischung der Materialien zu verhindern. Die Kristallstruktur und Morphologie der nanoinselartigen ES Magnete wurden mit XRD und SEM überprüft. Die Kristallstruktur aller Proben zeigte eine hohe Ordnung mit einem chemischen Ordnungsparameter von $S \geq 0,86$. SEM Aufnahmen zeigten eine inselartige Struktur mit einer mittleren Inselgröße von 34 bis 56 nm. Diese Werte sind dem kritischen Parameter von 7 nm dickem FePt ($D_C \sim 55$ nm) ähnlich.

Die magnetischen Eigenschaften wurden mit SQUID Magnetometrie bestimmt. Durchgehend für alle eingestellten ES Nanomagnete zeigte die Hystereseschleife eine bevorzugte Richtung aus der Ebene bei RT. Für eine Dicke von 0,5 nm und 1 nm der Pt Zwischenlage wurde eine teilweise Kopplung beobachtet, bei 2 nm Dicke zeigte sich eine Entkopplung der magnetisch harten FePt-L1₀ und weichen Co Lage. Der perfekt gekoppelte ES Magnet ist klar von einstufigem Typ. Der teilweise gekoppelte ES Magnet beginnt einen Knick bei der weichmagnetischen Umkehrregion zu zeigen. Weiterhin hat der entkoppelte ES Magnet eine zweistufige Hysterese mit einem Knick. Das Koerzitivfeld wird auch kontrolliert über die Modifikation der Kopplung über die Dicke der Zwischenlage, während die Sättigungspolarisation sehr ähnlich ist. Die Kopplung reduziert H_C . Bei der Entkopplung tendiert die Koerzitivität des FePt dazu wieder anzuwachsen. Für mikromagnetische Studien wurde aus den temperaturabhängigen Hystereseschleifen die Sättigungspolarisation J_s , das Koerzitivfeld H_C , die

Anisotropiekonstante K_1 und die Austauschsteifigkeit A bestimmt. Diese Parameter liefern Informationen über die Domänencharakteristika wie Wandenergie γ , Austauschlänge l_K und die Dicke der Domänenwand δ .

Der magnetische Umschaltmechanismus wurde im Hinblick auf die Mikrostrukturparameter α und N_{eff} analysiert. Nur der hartmagnetische FePt Film hatte das höchste $\alpha = 0,92$ und $N_{\text{eff}} = 1,93$ nahe bei $\alpha = 1$ und $N_{\text{eff}} = 0$ im idealen Nukleationsfall. Die perfekte Kopplung reduziert das Nukleationsfeld auf $1/5$. Die Entkopplung ist korreliert mit einer Reduktion der Parameterwerte zu $\alpha = 0,41$ und $N_{\text{eff}} = -0,08$ für 2 nm Dicke der Zwischenlage. Der negative Wert für N_{eff} deutet auf unvollständige Domänenwände hin. Aber das Koerzitivfeld und die Parameter des Hartmagneten FePt wird nicht erreicht auf Grund des Einflusses der weichmagnetischen Schicht. Insbesondere steigt der Wert von α bei Entkopplung an, was direkt die Stärke der Kopplung erklärt.

Diese umfassenden FORCs können über eine Irreversibilität der Domänen interpretiert werden. Die FORC Dichte Diagramme aller Proben zeigen eine breite Verteilung des Koerzitivfeldes. Aber ein Einfluss der weichmagnetischen Lage, auch für die entkoppelten Proben, kann nicht beobachtet werden. Allerdings weisen die ausgedehnten FORCs eine Verlagerung der Interaktionsfeldverteilung bei $H_C = 0$, verursacht durch das weichmagnetische Umschalten.

Messungen des zirkularen magnetischen Röntgendiffraktions (XMCD) wurden durchgeführt um die elementspezifischen magnetischen Eigenschaften quantitativ zu untersuchen. Die Absorptionsspektren wurden im oberflächensensitiven Sekundärelektronenausbeutemodus (TEY) an der Fe $L_{2,3}$ -Kante im harten FePt und an der Co $L_{2,3}$ -Kante im weichen Magneten erhalten. Wie erwartet ist das gesamte magnetische Moment des Fe erhöht von $2,54 \mu_B/\text{Atom}$ für Kopplung auf $2,81 \mu_B/\text{Atom}$ für Entkopplung und für Co von $1,58 \mu_B/\text{Atom}$ auf $2,06 \mu_B/\text{Atom}$. Weiterhin wurden Hystereseschleifen ebenfalls an der L_3 -Kante gemessen, die zeigen, dass sich die Fe und Co Komponenten ähnlich verhalten im perfekt gekoppelten ES Magneten. Hingegen schaltet im entkoppelten Magneten die Co Hysterese des Weichmagneten früher als die Fe Hysterese des Hartmagneten. Die Resultate der SQUID und XMCD Messungen wurden verglichen und bestätigt, dass sie übereinstimmen.

Realisierung hoher Energieprodukte mit hohen Koerzitivfeldern in $L1_0$ FePt inselartigen Nanostrukturen dünner Filme

Die chemisch geordnete FePt Phase ist eine der hartmagnetischen Systeme mit höchster Koerzitivität. Da in dünnen Schichten ein höchster Wert für 7 nm Dicke von FePt erwartet wird, wurden die entsprechenden Lagen auf einem MgO (100) und einem $(\text{LaAlO}_3)_{0,3}(\text{SrTaAlO}_6)_{0,7}$ (100) Substrat unter gleichen Bedingungen abgeschieden. Die Gitterkonstante beträgt für $L1_0$ -FePt $a = 3,85 \text{ \AA}$ und $c = 3,17 \text{ \AA}$. Die Gitterkonstante von MgO und LSAT sind $a = 4,212 \text{ \AA}$ und $a = 3,87 \text{ \AA}$. Die Grundidee war eine Reduktion der Fehlanpassung zwischen beiden Systemen durch Wärmebehandlung bzw. die Wahl des neuen Substrates. Die MgO Probe wurde dabei auf $800 \text{ }^\circ\text{C}$ für eine Stunde geheizt und dann schnell abgekühlt um die $L1_0$ Phase an der Ober- und Grenzfläche zu stabilisieren.

Die ursprüngliche Probe MgO (im Folgenden MgO genannt) zeigte eine Koerzitivität von $4,14 \text{ T}$. Nach der Wärmebehandlung (im Folgenden Heat genannt) war diese Koerzitivität auf $6,06 \text{ T}$ angewachsen. Für die FePt-Schicht auf LSAT (im Folgenden LSAT genannt) wurde ebenfalls eine hohe Koerzitivität von $6,17 \text{ T}$ erreicht. Auch die Sättigungspolarisation erhöht sich leicht durch Wärmebehandlung auf $1,76$, war aber bei LSAT mit $1,68$ etwas kleiner. Die Erhöhung der Koerzitivität bei entsprechender

Sättigungsmagnetisierung führt zum Anwachsen des Energieproduktes $(BH)_{\max}$ auf 65,7 MGOe für die MgO-Probe, 75,6 MGOe für die Heat-Probe und 73,6 MGOe für die LSAT Probe.

Neue Proben, die mit Au mit einer Dicke von 3 nm bedeckt wurden als leitende Schicht, wurden für XMCD Messungen im TEY Modus präpariert. Durch die Au Lage auf der Oberfläche der Nanomagnete ist diese geschützt vor Oxidation. Überraschenderweise erhöhte diese Bedeckung die Polarisierung zu 1,85 T für die MgO und 2,03 T für die Heat- und LSAT Probe. Dadurch ist trotz der etwas reduzierten Koerzivität das maximale Energieprodukt $(BH)_{\max}$ auffällig angewachsen insbesondere stark für die LSAT Probe zu 97,1 MGOe nur durch Aufbringen der Au Bedeckung.

Die XMCD Resultate zeigten ein höchstes magnetisches Moment für die Heat Probe mit $2,85 \mu_B$ pro Eisenatom, während die Fe Momente für Heat und LSAT kleiner waren. Die Hystereseschleifen aufgenommen an der Fe L_3 -Kante zeigten eine höhere Koerzivität als die SQUID Resultate für alle drei Systeme. Die Ursachen dieses Phänomens konnte bisher nicht geklärt werden und erfordern weitere hochpräzise Messungen, die auch auf die L_2 -Kante ausgedehnt werden sollten. Auch die signifikante Erhöhung der Sättigungspolarisation der FePt Nanokörner durch eine einfache Au Bedeckung spiegelt sich nicht in der entsprechenden Analyse der XMCD Daten wieder, was weitere kombinierte SQUID und XMCD Studien notwendig macht.

Dennoch konnte in dieser Doktorarbeit gezeigt werden, dass die Wärmebehandlung von 7 nm magneto-gesputterten FePt $L1_0$ und das Aufbringen der entsprechenden Lagen auf LSAT eine deutliche Erhöhung der Koerzivität und des maximalen Energieproduktes zur Folge hat. Zusätzlich verbessert eine Au Schutzschicht die Sättigungsmagnetisierung und damit das Energieprodukt noch weiter. Die Resultate, die in dieser Dissertation erhalten wurden, zeigen – unseres Wissens nach – das höchste Energieprodukt, das jemals bis heute experimentell realisiert wurde. Der Wert von 97 MGOe für 7 nm FePt $L1_0$ auf LSAT übersteigt die höchsten bisher publizierten Werte von 61 MGOe für FeCo/NdFeB um mehr als 50 %.

Appendix A

A.1 Sputtering condition for Fe₅₁Pt₄₉

The used magneto co-sputtering device can sputter three kinds of material together. To deposit high-quality thin films, the condition of sputtering has to be optimized for the purpose. The FePt is formed two phase of A1 phase (face-centered cubic, fcc) and L₁₀ phase (face-centered tetragonal, fct) from Fe₄₅Pt₅₅ to Fe₆₅Pt₃₅. The purpose of our work is to fabricate L₁₀-FePt hard magnet as the atomic ratio of Fe₅₁Pt₄₉.

The conditions for sputtering are vacuum pressure, temperature, sputter power and film growth rate.

The base vacuum pressure is 3×10^{-8} mbar. Moreover, Ar pressure during sputtering is 5×10^{-3} mbar. The temperature is set for FePt phase to 800 °C.

The attempts and WDX results were failed and succeed to be Fe₅₁Pt₄₉ are shown by Tables A1-3.

Power for Fe: 95 W Power for Pt: 30 W Time per nanometer: 6.7 s/nm Film growth rate : 0.149 nm/s								
K-Ratio Fe	K-Ratio Pt	t ρ[μg/cm ²]	wt% Fe	wt% Pt	at% Fe	at% Pt	Density	Thickness t [nm]
0.03150	0.10600	70.30	24.59	75.40	53.34	46.66	15.08	46.90
		± 0.74	0.27	0.27	0.36	0.36	0.050	0.50

Table A 1.1 This condition made Fe₅₃Pt₄₇ with thicker than the target thickness.

Power for Fe : 90 W Power for Pt : 30 W Time per nanometer : 7.46 s/nm Film growth rate : 0.134 nm/s								
K-Ratio Fe	K-Ratio Pt	t ρ[μg/cm ²]	wt% Fe	wt% Pt	at% Fe	at% Pt	Density	Thickness t [nm]
0.02150	0.09320	59.90	20.42	79.58	47.36	52.64	15.880	37.72

Table A 1.2 This condition made Fe₄₇Pt₅₃ with thinner than target thickness

The optimized condition of sputtering for L₁₀-Fe₅₁Pt₄₉ is

Power for Fe: 105 W Power for Pt: 30 W Time per nanometer: 7.27 s/nm Film growth rate : 0.137 nm/s								
K-Ratio Fe	K-Ratio Pt	t ρ[μg/cm ²]	wt% Fe	wt% Pt	at% Fe	at% Pt	Density	Thickness t [nm]
0.02520	0.09380	62.30	22.92	77.08	51.05	48.95	15.390	40.48

Table A 1.3 This condition made L₁₀-Fe₅₁Pt₄₉ with proper target thickness

A.2. The nanoimprint lithography (NIL) process (IPS, STU, O₂ Plasma treatment and ICP-RIE)

The nanosized patterns of exchange-spring magnets are fabricated by NIL. The optimized NIL process will be shown in this section.

The NIL uses a master stamp. The schematic of nanostructure in Fig. 5.6 shows transfer process from the master stamp to the real nanomagnet pattern. In this work, the stamp is fabricated on Si wafer with Electron beam lithography by Obducat. The structured wafer is covered with the anti-sticking layer. Fig A2.1 shows master stamp image from obducat. The feature size is 60 nm diameters, 150 nm periods and 90 nm heights.

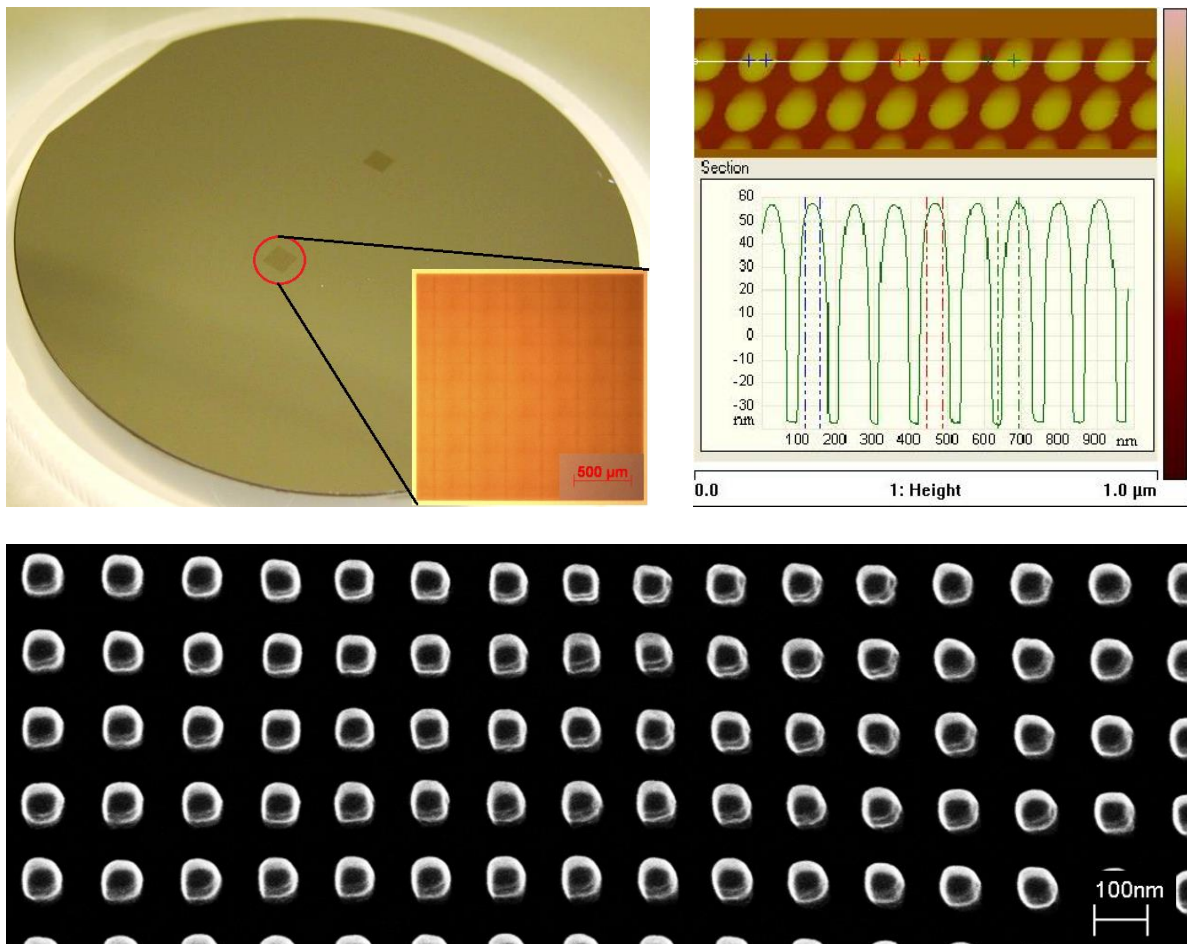


Fig A.2.1 The master stamp structure. The optical microscopy and AFM images from Obducat and SEM image from our institute.

The fabrication steps.

1. Photoresist coating on thin film
2. IPS (Intermediate Polymer Stamp) imprint step to make replica
3. STU (Simultaneous Thermal and UV) imprint step on lacquer
4. O₂-Plasma treatment to remove the resist and to open the film
5. ICP-RIE (Inductively Coupled Plasma-Reactive Ion Etching) to etching the film

The optimized fabrication process

1. **The photoresist on thin film:** The photoresist TU-7 is spin coated on cleaned thin film with 3000 rpm for 60 s.

Spin coated resist on thin film is baked for 60 s.

2. **NIL process** (Eitre 3, Obducat)

IPS imprint: The master stamp is covered with IPS foil for a negative replica.

IPS foil is imprinted with thermal imprinting. Increasing the temperature above glass temperature, give pressure and decrease the temperature below glass temperature, demolding.

Increasing temperature at 160 °C and pressure of 40 bars for the 60s.

Decreasing temperature at 60 °C and demold the IPS foil from the master stamp.

Fig A2.2 shows SEM and AFM images of IPS negative replica.

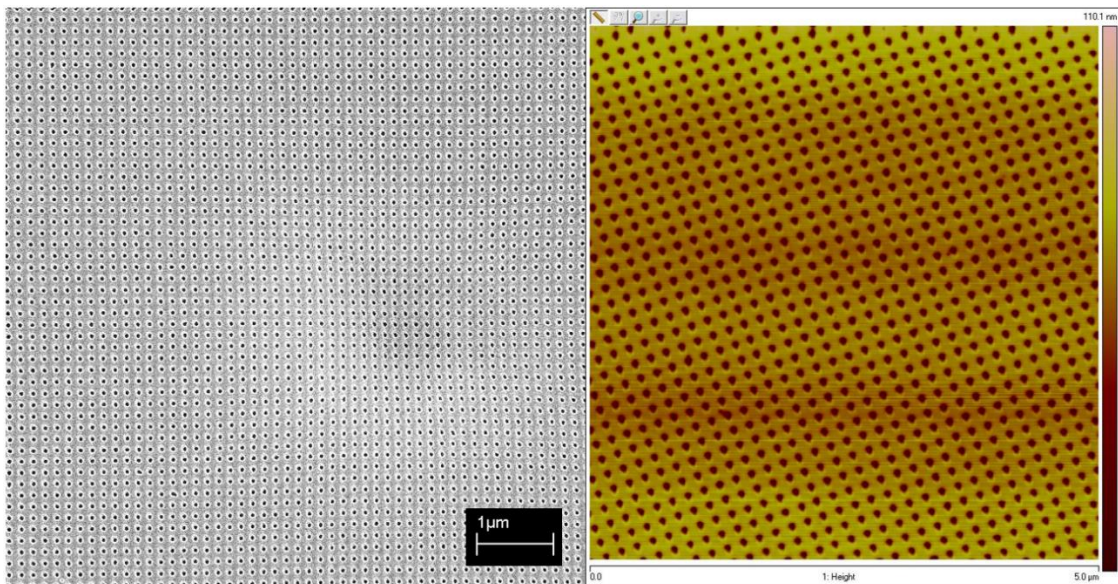


Fig A2.2 SEM and AFM images of IPS negative replica.

STU imprint: The negative replica is transferred to resist by the same structure with a master stamp. The resist on thin film is covered with IPS foil to transfer the structure to lacquer.

STU imprint is combined thermal and UV imprint. During thermal imprint, UV light is exposed to the photoresist.

Increasing temperature at 70 °C and pressure of 30 bars for the 60s

Expose the UV light for the 60s under the temperature and pressure.

Keep the temperature and pressure for 120s without UV light and demold the foil form a thin film.

AFM image showing 60 nm diameter and 150 nm period nanopattern is imprinted on the resist, in fig. A.2.3.

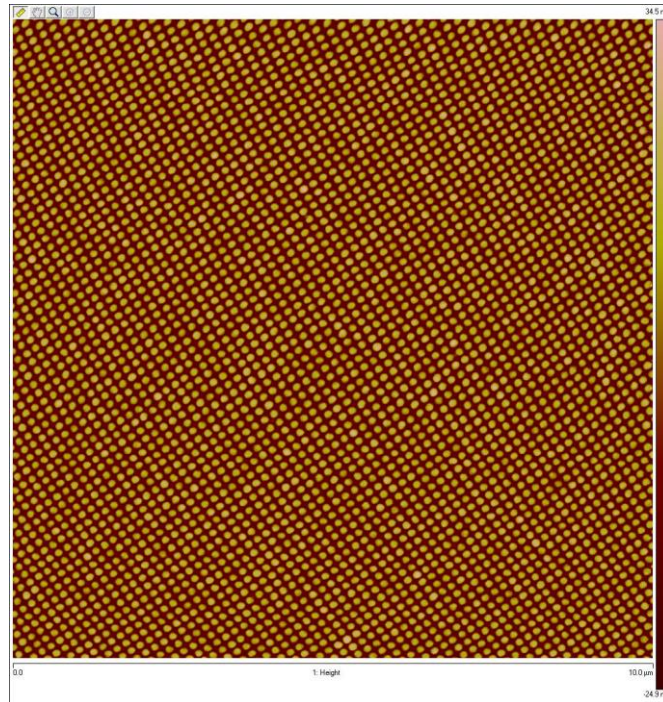


Fig. A.2.3 AFM image of 60 nm / 150 nm pattern on resist after NIL process

3. **O₂-plasma treatment** (prep.2, GaLa Instrument).

To open material between dots over keeping dots structure, the power and time have to be optimized O₂-plasma with consideration of etching ratio.

This work is used 30 Watt power and 5 min.

4. **ICP-RIE** (Plasmalab 80plus, Oxford Instruments): The structures are transferred to thin film.

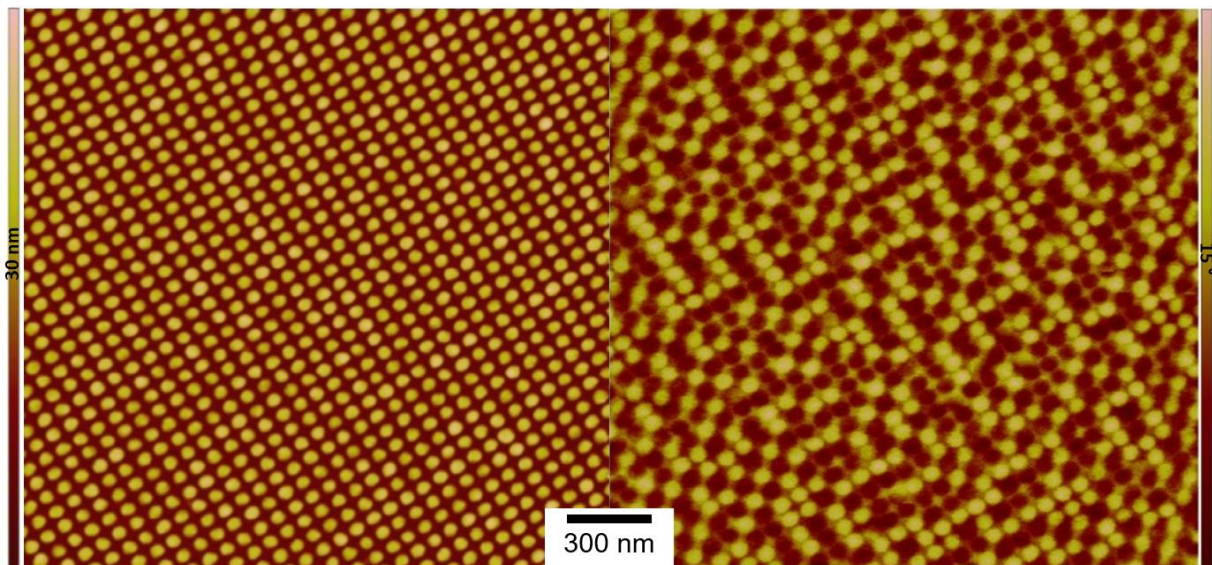
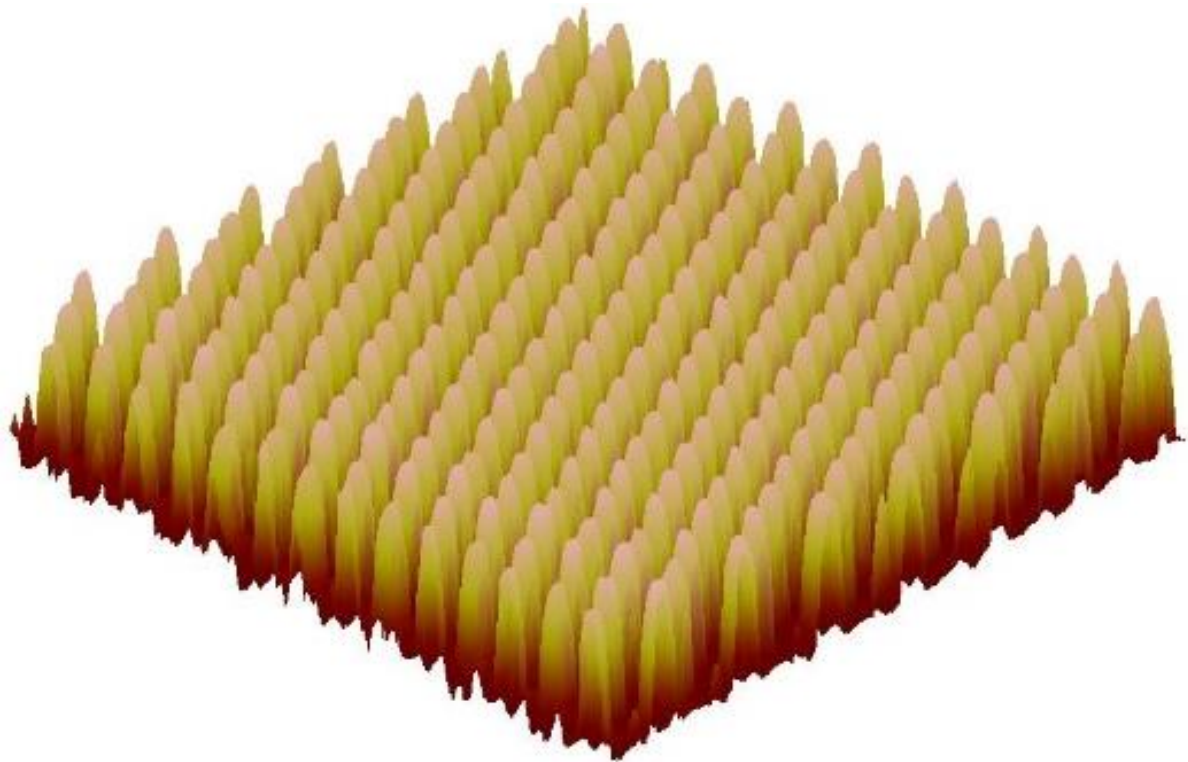
The etching ratio depends on several factors, such as temperature, chamber pressure, gas flow, ICP generator power, RF generator power and etching time. In this work, only physical etching is used with Argon gas, no chemical etching,

Temperature set at -10 °C due to hitting of ions increase the sample temperature. 1.8e⁻⁶ Torr pressure, 20 sccm gas flow, 100 W ICP generator power, 300 W RF generator power are used for few seconds. The etching rate of the resist is a factor of 2.7 larger than the etching rate of FePt.

After all of the process done for fabrication, AFM and MFM images are shown in Fig. 5.6.

A.3. The structured pattern images of 3-D and down scale.

The regular arrange of nanomagnet pattern, and the height of 80 – 90 nm of each nanodot are confirmed by 3-D AFM image.



A.4 EDX results of t_3 and t_7 nanodots

The 3 nm and 7 nm thickness of Co layer are formed nanodots structure no thin film. The thicknesses of Co layer in exchange-spring nanomagnet were verified by EDX measurement.

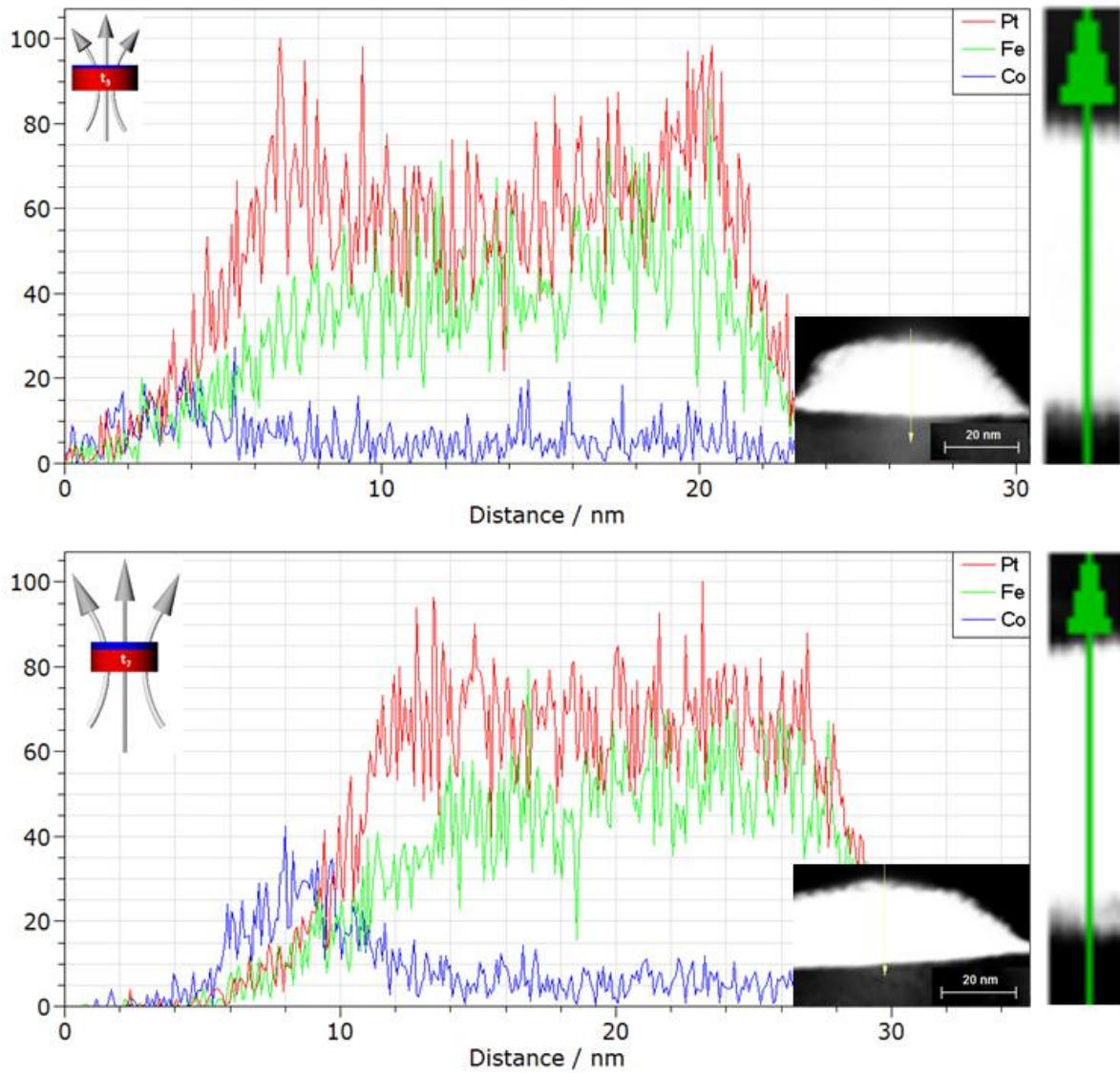
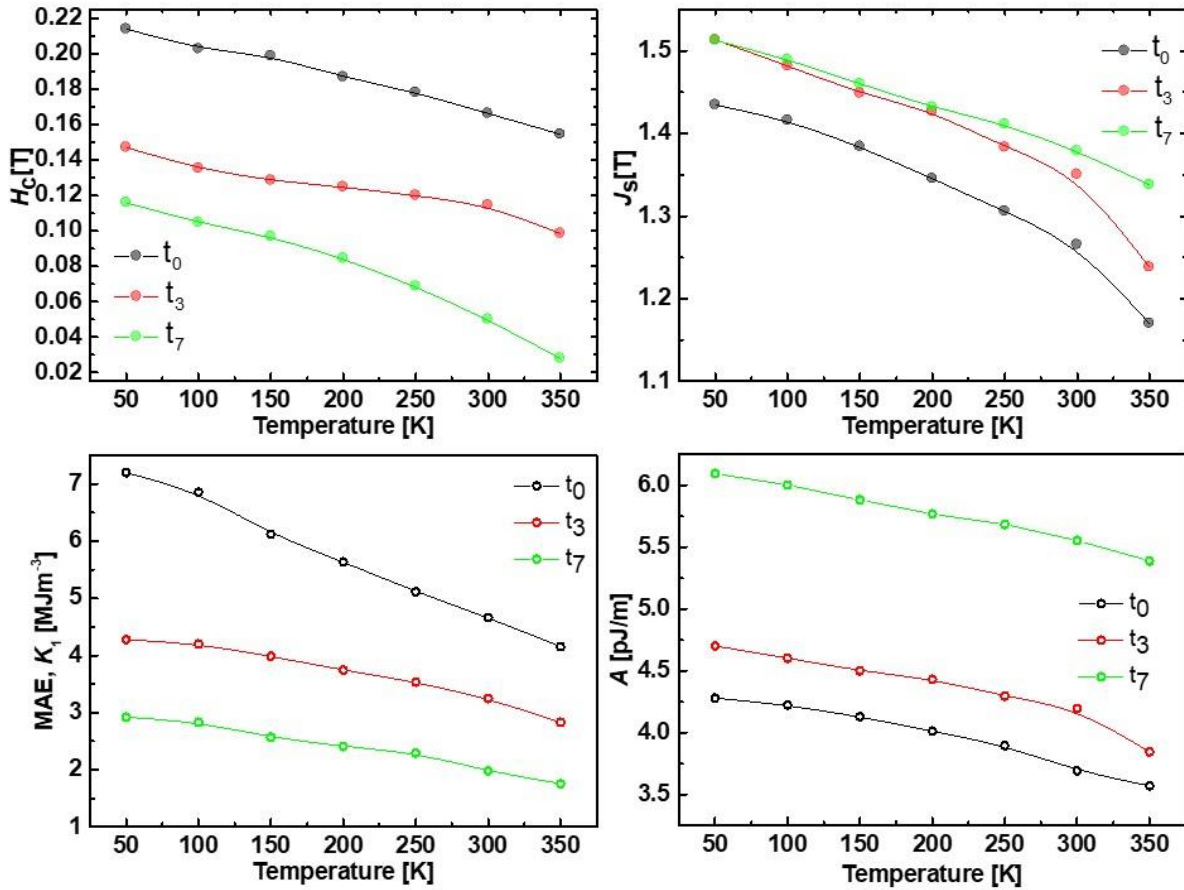


Fig. A.4 Confirmation of cobalt and FePt thickness in t_3 and t_7 by EDX measurements

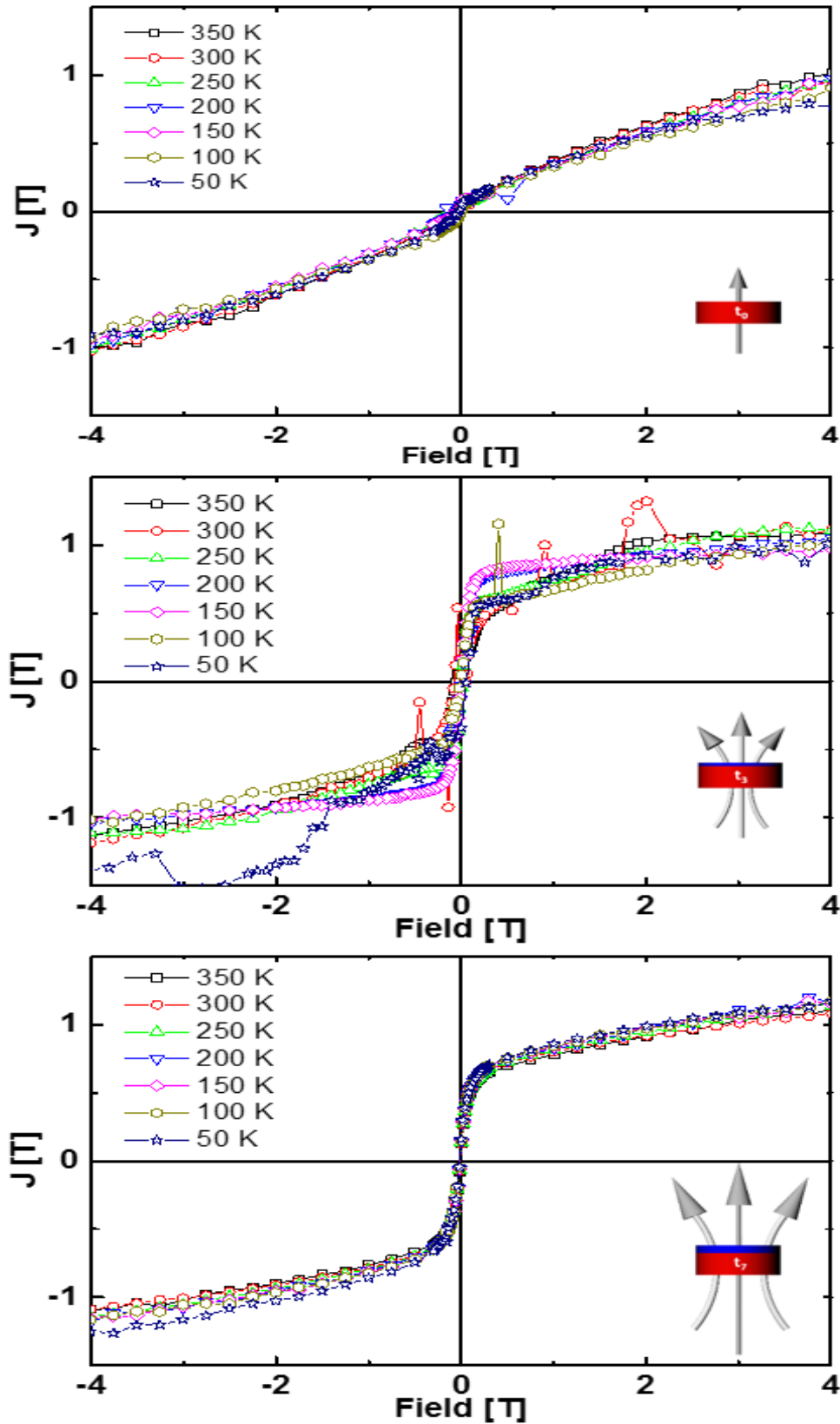
A.5. Magnetic parameters of exchange-spring multilayers.

The experimental result of magnetic parameters (H_C , J_S , K_1 , and A) in exchange spring multilayers with different thickness of the Co soft magnetic layer is presented.



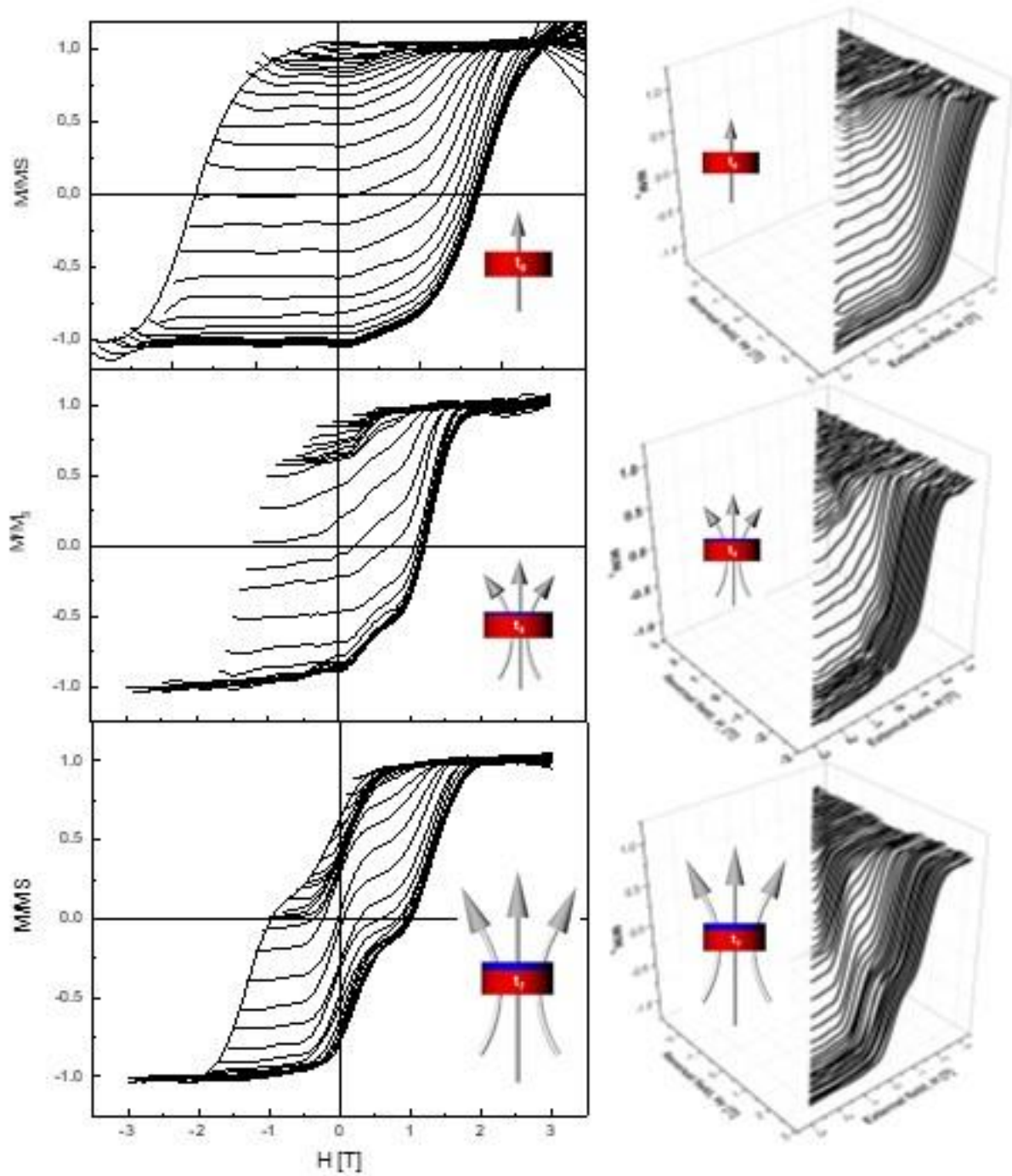
A.6. The in-plane hysteresis loops of nanopatterns

Temperature dependent hysteresis loops of nanopatterns t_0 , t_3 , and t_7 samples. The ES magnet patterns which include Co soft layers are shows easy to magnetize to in-plane direction.



A.7 The minor loops of FORCs measurement

The three kinds of ES nanomagnet patterns have been measured first order reversal curves methods. Fig. A.7 shows minor loops of FORCs before analysis to FORCs density.



A.8 The switching field distribution (SFD) by derivation

The switching field distribution SFD is obtained from FORCs density at peak of coercivity distribution. The pure $L1_0$ -FePt has broader distribution with higher coercivity. The perfectly coupled ES magnet has narrower distribution while higher intensity. The partially coupled ES magnet has two parts of reversal behavior with decoupled and coupled parts. The integration of FORCs explains the each nanomagnet becomes a hysteron in Preisach model.

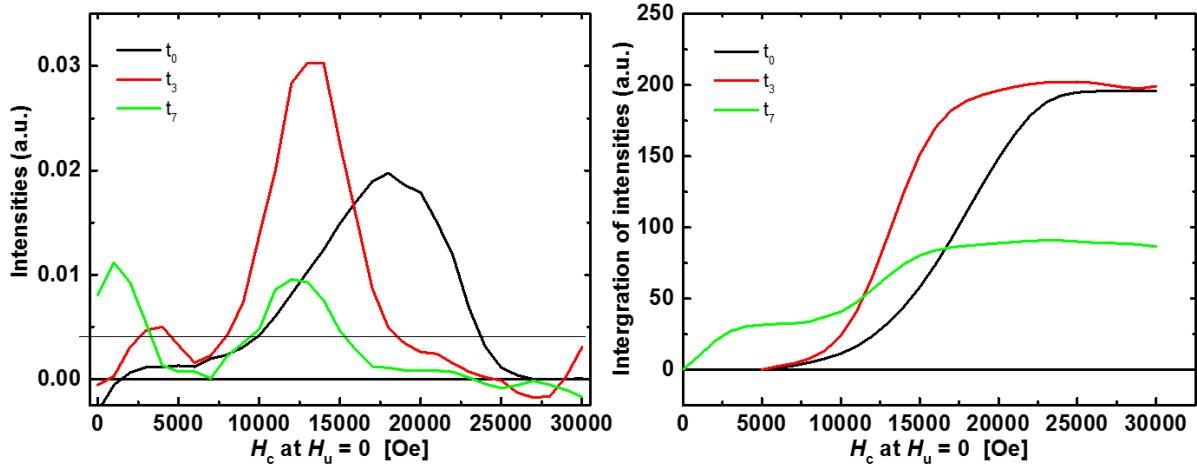
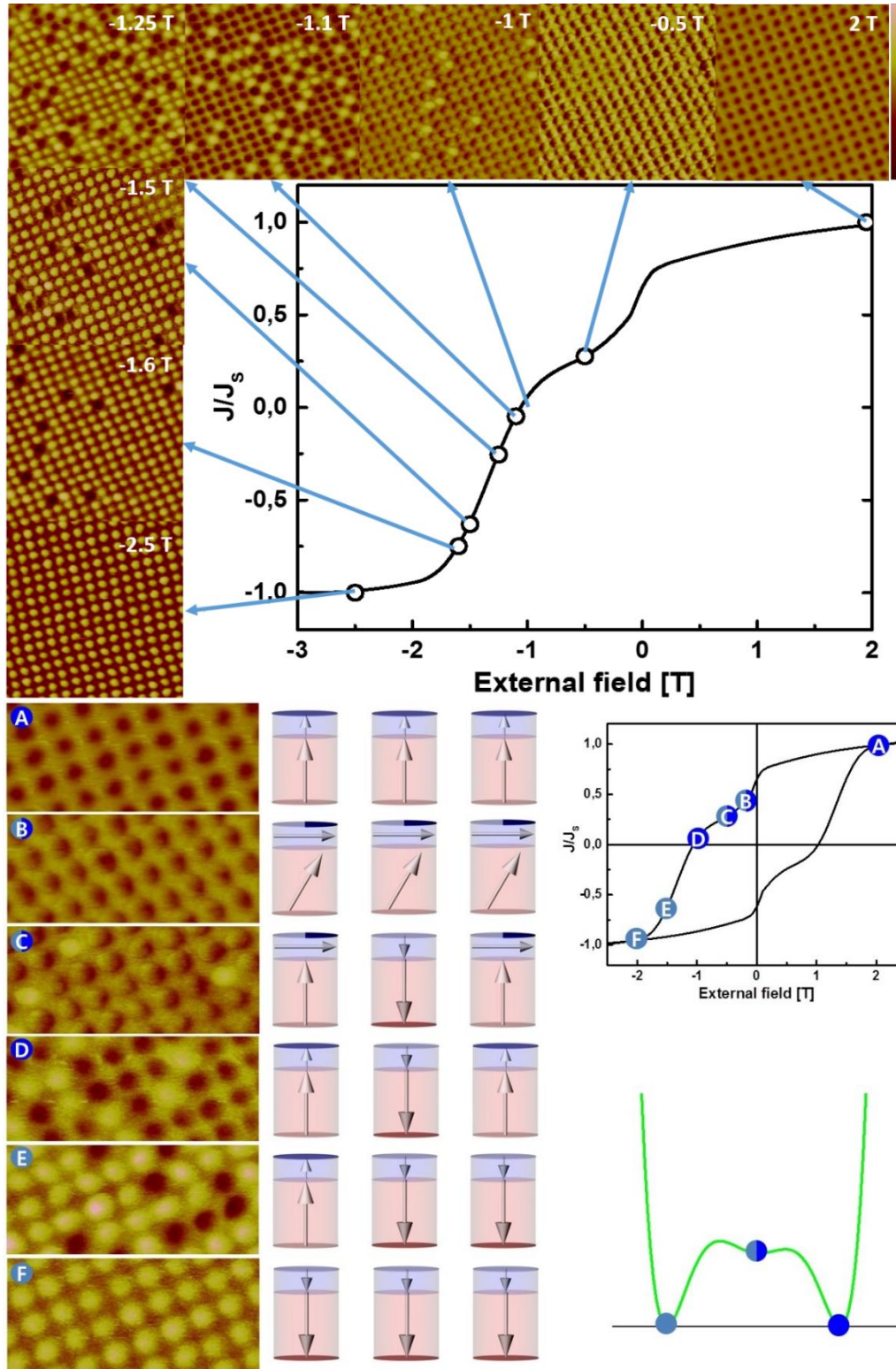


Fig. A 8 The coercive field distribution at $H_u=0$ Oe.

	H_c FWHM [Oe]	H_u FWHM [Oe]
t_0	~9900	~2800
t_3	~4900	~1800
t_7	~7300	~2900

A.9 The microscopic magnetic reversal process by the MFM images at the certain field.

The hard and the soft layers in the t_7 sample are partially coupled each other. MFM images of certain fields show magnetic switching behavior with domain structures. And the magnetic reversal behavior assumed and illustrated below.



A.10 AFM and MFM ridges at various fields

To investigate the reason for the two steps of the hysteresis loop, several line intensity analysis of AFM and MFM measurements were performed at various fields. The results are shown in Figs A.10.1. The height and width of each nanomagnet can be directly derived from the AFM (black line), and magnetic switching from the MFM (green line). Fig. A.10.1 shows the AFM and MFM ridges at fields where both layers have either switched or not. The MFM images in this range are the same MFM images as in the as-etched state after fabrication. As can be seen from the figure, a thicker nanomagnet keeps the magnetization from switching. In fig.A.10.1 bottom, the magnets that switch latest, i.e. in highest field, only, can be seen. A higher height or a flat switch later.

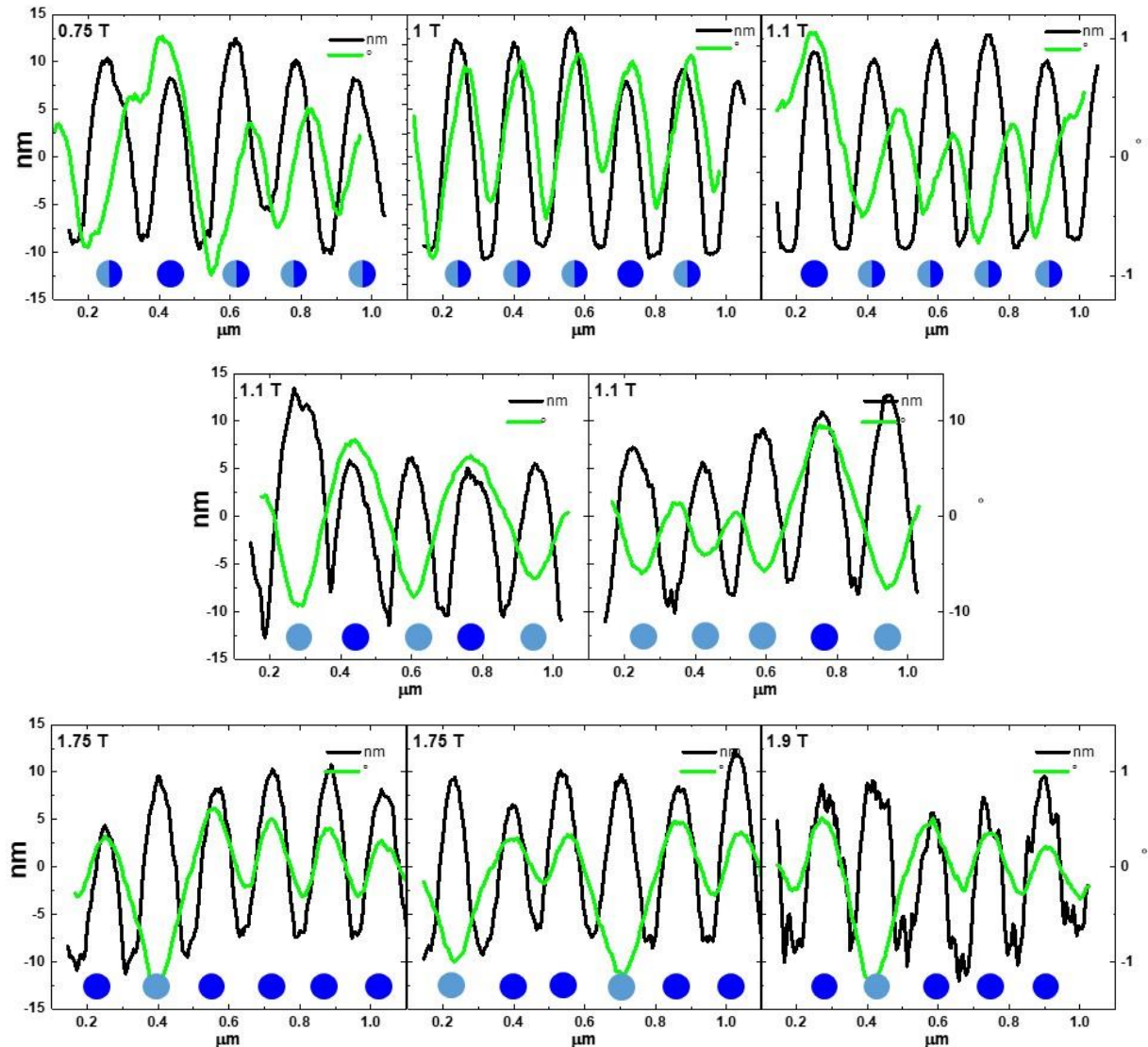


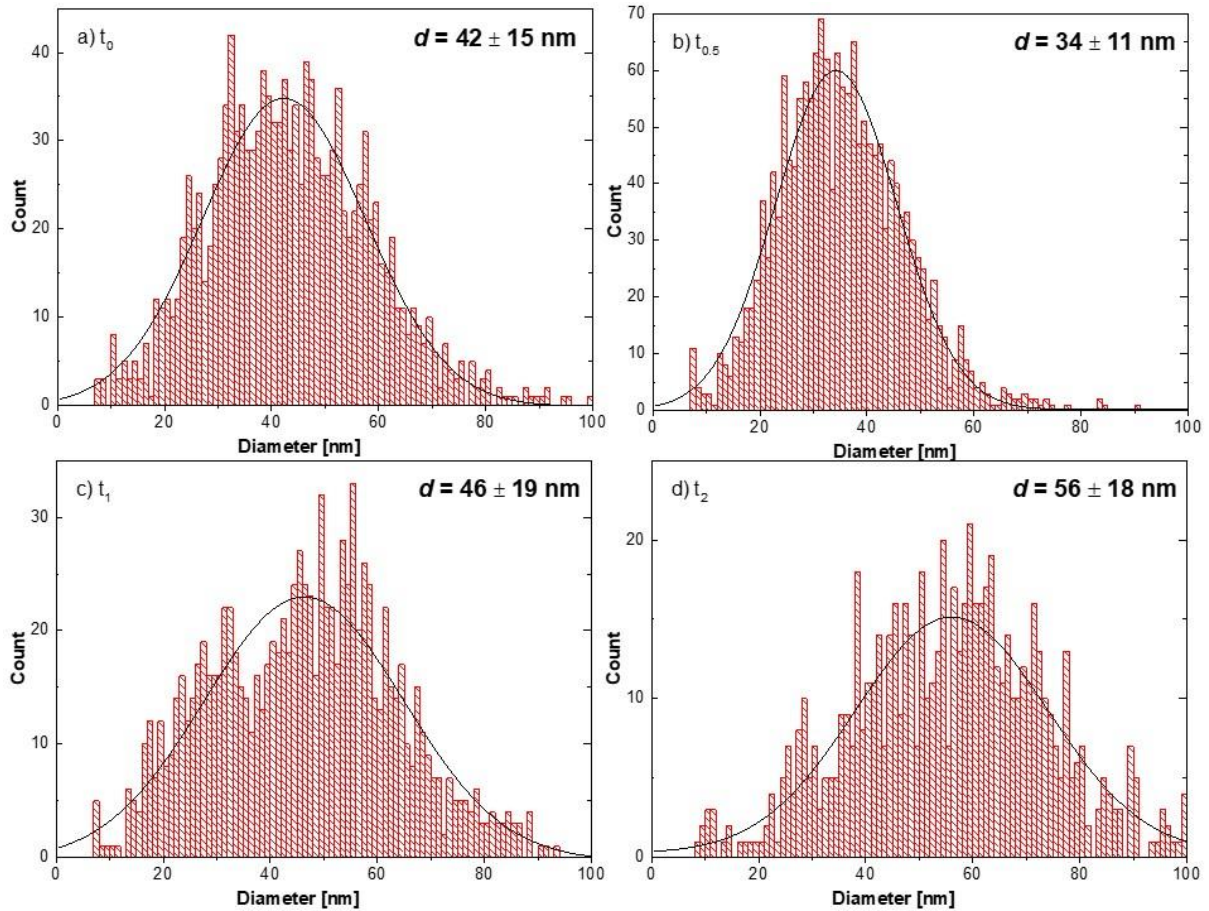
Fig. A. 10. 1 The profiles of AFM (black) and MFM (green) ridges at earlier switching, 1.1 T, 1.75 T and 1.9 T. The domains represent colors of blue (up) and sky-blue (down). Smaller magnets are earlier switched.

At field of 0.75 T and 1 T, two domains are formed, as visible in the top view of MFM images. They are indicated by dark and light blue colors. A nanomagnet, which contains both colors, seems to have two magnetic domains. The earlier switched nanomagnets (i.e. switched at lower field) show less height in MFM. The decoupled parts of the Co layers in each nanomagnet are switched from 0 to -1 T.

Appendix B

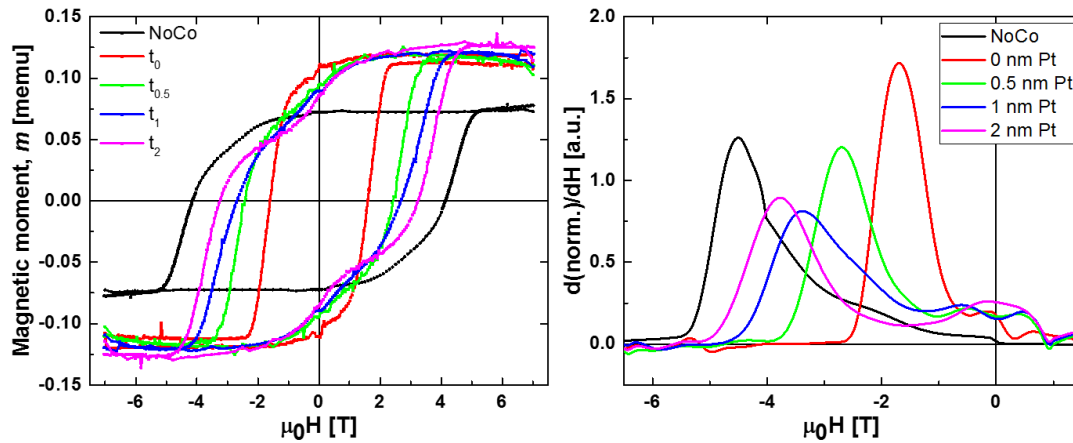
B.1 The grain size distributions

The grain size distributions of $L1_0$ -FePt/ Pt/ Co/ Pt exchange-spring multilayers on MgO(100) substrate, were counted and calculated from SEM images. The average size and the particle size distributions are analyzed. A total thickness increases, the packing area and grain size increases. The average grain diameters d and diameter range are t_0 : 42 ± 15 nm, $t_{0.5}$: 34 ± 11 nm, t_1 : 46 ± 19 nm and t_2 : 56 ± 18 nm. The t_2 sample has bigger than 100 nm grains, too. The particle sizes are related to the critical domain size, D_C and the switching diameter D_{sw}



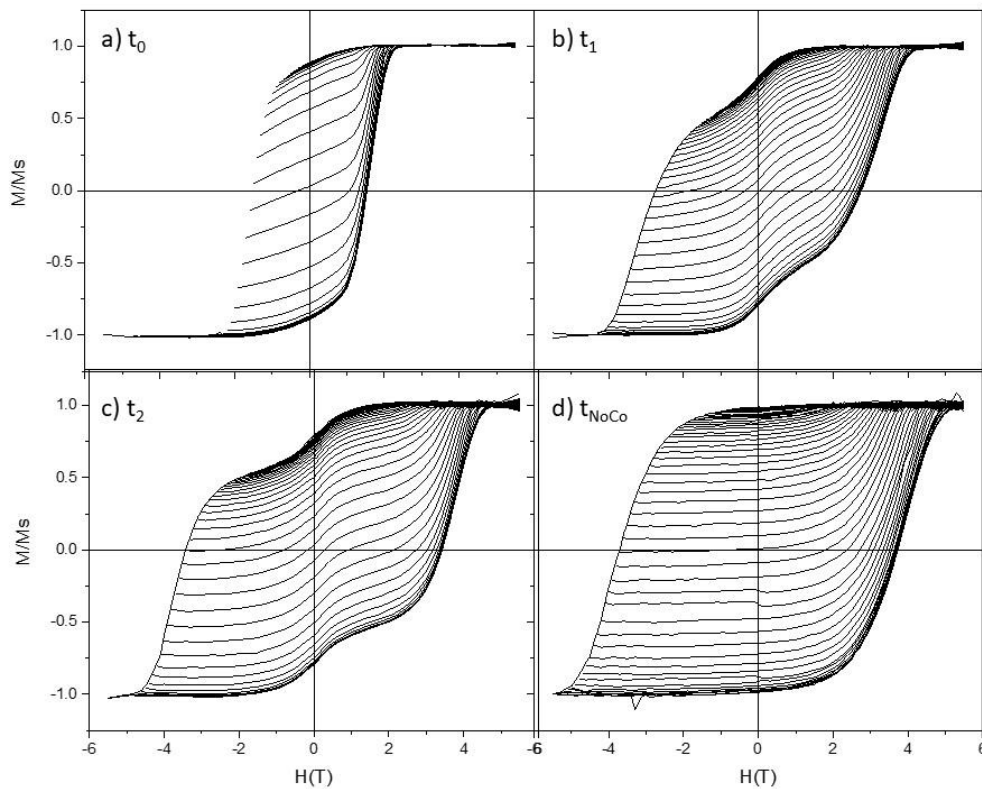
B.2 Hysteresis loops of magnetic moment and Switching field distribution (SFD) by derivation.

The out-of-plane hysteresis loops (magnetic polarization and magnetic moments) and switching field distribution (SFD) of $L1_0$ -FePt/ Pt/ Co/ Pt exchange-spring magnetic multilayers and FePt thin film on MgO(100) substrate at RT.



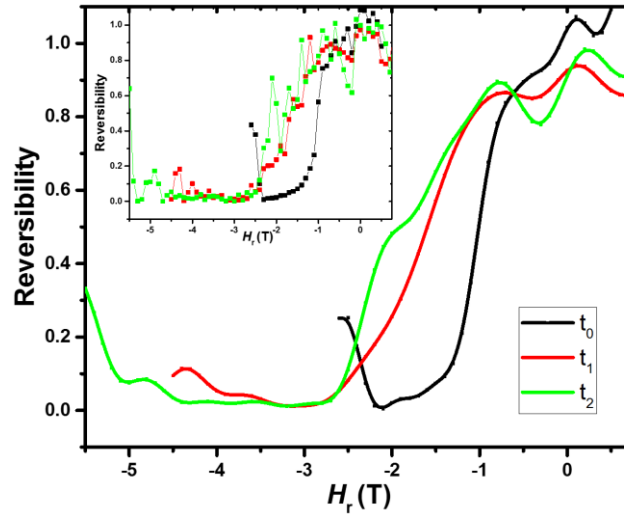
B.3 The minor loops of FORCs measurement

The tuned exchange spring multilayer by interlayer thickness have been measured by FORCs methods using SQUID magnetometry



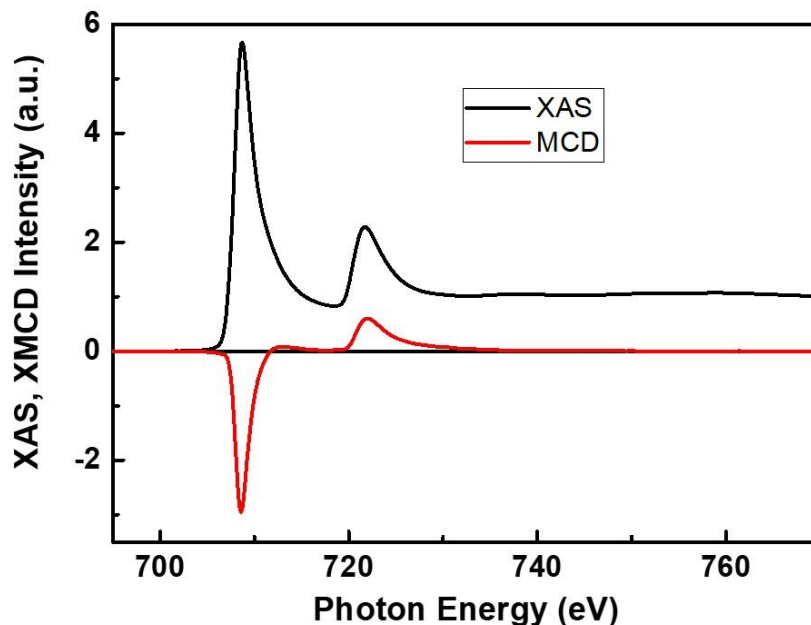
B.4 The reversibility of exchange-spring multilayers.

Moreover, reversibility, η is calculated by $\eta = \chi_{FORC} / \chi_{Hyst}$ in section 4.2.3.2. The η results support influence of the Co soft magnet layer in exchange-spring multilayers. Fig shows the η variations. The soft magnet pushes the hard magnet to reverse. Despite equal quantities of hard and soft, according to coupling strength, reversibility is also affected.



B.5 XAS and XMCD spectra of FePt of bulk (40 nm thickness)

The pure $L1_0$ -FePt have been investigated by XMCD measurement. The shape of spectra in ES magnet was compared with $L1_0$ -FePt spectra of 40 nm. The magnetic moments of bulk sample of 40 nm thickness were analyzed by Sum Rules. Fe has orbital moment of 0.25 bohr magneton and spin moment of 2.21 bohr magneton.



B.6 Angle dependent XMCD measurements for ξ and T_Z

To study anisotropy change, 60° angle-dependent measurements were fulfilled. The XAS and XMCD spectra with angle are in fig. B 5.1.

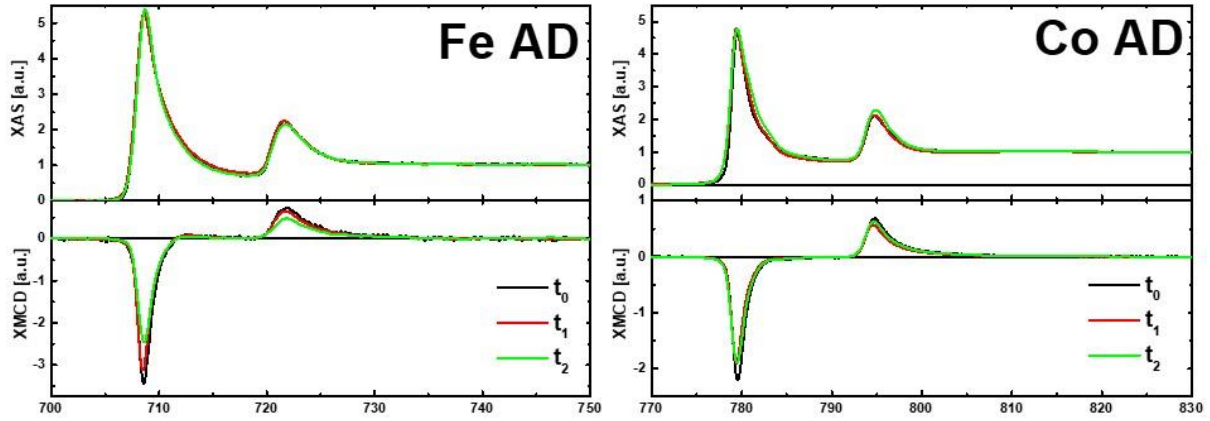


Fig B 5.1 Normalized XAS and XMCD spectra. XAS and XMCD spectra were measured at RT and saturation field with 60° angle dependent measurement.

The angle dependent spectra also show highest intensities spectra of t_1 in Fe edges and t_2 in Co edges. The spectra of angle-dependent measurements at RT and 6 T were analyzed sum rules in Table 6.6.

AD		m_s [μ_B]	m_l [μ_B]	m_{total} [μ_B]	m_l/m_s ratio
Fe	t_0	2.64	0.28	2.92	0.1
	t_1	2.31	0.25	2.56	0.11
	t_2	2.01	0.24	2.24	0.12
Co	t_0	1.81	0.17	1.98	0.09
	t_1	1.46	0.15	1.61	0.1
	t_2	1.41	0.13	1.54	0.1

Table B 5.1 The sum rules results of XMCD measurement at 60° angle incidence. Spin, orbital and total magnetic moment and the ratio of orbital to spin.

The overall behaviors are similar both NI and AD results.

The magnetic dipole moment term $\langle T_z \rangle$, the variation of orbital magnetic moment Δm_l and spin-orbit constant ξ can be calculated with NI results and AD result.

AD		T_z [μ_B]	Δm_l	MAE [meV/atom]	ξ [meV]
Fe	t_0	-0.002	-0.12	3.96	10.12
	t_1	0.026	-0.05	4.47	14.13
	t_2	0.034	0.03	7.21	29.91
Co	t_0	0.004	0.07	0.702	3.61
	t_1	-0.003	0.04	0.634	3.85
	t_2	0.002	0.03	0.253	1.56

Table B 5.2 The dipole moment T_z , the variation of orbital magnetic moment Δm_l , magnetocrystalline anisotropy energy, MAE of atom and spin-orbit constant ξ of exchange-spring multilayers.

All of the dipole terms are negligible. It is less than 1% to spin moment. Nevertheless, the tendency according to coupling can be confirmed. The variation of the orbital magnetic moment of Fe is increased by decoupling. Whereas Δm_l of Co is increased by coupling. The spin-orbit constant ζ of Fe is corresponded to increasing of the magnetocrystalline anisotropy energy and orbital moments. The Co is released from L1₀-FePt hard magnets by decoupling. All of XMCD analysis results are displayed to see tendency each values by interlayer thickness in B 5.2.

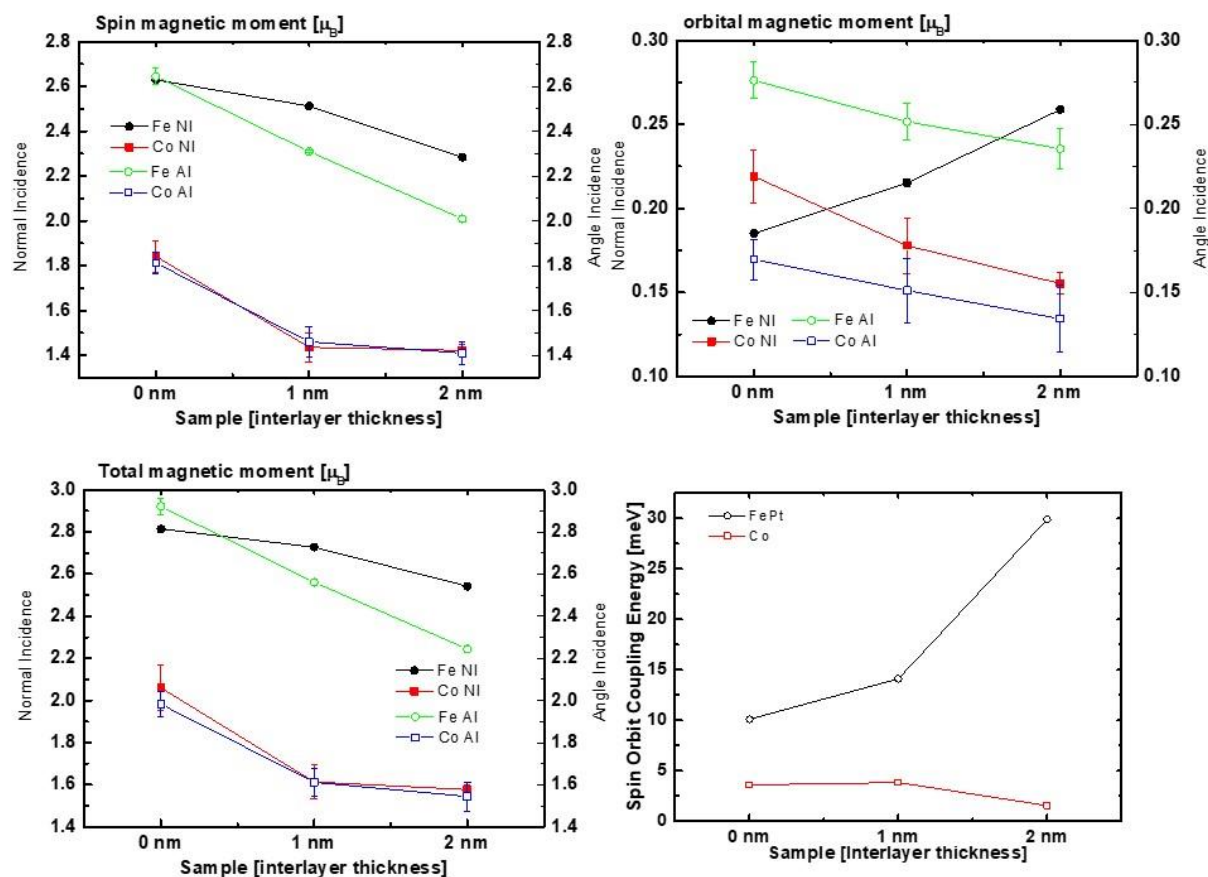


Fig. B 5.2 The sum rules results from XAS and XMCD spectra. Spin magnetic moment (up-left), orbital magnetic moment (up-right) and total magnetic moment (down-left) are analyzed by Sum Rules. The spin-orbit constant ζ are obtained Bruno model which is a relation of anisotropy, spin, orbit moment and energy split.

B.7 Normalized hysteresis loops at L₃-edge

Normalized hysteresis loops measured by SQUID and XAS are compared. According to coupling, magnetic reversal behavior of the Co soft layer is changed. The coercivity of Co in perfectly coupled sample is similar with Fe. In partially coupled sample, it reduced half of Fe coercivity. The switching of Fe and Co is behaved, independently in de-coupled sample. (Fig. B. 6. 1 upper) The angle dependent measurements are also similar. (Fig. B. 6. 1 bottom)

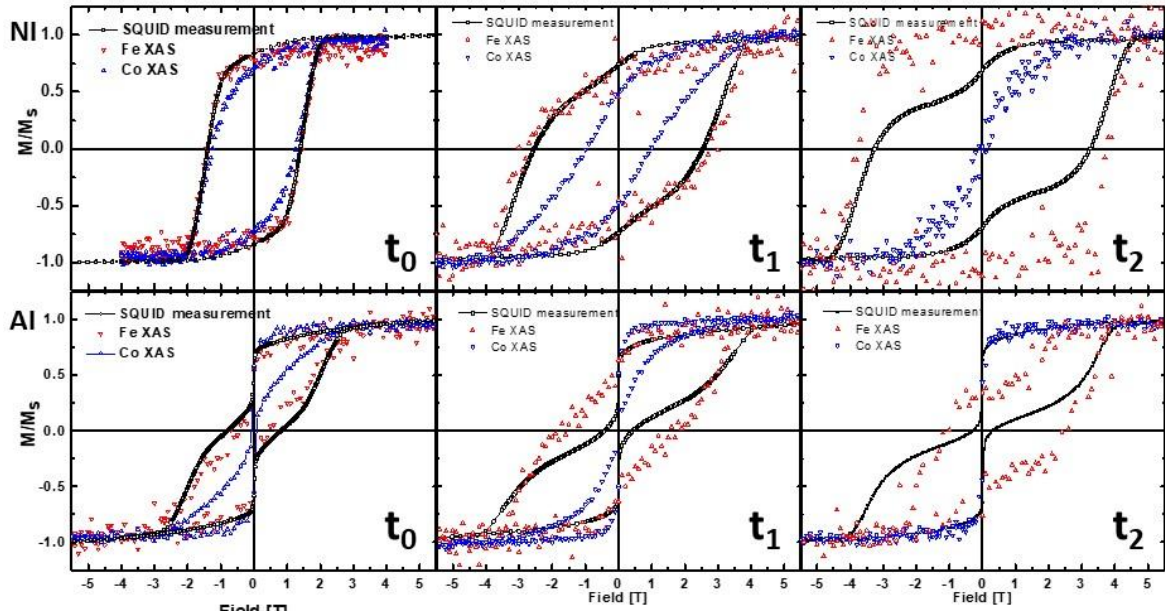


Fig B.6.1 The hysteresis XMCD and SQUID data. Upper line: in normal incidence (NI) and bottom line: in 60° angle-dependent measurements (AD) of exchange-spring multilayers with different interlayer thickness. Left to right is samples t_0 to t_2 .

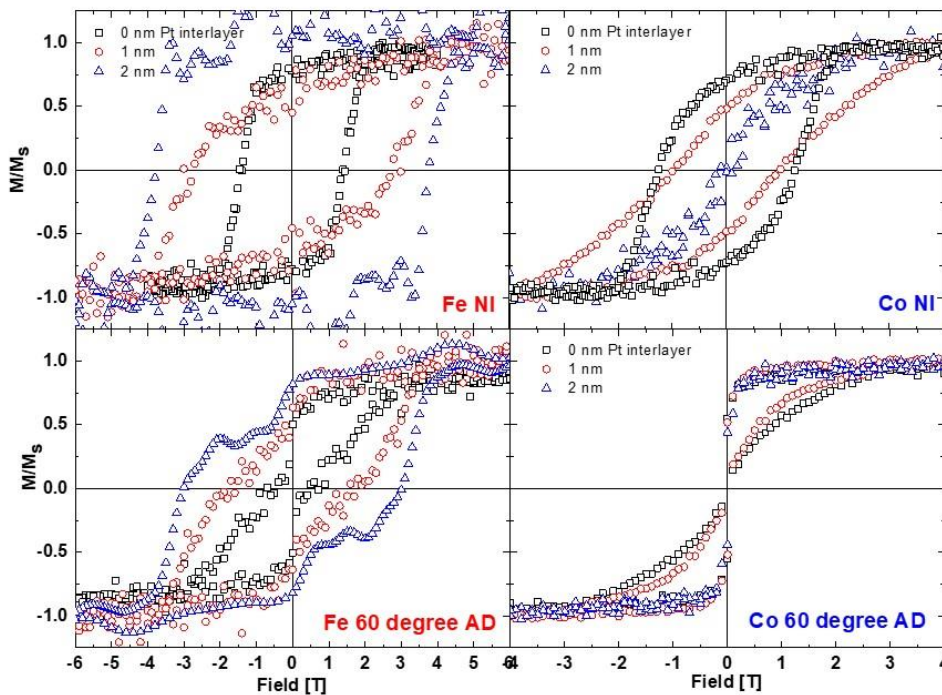
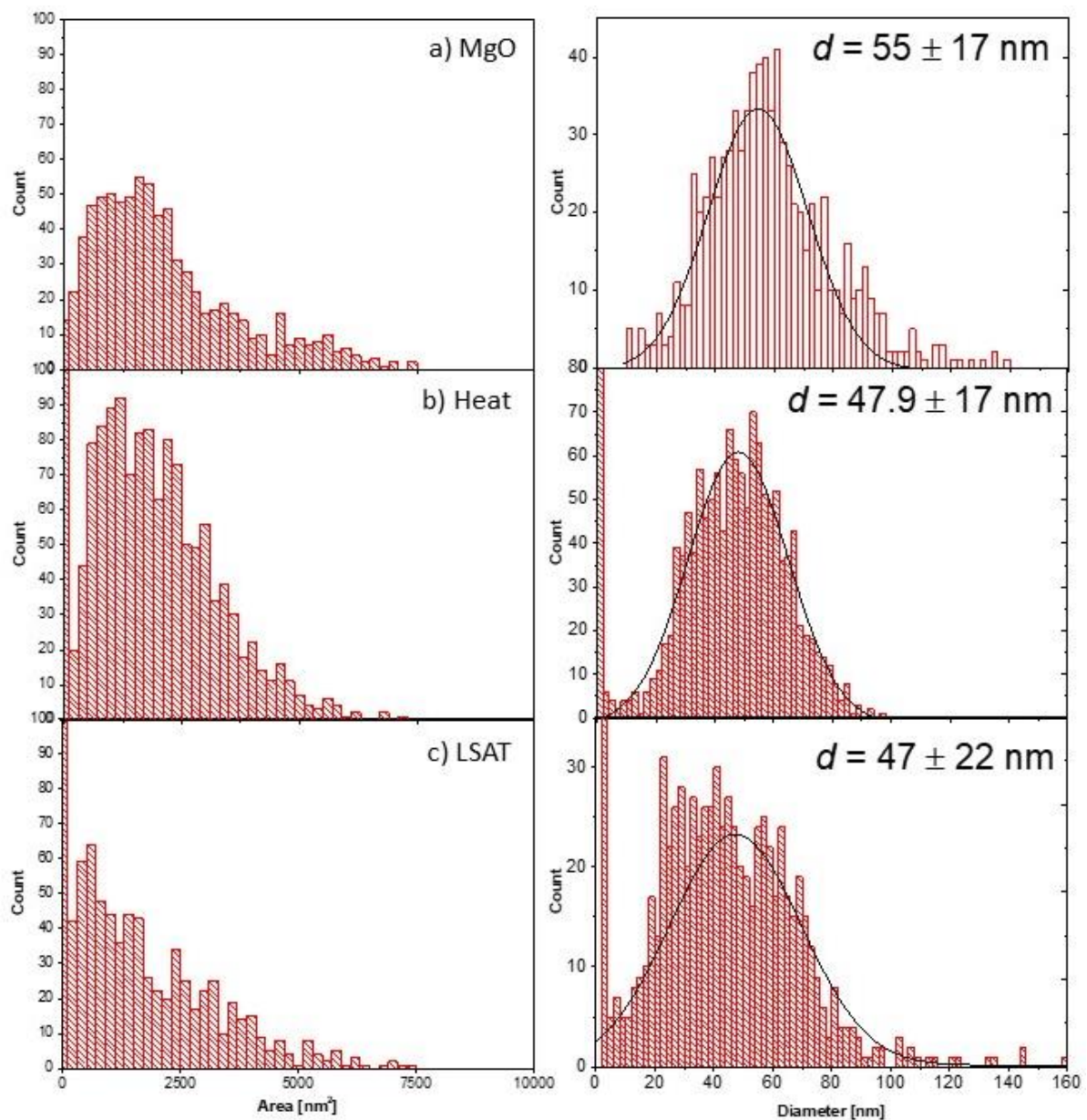


Fig B.6.2 Comparison of Fe and Co hysteresis loops by each samples. Upper left : Fe normal incidence (NI), Upper right: Co NI, bottom left: Fe angle dependent (AD) and bottom right: Co AD.

Appendix C

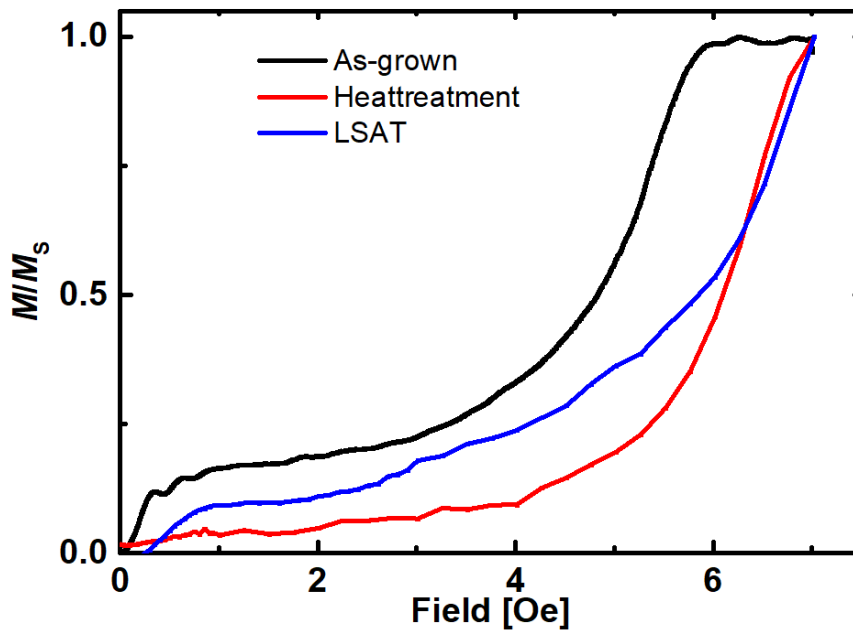
C.1 Distribution of grain size of uncovered 7 nm L1₀-FePt samples.

MgO has bigger grain size. MgO and Heat have similar distribution. However, Heat and LSAT have smaller area.



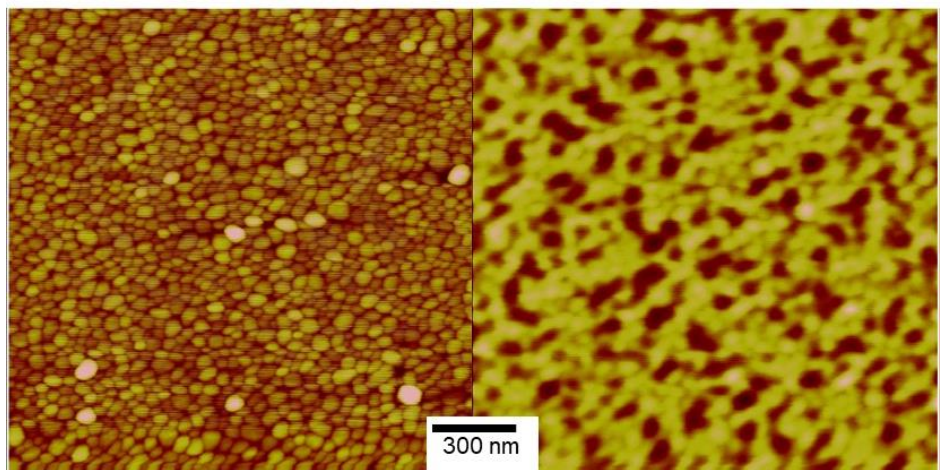
C.2 The initial magnetization curves

The MgO sample is first increased at low field, next is LSAT, and last is Heat sample. The critical size of FePt is 40- 60 nm depends on the thickness of films. For 7 nm FePt is $D_c = \sim 34$ nm by experiment. All samples are bigger than the critical size. Those grains are formed multi-domains. The multi-domains are magnetized even lower field. Heat and LSAT samples have many of single domain grains. To rotate the magnetization of single domains, it needs more energy. So, increasing of magnetization in heat sample is started at higher field. However, the LSAT sample has grain sized distributions variously from single domains to multi-domains. So, LSAT shows two steps behavior at the low and high field.



C.3 MFM image

The 7 nm thickness $L1_0$ -FePt thin film is granular structure. Few grains form the magnetic domain with the same direction.



Literature

- [1] P. Gambardella, S. Rusponi, M. Veronese, S.S. Dhesi, C. Grazioli, A. Dallmeyer, I. Cabria, R. Zeller, P.H. Dederichs, K. Kern, C. Carbone, H. Brune, Giant Magnetic Anisotropy of Single Cobalt Atoms and Nanoparticles, *Science*, 300 (2003) 1130-1133.
- [2] D.J. Carnevale, M. Shatruk, G.F. Strouse, Ligand Passivated Core–Shell FePt@Co Nanomagnets Exhibiting Enhanced Energy Product, *Chemistry of Materials*, 28 (2016) 5480-5487.
- [3] T. Bublath, D. Goll, Influence of dot size and annealing on the magnetic properties of large-area L10-FePt nanopatterns, *Journal of Applied Physics*, 110 (2011) 073908.
- [4] H. Zeng, J. Li, J.P. Liu, Z.L. Wang, S. Sun, Exchange-coupled nanocomposite magnets by nanoparticle self-assembly, *Nature*, 420 (2002) 395-398.
- [5] C.b. Rong, D. Li, V. Nandwana, N. Poudyal, Y. Ding, Z.L. Wang, H. Zeng, J.P. Liu, Size-Dependent Chemical and Magnetic Ordering in L10-FePt Nanoparticles, *Advanced Materials*, 18 (2006) 2984-2988.
- [6] F. Preisach, Über die magnetische Nachwirkung, *Zeitschrift für Physik*, 94 (1935) 277-302.
- [7] M. Rosu, T. Jokinen, E. Demeter, Simulation Of The Magnetic Hysteresis In NdFeB Permanent Magnet Using Preisach's Model, *Proceedings of the 6th International Conference on Optimization of Electrical and Electronic Equipments*, 1998, pp. 11-14.
- [8] J. Stöhr, H.C. Siegmann, *Magnetism: From Fundamentals to Nanoscale Dynamics*, Springer 2006.
- [9] S. Blundell, *Magnetism in Condensed Matter (Oxford Master Series in Physics)*, Oxford University Press, USA 2001.
- [10] M.F. Helmut Kronmüller, *Micromagnetism and the Microstructure of Ferromagnetic Solids* Cambridge University Press; 1 edition (September 29, 2003) 2003.
- [11] C. Kittel, *Introduction to solid state physics*, Wiley 1976.
- [12] C.T. Chen, Y.U. Idzerda, H.J. Lin, N.V. Smith, G. Meigs, E. Chaban, G.H. Ho, E. Pellegrin, F. Sette, Experimental Confirmation of the X-Ray Magnetic Circular Dichroism Sum Rules for Iron and Cobalt, *Physical Review Letters*, 75 (1995) 152-155.
- [13] Y.M. D. Harimoto, *Hitachi Met. Tech. Rev. (in Japanese)*, 23 (2007) 69.
- [14] E.C. Stoner, E.P. Wohlfarth, A Mechanism of Magnetic Hysteresis in Heterogeneous Alloys, *Philos Tr R Soc S-A*, 240 (1948) 599-642.
- [15] H. Kronmüller, Theory of Nucleation Fields in Inhomogeneous Ferromagnets, *physica status solidi (b)*, 144 (1987) 385-396.
- [16] I.D. Mayergoyz, *Mathematical Models of Hysteresis*, Springer-Verlag New York 1991.
- [17] A.J. Newell, A high-precision model of first-order reversal curve (FORC) functions for single-domain ferromagnets with uniaxial anisotropy, *Geochemistry, Geophysics, Geosystems*, 6 (2005) n/a-n/a.
- [18] I.D. Mayergoyz, Hysteresis models from the mathematical and control theory points of view, *Journal of Applied Physics*, 57 (1985) 3803-3805.
- [19] C.R. Pike, A.P. Roberts, K.L. Verosub, Characterizing interactions in fine magnetic particle systems using first order reversal curves, *Journal of Applied Physics*, 85 (1999) 6660-6667.

- [20] C.R. Pike, A.P. Roberts, M.J. Dekkers, K.L. Verosub, An investigation of multi-domain hysteresis mechanisms using FORC diagrams, *Physics of the Earth and Planetary Interiors*, 126 (2001) 11-25.
- [21] C.-I. Dobrotă, A. Stancu, Tracking the individual magnetic wires' switchings in ferromagnetic nanowire arrays using the first-order reversal curves (FORC) diagram method, *Physica B: Condensed Matter*, 457 (2015) 280-286.
- [22] F. Béron, L. Clime, M. Ciureanu, D. Ménard, R.W. Cochrane, A. Yelon, Reversible and quasireversible information in first-order reversal curve diagrams, *Journal of Applied Physics*, 101 (2007) 09J107.
- [23] J.E. Davies, O. Hellwig, E.E. Fullerton, J.S. Jiang, S.D. Bader, G.T. Zimányi, K. Liu, Anisotropy dependence of irreversible switching in Fe/SmCo and FeNi/FePt exchange spring magnet films, *Applied Physics Letters*, 86 (2005) 262503.
- [24] C.R. Pike, C.A. Ross, R.T. Scalettar, G. Zimanyi, First-order reversal curve diagram analysis of a perpendicular nickel nanopillar array, *Physical Review B*, 71 (2005) 134407.
- [25] J.E. Davies, O. Hellwig, E.E. Fullerton, G. Denbeaux, J.B. Kortright, K. Liu, Magnetization reversal of Co/Pt multilayers: Microscopic origin of high-field magnetic irreversibility, *Physical Review B*, 70 (2004) 224434.
- [26] C.W. Abert, *Discrete Mathematical Concepts in Micromagnetic Computations*, Staats- und Universitätsbibliothek Hamburg, Hamburg, 2013.
- [27] J.D. Jackson, *Classical electrodynamics*, Wiley1975.
- [28] H. Kronmüller, M. Fhnlé, *Micromagnetism and the Microstructure of Ferromagnetic Solids*, Cambridge University Press2003.
- [29] A. Hubert, R. Schäfer, *Magnetic Domains: The Analysis of Magnetic Microstructures*, Springer1998.
- [30] A.H. Morrish, *The physical principles of magnetism*, Wiley1965.
- [31] R.P. Feynman, F.R.P.S.M.L.L.R. B, R.B. Leighton, M. Sands, *The Feynman Lectures on Physics, Desktop Edition Volume II: The New Millennium Edition*, Basic Books2013.
- [32] R.M. Bozorth, *Ferromagnetism*, Wiley1993.
- [33] M. Noske, *Ultraschnelles Vortextkernschalten*, *Modern Magnetic Systems*, Universität Stuttgart, Stuttgart, 2015, pp. 227.
- [34] B.D. Cullity, C.D. Graham, *Introduction to Magnetic Materials*, Wiley2009.
- [35] W.F. Brown, Virtues and Weaknesses of the Domain Concept, *Reviews of Modern Physics*, 17 (1945) 15-19.
- [36] E.H. Frei, S. Shtrikman, D. Treves, Critical Size and Nucleation Field of Ideal Ferromagnetic Particles, *Physical Review*, 106 (1957) 446-455.
- [37] H. Kronmüller, S. Parkin, *Handbook of magnetism and advanced magnetic materials: Spintronics and magnetoelectronics*, John Wiley & Sons2007.
- [38] H. Kronmüller, K.D. Durst, M. Sagawa, Analysis of the magnetic hardening mechanism in RE-FeB permanent magnets, *Journal of Magnetism and Magnetic Materials*, 74 (1988) 291-302.
- [39] H. Kronmüller, K.D. Durst, G. Martinek, Angular dependence of the coercive field in sintered Fe₇₇Nd₁₅B₈ magnets, *Journal of Magnetism and Magnetic Materials*, 69 (1987) 149-157.
- [40] D. Goll, M. Seeger, H. Kronmüller, Magnetic and microstructural properties of nanocrystalline exchange coupled PrFeB permanent magnets, *Journal of Magnetism and Magnetic Materials*, 185 (1998) 49-60.

- [41] M. Faraday, Experimental Researches in Electricity. Nineteenth Series, Philosophical Transactions of the Royal Society of London., 136 (1846) 1-20.
- [42] J. Kerr, XLIII. On rotation of the plane of polarization by reflection from the pole of a magnet, Philosophical Magazine Series 5, 3 (1877) 321-343.
- [43] G. Schütz, W. Wagner, W. Wilhelm, P. Kienle, R. Zeller, R. Frahm, G. Materlik, Absorption of circularly polarized x rays in iron, Physical Review Letters, 58 (1987) 737-740.
- [44] G. Schütz, M. Knülle, R. Wienke, W. Wilhelm, W. Wagner, P. Kienle, R. Frahm, Spin-dependent photoabsorption at the L-edges of ferromagnetic Gd and Tb metal, Zeitschrift für Physik B Condensed Matter, 73 (1988) 67-75.
- [45] G. Schütz, R. Wienke, W. Wilhelm, W. Wagner, P. Kienle, R. Zeller, R. Frahm, Strong spin-dependent absorption at the L₂-edges of 5d-impurities in iron, Zeitschrift für Physik B Condensed Matter, 75 (1989) 495-500.
- [46] C.T. Chen, F. Sette, Y. Ma, S. Modesti, Soft-x-ray magnetic circular dichroism at the $L_{2,3}$ edges of nickel, Physical Review B, 42 (1990) 7262-7265.
- [47] E. Goering, S. Gold, G. Schutz, Ho-Fe-Garnet soft XMCD measurements below and above the compensation temperature, Journal of Synchrotron Radiation, 8 (2001) 422-424.
- [48] B.T. Thole, P. Carra, F. Sette, G. van der Laan, X-ray circular dichroism as a probe of orbital magnetization, Physical Review Letters, 68 (1992) 1943-1946.
- [49] P. Carra, B.T. Thole, M. Altarelli, X. Wang, X-ray circular dichroism and local magnetic fields, Physical Review Letters, 70 (1993) 694-697.
- [50] Dr. h.c. Hermann Haken, D.H.C. Wolf, The Physics of Atoms and Quanta, Springer Berlin Heidelberg 2000.
- [51] E. Goering, A. Bayer, S. Gold, G. Schütz, M. Rabe, U. Rüdiger, G. Güntherodt, Strong Anisotropy of Projected d Moments in Epitaxial CrO_2 Films, Physical Review Letters, 88 (2002) 207203.
- [52] L. Gerrit van der, Microscopic origin of magnetocrystalline anisotropy in transition metal thin films, Journal of Physics: Condensed Matter, 10 (1998) 3239.
- [53] R. Wu, A.J. Freeman, Limitation of the Magnetic-Circular-Dichroism Spin Sum Rule for Transition Metals and Importance of the Magnetic Dipole Term, Physical Review Letters, 73 (1994) 1994-1997.
- [54] J. Stöhr, H. König, Determination of Spin- and Orbital-Moment Anisotropies in Transition Metals by Angle-Dependent X-Ray Magnetic Circular Dichroism, Physical Review Letters, 75 (1995) 3748-3751.
- [55] P. Bruno, Tight-binding approach to the orbital magnetic moment and magnetocrystalline anisotropy of transition-metal monolayers, Physical Review B, 39 (1989) 865-868.
- [56] D. Weller, J. Stöhr, R. Nakajima, A. Carl, M.G. Samant, C. Chappert, R. Mégy, P. Beauvillain, P. Veillet, G.A. Held, Microscopic Origin of Magnetic Anisotropy in Au/Co/Au Probed with X-Ray Magnetic Circular Dichroism, Physical Review Letters, 75 (1995) 3752-3755.
- [57] G.v.d. Laan, I.W. Kirkman, The 2p absorption spectra of 3d transition metal compounds in tetrahedral and octahedral symmetry, Journal of Physics: Condensed Matter, 4 (1992) 4189.
- [58] E.G. Gisela Schütz, Hermann Stoll, Synchrotron Radiation Techniques, in: H. Kronmüller (Ed.) Handbook of Magnetism and Advanced Magnetic Materials, Wiley 2007, pp. 1309.
- [59] P. Tartaj, Nanomagnets-From Fundamental Physics to Biomedicine, Current Nanoscience, 2 (2006) 43-53.

- [60] V. Salgueiriño-Maceira, M.A. Correa-Duarte, M. Spasova, L.M. Liz-Marzán, M. Farle, Composite Silica Spheres with Magnetic and Luminescent Functionalities, *Advanced Functional Materials*, 16 (2006) 509-514.
- [61] M. Todorovic, S. Schultz, J. Wong, A. Scherer, Writing and reading of single magnetic domain per bit perpendicular patterned media, *Applied Physics Letters*, 74 (1999) 2516-2518.
- [62] R. Wang, O. Dmitrieva, M. Farle, G. Dumpich, M. Acet, S. Mejia-Rosales, E. Perez-Tijerina, M.J. Yacaman, C. Kisielowski, FePt Icosahedra with Magnetic Cores and Catalytic Shells, *The Journal of Physical Chemistry C*, 113 (2009) 4395-4400.
- [63] A. Jordan, R. Scholz, P. Wust, H. Schirra, S. Thomas, H. Schmidt, R. Felix, Endocytosis of dextran and silan-coated magnetite nanoparticles and the effect of intracellular hyperthermia on human mammary carcinoma cells in vitro, *Journal of Magnetism and Magnetic Materials*, 194 (1999) 185-196.
- [64] E.F. Kneller, R. Hawig, The exchange-spring magnet: a new material principle for permanent magnets, *IEEE Transactions on Magnetics*, 27 (1991) 3588-3560.
- [65] A.D. Volodchenkov, Y. Kodera, J.E. Garay, Synthesis of strontium ferrite/iron oxide exchange coupled nano-powders with improved energy product for rare earth free permanent magnet applications, *Journal of Materials Chemistry C*, 4 (2016) 5593-5601.
- [66] J.-H. Lee, J.-t. Jang, J.-s. Choi, S.H. Moon, S.-h. Noh, J.-w. Kim, J.-G. Kim, I.-S. Kim, K.I. Park, J. Cheon, Exchange-coupled magnetic nanoparticles for efficient heat induction, *Nat Nano*, 6 (2011) 418-422.
- [67] P.M.S. Monteiro, D.S. Schmool, Magnetization dynamics in exchange-coupled spring systems with perpendicular anisotropy, *Physical Review B*, 81 (2010) 214439.
- [68] A.P. Guimarães, *Principles of Nanomagnetism The Basis of Nanomagnetism*, Springer Berlin Heidelberg, 2009.
- [69] R. Wiltschko, *Magnetic Orientation in Animals*, Springer-Verlag Berlin Heidelberg, 1995, pp. XVII, 297.
- [70] Z.Z.B.a.R.H. Victora, *Advances in Magnetic Data Storage Technologies*, Proceedings of the IEEE, 96 (2008) 1749-1753.
- [71] S. Sun, H. Zeng, Size-Controlled Synthesis of Magnetite Nanoparticles, *Journal of the American Chemical Society*, 124 (2002) 8204-8205.
- [72] P. Gambardella, A. Dallmeyer, K. Maiti, M.C. Malagoli, W. Eberhardt, K. Kern, C. Carbone, Ferromagnetism in one-dimensional monatomic metal chains, *Nature*, 416 (2002) 301-304.
- [73] O. Fruchart, A. Thiaville, Magnetism in reduced dimensions, *Comptes Rendus Physique*, 6 (2005) 921-933.
- [74] F.H. V. Francois-Lavet, L. Stainier, L. Noels, C. Geuzaine, Vectorial Incremental Nonconservative Consistent Hysteresis model, *Proceeding of the Fifth International Conference on advanced COmputational Methods in Enginnering (ACOMEN 2011)*, DOI (2011) 10.
- [75] B. Cornut, J.L. Porteseil, C.n.d.l.r.s.L.d.m.L. Néel, *Soft Magnetic Materials 13: SMM 13*, September 24-26, 1997, Grenoble, France, EDP Sciences1998.
- [76] D.C. Jiles, *Introduction to Magnetism and Magnetic Materials*, Second Edition, Taylor & Francis1998.
- [77] G.E. Fish, *Soft magnetic materials*, Proceedings of the IEEE, 78 (1990) 947-972.

- [78] C.-W. Chen, CHAPTER 4 - MAGNETIC PROPERTIES, Magnetism and Metallurgy of Soft Magnetic Materials, Elsevier 1977, pp. 98-170.
- [79] H.W. Werner Martienssen, Springer Handbook of Condensed Matter and Materials Data, Springer-Verlag Berlin Heidelberg, 2005, pp. XVIII, 1121.
- [80] D. Paul, Domain wall pinning in the hard permanent magnet $\text{Sm}_{2.0}\text{Co}_{10.0}\text{Cu}_{1.48}\text{Fe}_{3.16}\text{Zr}_{0.194}$, IEEE Transactions on Magnetics, 16 (1980) 1003-1005.
- [81] E.P. Wohlfarth, Hard magnetic materials, Advances in Physics, 8 (1959) 87-224.
- [82] M. Zakotnik, C.O. Tudor, Commercial-scale recycling of NdFeB-type magnets with grain boundary modification yields products with 'designer properties' that exceed those of starting materials, Waste Management, 44 (2015) 48-54.
- [83] O. Gutfleisch, J. Lyubina, K.H. Müller, L. Schultz, FePt Hard Magnets, Advanced Engineering Materials, 7 (2005) 208-212.
- [84] M.R. Visokay, R. Sinclair, Direct formation of ordered CoPt and FePt compound thin films by sputtering, Applied Physics Letters, 66 (1995) 1692-1694.
- [85] M.S. Bhuiyan, B.J. Taylor, M. Paranthaman, J.R. Thompson, J.W. Sinclair, Microstructure and magnetic properties of electrodeposited cobalt films, Journal of Materials Science, 43 (2008) 1644-1649.
- [86] Y.H.K. C. W. Kim, D. K. Lee, I. C. Jeong, H. W. Kwon, Y. S. Kang, A Study of Exchange-Coupling Effect on $\text{Nd}_2\text{Fe}_{14}\text{B}$ / α -Fe Forming Core/Shell Shape, Solid State Phenomena, 119 (2007) 147-150.
- [87] R. Coehoorn, D.B. de Mooij, C. de Waard, Meltspun permanent magnet materials containing Fe₃B as the main phase, Journal of Magnetism and Magnetic Materials, 80 (1989) 101-104.
- [88] R. Skomski, J.M.D. Coey, Giant energy product in nanostructured two-phase magnets, Physical Review B, 48 (1993) 15812-15816.
- [89] A. Manaf, R.A. Buckley, H.A. Davies, New nanocrystalline high-remanence Nd-Fe-B alloys by rapid solidification, Journal of Magnetism and Magnetic Materials, 128 (1993) 302-306.
- [90] E.E. Fullerton, J.S. Jiang, S.D. Bader, Hard/soft magnetic heterostructures: model exchange-spring magnets, Journal of Magnetism and Magnetic Materials, 200 (1999) 392-404.
- [91] J. Ding, P.G. McCormick, R. Street, Remanence enhancement in mechanically alloyed isotropic $\text{Sm}_7\text{Fe}_{93}$ -nitride, Journal of Magnetism and Magnetic Materials, 124 (1993) 1-4.
- [92] A.J. Zambano, H. Oguchi, I. Takeuchi, Y. Choi, J.S. Jiang, J.P. Liu, S.E. Lofland, D. Josell, L.A. Bendersky, Dependence of exchange coupling interaction on micromagnetic constants in hard/soft magnetic bilayer systems, Physical Review B, 75 (2007) 144429.
- [93] J.L. Liao, X.H. Zhang, B. Ma, Z.Z. Zhang, Q.Y. Jin, Magnetization reversal of L10 FePt/Co/Fe trilayers, Journal of Applied Physics, 109 (2011) 07B769.
- [94] B.M. Lairson, M.R. Visokay, R. Sinclair, B.M. Clemens, Epitaxial PtFe(001) thin films on MgO(001) with perpendicular magnetic anisotropy, Applied Physics Letters, 62 (1993) 639-641.
- [95] N.H. Goo, Formation of hard magnetic L10-FePt, Modern Magnetic Systems, University of Stuttgart, Max Planck Institut für Metallforschung, Stuttgart, 2007.
- [96] A. Sakuma, First Principle Calculation of the Magnetocrystalline Anisotropy Energy of FePt and CoPt Ordered Alloys, Journal of the Physical Society of Japan, 63 (1994) 3053-3058.
- [97] T. Shima, K. Takanashi, Y.K. Takahashi, K. Hono, Coercivity exceeding 100kOe in epitaxially grown FePt sputtered films, Applied Physics Letters, 85 (2004) 2571-2573.

- [98] C.P. Luo, D.J. Sellmyer, Magnetic properties and structure of Fe/Pt thin films, *IEEE Transactions on Magnetics*, 31 (1995) 2764-2766.
- [99] D.A. Young, PHASE DIAGRAMS OF THE ELEMENTS, Office of Scientific and Technical Information, 1975, pp. 64.
- [100] H. Li, S. Liao, A magnetic-field-assisted solution-phase route to cobalt thin film composed of cobalt nanosheets, *Journal of Materials Chemistry*, 19 (2009) 5207-5211.
- [101] S. Sun, C.B. Murray, D. Weller, L. Folks, A. Moser, Monodisperse FePt Nanoparticles and Ferromagnetic FePt Nanocrystal Superlattices, *Science*, 287 (2000) 1989-1992.
- [102] C. Levent, C.H. George, Chemically synthesized FePt nanoparticles with controlled particle size, shape and composition, *Nanotechnology*, 20 (2009) 485602.
- [103] G. Roman, M. Martin, P.S. Joachim, Block copolymer micelle nanolithography, *Nanotechnology*, 14 (2003) 1153.
- [104] A.G. Mark, J.G. Gibbs, T.-C. Lee, P. Fischer, Hybrid nanocolloids with programmed three-dimensional shape and material composition, *Nat Mater*, 12 (2013) 802-807.
- [105] C.G. Willson, R.R. Dammel, A. Reiser, *Photoresist materials: a historical perspective*, 1997, pp. 28-41.
- [106] A. Breitling, D. Goll, Hard magnetic FePt thin films and nanopatterns, *Journal of Magnetism and Magnetic Materials*, 320 (2008) 1449-1456.
- [107] O. Kazakova, M. Hanson, E.B. Svedberg, Magnetic properties of FePt circular dots, *IEEE Transactions on Magnetics*, 39 (2003) 2747-2749.
- [108] Z.J. Yan, S. Takahashi, Y. Kondo, J. Ariake, T. Sakon, D.S. Xue, S. Ishio, Fabrication and magnetic properties of small FePt dot arrays, *Journal of Physics D: Applied Physics*, 44 (2011) 185002.
- [109] S.Y. Chou, P.R. Krauss, W. Zhang, L. Guo, L. Zhuang, Sub-10 nm imprint lithography and applications, *Journal of Vacuum Science & Technology B*, 15 (1997) 2897-2904.
- [110] C. Chin, Fabrication of Metallic Nanoparticle Arrays, *Journal of Young Investigators*, DOI (2007) 116.
- [111] T. Bublat, D. Goll, Large-area hard magnetic L1₀-FePt nanopatterns by nanoimprint lithography, *Nanotechnology*, 22 (2011) 315301.
- [112] W.H. Bragg, W.L. Bragg, The Reflection of X-rays by Crystals, *Proceedings of the Royal Society of London. Series A*, 88 (1913) 428-438.
- [113] A.I.B. John Clarke, *The SQUID Handbook: Fundamentals and Technology of SQUIDs and SQUID Systems*, Volume I, Wiley 2006.
- [114] L.D. Jackel, R.A. Buhrman, Noise in the rf SQUID, *Journal of Low Temperature Physics*, 19 (1975) 201-246.
- [115] R.B.G.a.F.R. Fickett, UNITS FOR MAGNETIC PROPERTIES, in: N.B.o.S. U.S. Department of Commerce (Ed.), Boulder, Colorado, 80303, 1985.
- [116] W. Sucksmith, J.E. Thompson, The Magnetic Anisotropy of Cobalt, *Proceedings of the Royal Society of London. Series A. Mathematical and Physical Sciences*, 225 (1954) 362-375.
- [117] A. Aharoni, Demagnetizing factors for rectangular ferromagnetic prisms, *Journal of Applied Physics*, 83 (1998) 3432-3434.
- [118] M. Sato, Y. Ishii, Simple and approximate expressions of demagnetizing factors of uniformly magnetized rectangular rod and cylinder, *Journal of Applied Physics*, 66 (1989) 983-985.

- [119] T.O. Paine, L.I. Mendelsohn, F.E. Luborsky, Effect of Shape Anisotropy on the Coercive Force of Elongated Single-Magnetic-Domain Iron Particles, *Physical Review*, 100 (1955) 1055-1059.
- [120] J. Gräfe, M. Schmidt, P. Audehm, G. Schütz, E. Goering, Application of magneto-optical Kerr effect to first-order reversal curve measurements, *Review of Scientific Instruments*, 85 (2014) 023901.
- [121] E.P. Amaladass, Magnetism of amorphous and highly anisotropic multilayer systems on flat substrates and nanospheres, Max-Planck-Institut für Metallforschung, UNIVERSITÄT STUTTGART, Stuttgart, 2008, pp. 120.
- [122] I.f.B.P.a.T. (IBPT), ANKA Accelerator, 2016.
- [123] G.B. Herman Winick, Klaus Halbach and John Harris, Wiggler and undulator magnets, *Physics Today* 34 (1981) 50.
- [124] ESRF, What is a synchrotron?
- [125] P. Preuss, The International Linear Collider
Part 2: Bright Beams of Electrons and Positrons, 2005.
- [126] S.-A. Carolin, X-ray absorption spectroscopy on magnetic nanoscale systems for modern applications, *Reports on Progress in Physics*, 78 (2015) 062501.
- [127] B.T. Thole, G. van der Laan, J.C. Fuggle, G.A. Sawatzky, R.C. Karnatak, J.M. Esteve, 3d, *Physical Review B*, 32 (1985) 5107-5118.
- [128] M. Abbate, J.B. Goedkoop, F.M.F. de Groot, M. Grioni, J.C. Fuggle, S. Hofmann, H. Petersen, M. Sacchi, Probing depth of soft x-ray absorption spectroscopy measured in total-electron-yield mode, *Surface and Interface Analysis*, 18 (1992) 65-69.
- [129] R. Nakajima, J. Stöhr, Y.U. Idzerda, Electron-yield saturation effects in L-edge x-ray magnetic circular dichroism spectra of Fe, Co, and Ni, *Physical Review B*, 59 (1999) 6421-6429.
- [130] E.J. Goering, Untersuchungen zur mikroskopischen Ursache der magnetokristallinen Anisotropie mit Hilfe des magnetischen Röntgenzirkulardichroismus und der resonanten magnetischen Röntgenreflektometrie, Würzburg, 2002.
- [131] B.L. Henke, E.M. Gullikson, J.C. Davis, X-Ray Interactions: Photoabsorption, Scattering, Transmission, and Reflection at $E = 50\text{-}30,000$ eV, $Z = 1\text{-}92$, *Atomic Data and Nuclear Data Tables*, 54 (1993) 181-342.
- [132] X-Ray Interactions With Matter.
- [133] T. Bublat, D. Goll, Temperature dependence of the magnetic properties of L10-FePt nanostructures and films, *Journal of Applied Physics*, 108 (2010) 113910.
- [134] I. Galanakis, M. Alouani, H. Dreyssé, Calculated magnetic properties of low-dimensional systems: the AuCu- and AuCu₃-type ferromagnets, *Journal of Magnetism and Magnetic Materials*, 242 (2002) 27-32.
- [135] R.S.J.M.D. Coey, Permanent magnetism, Institute of Physics Pub, Bristol, UK 1999.
- [136] Y. Liu, T.A. George, R. Skomski, D.J. Sellmyer, Aligned and exchange-coupled FePt-based films, *Applied Physics Letters*, 99 (2011) 172504.
- [137] M.J. Kramer, R.W. McCallum, I.A. Anderson, S. Constantinides, Prospects for Non-Rare Earth Permanent Magnets for Traction Motors and Generators, *JOM*, 64 (2012) 752-763.
- [138] J.P. Liu, C.P. Luo, Y. Liu, D.J. Sellmyer, High energy products in rapidly annealed nanoscale Fe/Pt multilayers, *Applied Physics Letters*, 72 (1998) 483-485.

- [139] W.-B. Cui, Y.K. Takahashi, K. Hono, Nd₂Fe₁₄B/FeCo Anisotropic Nanocomposite Films with a Large Maximum Energy Product, *Advanced Materials*, 24 (2012) 6530-6535.
- [140] R.F. Sabiryanov, S.S. Jaswal, Electronic structure and magnetic properties of hard/soft multilayers, *Journal of Magnetism and Magnetic Materials*, 177 (1998) 989-990.
- [141] S.K. Jain, B.L. Chittari, V. Kumar, Optimum thickness of soft magnetic phase in FePt/FeCo permanent magnet superlattices with high energy product and large magnetic anisotropy energy, *AIP Advances*, 6 (2016) 025027.

Acknowledgement

There are many of grateful for. First of all, Thank God for a guiding hand. And more than anyone, I would like to thank Prof. Dr. Gisela Schütz having me as a doctoral student at the Max-Planck-Institute for Intelligent Systems. With her scientific advice and personal support and encouragement, I could enjoy all scientific activities. Especially, her wealth knowledge of XMCD brought me to be confident about my research on element specific study of exchange-spring magnets. I would like to especially thank my supervisor PD Dr. Eberhard Goering who guided me and discussed the experience a lot during my Ph.D. period. I am grateful to Prof. Dr. Sebastian Loth being a committee member of my thesis.

Many thanks to all my colleagues at department of the Modern Magnetic Systems; Ms. Monika Kotz for her great administrative support, Yu-Chun Chen, Sapana Tripathi and Thomas Tietze for my beam time helpers, I would also like to thank the members of Working Group Goering (Magnetic X-ray Spectroscopy Joachim Gräfe, Mathias Schmidt and Patrick Audehm for their understanding and enjoyment, Claudia Stahl and Stephen Ruoß for SQUID magnetometry and 14 office mates, especially, Thomas Bublat, Andreas Dietz, Jonathan Bauch, and Robert Sittig for their kind helps with always smiley faces. Among them, Felix Groß and Daan Boltje gave me exciting and dynamic office life. There were many other people who helped me in MPI-Stuttgart. Thanks to Reinhart Völker and Frank Thiele for samples preparation, Theresa Dragon and Peter Kopold for kindly assist in preparing and measurement TEM, Dr. Helga Hoier in Maier department for XRD measurement. In Anka, Dr. Meng-Jie Huang, Dr. Peter Nagel, and Dr. Stefan Schuppler for helping in WERA beamline.

I would like to also thank Dr. Hans-Georg Libuda (Coordinator of International Max Planck Research School for Condensed Matter Science, formerly IMPRS - Advanced Materials) for his kind and constant help throughout my Ph.D. periods.

Special thanks to all of my Korean colleagues and friends in Stuttgart. Especially, Dr. Hyunchul Oh, Dr. Hyeon-Ho Jeong, Dr. Soon Jung Jung, Dr. Gihun Ryu, Dr. Songhak Yoon and Dr. Sungkyun Choi who taught, encouraged and helped me to overcome many difficulties in my research and German life.

I thank pastors and members of Nambugemeinde Kirche in Stuttgart and Hindol Church in Korea for praying during my Ph.D. periods.

Most importantly, I would like to express sincere thanks to my family. First is my beloved wife Bohyun Kim for her entire support, quiet patience, unwavering love and trust on me. I must also thank my parents and brother who encourage and supported me and never gave up hope for me.

Curriculum Vitae

Name: Kwanghyo Son
Date of Birth: 16. 11. 1982
Place of Birth: Seoul / Republic of Korea (South Korea)

Education

Sep. 2011 – Oct. 2017 Ph.D. in Physics
at Max Planck Institute for Intelligent Systems (MPI-IS),
Stuttgart, Germany
Advisor: Prof. Dr. Gisela Schütz

Mar. 2009 – Feb. 2011 M. Sc., Department of Physics,
Kookmin Graduate School, Seoul, Rep. of Korea
Advisor: Prof. Zeehoon Jang

Mar 2002 – Feb 2009 B. Sc., Department of Nano and Electronic Physics (Advanced)
The College of Natural Science,
Kookmin University, Seoul, Rep. of Korea
Advisor: Prof. Zeehoon Jang

Publication list

1. **K. Son**, Y.-C. Chen, S. Tripathi, T. Tietze, P. Nagel, S. Schuppler, G. Schütz, E. Goering, “Observation of magnetic reversal process in tuned exchange-spring nanomagnet by XMCD spectroscopy.” (in preparation)
2. **K. Son**, G. Ryu, H.-H. Jeong, P. Fisher, E. Goering, G. Schütz, “Enhancement of huge coercivity and maximum energy product in the rare-earth free hard magnet by two methods.” (in preparation)
3. **K. Son**, G. Schütz, E. Goering, “Magnetization reversal process of tuned exchange-spring nanomagnet patterns.” (in preparation)
4. **K. Son**, G. Schütz, E. Goering, “Programmable magnetic properties of exchange-spring artificial nanopatterns.” (in preparation)
5. **K. Son**, E. Goering, M. Hirscher, H. Oh, “Magnetic Behavior of Single-Chain Magnets in Metal Organic Frameworks CPO-27-Co”, *Journal of Nanoscience and Nanotechnology*, 17, 7541-7546, 2017
6. S. Yoon, **K. Son**, H. Hagemann, M. Widenmeyer, A. Weidenkaff, “Cr-substituted $\text{Ba}_2\text{In}_2\text{O}_5(\text{H}_2\text{O})_x$ ($x = 0.16, 0.74$)”, *Solid State Sciences*, 73, 1-6, 2017

7. H.-H. Jeong, M. Alarcón-Correa, A. G. Mark, **K. Son**, T.-C. Lee, P. Fisher, “Corrosion protected hybrid nanoparticles”, *Advanced Science*, 1700234, 2017
8. **K. Son**, J. N. Park, Sungwon Yoon, B. J. Suh, K. J. Cho, K. H. Kim, Z. H. Jang, “Magnetic Properties of Helicobacter Pylori Ferritins Genetically Prepared Under Different Biomineralization Conditions”, *Journal of Magnetism*, 21 (1), 20-24, 2016
9. G. Ryu, **K. Son**, “Surface defect free growth of a spin dimer TlCuCl_3 Compound crystals and investigations on its optical and magnetic properties”, *Journal of Solid State Chemistry*, 237, 358-363, 2016
10. G. Ryu, **K. Son**, G. Schütz, “Growth and characterization of large weak topological insulator Bi_2TeI single crystal by Bismuth self-flux method”, *Journal of Crystal Growth*, 440, 26-30, 2016
11. H.-H. Jeong, A.G. Mark, T.-C. Lee, **K. Son**, W. Chen, M. Alarcón-Correa, I. Kim, G. Schütz, P. Fisher, “Selectable Nanopattern Arrays for Nanolithographic Imprint and Etch-Mask Applications”, *Advanced Science*, 1500016, 2015 (**Front cover**)
12. **K. Son**, S. H. Kim, Z. H. Jang, B. J. Suh, “Development of a Pulsed Magnet System”, *New Physics: Sae Mulli*, Vol. 64, No. 6, pp. 638-643, 2014 (**Highlight**)
13. D. Sivanesan, **K. Son**, H.-J. Lee, K. T. Park, Z. H. Jang, B. J. Suh, S. Yoon, “Synthesis and magnetic characterization of a cubane-type Mn_4 cluster, housed in a sterically hindered carboxylate ligand pocket”, *Polyhedron*, Vol. 50, pp. 339-344, 2013.
14. **K. Son** and Z. H. Jang, “NMR Investigation of Ag Nanoparticles”, *Journal of the Korean Physical Society (JKPS)*, Vol. 62, No. 2, pp. 292-296, 2013.